Estimation and Modelling of Anisotropy in Vertical and Walkaway Seismic Profiles at Two North Caucasus Oil Fields

by

Colin P. Slater

(B.Sc., University of Edinburgh)

Thesis submitted for the degree of Doctor of Philosophy
Department of Geology and Geophysics
University of Edinburgh
1997

To

Lydie and Marie-Louise

ABSTRACT

This thesis considers anisotropy of seismic wave propagation at two oil fields in the North Caucasus region of Russia. In both oil fields, the reservoir zone displays a strong lateral variation in productivity which is thought to be caused by variations in fracture intensity. Such fractures may cause azimuthal anisotropy which can be detected in Vertical Seismic Profiles (VSPs) and Walkaway VSPs. The main aim of the thesis is to characterize this azimuthal anisotropy at three of the oil wells in these fields and to compare this anisotropy with productivity.

At each of the three wells, I determine azimuthal anisotropy from VSPs by the application of techniques for estimating shear-wave splitting. I find that the polarization direction of the fast shear-wave at all three wells is aligned approximately NNE-SSW. At two of the wells, forward modelling shows that the shear-wave splitting parameters in the top 1 km can be closely matched by a model containing aligned, vertical fractures, striking NNE-SSW, in approximately the top 1 km. I am unable to resolve the anisotropy of the reservoir zone at these two wells.

At the third well, strong azimuthal anisotropy of the reservoir zone is indicated by a large decrease of time delay between shear-waves propagating along vertical raypaths. This decrease is interpreted as an orthogonal rotation of the fast shear-wave polarization direction at a depth just above the reservoir zone. Using forward modelling, I successfully match these observations with three different fractured reservoir models: the first model contains vertical fractures striking orthogonal to the presumed maximum horizontal stress direction; the second model has dipping fractures striking parallel to the maximum horizontal stress direction; and the third model has a distribution of fractures with a high internal pore-fluid pressure. Consideration of only vertical raypaths through the reservoir cannot discriminate between these models. However, modelling of non-vertical propagation from far-offset VSPs suggests that the dipping fracture model is the better model, although the lack of observations above the reservoir at this well means that other interpretations cannot be excluded.

Walkaway VSPs, acquired at one of the oil fields, display anomalously-fast SV arrivals from in-line sources. Forward modelling shows that isotropic velocities that match the arrival times in a near-offset VSP cannot match the arrival-time behaviour observed in the Walkaways. In particular, the modelling indicates that velocities increase substantially as the direction of propagation moves away from the vertical direction. Such behaviour is observed along four walkaway directions at two wells and is interpreted as strong Transverse Isotropy with a Vertical Axis of symmetry (TIV). I use forward modelling to determine a TIV model that reproduces the arrival times of all the main compressional and shear-wave phases. This model confirms that the anomalously-fast SV arrivals are generated near cusps on the group-velocity surface. Such anisotropic cusps are caused by high curvature of the SV phase-velocity surface. Modelling the amplitudes of the cusp phases indicates that most of the TIV is concentrated in the 1.2 km-thick interval of near-continuous Maikop clay. Three-component coupling of signals is observed on the seismograms. To model the coupling I include, within the top 1 km, the vertical-crack anisotropy estimated from the VSPs. In the final model, the Maikop clay has strong TIV defined by 41% SH- and 25% SV-anisotropy.

ACKNOWLEDGEMENTS

First, I wish to thank Stuart Crampin, my supervisor, for his enthusiasm and encouragement during my studies. He has always made himself available to answer my questions on anisotropy and to give advice on my research. I would also like to thank Bob Pearce, my second supervisor, for the support and valuable guidance he has given to me while I was writing this thesis.

I gratefully acknowledge the financial support of the BGS and the sponsors of the Edinburgh Anisotropy Project, allowing me to attend various conferences in the U.K. and abroad, including the 5IWSA in Banff, Canada, and the EAEG in Vienna, Austria.

Many members of staff and students at the BGS have helped me in my work. In particular, I would like to thank Phil Wild for his help with computer programs; Ruth Addinall, Hugh Gough and Charlie Fyfe for their help and assistance in all other aspects of computing; Gareth Yardley, Brian Baptie and Steve Horne for the enjoyable discussions on science and anisotropy. I would like to thank especially Steve Horne for the interest he has shown in my work and the help he has given me.

I would like to express my gratitude and admiration to Leonid Brodov, Vasiliy Kuznetsov and their families for the generosity and warmth I received while on my visits to Russia.

I thank Stuart Crampin, Bob Pearce, Xiang-Yang Li, Enru Liu, Steve Horne and Lydie Slater for their time and effort spent reviewing parts of this thesis.

I would also like to thank my parents, Alex and Madeline, and my wee sister, Gemma, for all their kindness and support over the years. Above all, I would like to thank Lydie, my wife, for the effort she has made and the patience she has shown over these years.

CONTENTS

Inside back cover:

1. List of publications.
2. Slater, C., Crampin, S., Brodov, L.Y., and Kuznetsov, V.M., 1993. Observations of anisotropic cusps in transversely isotropic clay, *Can. J. Expl. Geophys.*, **29**, 216-226.

CHAPTER ONE

INTRODUCTION

1.1 INTRODUCTION

The number of experimental observations of seismic anisotropy in the Earth's crust has increased greatly during the last couple of decades (Crampin and Lovell, 1991). These numerous observations have come from analysing propagation through many rock types in many different geological environments (Crampin, 1994) and suggest that seismic isotropy is the exception rather than the rule at *in-situ* temperature and pressure conditions.

In crustal rocks, seismic anisotropy is attributed to structural ordering on a scale below the wavelength employed. An example of structural ordering is the alignment of cracks and fractures which are known to frequently control the propagation of fluids through sedimentary basins. Consequently, measurements from experiments designed to detect anisotropy may give important information on the small-scale structural order of hydrocarbon reservoirs (MacBeth, 1995). Mueller (1991), in one such experiment, interpreted variations in reflection amplitudes at the top of the Austin Chalk (Texas) in terms of seismic anisotropy induced by a zone of high fracture intensity. This interpretation was later confirmed by horizontal drilling, and resulted in a well with significantly higher productivity than surrounding wells.

In this thesis, I investigate the seismic anisotropy at two oil fields which display a strong lateral variation in productivity. The oil fields are within the North Caucasus foredeep and production, at depth of 2 km, is from the lowest 100 metres of a 1.2 km-thick sequence of near-continuous Maikop clay. The lateral variation in productivity is poorly understood. Though, it has been suggested that the productivity is linked to lateral variations in fracture intensity associated with basement faulting (Chepak *et al.*, 1983, Klubova, 1991, Naryzhnyy, 1986).

Shear-wave investigations of the internal structure of the claystone reservoir in the North Caucasus are aided by the simplicity of the overlying geology, extremely flat topography and low shear-wave velocities. Consequently, these oil fields represent an almost ideal laboratory for the study of seismic anisotropy.

1.2 THESIS OBJECTIVES

There are two principal aims of this thesis. The first aim is to determine whether there is a relationship between seismic anisotropy and productivity of the reservoir near the base of the Maikop clay. This is done by measurement and modelling of anisotropy parameters from Vertical Seismic Profiles (VSPs) at three wells in the two oil fields. The second aim is to interpret anomalously-fast shear-wave arrivals observed in walkaway VSPs at one of the oil fields. This is done by forward modelling of the walkaway VSP seismograms.

The structure of this thesis is as follows: in Chapter Two, I introduce the theory of wave motion in anisotropic media and associated phenomena utilized in subsequent chapters. Then I review the most likely causes of seismic anisotropy in sedimentary basins. Next, I give a summary of the algorithms used in this thesis to detect and quantify azimuthal anisotropy in the VSPs. Then I give a description of the method used to compute synthetic seismograms. Finally, I describe briefly the theories I use for describing the seismic response of cracked rock.

In Chapters Three and Four, I present a case study investigating shear-wave anisotropy in five VSPs recorded at three wells in two oil fields. In Chapter Three, I begin by giving a short summary of the geology of the study area. I then present the available information regarding oil productivity at the three wells. Next, I describe previous experiments on the seismic anisotropy of the Maikop clays, followed by a summary of the acquisition and processing of the VSP data. Finally, I describe the measurement of anisotropy parameters and compare the results from the three wells. I find that above the 2 km-deep reservoir zone, most of the azimuthal anisotropy appears to be confined to approximately the uppermost 1 km. This interval consists of a sequence of sandstone, limestone and clay layers overlying the near-continuous Maikop clay. With the exception of the reservoir zone, the Maikop clay appears to

be characterized by a lack of azimuthal anisotropy. Regarding the reservoir, I find that the anisotropy of the reservoir zone is indeterminable at two wells. However, at the third well, the reservoir zone displays anisotropy which is characterized by a pronounced decrease in time delay for near-vertical propagation.

In Chapter Four, I model the shear-wave splitting measurements from the five VSPs. Firstly, I consider the strong Transverse Isotropy with a Vertical axis of symmetry (TIV) determined in Chapter Five. I show that a slight tilt of the symmetry axis of the TIV is unlikely to be the cause of the azimuthal anisotropy in the layers above the Maikop clay. Next, I model the azimuthal anisotropy in the layers above the clay using a combination of aligned microcracks embedded in the strong TIV. It is found that the shear-wave splitting measurements in the upper 1 km at two wells, although quite different, are matched by models with similar distributions of microcracks. Finally, using iterative forward modelling, I determine three different cracked-reservoir models to match the anisotropy parameters in the reservoir zone at one well.

In Chapter Five, I model arrival times and amplitudes recorded in walkaway VSPs at one of the oil fields. I confirm, by matching with synthetic seismograms, that anomalously-fast shear-wave arrivals on the observed seismograms are associated with cusps in the group-velocity surface. The cuspidal phases are caused by strong TIV with SH-wave and qSV-wave anisotropies in the Maikop clay equal to 41% and 25%, respectively. These appear to be only the second reported observation of anisotropic cusps and they are the first to be confirmed by full waveform synthetic seismograms.

In Chapter Six, I review the findings of this thesis, present my conclusions and give some suggestions for future work in the North Caucasus oil fields.

In Appendix A, I describe a case study of near-surface anisotropy at a Russian field test site in the Jaroslavl region of Russia. It is included as an appendix because it is not directly related to the main body of work in this thesis and also because few firm conclusions are made. The lack of firm conclusions is due to inconsistencies in the reported acquisition parameters and a general lack of relevant information. However, the processed seismograms display shear waves of a high quality and yield stable estimates of anisotropy, therefore, if the necessary information were available definite conclusions could be made. In this study, multi-offset VSPs are processed and azimuthal anisotropy parameters are estimated. The anisotropy parameters from

the 230 m-deep well display a high degree of consistency and indicate that the near-surface at the test site has a vertical shear-wave anisotropy of 4%. Also, using forward modelling, I identify TIV in the near-surface and match SH arrival times in a far-offset VSP with a model characterized by up to 44% SH anisotropy.

CHAPTER TWO

SEISMIC ANISOTROPY: BACKGROUND THEORY AND PROCESSING METHODS

2.1 INTRODUCTION

In this section, I will introduce some of the fundamentals of seismic anisotropy relevant to understanding the work in this thesis. Firstly, though, I will explain what is implied when a medium is described as anisotropic.

If a measured physical property of a medium varies with direction, the medium is called "anisotropic" with respect to that property. If, on the other hand, the physical property is equal in all directions, the medium is called "isotropic". The term "seismic anisotropy" is usually used to refer to directional variation in physical properties of a displacement wavefield propagating through rock, although the medium is sometimes a synthetic laboratory material.

2.2 FUNDAMENTALS OF WAVE MOTION IN ANISOTROPIC MEDIA

The fundamental mathematical description of elastic wave propagation in anisotropic media has been known since the work of Love (1892). More recent detailed descriptions may be found in Musgrave (1970), Crampin (1981), and Helbig (1994). In this section, I will outline the important features of the mathematical description and then summarize some of the physical aspects of body-wave propagation in anisotropic media.

Stress and strain in a linearly-elastic solid can be related using the three-dimensional generalization of Hooke's Law:

$$\sigma_{jk} = c_{jkmn}\, \epsilon_{mn} \quad ; \tag{2-1}$$

where σ_{jk} is the element *jk* of the symmetric second-order stress tensor, ϵ_{mn} is the *mn* element of the second-order strain tensor, and c_{jkmn} is the element *jkmn* of the fourth-order stiffness tensor, $\boldsymbol{C}$. All subscripts take the values 1, 2 and 3, and Einstein's summation convention on repeated subscripts applies. The elements ϵ_{mn} of the strain tensor are defined by the spatial derivatives of the displacement vector $\boldsymbol{U}$:

$$\epsilon_{mn} = \tfrac{1}{2}(\partial u_m/\partial x_n + \partial u_n/\partial x_m) \; . \tag{2-2}$$

The stiffness tensor $\boldsymbol{C}$ comprises 3^4=81 elements of elastic constants with the following symmetries:

$$c_{jkmn} = c_{kjmn} = c_{mnjk} \; . \tag{2-3}$$

These symmetries, along with energy considerations, reduce the number of independent elastic constants of $\boldsymbol{C}$ to a maximum of 21 (Crampin, 1981). [This allows the elements of $\boldsymbol{C}$ to be written in a condensed form, c_{pq}, where the subscript pairs *jk* and *mn* are assigned to *p* and *q* respectively, according to: 11 ⇒ 1; 22 ⇒ 2; 33 ⇒ 3; 32 ⇒ 4; 31 ⇒ 5; 21 ⇒ 6.]

Substituting Eqn. 2-1 into Newton's Second Law relating force, density and acceleration, leads to the equations of motion for infinitesimal displacements of an elementary volume:

$$\rho \ddot{u}_j = c_{jkmn} \, u_{m,nk} \quad ; \tag{2-4}$$

where ρ is the density and $u_{m,nk}=\partial^2 u_m/\partial x_n \partial x_k$. A general expression for a homogeneous plane-wave travelling in a chosen direction can be substituted into Eqn. 2-4 to yield three simultaneous (Kelvin-Christoffel) equations. There are a number of ways of solving these equations. One way is to find numerical solutions by reformulating the equations as the following linear eigenvalue problem:

$$(\boldsymbol{T} - \rho \, v^2 \boldsymbol{I}) \, \boldsymbol{a} = 0 \; ; \tag{2-5}$$

where *v* is the plane-wave (phase) velocity in the chosen propagation direction, $\boldsymbol{T}$ is a 3×3 matrix with elements $\{c_{j1k1}\}$, $\boldsymbol{I}$ is the 3×3 identity matrix and $\boldsymbol{a}$ is the amplitude vector of the wave displacements.

Since $\boldsymbol{T}$ is a real symmetric positive-definite matrix, Eqn. 2-5 yields three real positive roots for ρv^2 with orthogonal eigenvectors $\boldsymbol{a}$. The three roots indicate that along the direction of plane-wave propagation there are, in general, three body-waves

travelling with different velocities and fixed orthogonal polarization vectors. The three body waves are: one *quasi* P-wave (*qP*) with approximate longitudinal particle motion; and two *quasi* shear-waves (*qS1* and *qS2*) with particle motion approximately transverse to the direction of propagation in two orthogonal directions. The phase-velocities of these three body waves vary with propagation direction in a way determined by the symmetry properties of the elastic constants within the stiffness tensor.

Shear-wave Splitting

For the last few decades, seismic exploration within sedimentary basins has been almost completely based on utilising reflected P-wave energy to image large-scale structural features. Although they have been extraordinarily successful in delineating the large structures, these P-wave surveys have been relatively unsuccessful in determining the internal structure of reservoirs, which is usually at a scale significantly below the seismic wavelength. Internal structures, such as fracture orientation, frequently control the flow of hydrocarbons within reservoirs. Therefore, obtaining knowledge about such small-scale features is vitally important for evaluation and extraction of the hydrocarbon reserves. Recent attempts to characterize remotely the internal structure of reservoirs have been based on the often made observation that reservoirs display some form of structural ordering below the seismic wavelength (MacBeth, 1993). Theoretically, rocks which possess a small-scale ordering will likely be anisotropic with respect to the seismic wavefield (Crampin *et al.*, 1986). The most distinguishing aspect of seismic wave propagation in anisotropic media are the fixed polarizations of the two *quasi*-shear waves along each propagation direction (Crampin, 1985). This is shown schematically in Fig. 2.1 for a typical Vertical Seismic Profile (VSP). It can be seen in Fig. 2.1 that upon entering the anisotropic medium, the plane shear-wave with transverse polarization aligned with the source polarization "splits" into two *quasi*-shear waves with different velocities and orthogonal polarizations fixed for the particular propagation direction. Such splitting is also referred to as birefringence or double refraction and is recognized in recorded seismograms as a characteristic signature of two orthogonally polarized shear-waves with a slower shear-wave arriving after a time delay relative to the faster shear-wave.

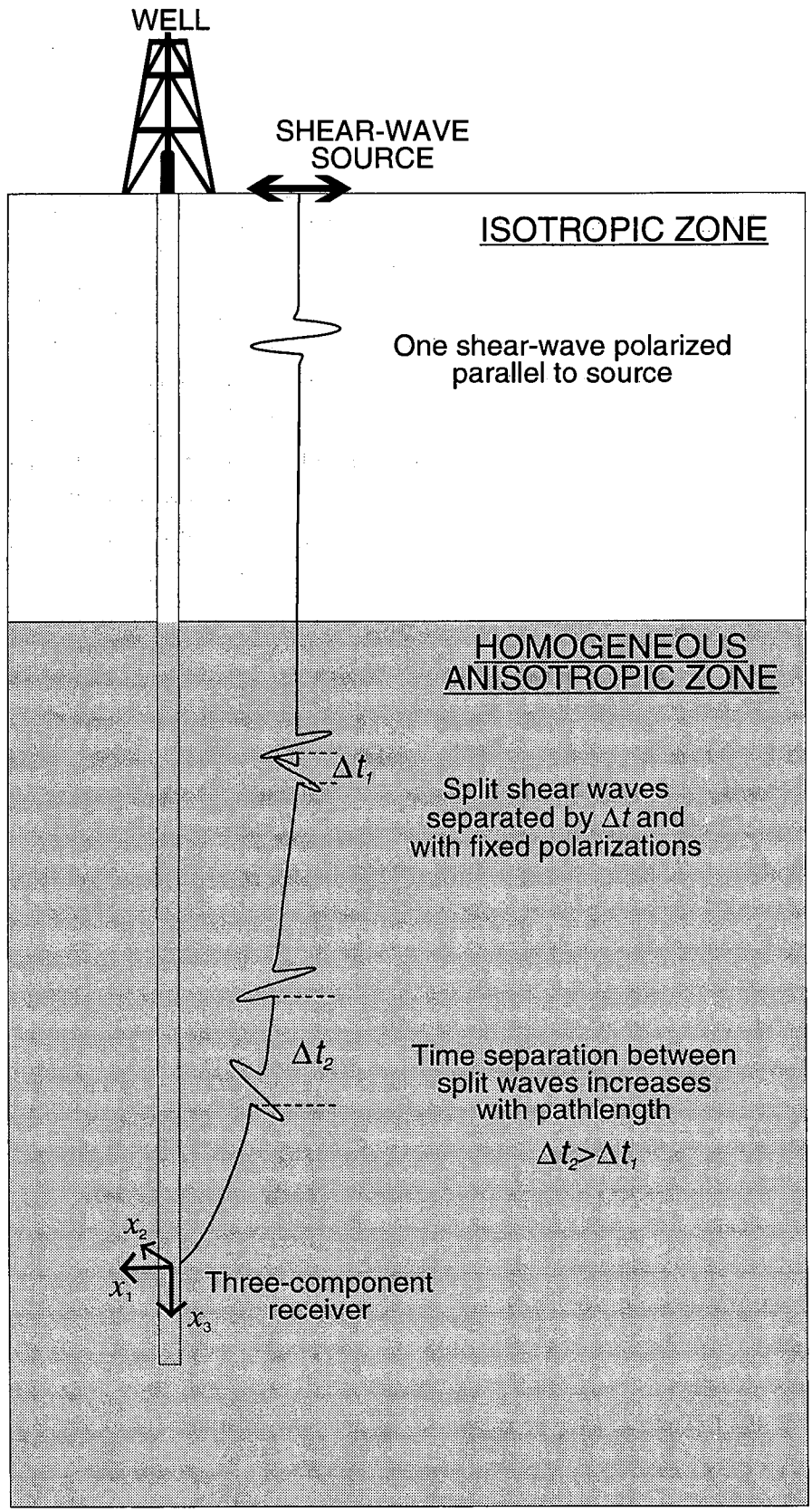

Figure 2.1: Schematic representation of shear-wave splitting recorded in a VSP. On entering an anisotropic zone, the source-polarized shear-wave splits into two polarizations fixed by the particular symmetry of the anisotropic media. The two shear waves propagate with different velocities resulting in a time separation between the two shear waves which increases with path length in the anisotropic zone.

Group Velocity

The general existence of two shear-waves with different velocities and orthogonal polarizations fixed for each propagation direction is fundamentally different from propagation in isotropic media. Another fundamental difference between wave motion in isotropic and anisotropic media is the deviation of the direction of energy transport from the wavefront normal, shown schematically in Fig. 2.2. The surface W in Fig. 2.2 represents a wavefront at a time τ travelling outwards from a point source located at the origin in a homogeneous anisotropic medium. After a time $\Delta\tau$ the wavefront has moved to the position indicated by the dashed surface W'. Energy propagates radially outwards in the homogeneous half-space and, along one particular ray direction at an angle ϕ to the x_1 axis, the energy travels distances equal to OA and OA' in times τ and $\tau+\Delta\tau$, respectively. The (group) velocity of energy transport along this ray direction is therefore equal to $(A'-A)/\Delta\tau$. The deviation between the ray direction and the wavefront normal is indicated in Fig. 2.2 by drawing the plane of equal phase (tangent) through A. The tangent has a normal at an angle θ to the x_1 axis and the deviation of energy transport from the wavefront normal is equal to $(\phi-\theta)$. The parallel tangents through points A and A' are true representations of wavefronts along one direction of energy transport. From considering the tangents at B and B', it is easily seen that the normal velocity is always less than the velocity of energy transport along the corresponding ray direction by a factor of $\cos(\phi-\theta)$. The normal (phase) velocity corresponding to a particular ray direction represents the velocity of a plane-wave in the medium with a propagation vector at angle θ to the x_1 axis.

2.3 CAUSES OF SEISMIC ANISOTROPY IN SEDIMENTARY BASINS

Crampin, Chesnokov and Hipkin (1984) give a concise classification and summary of the most likely causes of seismic anisotropy in the Earth's crust and upper mantle. In summary, the small-scale structural order which causes anisotropy in sedimentary basins are most likely to result from some or all of the following:

(i) lithological anisotropy of clay and shale (argillaceous) rocks due to foliation of clay minerals;

(ii) thin layering;

(iii) aligned fractures, cracks and pore space.

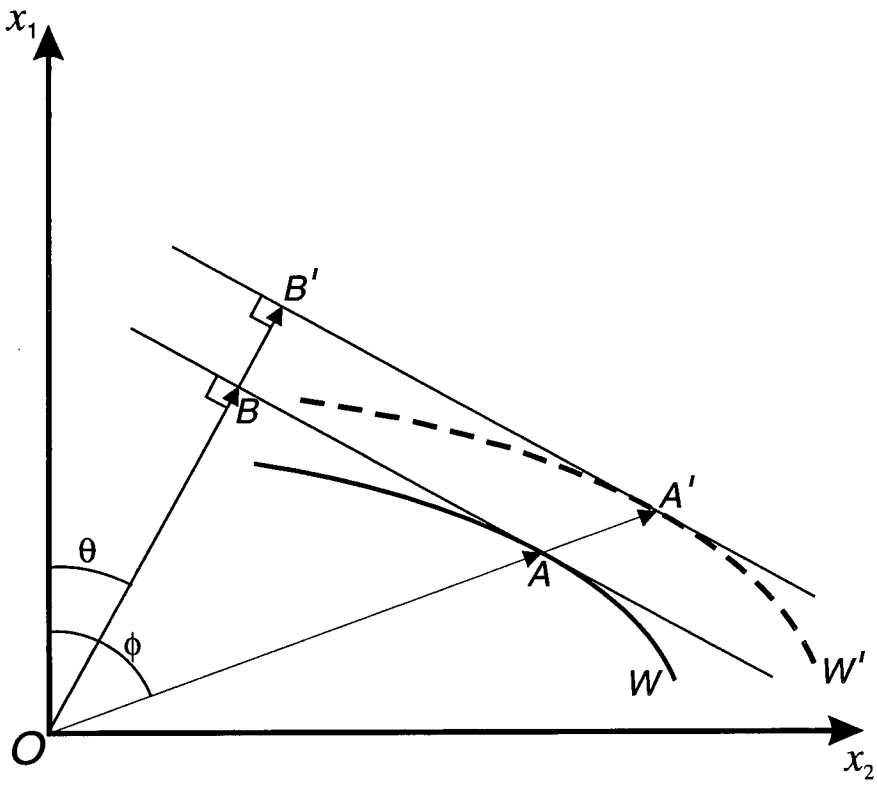

Figure 2.2: Schematic diagram illustrating the deviation of the direction of energy transport from the wavefront normal in anisotropic media. Energy travels to the point A along a radial direction at an angle ϕ-θ to the normal at point A.

All three mechanisms give rise to anisotropy with one axis of cylindrical symmetry, although the orientation of the axis is not the same in each case. This type of anisotropy is known as hexagonal symmetry or transverse isotropy and is defined by five independent elastic constants of the stiffness tensor. The three mechanisms are schematically shown in Fig. 2.3 along with typical equal-area projections of the fast (*qS1*) shear-wave horizontal polarization directions. It can be seen in Fig. 2.3 that for mechanisms (i) and (ii) the infinite-fold axis of rotation is normal to the bedding planes and therefore usually near vertical in sedimentary basins. Such anisotropy is typically referred to as Transverse Isotropy about a Vertical axis of symmetry (TIV).

Mechanism (iii), on the other hand, has an axis parallel to the crack or fracture normal direction. If this direction represents the direction of minimum principal stress then it is likely to be near horizontal for rocks at depths where the overburden lithostatic pressure exceeds the minimum horizontal stress (Crampin, 1990). This type of anisotropy is commonly referred to as Transverse Isotropy about a Horizontal axis of symmetry (TIH) and is characterized by azimuthal variations in the velocity of the shear-waves and distinctive azimuthal variations in the polarizations of the leading split shear-wave.

A medium formed by a combination of TIV and TIH anisotropies has a lower-order, orthorhombic symmetry defined by nine independent elastic constants. Models with orthorhombic symmetry have been used by Bush and Crampin (1991) to match anomalous shear-wave polarizations in VSPs recorded in the Paris Basin, and by Yardley and Crampin (1993) to match shear-wave splitting measurements in the Austin Chalk, Texas.

In this thesis, the seismograms display evidence of orthorhombic and TIV anisotropy: orthorhombic anisotropy in the uppermost 800-900 m and in the reservoir zone; and TIV through a 1.2 km-thick sequence of Maikop clay.

(a) Transverse Isotropy about a Vertical Axis of Symmetry

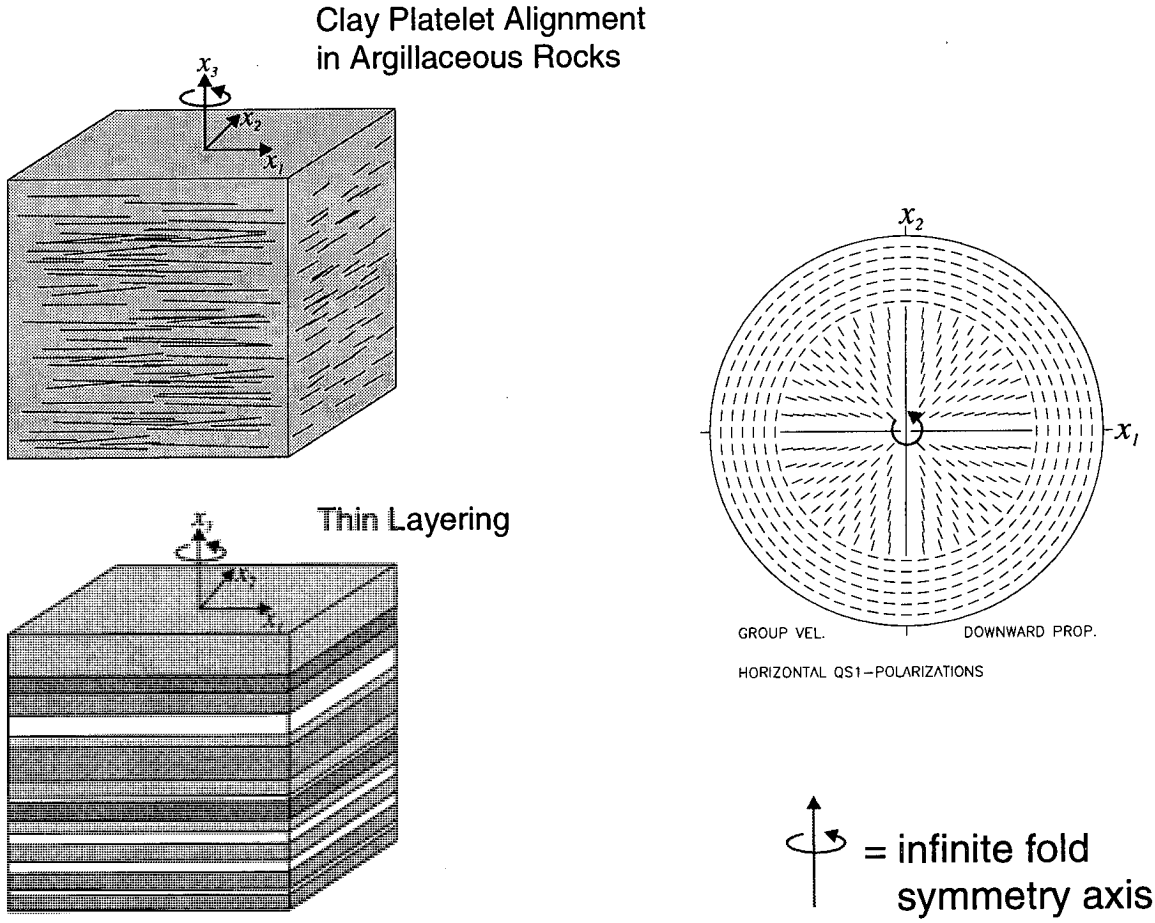

(b) Transverse Isotropy about a Horizontal Axis of Symmetry

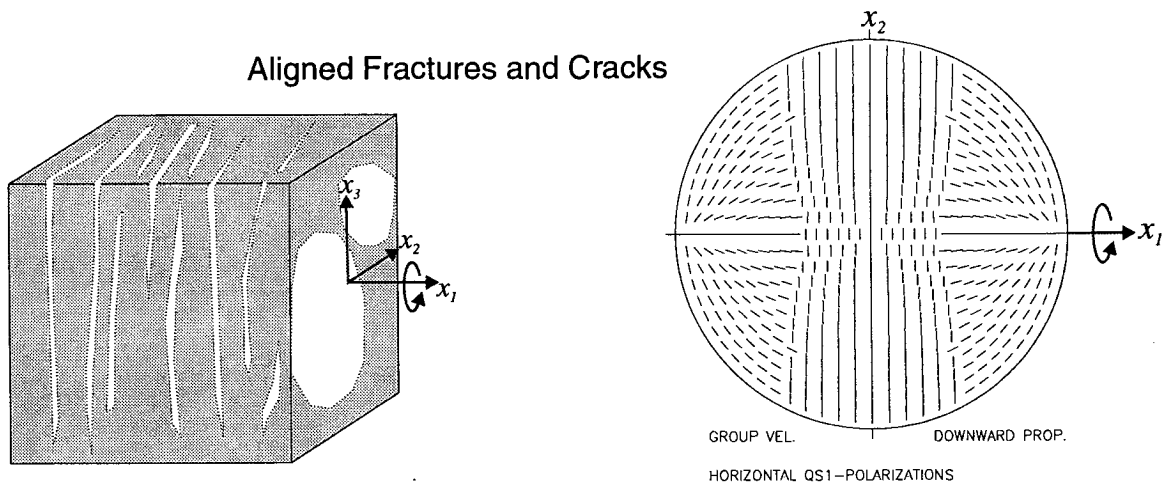

Figure 2.3: Schematic representation of the likely causes of seismic anisotropy in sedimentary basins which result in transverse isotropy about (**a**) a vertical symmetry axis and (**b**) a horizontal symmetry axis. The equal area plots on the right-hand side indicate the typical horizontal component of qS1 polarizations associated with the two different orientations of the symmetry axis.

2.3.1 Lithological Anisotropy of Argillaceous Rocks

Understanding the anisotropy of argillaceous rocks is important for exploration in sedimentary basins as these rocks constitute between 50-75% of the infill of most basins. (Argillaceous is the term often used to refer collectively to clay and shale rock types.) Strong seismic anisotropy of argillaceous rock has long been recognised in field experiments. For example, Jolly (1956) and Brodov *et al.* (1984) report horizontal SH velocities greater than vertical shear-wave velocities by factors of 2 and 1.4, respectively. Other relevant field observations include those of White, Martineau-Nicoletis and Monash (1983), Robertson and Corrigan (1983), and Banik (1984). Almost all field experiments have indicated that argillaceous rocks are transversely isotropic about a direction normal to the bedding. This has been confirmed by ultrasonic laboratory measurements of P-wave velocities by Kaarsberg (1959) and of P- and shear-wave velocities by Jones and Wang (1981). It is now widely accepted that the anisotropy of argillaceous rocks is caused by the alignment of thin clay platelets parallel to the bedding planes, which is routinely observed in scanning electron micrographs of shales.

One method of predicting the anisotropy of argillaceous rocks has been developed by Hornby, Schwartz and Hudson (1994). The method is based on a new processing technique for estimating the distribution of clay platelet alignments from scanning electron micrographs and calculates effective elastic constants assuming hexagonal symmetry.

2.3.2 Thin Layering

Postma (1955) and Backus (1962) have shown theoretically that propagation of seismic waves though a sequence of isotropic layers which are thin compared to the wavelength is equivalent to propagation through a homogeneous transversely isotropic medium. In horizontally stratified basins, every vertical plane is a plane of mirror symmetry therefore the shear-waves split into strictly SH and SV polarizations and the velocity of propagation of a particular wave type is determined by the angle of propagation relative to the symmetry axis.

2.3.3 Aligned Fractures, Cracks and Pore Space

The hypothesis known as extensive-dilatancy anisotropy (EDA) - which states that the earth is pervaded by a distribution of stress-aligned fluid filled cracks - was introduced by Crampin, Evans and Atkinson (1984) to explain the apparently stress-aligned polarizations of split shear waves along ray paths through many different crustal rock types. Soon afterwards, Crampin (1987) extended this hypothesis to include larger fractures and partially oriented pore space which are probably not directly stress induced but are stress aligned. A comprehensive account of the main arguments for accepting the hypothesis has been presented by Crampin (1993b) who, in the same paper, includes a useful summary of observations of seismic anisotropy. Recent work from Zatsepin and Crampin (1997) on developing an Anisotropic Poro-Elastic (APE) theory of cracked rock suggests that open EDA microcracks are predominantly intergranular microcracks with the crack normals arranged in a distribution about the minimum principal component of the stress-field.

2.4 DETECTION OF SHEAR-WAVE SPLITTING IN SEDIMENTARY BASINS

At present, the most reliable method of characterizing seismic anisotropy in sedimentary basins is by analysing shear-waves using three-component seismograms recorded in VSPs (Crampin, 1983). This is principally for three reasons: firstly, recording at depth avoids free-surface complications which can affect the shear-waves when recording on the surface (Evans, 1984); secondly, the direct wavefield recorded at a downhole receiver has a large signal-to-noise ratio compared to typical reflections recorded at the surface; and thirdly, the recording of transmitted arrivals at different depths allows depth variations of anisotropy to be easily recognised.

Figure 2.1 schematically illustrates shear-wave recording in a near-offset VSP. The shear-waves are excited at the surface by a horizontal force and propagate along near-vertical raypaths through an anisotropic zone caused, for example, by vertical fractures. Within the fractured zone, the shear-wave splits into two independent shear-waves with orthogonal horizontal polarizations which are subsequently recorded downhole by the two horizontal receiver components. Commonly, recordings are made from two sources with orthogonal horizontal polarizations. This produces a

more complete seismic response and allows shear-wave splitting measurements to be made by the application of dual-source techniques which are generally more stable than measurements made from single-source recordings. In the VSPs analyzed in this thesis, some levels were recorded with one horizontal source polarization and others with two orthogonal horizontal polarizations. Therefore, to extract the splitting parameters from all receiver levels, I apply both single- and dual-source techniques. I now give some details on the particular techniques used in this thesis.

DTS Single-source Technique

In this thesis, I use the Direct Time Series (DTS), single-source, method of Campden (1990) to extract the shear-wave splitting parameters from datasets recorded with one horizontal source polarization. Other single-source methods were tried but, although they gave generally similar results to DTS, they were found to be less stable. The DTS technique assumes that the shear waves are split orthogonally and works by first aligning the X and Y receiver components so they lie parallel and perpendicular to the source polarization direction. This arrangement is shown schematically in Fig. 2.4, where the source function is $s_x(t)$. Next, the receiver components, X and Y, are incrementally rotated in steps of 1° over a range of 180°. After each rotation, the technique assumes that the rotated receivers X' and Y' are aligned with the fast (*qS1*) and slow (*qS2*) split shear-waves, respectively, as shown in Fig. 2.4. If they are aligned, the rotated receiver components X' and Y' record the *qS1* and *qS2* waveforms with amplitudes equal to $s_x(t)\cos\theta$ and $s_x(t)\sin\theta$, respectively. Therefore, for each angle of rotation, the technique cross-multiplies the two receiver components X' and Y' by $\sin\theta$ and $\cos\theta$, respectively, and searches for the minimum difference between the components over a range of negative time shifts applied to the X' component. Finally, the technique searches for the global minimum difference as a function of the rotation angle θ and the relative time shift. The angle corresponding to the global minimum is the *qS1* direction with respect to the source direction.

DCT and DIT Dual-source Techniques

I use two techniques, DCT and DIT, to measure shear-wave splitting in dual-source VSP datasets recorded with two orthogonal source polarizations in the horizontal plane (Zeng and MacBeth, 1993b). The techniques are based on a vector convolutional

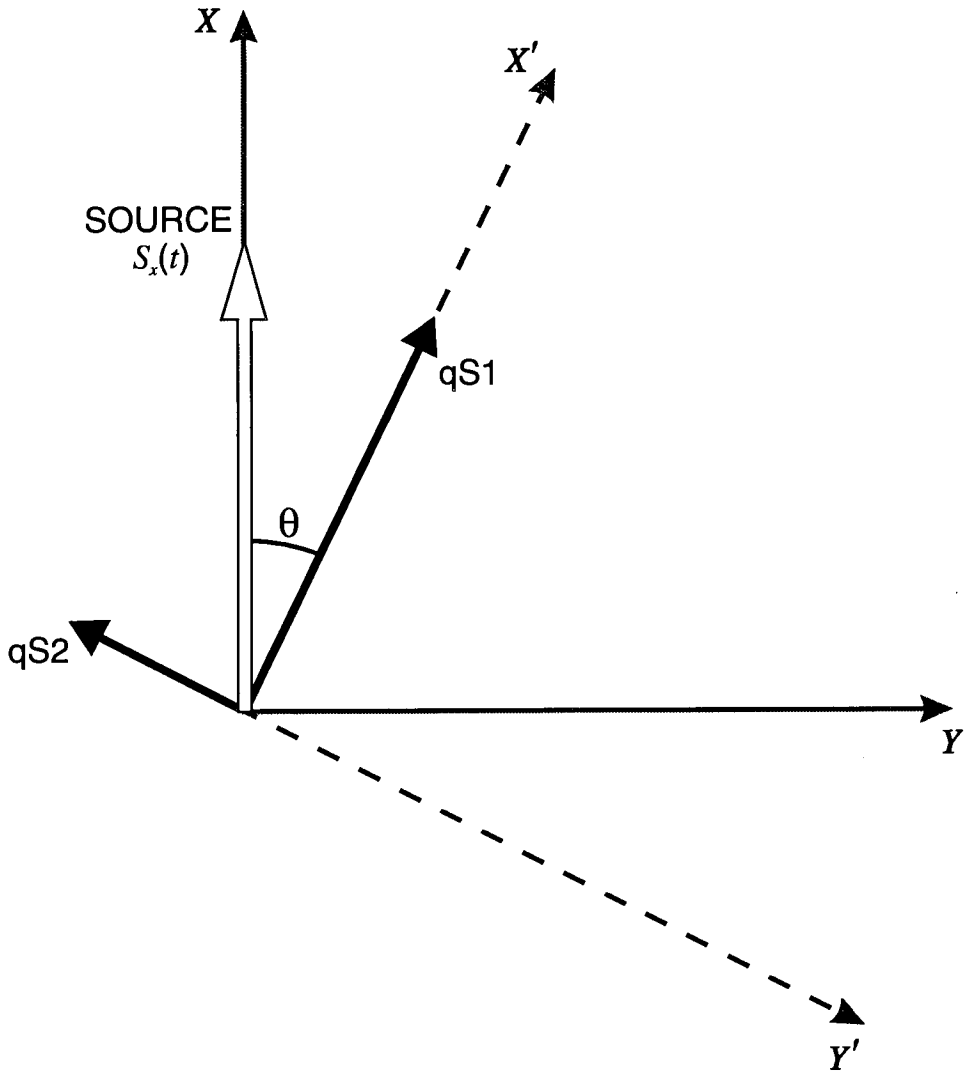

Figure 2.4: Graphic illustration of the DTS single-source technique used to determine the qS1 polarization direction of the fast split shear-wave and the relative time delay between split shear-waves.

Earth model. They assume a simplified 1D earth structure, medium homogeneity, near-vertical propagation and a horizontal plane of symmetry. The displacements of the direct wavefield recorded downhole by the two horizontal geophones, $\boldsymbol{G}(t)$, from two orthogonal surface sources, $\boldsymbol{S}(t)$, may be expressed as:

$$\boldsymbol{G}(t) = \left[\boldsymbol{R}^{T}(\theta)\boldsymbol{\Lambda}(t;t_f,t_s)\boldsymbol{R}(\theta)\right] * \boldsymbol{S}(t); \tag{2-6}$$

where * represents a convolution in the time domain and θ is the polarization of the leading split shear-wave with respect to the radial direction. $\boldsymbol{R}(\theta)$ is a conventional rotation matrix given by :

$$\boldsymbol{R}(\theta) = \begin{bmatrix} \cos\theta & \sin\theta \\ -\sin\theta & \cos\theta \end{bmatrix}; \tag{2-7}$$

and $\boldsymbol{\Lambda}(t)$ is an operator describing the fast and slow split shear-wave arrival times represented by the matrix:

$$\boldsymbol{\Lambda} = \begin{bmatrix} \lambda_f(t) & 0 \\ 0 & \lambda_s(t) \end{bmatrix}. \tag{2-8}$$

For sources and receivers aligned along the inline and crossline directions, indicated by subscripts X and Y, respectively, the recorded data matrix is represented by:

$$\boldsymbol{G}(t) = \begin{bmatrix} d_{XX}(t) & d_{XY}(t) \\ d_{YX}(t) & d_{YY}(t) \end{bmatrix}; \tag{2-9}$$

and the source matrix by:

$$\boldsymbol{S}(t) = \begin{bmatrix} s_X(t) & 0 \\ 0 & s_Y(t) \end{bmatrix}. \tag{2-10}$$

Thus, $d_{XY}(t)$ in Eqn. 2-9 represents the time series recorded on the crossline (Y) receiver from an inline (X) source. Early methods of solving Eqn. 2-6 to obtain the fast split shear-wave polarization, θ, were based on computationally-intensive numerical rotations of the recorded data matrix (Alford, 1986). The DCT technique of Zeng and MacBeth (1993b) efficiently determines an algebraic solution of Eqn. 2-6

for θ under the principal assumption that a uniform anisotropic medium exists between source and receiver. The method is essentially an algebraic least-squares minimization of the off-diagonal energy on the recorded data matrix, $\boldsymbol{G}(t)$, over the whole time window containing the main shear-wave arrivals. After estimating the polarization angle, θ, the data matrix is then rotated by this angle, which is equivalent to aligning the X and Y components of the source and receiver into the fast and slow shear-wave polarization directions, respectively. The relative time delay separating the two shear waves, $\Delta t=(t_f-t_s)$, is then obtained by cross-correlation of the main diagonals of the rotated data matrix.

If the recorded data matrix is not symmetric, it is inappropriate to apply the DCT technique. Asymmetry of the data matrix may arise from a number of causes. The two most likely causes are: (i) a change in anisotropic structure between the source and receiver; and (ii) a misalignment between the source and receiver components. The DIT technique from Zeng and MacBeth (1993b), which is based on the developments of Igel and Crampin (1990), can detect asymmetry in the data matrix. It therefore provides a valuable check on the validity of the assumptions under which shear-wave splitting measurements are made. Physically, the DIT technique may be imagined as independent rotations of the source and geophone components to obtain two estimates of the fast shear-wave polarization: one near to the source and the second near to the receiver. Equation 2-6 then becomes:

$$\boldsymbol{G}(t) = \left[\boldsymbol{R}^{T}(\theta_G)\boldsymbol{\Lambda}(t;t_f,t_s)\boldsymbol{R}(\theta_S)\right] * \boldsymbol{S}(t)\,; \tag{2-11}$$

where θ_G and θ_S represent the separate rotation angles applied to the geophone and source components, respectively. In practice, the DIT solutions for θ_G and θ_S are found by algebraic minimization of the energy on the off-diagonal data matrix components. The time delay is found by cross-correlation of the main-diagonal components after minimizing the off-diagonal energy. A significant difference between θ_G and θ_S is an indicator of some form of data matrix asymmetry.

2.5 SYNTHETIC SEISMOGRAMS IN ANISOTROPIC ROCK

To interpret properly the shear-wave splitting measurements from the techniques described in the previous section, it is nearly always necessary to calculate synthetic

seismograms through simplified realistic Earth models. An introduction to the calculation of synthetic seismograms in anisotropic structures can be found in Crampin (1981). I use the ANISEIS (Version 5.2) modelling package (Taylor, 1994) to calculate synthetic seismograms through anisotropic and isotropic models. ANISEIS uses an anisotropic reflectivity method (Booth and Crampin, 1983) to calculate full plane-wave responses of models consisting of parallel layers of homogeneous isotropic or anisotropic layers. Full waveform synthetic seismograms from point sources are computed by double contour integration over horizontal slowness and azimuthal angle in the horizontal plane (Taylor, 1987). However, genuine three-dimensional calculations are extremely lengthy, and for most problems involving weak azimuthal anisotropy it is possible to calculate approximate solutions. This is done by representing the azimuthal variations by Bessel functions of zero order. In this thesis, most seismograms are calculated using the Bessel function approximation. I have, however, verified some of my final, best-fitting models by recalculating the seismograms using full azimuthal integration. For the models tried, I found that the seismograms calculated with full and approximate integration methods showed negligible differences both in appearance and in the associated shear-wave splitting parameters calculated using the techniques described in Section 2.5.

2.6 MODELLING ELASTIC ANISOTROPY OF ROCKS

Here, I introduce two different formulations which I use to specify the elastic constants of azimuthally anisotropic materials for matching shear-wave splitting measurements along near-vertical ray paths in VSPs.

Hudson Theory

The first formulation I use is that developed by Hudson (1986 and 1991) to simulate scattering of elastic waves by thin fluid-filled penny-shaped cracks. It is based on expressions of the strain due to a single ellipsoidal inclusion developed by Eshelby (1957). Hudson's formulations assume that the cracks are isolated, sparsely and uniformly distributed, small in comparison to the seismic wavelength and are filled

with an isotropic material more compliant than the surrounding matrix. The parameters used to define a dilute concentration of Hudson cracks in an isotropic matrix rock are:

(i) cracks radius, r;

(ii) crack content, specified by density, Lamé constants (λ and μ), and viscosity (η);

(iii) crack aspect ratio, equal to the ratio of thickness to diameter of the crack, and;

(iv) crack density defined as $\epsilon=Nr^3/V$, where N is the density of cracks in volume V;

(v) crack orientation.

APE Theory

The second formulation I use for defining elastic constants of anisotropic materials is the Anisotropic Poro-Elastic (APE) theory developed by Zatsepin and Crampin (1997). This theory attempts to model the compliance of microcracks to changing physical conditions. By constructing an equation of state for pre-stressed fluid-saturated rock, Zatsepin and Crampin (1995) conclude that the mechanism for compliance of the microcracks is pressure-gradient driven fluid flow between intergranular cracks and pores at different orientations to the stress-field. If this equation of state is an accurate representation of dynamic *in-situ* cracks then, by theoretically altering physical parameters within the equation of state, it may be possible to predict changes in shear-wave splitting behaviour to real changes of *in-situ* conditions. Such a process could be applied to understanding *in-situ* conditions of hydrocarbon reservoirs to improve remote monitoring of hydrocarbon extraction and, therefore, recovery (Crampin and Zatsepin, 1995). The parameters used to define a distribution of fluid-filled APE microcracks in an isotropic or anistropic rock matrix with principal stresses aligned vertically and horizontally are:

(i) crack density, ϵ, and average aspect ratio;

(ii) density and P-wave velocity of the pore-fluid;

(iii) drained crack compressibility, c_{cr}, $[(\partial V/\partial\sigma_n)/V_o$, where V_o is the initial crack volume and V is the crack volume under applied normal stress $\sigma_n]$;

(iv) vertical, s_V, maximum horizontal, s_H, and minimum horizontal, s_h, principal differential components of the applied stress, normalised by the inverse of c_{cr}, [explicitly: $s_j=(\sigma_j-\sigma_h)\times c_{cr}$, where σ_j is the jth component of principal stress];

(v) the pore-fluid pressure p_f , normalised by the inverse of $c_{cr.}$

Although the oil productivity of the fields studied in this thesis is believed to be fracture controlled, the average fracture size is unknown. The average fracture size may therefore be of the order of tens of metres. The appropriateness of small isolated ellipsoidal inclusions, described by either the Hudson or APE theory, to model large-scale fractures is at the moment still unclear. An alternative approach to modelling fractures, based on infinitely-long parallel slip interfaces, was developed by Schoenberg (1980). However, Schoenberg and Douma (1988) and Liu *et al.* (1996) have shown that sets of elastic constants calculated using this method are identical in form to sets of constants calculated using thin (aspect ratio < 0.3) Hudson microcracks.

CHAPTER THREE

SHEAR-WAVE SPLITTING AT TWO NORTH CAUCASUS OIL FIELDS: VSP MEASUREMENTS

3.1 INTRODUCTION

Due to the low permeability of the rock matrix, hydrocarbon reservoirs in argillaceous rocks are commercially productive only when strongly fractured (Aguilera, 1980). Until recently, however, there has been no established method to detect and characterize fractures within reservoirs remotely, with the result that most of the known reservoirs in argillaceous rocks have been found accidentally while drilling towards prospects in other rock units.

Lewis *et al.* (1991), Mueller (1991), Cliet *et al.* (1991), and Yardley and Crampin (1993) have found that, for fracture-controlled production in carbonate rocks, a correlation exits between well productivity and degree of seismic anisotropy. This indicates that remote measurements of seismic anisotropy can be used to identify and characterize *in-situ* fracturing so that well positions and orientations may be optimized to intersect the maximum number of fractures and, therefore, maximize production.

Over extensive areas of the North Caucasus foredeep there is oil production from reservoirs in Maikop clays. However, within these oil fields productivity varies from zero to 100 bbl/day between wells drilled less than 500 m apart (L.Y. Brodov, personal communication, Neftegeofizika, Moscow). Production is believed to be related to fracturing, but little is understood about the *in-situ* fractures. Conflicting reports from laboratory work on cores from some fields report both vertical and horizontal microfractures within the clays. In this chapter, I attempt to quantify the degree of seismic anisotropy at three oil wells located in the North Caucasus foredeep in the hope that the measurements will provide information about the orientation and characteristics of the oil-filled inclusions in the clay reservoir layer. I estimate the

seismic anisotropy at each well by measuring shear-wave splitting parameters in multi-component VSPs. The results obtained in this chapter will modelled in Chapter Four to determine possible fracture orientations and densities.

3.2 GEOGRAPHICAL AND GEOLOGICAL BACKGROUND

As described in Chapter Two, the most likely geological causes of seismic velocity anisotropy are: fine layering, grain alignment, and stress controlled fractures, microcracks and orientated pore space. Hence, shear-wave splitting studies may, when properly interpreted and combined with other available geological and geophysical data, give valuable information about *in-situ* conditions such as fracture orientations (Crampin and Lovell, 1991; Mueller, 1991). In this section I present background geographical and geological information to help interpretation of the subsequent shear-wave splitting measurements.

First I describe the location of the Juravskoe and Vorobievskoe oil fields. Next, I give an outline of the regional tectonics and likely existing stress regime. Then, lastly, I give some details of the local geology around the Juravskoe and Vorobievskoe oil fields.

3.2.1 Location

The three wells analyzed come from two North Caucasus oil fields: one unproductive well, Well 87, and one productive well, Well 85, from the Juravskoe oil field; and one productive well, Well 29, from the neighbouring Vorobievskoe oil field [it should be noted that "Zhuravskoe" is often used as an alternative spelling for the Juravskoe oil field]. Figure 3.1 shows the location of the two oil fields. The fields are located in southern Russia, approximately 250 km north of the Caucasus mountains. The Juravskoe field lies south-west of the village of Blagodarnyy and 100 km east of Stavropol. The Vorobievskoe field lies immediately to the north-east of the Juravskoe field. In each oil field the reservoir zone is at about 2 km depth, approximately 100 m thick, and forms a gentle anticlinal structure with dips on the flanks ranging from 30 minutes to 2° (Klubova, 1991; Chepak *et al.*, 1983, L. Y. Brodov, personal communication, Neftegeofizika, Moscow).

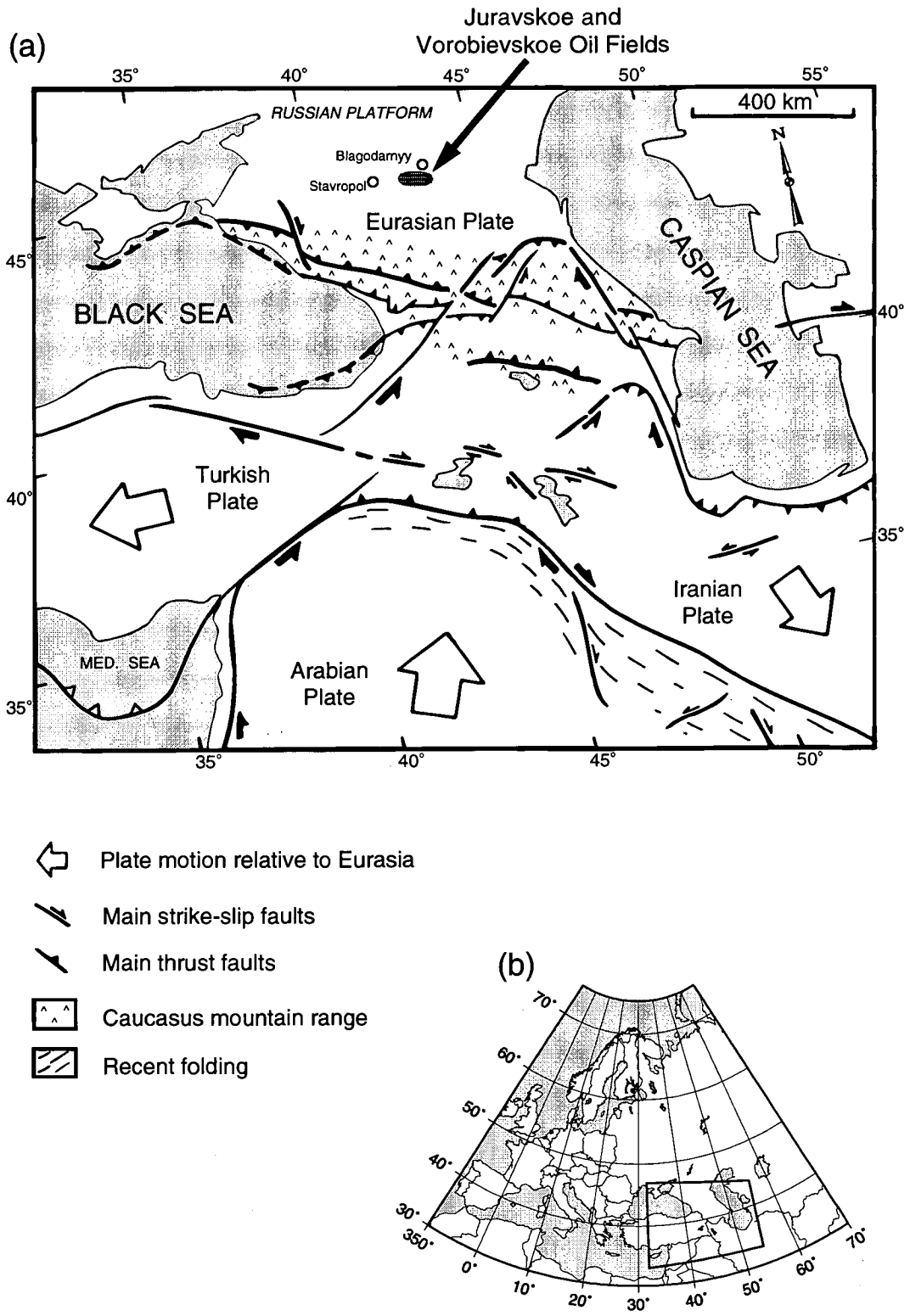

Figure 3.1: Major tectonics of the Caucasus region. (**a**) Map showing the location of the Juravskoe and Vorobievskoe oil fields and the major tectonic features of the Caucasus and surrounding areas (modified from H. Philip *et al.*, 1989), and (**b**) the outline of the area in (a) highlighted on a map of Europe.

3.2.2 Regional Tectonics and Stress

Detailed accounts of the complex tectonic evolution of the region have been presented by Zonenshain & Le Pichon (1986), Adamia *et al.* (1981), and Gamkrelidze (1986). Figure 3.1 shows the principal present-day tectonic features of the Caucasus and surrounding areas. The oil fields are located on the Russian (Scythian) platform north of the intersection of the Turkish and Iranian sections of the Alpine-Himalayan fold belt. At this intersection, a quadruple junction is formed between the Eurasian, Turkish, Iranian and Arabian plates. The recent tectonic movements relative to Eurasia are indicated in Fig. 3.1 by open arrows. The Arabian plate is moving relatively in a NNE direction towards the Eurasian plate, at a rate of about 4 cm per year (Gamkrelidze, 1986). Consequently, continent-continent collision is occurring at the boundary, with the shortening absorbed by the continuing uplift of the Caucasus mountains and the movement of the Turkish and Iranian plates WSW and SE respectively. Nowroozi (1971) and Philip *et al.* (1989) have shown that two major fault systems are developed in the Caucasus region: a NW-SE trending Alpine system running parallel to the foredeep, indicating thrusting to the NE, and a left-lateral strike-slip system oriented NNE, perpendicular to the Caucasus lineament.

Unfortunately, no local stress measurements in or near the oil field are available. However, the direction of maximum regional horizontal stress can be inferred from earthquake fault plane solutions. Figure 3.2 displays interpreted focal plane solutions from Nowroozi (1971) for events within the Caucasus and surrounding regions. The events located in the Caucasus region indicate a direction of maximum regional horizontal stress between N-S and NE-SW. This is consistent with the generalized stress map from Zoback (1992), which indicates a N-S regional stress direction for the region. It is also consistent with the earthquake focal plane analysis of Nikolayev (1979) which shows the maximum compressive horizontal stress in the region to be oriented NE-SW.

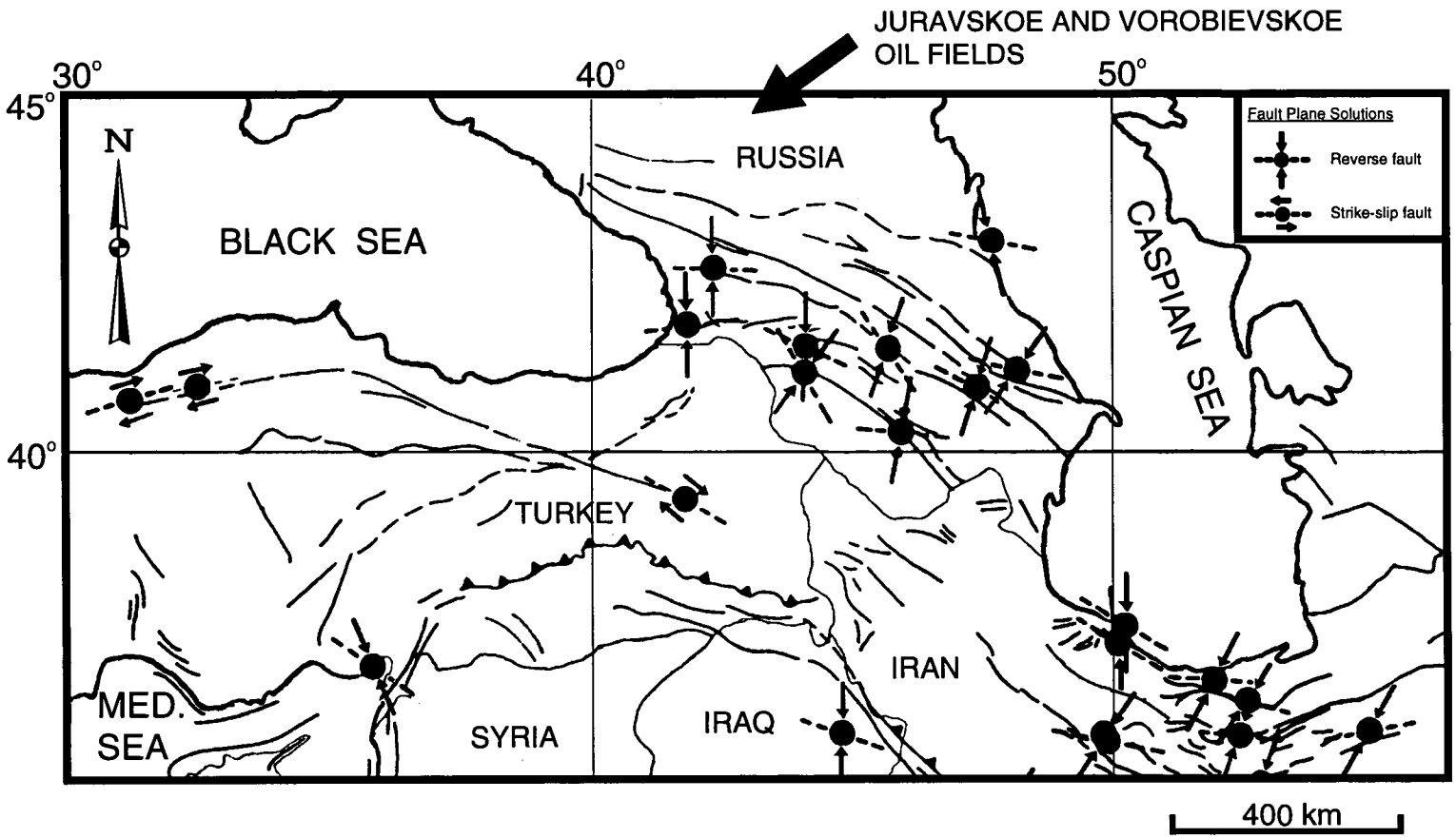

Figure 3.2: Maximum horizontal stress in the Caucasus region. Results from earthquake focal mechanism analysis indicating that the direction of maximum horizontal stress in the Caucasus is oriented between north and north-east (after Nowroozi, 1971). The arrows indicate, for strike-slip faults, the direction of motion, and for reverse faults, the direction of the compressional axis.

3.2.3 Geology

The northern Caucasus foredeep, the back-arc basin of the Greater Caucasus, forms the southern boundary of the Russian platform. It consists of a Hercynian basement overlain by up to 13 km of Mesozoic and Cenozoic sediments. Figure 3.3 shows the geology, determined previously by well logs, seismic reflection profiling and VSP surveys, to the base of Well 87. Essentially, the geology consists of a horizontally-bedded sequence, about 600 m thick, of Middle Miocene-Pliocene clays, sandstones and limestones overlying the 1400 m thick Maikop Series of Middle Oligocene-Lower Miocene rocks (Nalivkin, 1973; Kunin, Kosova, and Blokhina 1990). Below the Maikop Series are Palaeogene clays and marls to the base of the wells.

3.2.4 Maikop Series

The Maikop series covers a vast area (>100 000 km^2) from Bulgaria to the Caspian sea. Within the Juravskoe and Vorobievskoe oil fields the Maikop Series lithology can be separated into two main sections: an upper alternating sandstone and clay sequence, and a lower near continuous clay interval of approximately 1200 m thickness. The boundary between these two zones is clearly identifiable at a depth of 750 m on the resistivity log in Fig. 3.3. The reservoir zone consists of highly consolidated claystone and is located within the Middle Maikop and Lower Maikop (Batalpashinskian) formations at the base of the thick continuous clay interval.

The following conditions of the area surrounding the oil fields are favourable for the recording of transmitted shear-waves using VSPs, making it an almost ideal experimental site for the study of seismic anisotropy:

i) *flat topography* - aids accurate source positioning and reproducibility;

ii) *structurally simple* - few structure induced polarization anomalies, helps simplify interpretation and modelling;

iii) *few reflections within the continuous clays* - maintains a large relative amplitude of transmitted energy, thus aiding the measurement of shear-wave splitting parameters;

iv) *low average shear-wave velocity* (about 660 ms^{-1} to the base of the wells) - a large time delay for a given percentage of anisotropy is expected, aiding identification and measurement of shear-wave splitting [for a constrained Poisson's ratio and percentage

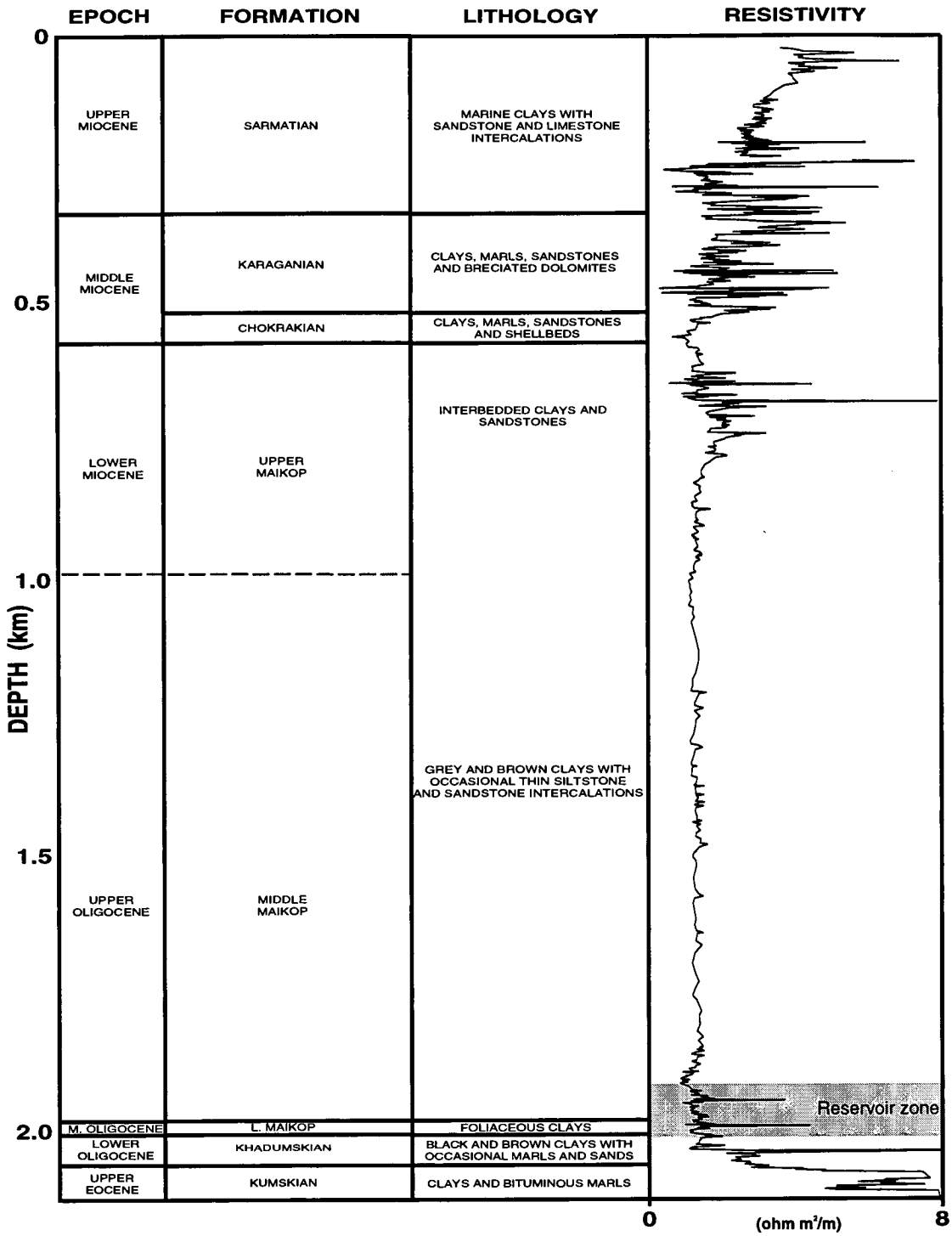

Figure 3.3: Well 87 resistivity log, interpreted formations, and lithological descriptions. The dashed line at about 1.2km indicates that the boundary between Upper and Middle Maikop is undetermined at the well. The reservoir zone is approximately 100m thick and located near the base of the Maikop. The near constant low resistivity, in the depth interval 750m to 2000m, is characteristic of the continuous sequence of Maikop clays.

azimuthal shear-wave anisotropy (crack density), the time delay per km for propagation through aligned microfractures is inversely proportional to the matrix shear-wave velocity (Crampin, 1993a)].

3.3 OIL PRODUCTIVITY

Within the Juravskoe and Vorobievskoe oil fields commercial oil production is from the lowest 100 m of the Maikop Series. The reservoir zone is overpressured (Naryzhnyy, 1986). Figure 3.4 shows the position of the Maikop formations near the base of the three wells together with the results of oil production tests. Well 85 was tested within and just above the Lower Maikop, and produced oil at 18 m^3 per day (113 barrels per day). Well 87, 5 km from Well 85 within the Juravskoe field, showed no production when tested within the lowest 100 m of the Maikop. The well in the Vorobievskoe field, Well 29, located 26 km from Well 85, was recently tested near the base of the Maikop (L.Y. Brodov, personal communication, Neftegeofizika, Moscow). However, the field's present owners are unwilling to give me the results because of the commercial importance of these data. This well is already known to be commercially productive from below 2140 m, below the zone of interest studied in this chapter.

Lateral variation in productivity within the fields is pronounced: productivity varies from zero to 100 barrels per day between wells less than 500 m apart (L.Y. Brodov, personal communication, Neftegeofizika, Moscow). The reasons for this are not well understood. It has been suggested that fluid flow occurs through intersecting vertical fractures, and that production variability is caused by lateral variations in fracture density associated with basement faulting (Naryzhnyy, 1986; Chepak *et al.*, 1983; Klubova, 1991). Vertical microfractures in limy Maikop clays have been observed by Teslenko and Korotkov (1967) in cores from fields near Krasnodar, although no strike direction of the microfractures is given. There are, contrastingly, reports of horizontal fracturing within the Maikop clays. For example, Bochkarev and Yevik (1990) describe subhorizontal fractures with a density of 60-900 per metre and dilatancy of 0.01-0.3 mm. However, these are most likely intergranular microfractures related to the microfabric of the clays, associated with stress-relief cracking in the

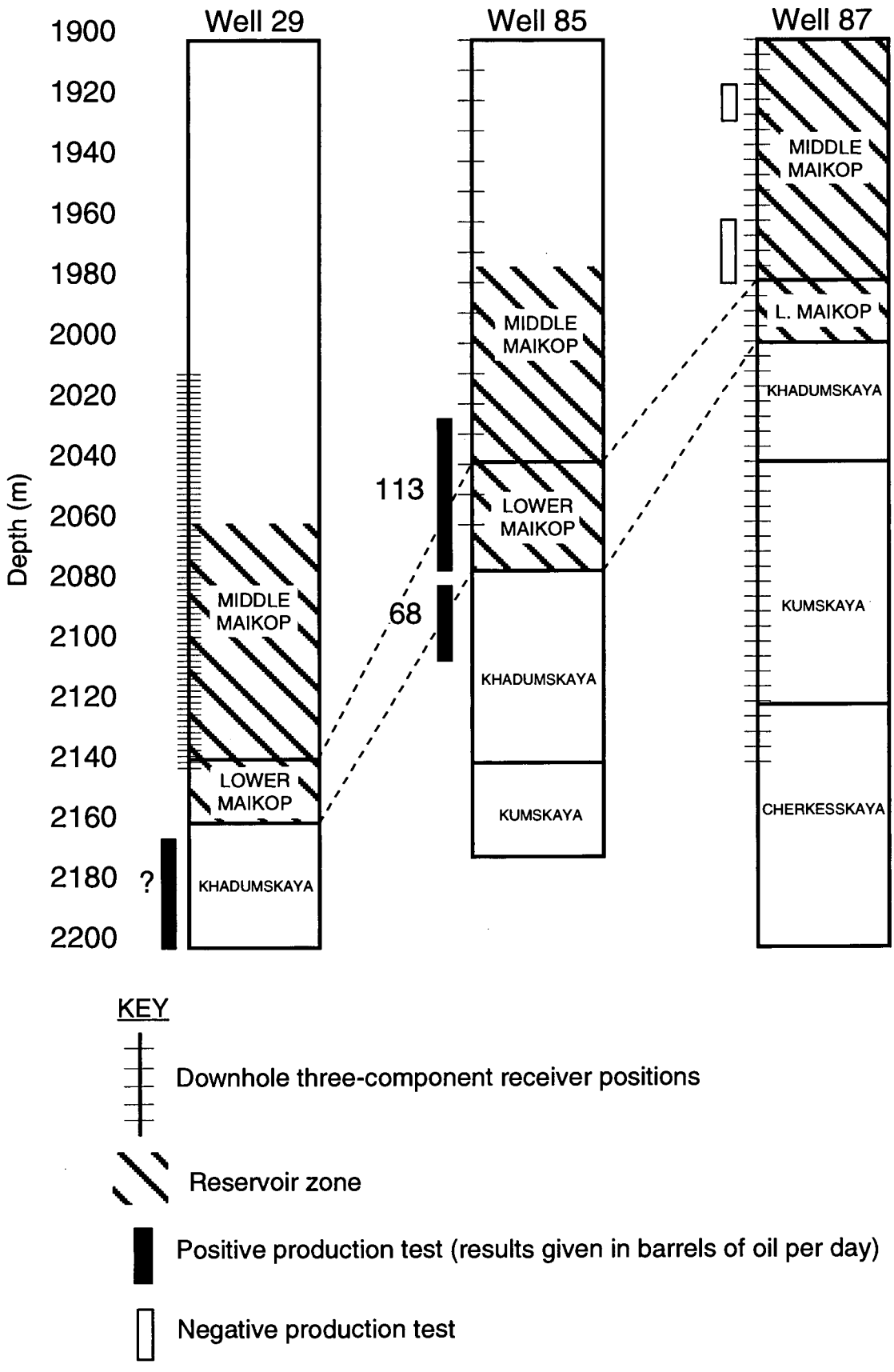

Figure 3.4: VSP receiver positions and production test intervals in the lower section of Wells 29, 85 and 87. Unfortunately, the details of positive tests in Well 29 are unavailable. The receivers are located at intervals of 2m in Well 29, 10m in Well 85 and 5m in Well 87.

cores, and therefore may have little relevance to the geometry of the *in-situ* fractures in productive zones.

3.4 PREVIOUS STUDIES OF MAIKOP CLAY ANISOTROPY

There is very little information available about the seismic anisotropy of Maikop clay oil fields. A field study by Galperina and Galperin (1987) is the only known previous work on the seismic anisotropy of Maikop clays. Their study area is located on the Taman Peninsula, about 500 km west of the Juravskoe and Vorobievskoe oil fields. Their main objective was to determine whether any shear-wave azimuthal anisotropy is associated with pronounced clay diapirism in the area.

To estimate azimuthal anisotropy, Galperina and Galperin (1987) plot arrival-time variations of split shear-waves for propagation from shots at 50 m depth to surface receivers along several azimuths. They find that along these subhorizontal raypaths in the near-surface the shear-waves split into SH and SV phases with no azimuthal asymmetry in arrival time. Therefore, within the accuracy of the method (2%), they conclude that the Maikop clays possess no azimuthal anisotropy, and are characterized by TIV with a horizontal velocity ratio (SH/SV) of 1.2. I suggest that, based on these shallow raypaths, their conclusion is only relevant for the clays present in the near-surface and cannot be used to infer an absence of azimuthal anisotropy within deep Maikop clays, such as those studied in this chapter. This is because, at depth, the *in-situ* conditions such as stress and temperature which may control some mechanisms of anisotropy, will be substantially different from the near-surface and may give rise to azimuthal anisotropy (Crampin, 1990).

In the same study, Galperina and Galperin (1987) recorded shear waves propagating through deeply buried clays. They present VSP data recorded in a 3 km deep well from a surface source with an offset 600 m from the well. Shear-wave splitting is identified through the whole section. The time delay between the split shear waves reached a maximum of 0.6 s at 1.5 km depth, and is then constant to the base of the well. Unfortunately, they did not attempt to explain the time delay behaviour and, in particular, the symmetry systems required to produce such a large delay for near-vertical propagation to the lowest receiver levels. If their conclusion from the near-horizontal raypaths is correct, and the clays are characterized by TIV,

then, as each sagittal plane is a plane of symmetry, the shear-waves should split into strictly SV and SH phases (Musgrave, 1970, P.95), meaning each phase would be recorded separately on radial and transverse components. However, in the deep VSP, both shear-wave polarizations were recorded on the radial component, indicating that neither phase is radially polarized and implying that the section is not characterized by TIV.

The azimuthal isotropy expected in clay rocks, and possibly confirmed in Maikop clays by the Galparina and Galperin (1987) study, is favourable for the identification of fracture induced azimuthal anisotropy in the clays. This is because any azimuthal anisotropy observed along vertical raypaths is more likely to be caused by fractures and not by inherent features of the clay.

3.5 VSP ACQUISITION GEOMETRIES

The acquisition of high-energy shear-wave VSPs to investigate the anisotropic nature of the sedimentary rocks, requires equipment, source-receiver geometries, and field procedures different from those used in the acquisition of more conventional P-wave VSPs acquired under the assumption of isotropy. In this section I first describe the equipment and experimental procedures common to the acquisition of the shear-wave VSP experiments at all of the three wells. Then, in separate sections, I describe the source-receiver geometries specific to the acquisition at each individual well.

3.5.1 Acquisition Details Common to All VSPs

All acquisition equipment was manufactured in Russia and provided by Neftegeofizika, Moscow. At each well site, polarized shear waves were generated by an impulsive electrodynamic source. The source was truck-mounted and known as VEIP-40. Figure 3.5a shows an example of a source truck. Each truck has three source units, each with its own base plate (Fig. 3.5b). Two units are mounted across the centre and one at the rear of the truck, together producing a horizontal force perpendicular to the truck direction with a peak frequency of 16 Hz. The force imparted to each baseplate comes from discharging a large bank of capacitors through coils surrounding a metal core, which is encased in a metal cylinder and mounted

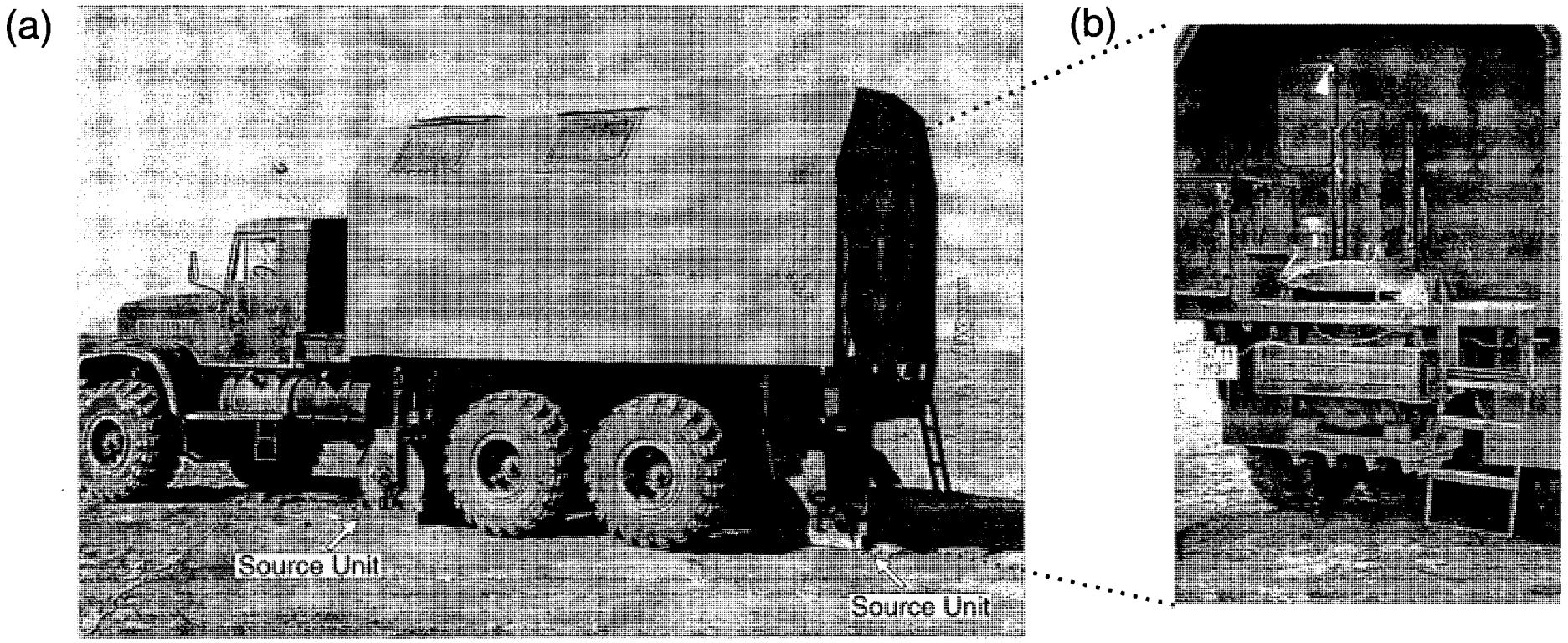

Figure 3.5: VEIP-40 impulsive electromechanical source truck. (**a**) The Russian-made source is a converted army truck mounted with three source units (two across the centre and one at the rear) which generate a source polarization perpendicular to the truck direction. (**b**) The toothed baseplate of each source is coupled to the ground using the weight of the truck, and the impulse to the baseplate is from a metal core striking the end of the cylinder mounted above each baseplate. The core is propelled by discharging a large bank of capacitors through coils within the cylinder.

above each base plate. The discharging current propels the metal core against the side of the containing cylinder. By reversing the current direction it is possible to reverse the polarity of the generated shear-waves.

For each source polarization direction the source signals were stacked (up to 32 times for the deeper receiver levels) with both positive and negative polarities and then written, with a 1 ms sample rate, to tape. Recording both polarities allows, in later processing, the compressional-wave energy to be cancelled and the shear-wave energy to be enhanced (by subtracting, from each other, the seismograms recorded from sources with opposite polarities). I specify the source aligned nearest to the inline direction as *X* and the source nearest the crossline direction as *Y* (the choice at Well 87 is arbitrary as the sources are aligned 45° to the sagittal plane).

All three wells were cased and within 1.5° of vertical. The wavefield was recorded in the wells by a three-component seismometer, mounted inside a sonde in an orthogonal XYZ configuration. At each recording level the 60 kg sonde was clamped against the borehole wall by an electromechanical locking arm, with a locking force in excess of 2000 Newtons.

A summary of the equipment parameters used in the acquisition at the three well sites is given in Table 3.1. The following sections give details of VSP acquisition specific to each well site.

3.5.2 Well 85 VSP Acquisition

During September and October 1991, one near-offset VSP (W85N) was acquired with shear-wave sources. Figure 3.6 shows a plan view of the experimental layout of the sources from the wellhead, and Table 3.2 lists the source locations and polarizations. Table 3.3 contains the receiver depth levels and the shear-wave sources recorded at each level. The near-offset VSP was recorded with one source polarization for receiver depths between 100 m and 1700 m, and two orthogonal source polarizations between 1700 m and 2060 m. Receiver interval spacing varied with depth, from 20 m near the surface to 10 m below 400 m.

To determine the orientation of the downhole receivers, high-energy compressional waves were generated by explosives in two shallow boreholes, offset 514 m from the well and separated by 60°.

TABLE 3.1: General Details of Acquisition Parameters.

Shear-wave source	Electrodynamic VEIP-40 truck
Peak frequency	16 Hz
Compressional-wave source	Explosive, 400g blocks detonated in shallow boreholes
Peak frequency	100 Hz
Geophone system	Downhole, orthogonal three-component, moving coil
Natural frequency	10 Hz
Field filters	10 Hz low-cut, 50 Hz notch
Sample rate	1 ms
Record length	6 s

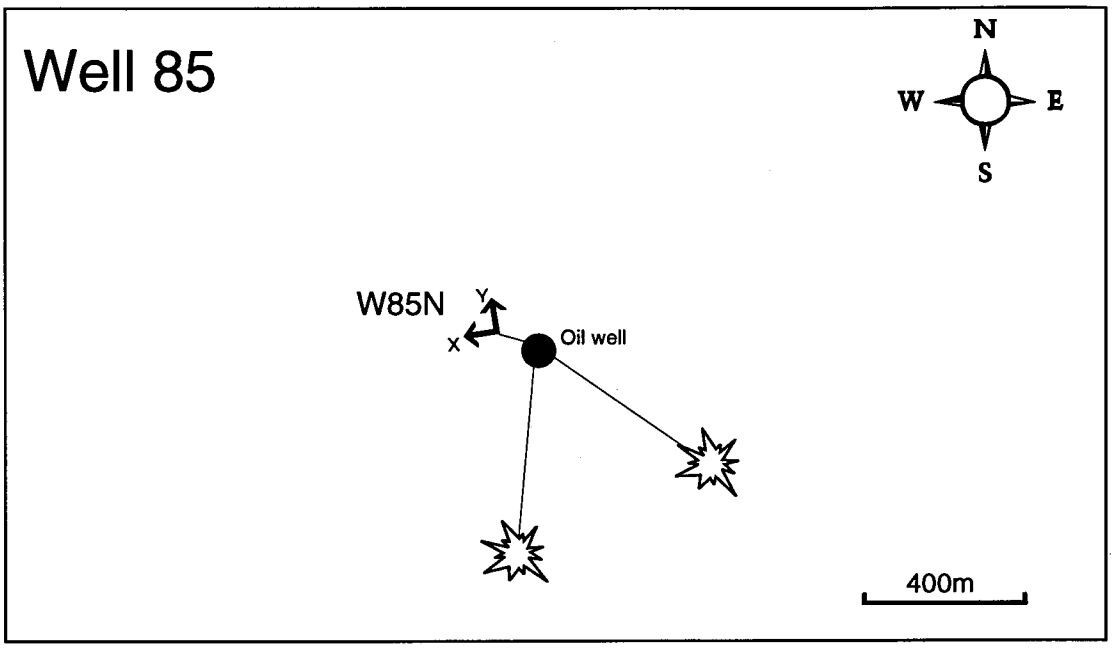

Figure 3.6: Plan view of VSP acquisition at the productive well, Well 85. Polarized *S*-waves, generated by the VEIP-40 source trucks, are recorded downhole by a three component receiver. The VEIP-40 source positions and polarizations are given in Table 3.2. The receiver orientation in the horizontal plane is determined from *P*-waves generated by explosive sources offset 514 m along azimuths N125°E and N185°E.

WELL 85

SOURCE PARAMETERS

Table 3.2: VEIP-40 Source Location and Polarizations at Well 85

VSP	Offset (m)	Source Azimuth (N°E)	Source Polarizations (N°E)	
			X	**Y**
W85N	88	286	265	355

RECEIVER PARAMETERS

Table 3.3: Receiver Depths and VEIP-40 Polarizations Recorded at Well 85

VSP Depth Interval (m)	Receiver Depth Spacing (m)	Sources Recorded
100 - 400	20	**X**
400 - 1700	10	**X**
1700 - 2060	10	**X, Y**

3.5.3 Well 87 VSP Acquisition

During August and September 1991, one near-offset VSP (W87N) was acquired with shear-wave sources. Figure 3.7 shows a plan view of the experimental layout of the sources from the wellhead and Table 3.4 lists the source locations and polarizations. Table 3.5 contains the receiver depth levels and the shear-wave sources recorded at each level. Receiver spacing varied with depth, from 20 m near the surface to 5 m within and just above the reservoir zone. Single-source data were recorded between 100 m and 1500 m subsurface, and dual-source between 1650 m and 2130 m. Note that, due to time limitations, no recordings were made between the depths of 1500 m and 1650 m.

To determine the orientation of the downhole receiver, high energy compressional waves were generated by explosives in shallow boreholes, offset 520 m from the well and separated by 60°.

3.5.4 Well 29 VSP Acquisition

During the summer of 1993, three VSPs were acquired with shear-wave sources: one near-offset VSP (W29N), one far-offset VSP along azimuth N308°E (W29F1) and one far-offset VSP along azimuth N255°E (W29F2). Figure 3.8 shows a plan view of the experimental layout of the sources from the wellhead, and Table 3.6 details the source locations and polarizations.

To determine the sonde orientation within the well, one far-offset explosive source was located 645 m along azimuth N308°E next to the VEIP-40 source. For some receiver levels this source was not recorded. For these levels, I used compressional arrivals from far offset VEIP-40 sources to determine the downhole receiver orientation.

On the data tapes sent to me were two polarities for each source polarization in the *Y* direction, but only one polarity for each *X* source polarization. To maintain consistency of processing between *X* and *Y* source components, I select for processing only one polarity from the *Y* source together with the one available *X* polarity. This makes subtraction of opposite polarities, to remove compressional energy, impossible. The traces, however, contain little coherent compressional energy near to the shear-

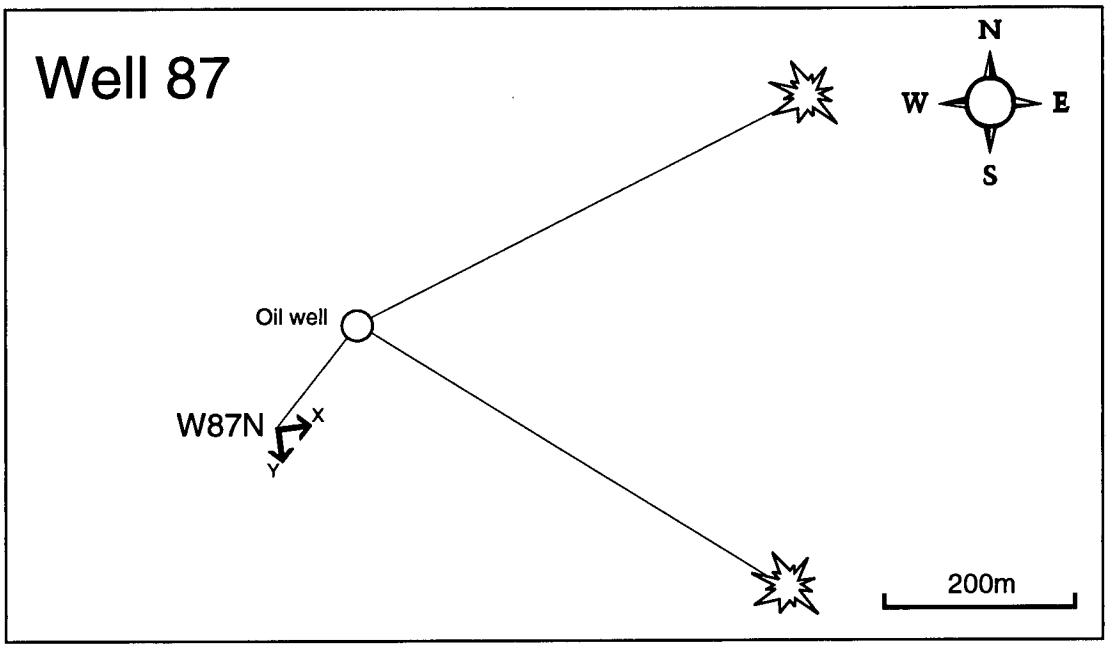

Key

↑ Veip-40 source polarization direction

Explosive source

Figure 3.7: Plan view of VSP acquisition at the unproductive well, Well 87. Polarized *S*-waves, generated by the VEIP-40 source trucks, are recorded downhole by a three component receiver. The VEIP-40 source positions and polarizations are given in Table 3.4. The receiver orientation in the horizontal plane is determined from *P*-waves generated by explosive sources offset 520 m along azimuths N063°E and N173°E.

WELL 87

SOURCE PARAMETERS

Table 3.4: VEIP-40 Source Location and Polarizations at Well 87

VSP	Offset (m)	Source Azimuth (N°E)	Source Polarizations (N°E)	
			X	**Y**
W87N	135	218	83	173

RECEIVER PARAMETERS

Table 3.5: Receiver Depths and VEIP-40 Polarizations Recorded at Well 87

VSP Depth Interval (m)	Receiver Depth Spacing (m)	Sources Recorded
100 - 200	20	**X**
200 - 1500	10	**X**
1650 - 1900	10	**X, Y**
1900 - 2130	5	**X, Y**

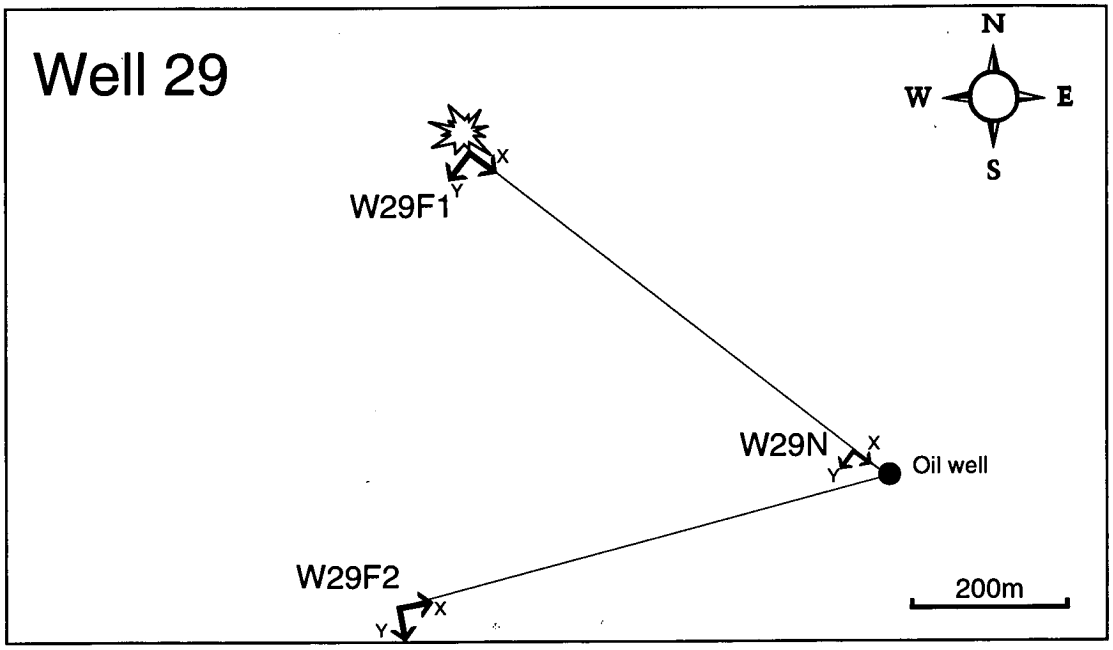

Key

↑ Veip-40 source polarization direction

Explosive source

Figure 3.8: Plan view of VSP acquisition at the productive Well 29. Polarized *S*-waves, generated by the VEIP-40 source trucks, are recorded downhole by a three component receiver. The VEIP-40 source positions and polarizations are given in Table 3.6. The receiver orientation in the horizontal plane is determined from *P*-waves generated by the offset VEIP-40 sources.

WELL 29

SOURCE PARAMETERS

Table 3.6: VEIP-40 Source Locations and Polarizations at Well 29

VSP	Offset (m)	Source Azimuth (N°E)	Source Polarizations (N°E)	
			X	**Y**
W29N	65	306	126	217
W29F1	645	308	127	217
W29F2	623	255	84	170

RECEIVER PARAMETERS

Table 3.7: Receiver Depths and VEIP-40 Polarizations Recorded at Well 29

VSP Depth Interval (m)	Receiver Depth Spacing (m)	Sources Recorded		
		W29N	**W29F1**	**W29F2**
2010 - 2138	2	**X, Y**	**X, Y**	**X, Y**

waves (Figs. 3-14 to 3-16). Therefore, I do not believe that this is a serious problem for the estimation of shear-wave splitting at this well.

Receivers at Well 29 were located every 2 m between the depths of 2010 m and 2140 m (Table 3.7). This depth increment is small and gives many observations through the zone of interest near the base of the Maikop Series.

3.6 DATA PROCESSING

The flowchart in Fig. 3.9 outlines the processing sequence I use to measure shear-wave splitting in the VSP datasets. In this section I describe the processing steps performed on the multi-component data prior to the application of shear-wave splitting measurement techniques.

3.6.1 Initial Processing

All VSP data were received in SEGY format, and consisted of pre-stacked traces from opposite positive and negative shots, recorded with a 1 ms sample rate. At the time of processing the data from Well 87 and Well 85, there was insufficient online storage space to hold the data when sampled at 1 ms. Therefore, to reduce the datasets to a more manageable size, I resampled these data in the frequency domain from 1 ms to 2 ms. This preserves all frequencies up to 250 Hz and therefore has no effect on the recorded shear-waves, which occupy a frequency band between 4 Hz and 30 Hz. The Well 29 data, processed last, were not resampled because storage space had increased prior to their processing.

After resampling, the traces were sorted and edited to remove noise spikes. Next, the compressional energy in the wavefield was reduced. This was done by subtracting, from each other, the seismograms recorded with opposite polarity of shear-wave source.

In general, to measure unambiguously the *qS1* polarization direction of split shear waves using DIT and DCT, it is vital to know the coordinate system of either the sources or receivers (Yardley, 1994). In other words, one must know whether the sources or receivers form either a right- or left-handed system. If the "handedness" of either can be determined, then one of the two DIT estimates of polarisation is

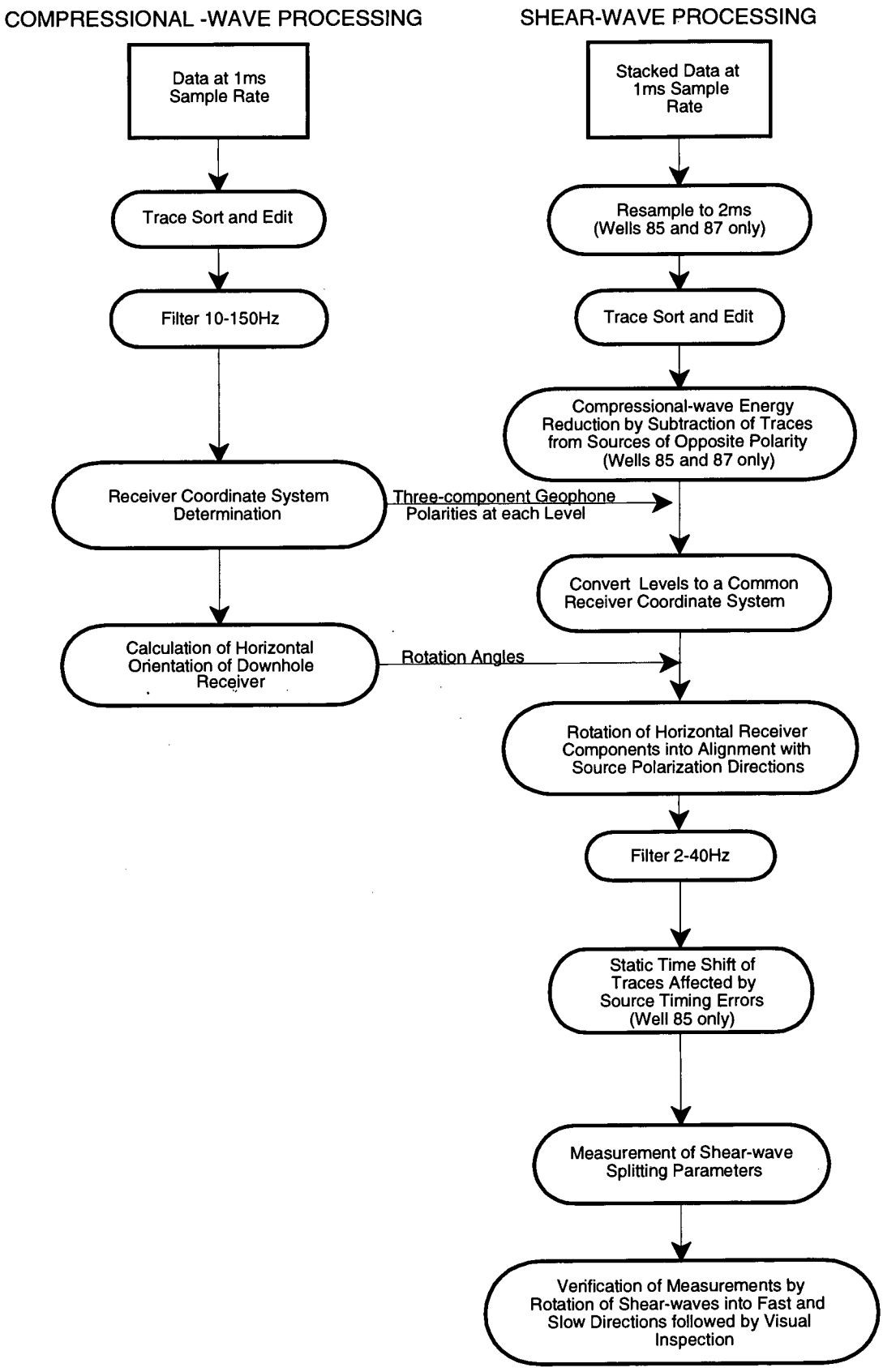

Figure 3.9: Processing flow applied to the multicomponent VSP data to determine shear-wave splitting parameters. With the exception resampling and static time shifting, all processing steps are common to the data from the three wells.

known with certainty. Therefore, if the two DIT estimates differ significantly because of a difference between source and receiver coordinate systems, a flip of the undetermined system should resolve the difference (MacBeth *et al.*, 1994). Unfortunately, the handedness of the sources at each well is unknown. Tap test results, which would define the receiver coordinate system, are also unavailable for these VSPs. Instead, I identify the handedness of the receiver at each depth for each VSP, by using the direct P-wave arrivals from two far-offset sources. The method is explained in Fig. 3.10. At Well 85 and Well 87, changes in the handedness of the receiver were determined and found to coincide with replacements of the sonde noted in the observer's logs. I convert each left-handed receiver to right-handed by reversing the polarity of the transverse component.

3.6.2 Rotation of Horizontal Receiver Components

I use the direct P-wave from far-offset sources to estimate the horizontal-plane orientation of the downhole receiver. At each depth, the orientation is estimated by finding the maximum energy direction in the horizontal plane within a 200 ms window enclosing the direct P-wave. This method is valid even in strongly anisotropic media because, for anisotropy up to 40% the P-wave polarization direction deviates by less than 5° from the ray direction (Crampin, Stephen and McGonigle, 1982). At Well 85 and Well 87, arrivals from the dynamite sources are used, whereas at Well 29 arrivals from both dynamite and VEIP-40 sources are used. To validate the orientation angles, I calculate the orientation angle separately from P-wave arrivals generated by the two sources located along different azimuths. Ideally the difference between the two estimates of receiver orientation at each level would be zero. Over the whole depth range of each VSP, I find that the average difference between orientations estimates was less than 4°, with a mean deviation of less than 6°.

After determining the receiver orientation, I rotate the horizontal receiver components into alignment with the surface VEIP-40 polarization directions, so that for each VSP the sources and receivers share a common set of coordinate axes (marked as X and Y in Figures 3.6 to 3.8).

Amplitude spectra of clean shear-wave arrivals show that the shear-wave energy is contained between 4 Hz and 30 Hz. Therefore, after reorientation, I filter the data

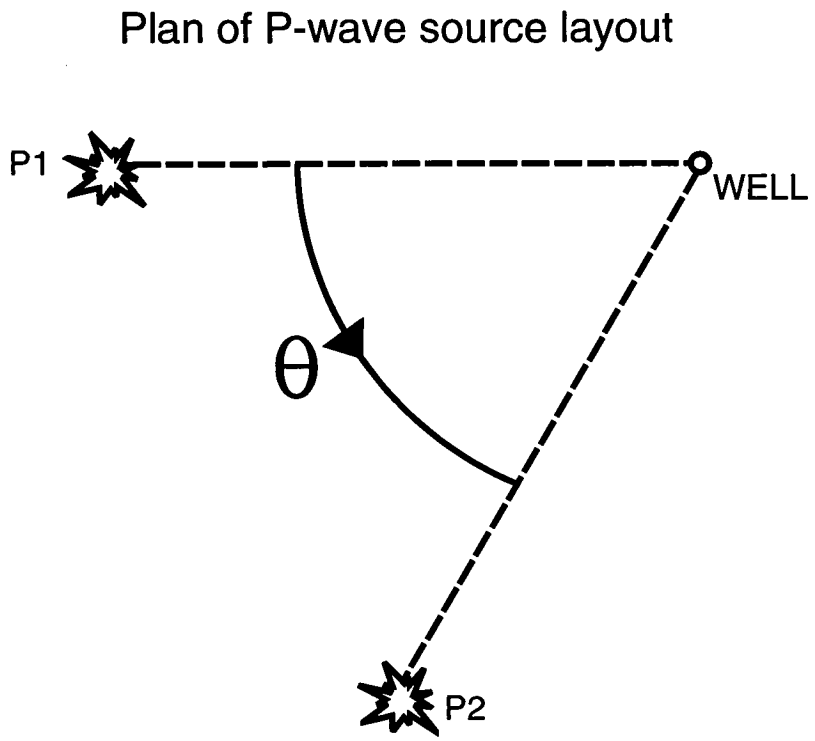

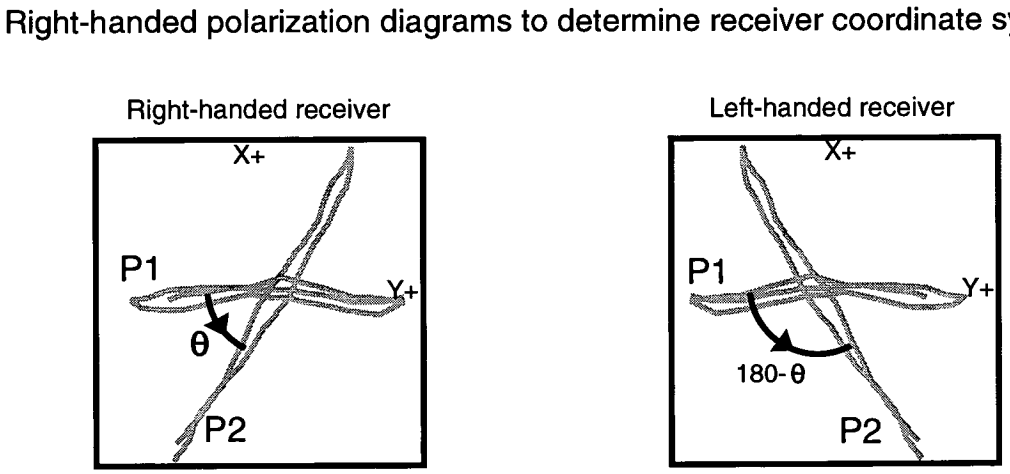

Figure 3.10: Determination of receiver "handedness". Both polarisation diagrams are plotted with a right-handed coordinate system and θ is measured anticlockwise. If the P2 plane of polarization is θ degrees from P1 then the receiver is right-handed. Otherwise, if the P2 polarization is 180-θ degrees from P1, then the receiver is left-handed.

to remove some high frequency interference in the data using a bandpass filter from 2 Hz to 40 Hz. FK filtering to remove upgoing energy was tried, but did not improve the measurements of shear-wave splitting as there is little upgoing energy in the VSPs.

At Well 85, triggering problems of the VEIP-40 trucks resulted in signals with a static time delay of 50 ms for some receiver levels. To display the traces correctly and to compare with synthetic seismograms, I advanced the delayed traces by 50 ms. Delays affect all receiver components at each affected level. Therefore, even if uncorrected, the delays have no effect on the shear-wave splitting estimation techniques applied in this chapter, as these techniques search each level separately for a relative time difference between split shear waves.

3.6.3 Well 85 Seismograms

Figure 3.11 shows the Well 85 VSP data after applying the data conditioning steps described above. The data are displayed in a "standard" four-component matrix, where each row of the matrix represents a common source polarization direction, and each column represents a common receiver direction (the vertical receiver components are not displayed because, except for a few upper levels, they contain very little energy from the vertically propagating shear-waves). The direct shear-wave signal consists of about two cycles (120 ms), with small amplitude, short-pathlength multiples immediately following the direct arrival. There is very little reflected energy: the only observable reflections originate just above and below the Maikop clays at 800 m and 2150 m, respectively. Off-diagonal energy is present in the four-component data matrix and increases relatively with depth.

Horizontal-plane PD's in Fig. 3.13a, selected every 200 m, show an increase in ellipticity with depth associated with the increase in off-diagonal energy. The arrivals on the PD's display linearity in the top 200 m, followed by a regular increase in ellipticity down to about 1.8 km depth. The increase in ellipticity with depth may result from an increasing time delay between split shear-waves and, if so, is a clear demonstration of shear-wave splitting through a sedimentary sequence. Below 1.8 km depth the PD's display some irregularity, showing both increases and decreases in ellipticity.

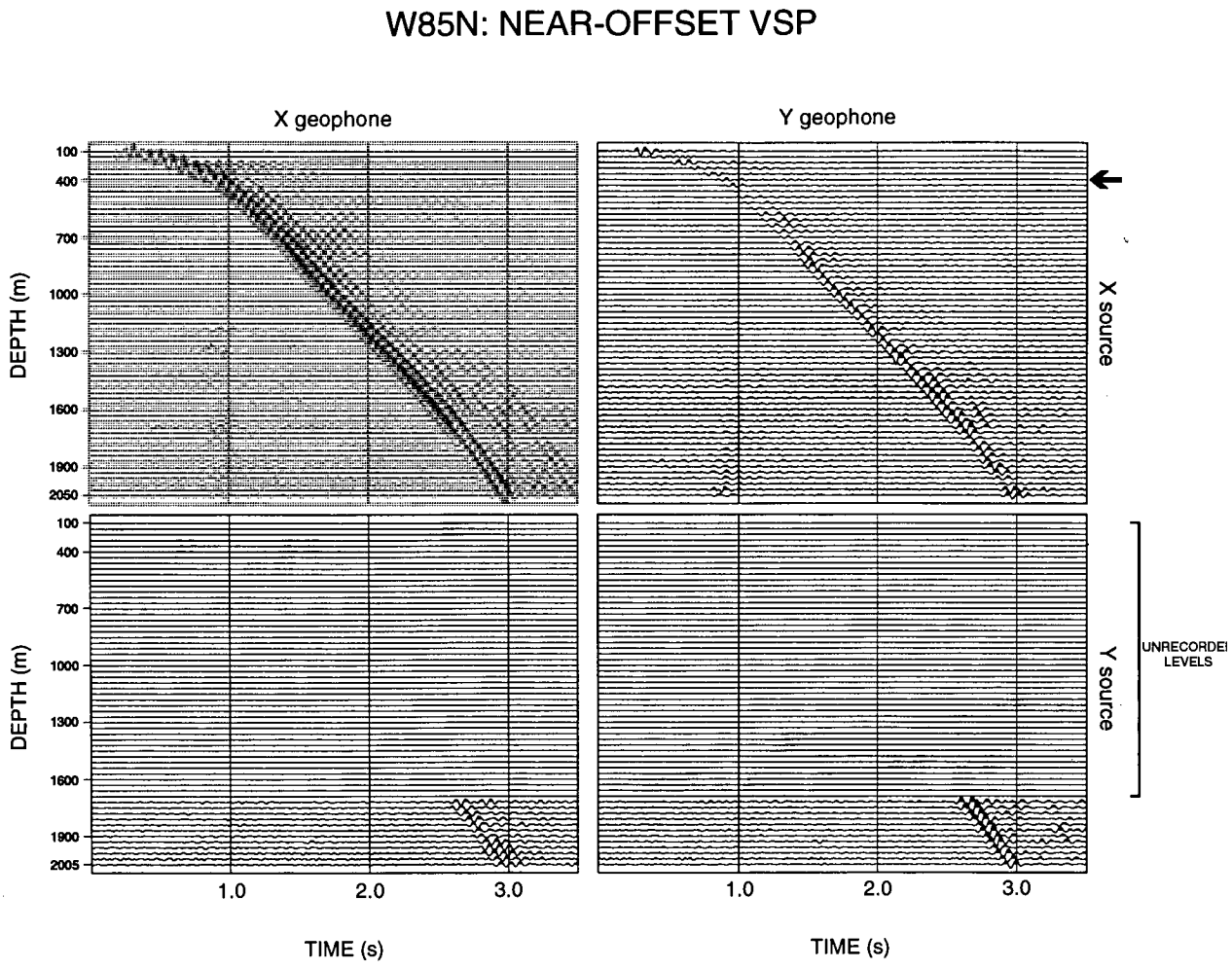

Figure 3.11: Four-component near-offset VSP at Well 85. Crossover energy on the off-diagonals may indicate anisotropy. Scaling is relative between components for each receiver level. For clarity of display every third receiver level is shown. The black arrow indicates the depth at which the receiver spacing changes from 20 m to 10 m.

3.6.4 Well 87 Seismograms

Figure 3.12 shows the conditioned near-offset VSP data The seismograms show clear shear-wave signals with a high signal-to-noise ratio. The reverberations in the signal probably result from short-pathlength multiples, generated between the surface and a known sandstone layer at approximately 5 m depth. The consistent appearance of the arrivals between levels in the top 1500 m suggests good reproducibility of the source.

Substantial energy is present on the off-diagonal components. This may indicate nonparallel (poorly reoriented) sources and geophones, or azimuthal anisotropy. Figure 3.13b shows horizontal-plane polarization diagrams of the shear-wave arrivals from the X source polarization, selected every 200 m. High ellipticity of the arrivals eliminates a straightforward source-geophone reorientation problem as the cause of the off-diagonal energy. If the ellipticity is indicative of shear-wave splitting, then the high elipticity at the shallowest receiver depths indicates a rapid build up of time delay above the shallow receivers, implying substantial azimuthal anisotropy in the near-surface.

3.6.5 Well 29 Seismograms

Figures 3.14, 3.17 and 3.19 show seismograms from the three VSPs recorded at Well 29. The data quality is very high. The similarity of the shear-wave arrivals between levels signifies that the rotation of the receiver components using the P-wave arrivals from the VEIP-40 source, instead of from the explosive source, has worked well. All three VSPs show shear-waves with a high signal-to-noise ratio and similar pulse shapes at all receiver depths. There is one observable reflected wave, generated from more than 100 m below the section. It arrives approximately 250 ms after the direct arrival at the deepest receiver and later at all shallower levels. Obviously, interference of other arrivals, such as reflections, with the direct shear-wave can decrease the reliability of shear-wave splitting estimates. The shear-wave splitting estimation techniques I apply later use a 200 ms window which excludes the reflected arrival and are, therefore, unaffected by this interference.

The near-offset VSP (W29N) in Fig. 3.14 has little energy on the off-diagonal components and subsequently linear arrivals in the polarization diagrams of Fig. 3.15a

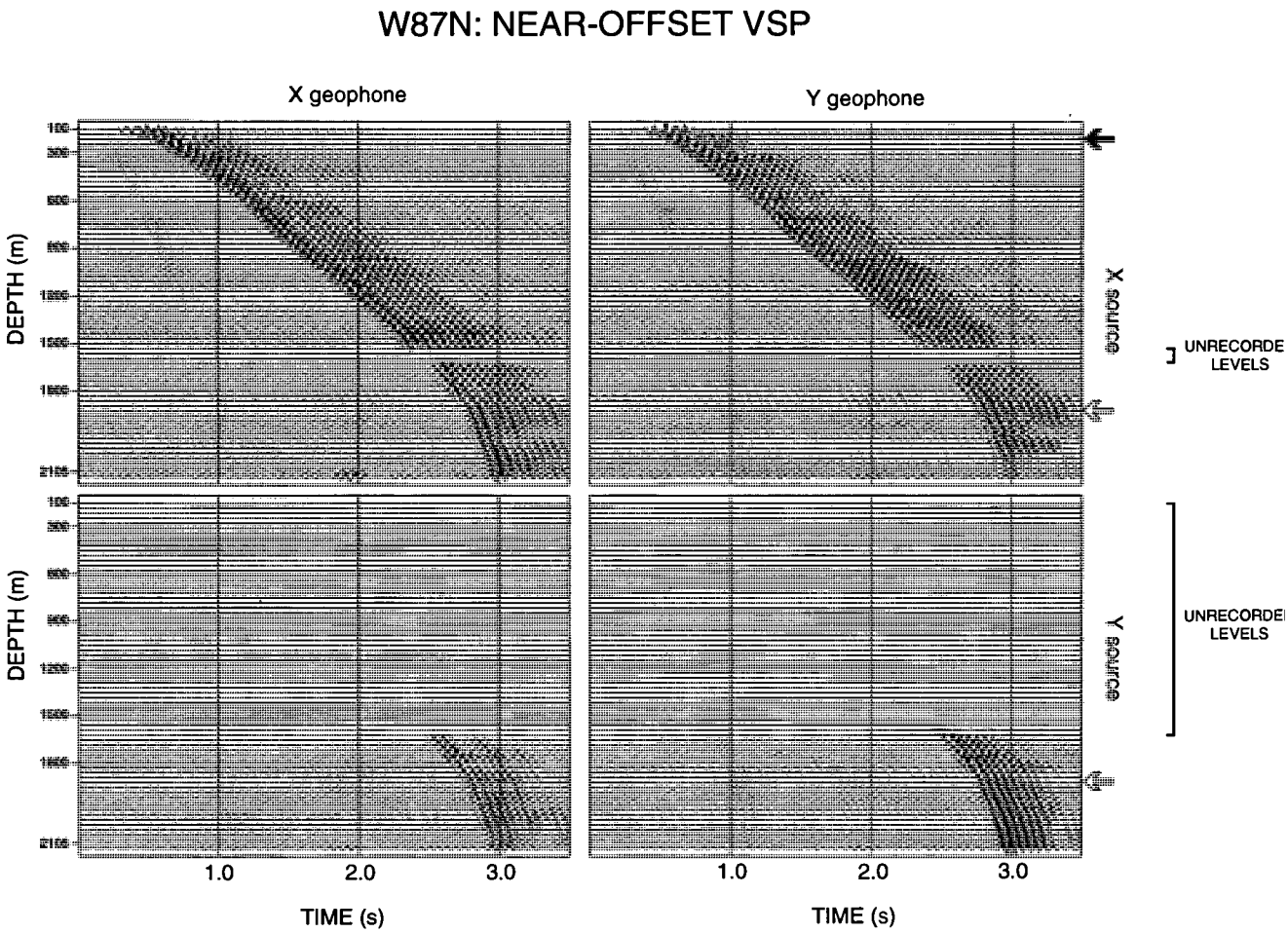

Figure 3.12: Four-component near-offset VSP at Well 87. Processed horizontal components, prior to the application of shear-wave splitting estimation techniques, are displayed with relative scaling between components at each receiver level. The crossover energy on the off-diagonal components may indicate anisotropy. For clarity of display every third level is displayed. Black and white arrows indicate changes in receiver spacing from 20 m to 10m, and from 10 m to 5 m, respectively.

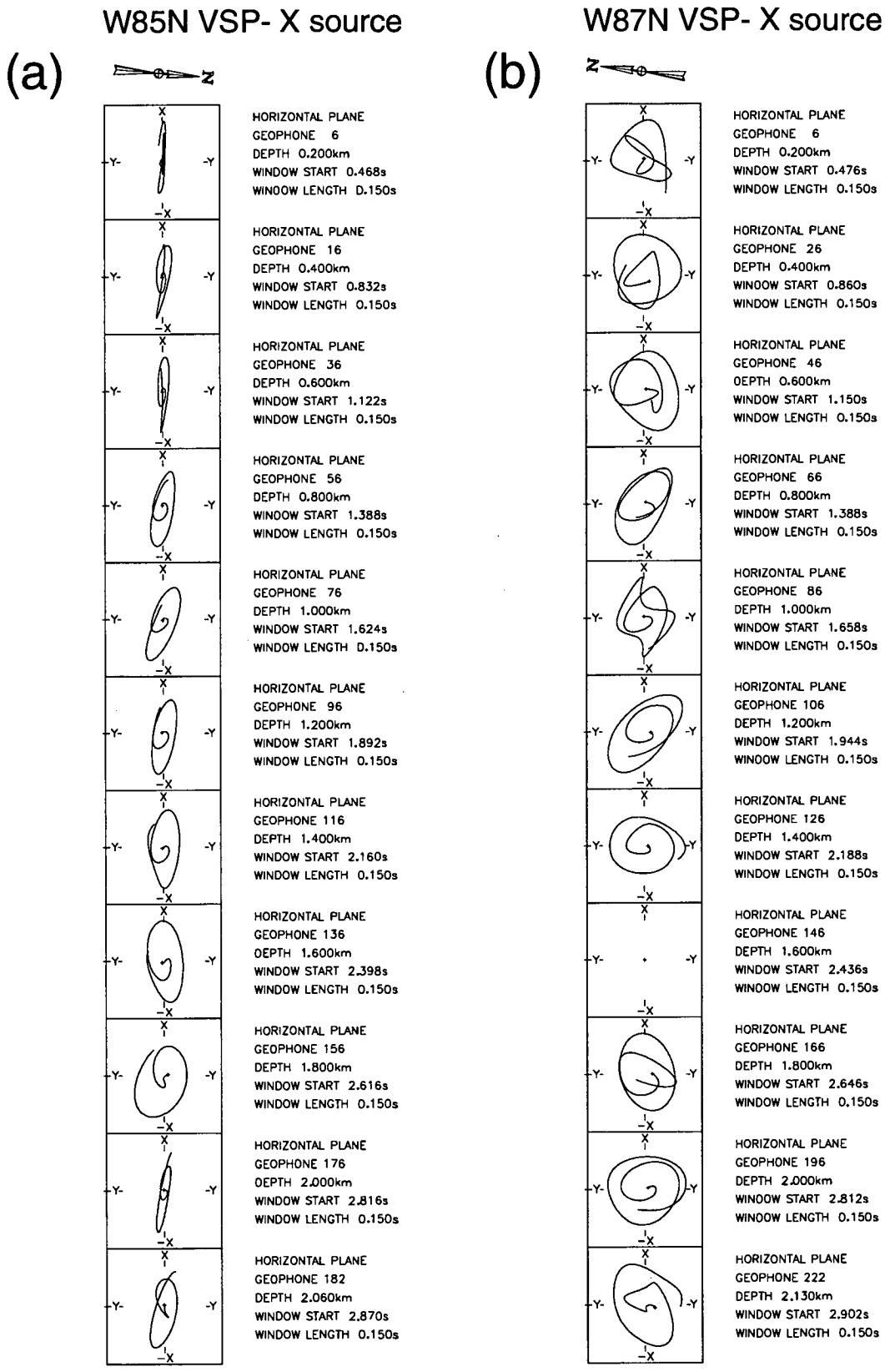

Figure 3.13: Horizontal-plane polarization diagrams from the near-offset VSPs at (**a**) Well 85 and (**b**) Well 87. At Well 85 ellipticity of the shear-waves gradually increases with depth, whereas at Well 87 the ellipticity is developed in the top 200 m.

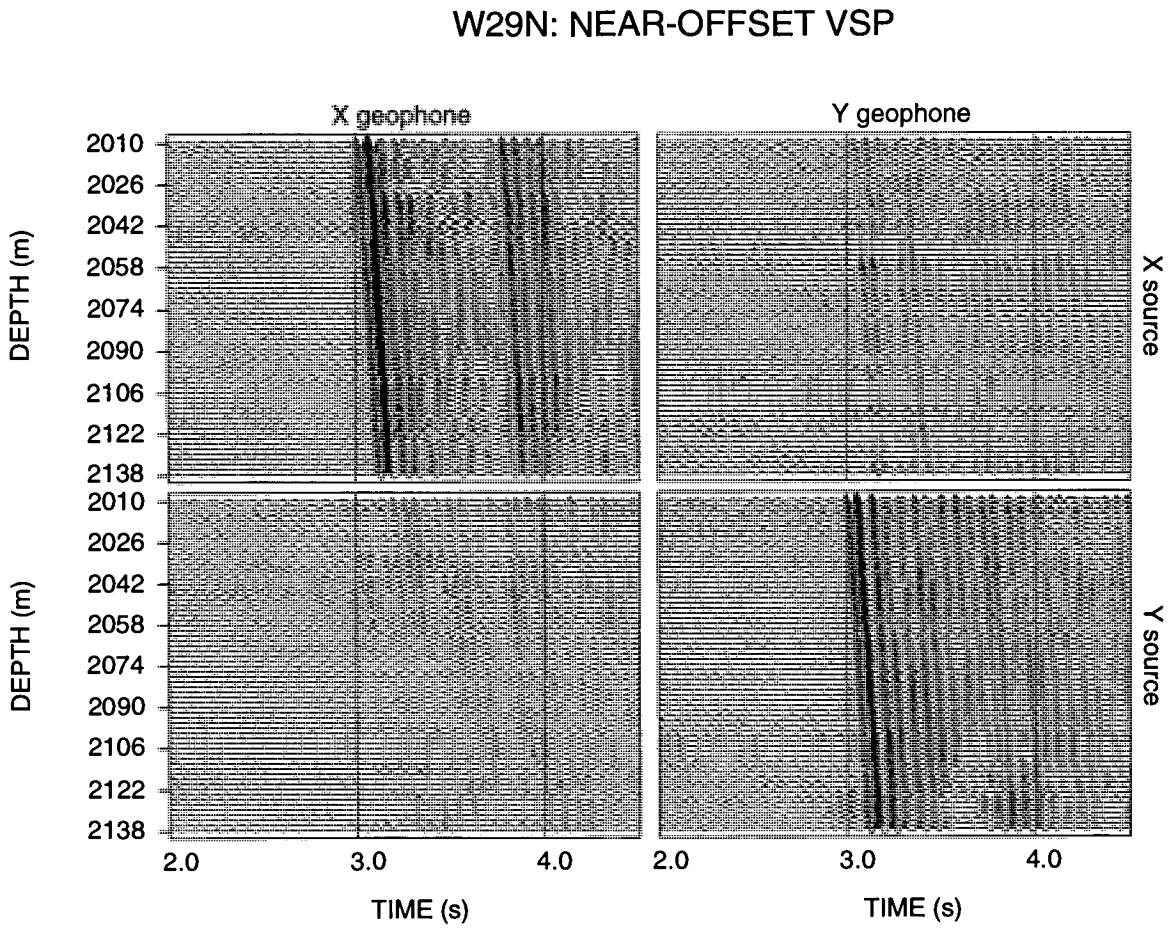

Figure 3.14: Near-offset dual-source VSP at Well 29. Little shear-wave energy on the off-diagonal components implies either isotropy or acquisition with the sources aligned with the natural polarization directions of the medium. Scaling is relative between the four components at each receiver level.

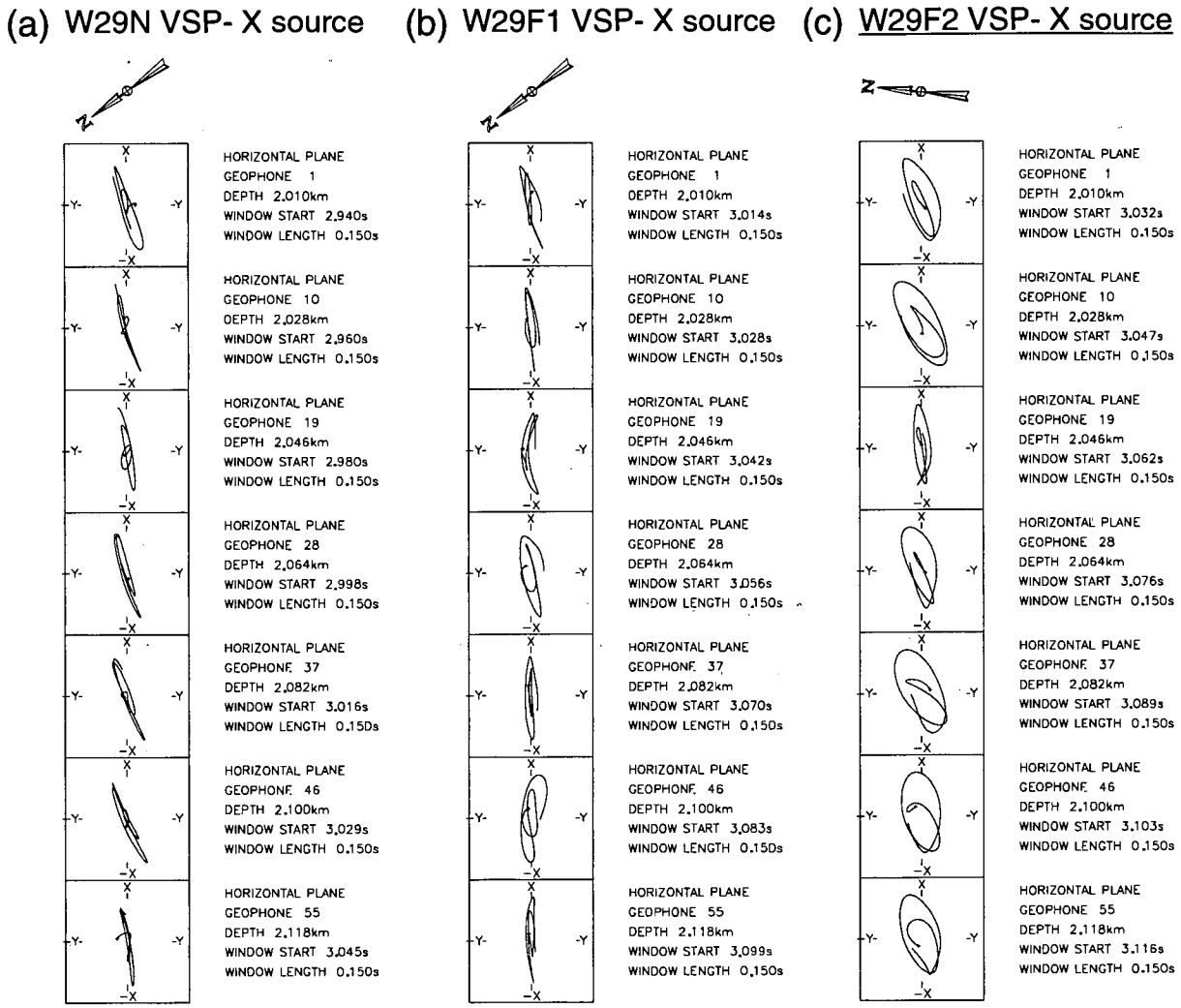

Figure 3.15: Horizontal-plane polarization diagrams of the near- and far-offset VSPs at Well 29 for the X source polarizations. The W29N and W29F1 VSPs have linear shear-wave arrivals, whereas the W29F2 VSP has elliptical arrivals.

are observed. This indicates either isotropy, in which case no shear-wave splitting has occurred, or acquisition with the sources and receivers aligned with the natural polarization directions of the medium. In the latter case, the fast split shear-wave would be recorded on one horizontal receiver component and the slow split shear-wave on the orthogonal component.

Because the data matrix is almost diagonal, the coordinate system of the sources can be resolved. Figure 3.16 shows the two main diagonal components, *XX* and *YY*, before and after a flip in the handedness of the source coordinate system. Inspection of the arrival times in the right-hand column shows that the signals on the *YY*-component arrive slightly earlier than those on the *XX*-component. This implies that a *qS1* direction is close to the *Y* direction, around N217°E.

Figure 3.17 shows the far-offset VSP (W29F1) which has a source offset of 645 m along azimuth N308°E. Similarly to the near-offset VSP, there is little energy on the off-diagonal components and, consequently, linear motion in the polarization diagrams of Fig. 3.15b. Determination of the source coordinate system is shown in Fig. 3.18. Inspection of the arrival times in the right-hand column of Fig. 3.18 reveals that the signals on the *XX*-component arrive earlier than those from the *YY*-component, indicating a *qS1* direction of around N308°E, orthogonal to that indicated by the near-offset VSP.

The four-component data matrix of the second far-offset VSP (W29F2) is shown in Fig. 3.19. Energy on the off-diagonal components and elliptical motion of the polarization diagrams in Fig. 3.15c indicate that shear-wave splitting is present in the data.

3.7 MEASUREMENT OF SHEAR-WAVE SPLITTING PARAMETERS

I now apply the shear-wave splitting measurement techniques, described in section 2.4, to measure the birefringence of the direct shear-wavefield at each well. These techniques were originally developed to measure the *qS1* direction and relative time delay between orthogonal split shear waves propagating along near vertical raypaths in materials characterized by either TIH anisotropy or a combination of TIV and TIH.

When analysing zero-offset VSPs, the horizontal plane has been commonly

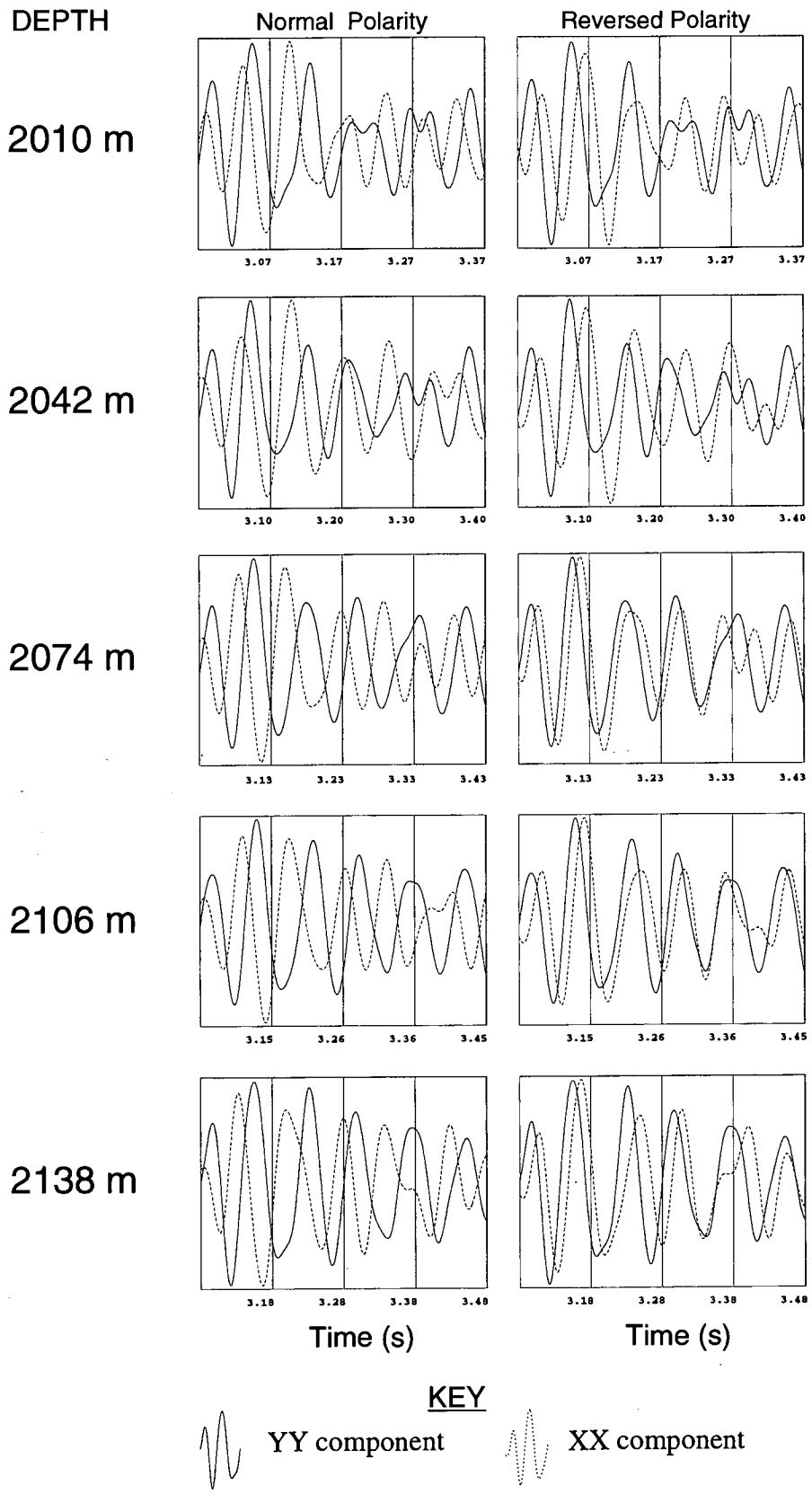

Figure 3.16: Resolving the coordinate system of the near-offset sources at Well 29. Selected main diagonal components from equally spaced receivers of the almost-diagonalized recorded data matrix (Fig.3.14) are shown without polarity reversals in the left-hand column. There is little similarity of the waveforms. In the right-hand column the polarity of the X source is reversed and the waveforms show strong similarity with a static shift indicating shear-wave splitting and a fast polarization direction close to the YY polarization direction (N37°E).

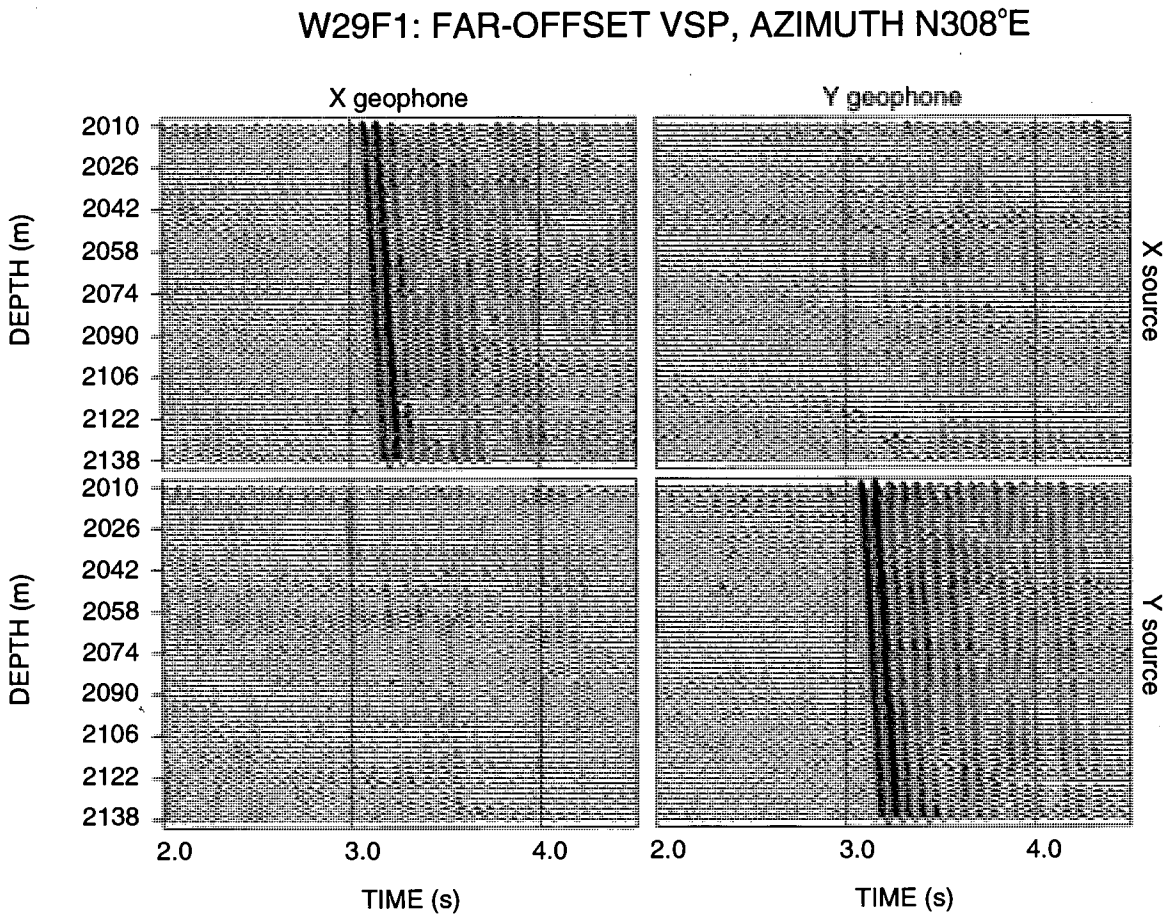

Figure 3.17: Far-offset dual-source VSP at Well 29 along azimuth N308°E. Little shear-wave energy on the off-diagonal components implies either isotropy or acquisition with the sources aligned along the natural polarization directions of the medium. Scaling is relative between the four components at each receiver level.

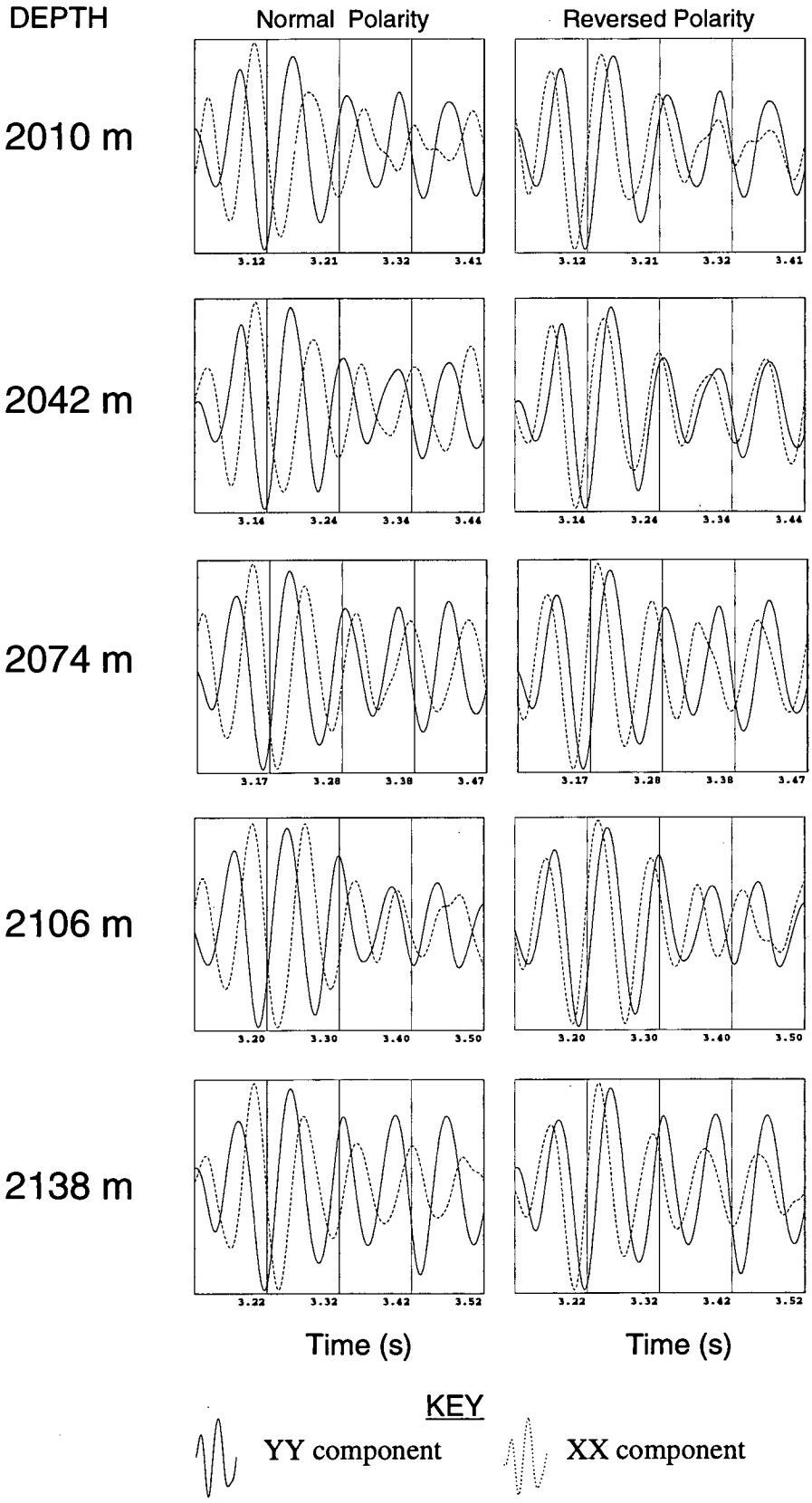

Figure 3.18: Resolving the coordinate system of the far-offset sources of the W29F1 VSP. The diagonal components from equally spaced receivers of the almost-diagonalized recorded data matrix (Fig.3.17) are shown without polarity reversals in the left-hand column. There is little similarity of the waveforms. In the right-hand column the polarity of the X source is reversed and the waveforms show strong similarity. The static shift indicates shear-wave splitting with a fast polarization direction close to the X source direction (N127°E), orthogonal to the direction observed in the near-offset VSP.

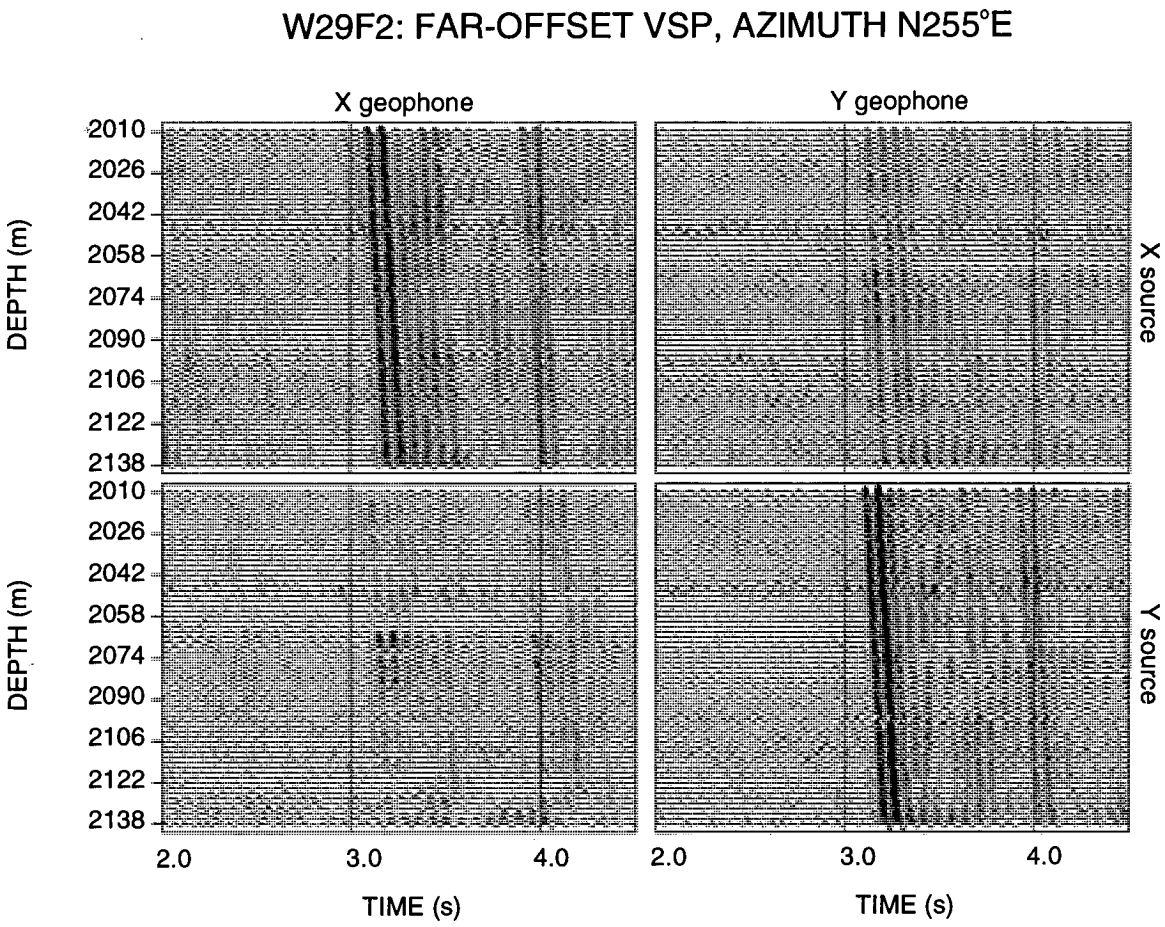

Figure 3.19: Far-offset dual-source VSP at Well 29 along azimuth N255°E. Shear-wave energy on the off-diagonal components may be indicative of anisotropy. Scaling is relative between the four components at each receiver level.

chosen for calculating and displaying polarization directions. For split shear waves propagating along non-vertical raypaths, such as those from far-offset sources, the projections of the shear-wave polarizations onto the horizontal plane are, in general, nonorthogonal. For such raypaths it is more appropriate to apply the techniques to the dynamic plane (the plane of maximum shear-wave energy), and then to project the estimated polarization directions back onto a horizontal reference frame. In this chapter, arrivals at the shallow receivers in the near-offset VSPs, and at all receivers in the far-offset VSPs, are likely to be propagating along high-incidence raypaths. I estimate the orientation of the dynamic plane for these raypaths by measuring the direction of maximum shear-wave energy in the sagittal plane over a 200 ms window using a covariance matrix method (Kanasewich, 1981).

The angle between the dynamic plane and the horizontal plane measured at Well 85 and Well 87 are shown in Fig. 3.20. (I could not make such measurements at Well 29 because the horizontal and vertical traces are not relatively scaled.) In isotropic structures these measurements would represent the incidence angle of the arrival at each geophone. Also shown in Fig. 3.20 are the incidence angles of arrivals for straight-line raypaths between sources and receivers. In structures with increasing velocity with depth, a measured angle would be greater than the corresponding straight-line value. The measured incidence angles in Fig. 3.20 are, however, relatively much smaller. Possible explanations for this include: unequal sensitivity (scaling) of vertical and horizontal components; distortion to the shear-waveform due to interface effects or shear-wave splitting; and, most likely, a large decrease of velocity with depth occurring above the shallowest receivers.

The data were rotated about an axis normal to the sagittal plane by the angles in Fig. 3.20 and shear-wave splitting estimation techniques applied. The results were then verified by rotating the receiver components (and source components for dual-source measurements) parallel and perpendicular to the measured *qS1* direction, and visually inspecting the seismograms to confirm the similarity in waveform of the *qS1* and *qS2* arrivals. Finally, the results were projected onto the horizontal reference plane. To aid comparison between the three wells, all polarization directions are plotted relative to geographic north.

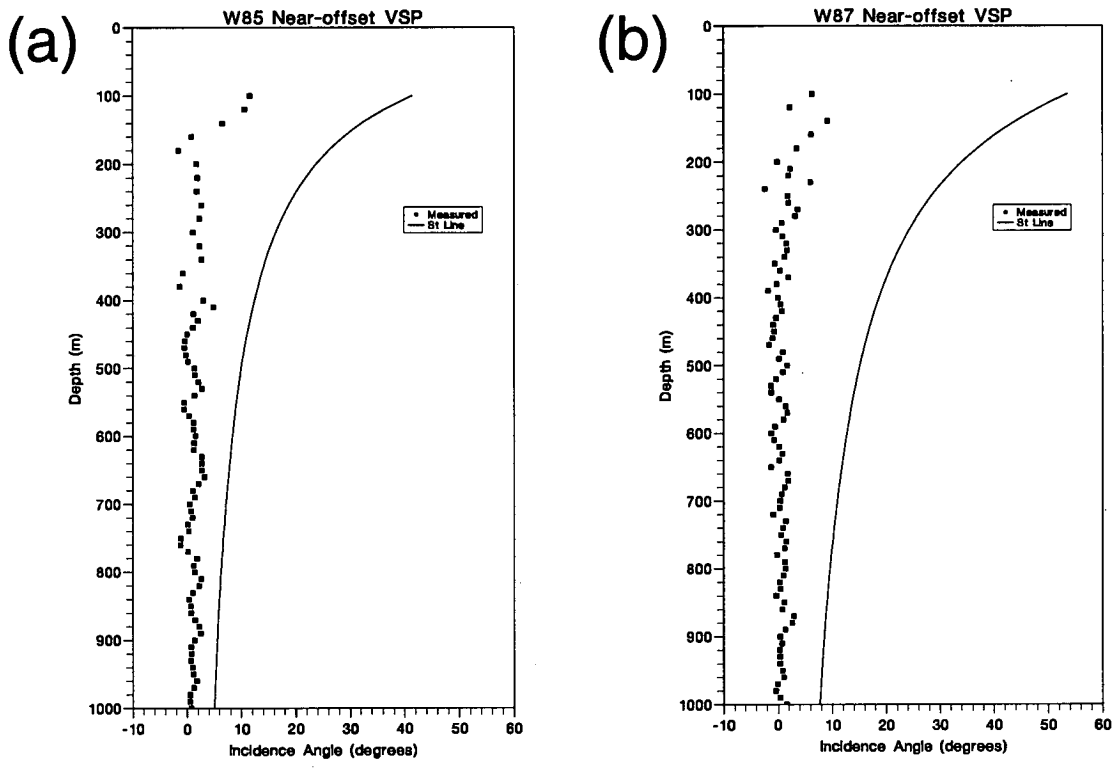

Figure 3.20: Estimated shear-wave incidence angles for the near-offset VSPs at (**a**) Well 85 and (**b**) Well 87. For reference, the incidence angles for straight line raypaths connecting source and receivers is plotted as a solid line.

3.7.1 Well 85

Single-source method

DTS was applied separately to arrivals from both *X*- and *Y*-source polarizations with window lengths varying from 60 ms to 500 ms. In general, the measurements of *qS1* direction and time delay were stable for all window lengths. The DTS results using a 140 ms window enclosing the direct arrival are displayed in Fig. 3.21. The results from the two sources agree closely. If the anomalous results in the near-surface (above 250 m) are excluded, the *qS1* polarization estimates in Fig. 3.21a appear constant with depth, although there is an increase of scatter with depth. The estimated polarization has an average value of N22°E with mean deviation equal to 8°. The time delay below 250 m gradually increases, reaching 16 ms at a depth of around 1000 m. Below 1000 m the delay appears constant, although the increasing scatter means no reliable interpretation can be made.

Dual-source methods

The DCT and DIT results for both the dual-source near-offset VSP are shown in Fig. 3.22. The scatter of the measurements over this interval is greatly reduced from those obtained using the single source method (Fig. 3.21). The near-offset *qS1* polarization remains constant over the interval. The average DCT *qS1* direction of N17°E with mean deviation equal to 5° agrees closely with the single-source estimate. The time delay increases from around 12 ms at the top of the interval to about 18 ms at 1960 m depth, and then possibly decreases to about 14 ms at 2060 m.

3.7.2 Well 87

Single-source method

The DTS method was applied separately to the data from each of the two source polarizations, *X* and *Y*. For each source, the window start time was specified by interactively picking the shear-wave arrival time at each receiver level. To determine the effect of window length on the estimation results, measurements were made with window lengths from 40 ms to 500 ms. The most stable results between receiver levels were obtained with a window length of around 80 ms. This length encloses

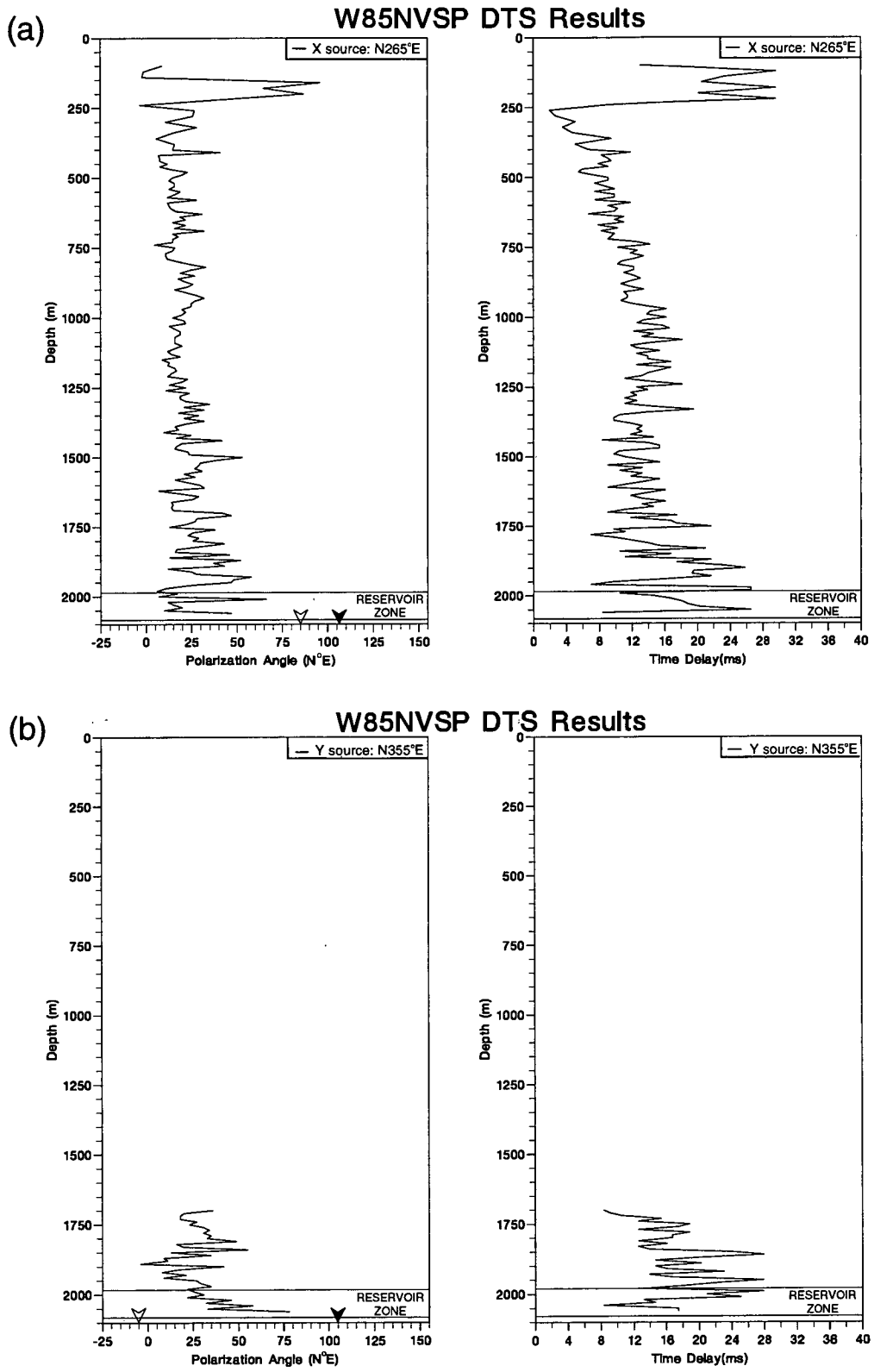

Figure 3.21: Single-source shear-wave splitting measurements at Well 85 from (**a**) X source and (**b**) Y source polarizations. The fast shear-wave polarization direction, of around N25°E, is constant with depth and is consistent between diffferent source polarizations. The filled and unfilled arrowheads mark the sagittal plane and the source polarization directions, respectively. Time delays increase to about 16 ms in the upper 1 km and are scattered about an average of 16 ms below 1 km for both source polarizations.

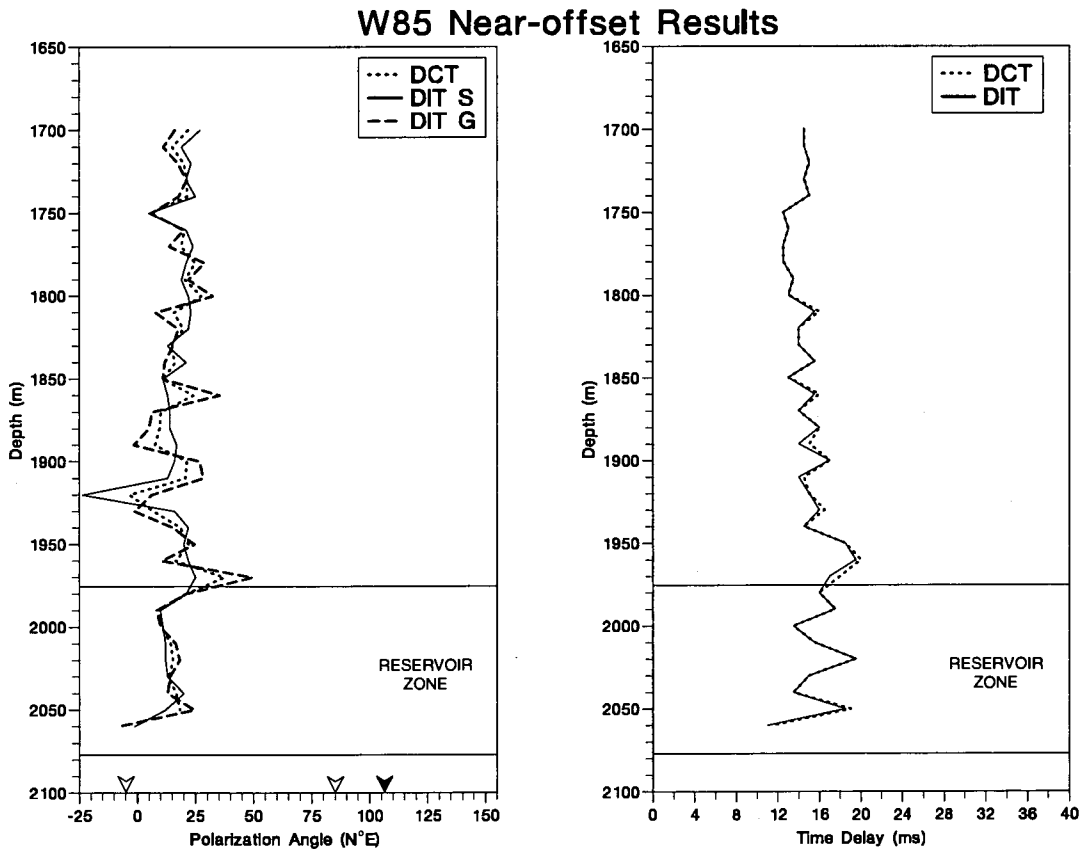

Figure 3.22: Dual-source shear-wave splitting measurements at Well 85. Good agreement between the DIT source and geophone measurements for the near-vertical raypthas indicates the absence of a change in qS1 direction with depth. The filled and unfilled arrowheads mark the sagittal plane and the source polarization directions, respectively.

about one and a half cycles of the shear-wave and excludes the high energy reverberations observed in Fig. 3.12. The DTS results for the 80 ms window length are shown in Fig. 3.23.

Between the depths of 100 m and 250 m both the *qS1* polarization and the time delay fluctuate widely, although they do appear to converge to the stable values observed below 250 m. Little confidence, however, can be attributed to the results above 250 m for the following reasons:

i) interference from other arrivals (such as interface waves and converted phases) present within the top 250 m, a consequence of the high inclination of the raypaths;

ii) possible anomalous phase shifts along the highly inclined raypaths caused by propagation outside the shear-wave window (Liu and Crampin, 1990);

Excluding the results above 250 m, the *qS1* polarization direction measurements from the *X*-source indicate a constant *qS1* direction with depth. The average direction is N25°E with mean deviation equal to 10°. The deviation from the average direction increases with depth. This increase may represent increasing errors caused by, possibly, a reduction in the signal-to-noise ratio of the shear-waves with depth (observed pulse lengthening with depth indicates increasing attenuation of the high frequencies), or increasing errors in tool reorientation (P-wave energy in the horizontal plane, used to determine the tool orientation, decreases with depth).

The time delay measurements from the *X*-source below 250 m appear to be scattered about a constant value. Assuming the delay is constant and the scatter is caused by acquisition technique and/or local borehole conditions, I average the measurements below 500 m and obtain a value of 24 ms with mean deviation equal to 3.1 ms. The time delay between the start times of the fast and slow shear-waves is difficult to estimate visually on the polarization diagrams in Fig. 3.13b. However, the high ellipticity of the top few PD's and the approximately constant ellipticity with depth agree a rapid build up of time delay in the near-surface which remains more or less constant with depth.

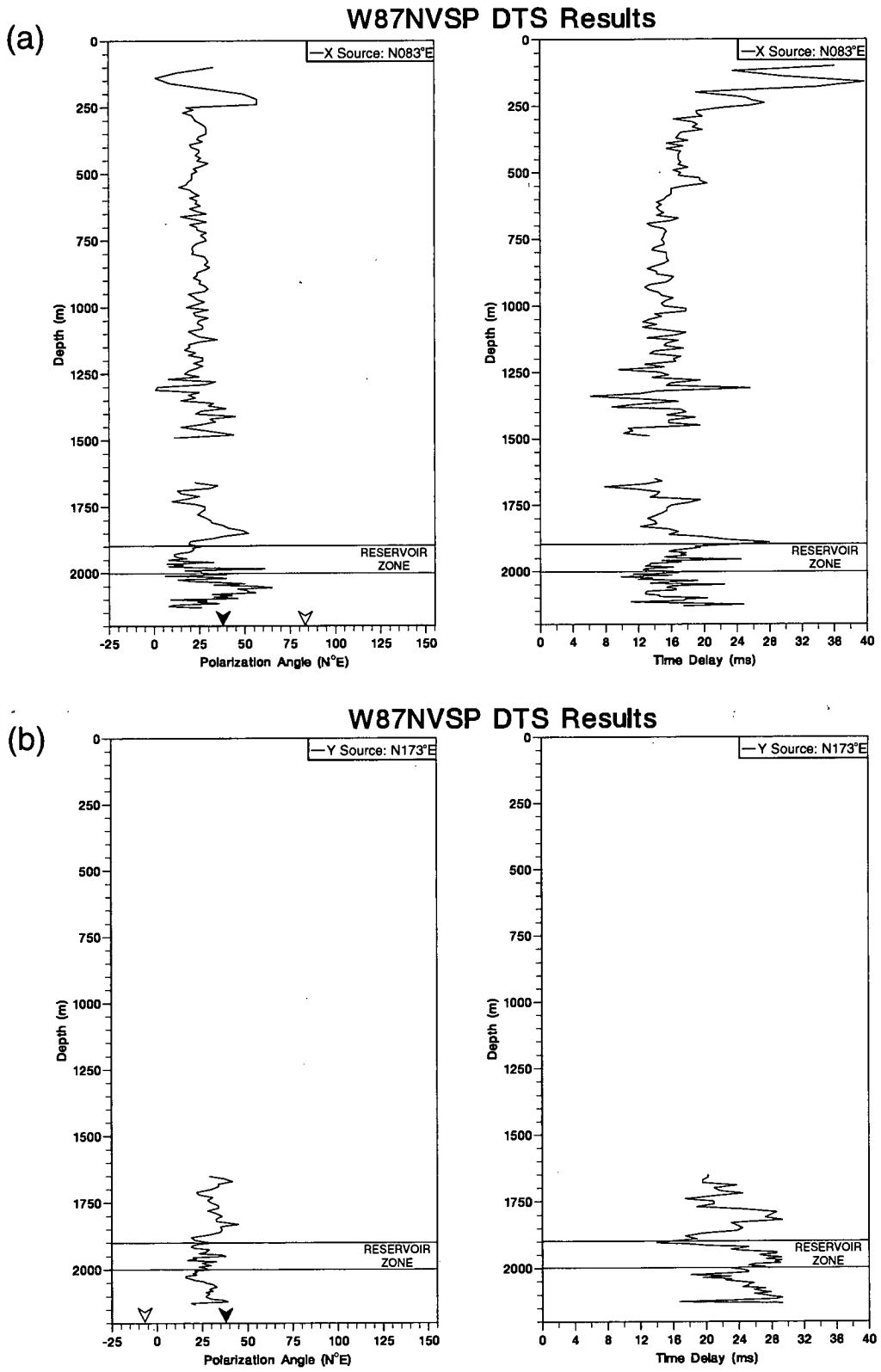

Figure 3.23: Single-source shear-wave splitting measurements at Well 87 from (**a**) X and (**b**) Y source polarizations. The fast shear-wave polarization direction, of around N25°E, is constant with depth and is consistent between the different source polarizations. The filled and unfilled arrowheads mark the sagittal plane and the source polarization directions, respectively. Time delays are scattered about an average of 16 ms for the source polarized along N83°E, and 22 ms for the source polarized along N173°E.

Dual source methods

I now describe the application of the dual-source shear-wave splitting estimation techniques DCT and DIT. The DIT method is applied to help identify and interpret asymmetry in the data matrix (MacBeth *et al.*, 1994). The dual-source results shown in Fig. 3.24 indicate a *qS1* direction between North and N35°E and a time delay varying between 12 ms and 20 ms, which, in general, agree with those from the DTS method (Fig. 3.23). The mean *qS1* direction over the whole depth interval using the DCT method is N12°E. At the top of the recording interval, the DIT source and geophone estimates of the *qS1* direction disagree by up to 40°, indicating asymmetry in the data matrix. A multicomponent overburden correction (Zeng, 1994), designed for four component data, was applied to the data matrix. However, no reliable deconvolution operator could be found to reduce the matrix to symmetry. This is most likely due to the large variation in the recorded waveforms with depth and the narrow bandwidth of the data.

Inspection of Fig. 3.24 shows that there is possibly a correlation between the time delay and the separation between source and geophone polarization measurements from DIT. In general, the measured time delay is large when the separation between the two polarization directions is large. Furthermore, the time delay appears to decrease or increase with respective decreases or increases in the separation of the polarizations. For instance, between 1650 m and 1820 m the separation between source and geophone polarizations decreases correspondingly with the time delay, and between 1820 m and 1900 m the time delay increases correspondingly with the separation in the polarization directions. Furthermore, below 1970 m the separation between source and geophone results is relatively small and, in agreement with the behaviour just described, the time delay is small.

The two most likely causes of a separation between DIT source and geophone measurements are: a change in the *qS1* direction with depth causing multiple shear-wave splitting (MacBeth and Yardley, 1992); and a misalignment between sources and geophones (Zeng and MacBeth, 1993a). It is likely, therefore, that the depth variations in the DIT source and geophone results may be related to either depth variations in geology or acquisition. To check this, I plot the *qS1* estimates in Fig. 3.25 alongside wireline logs of the interval. Some significant changes in the wireline logs are marked as likely changes in geology, and here appears little

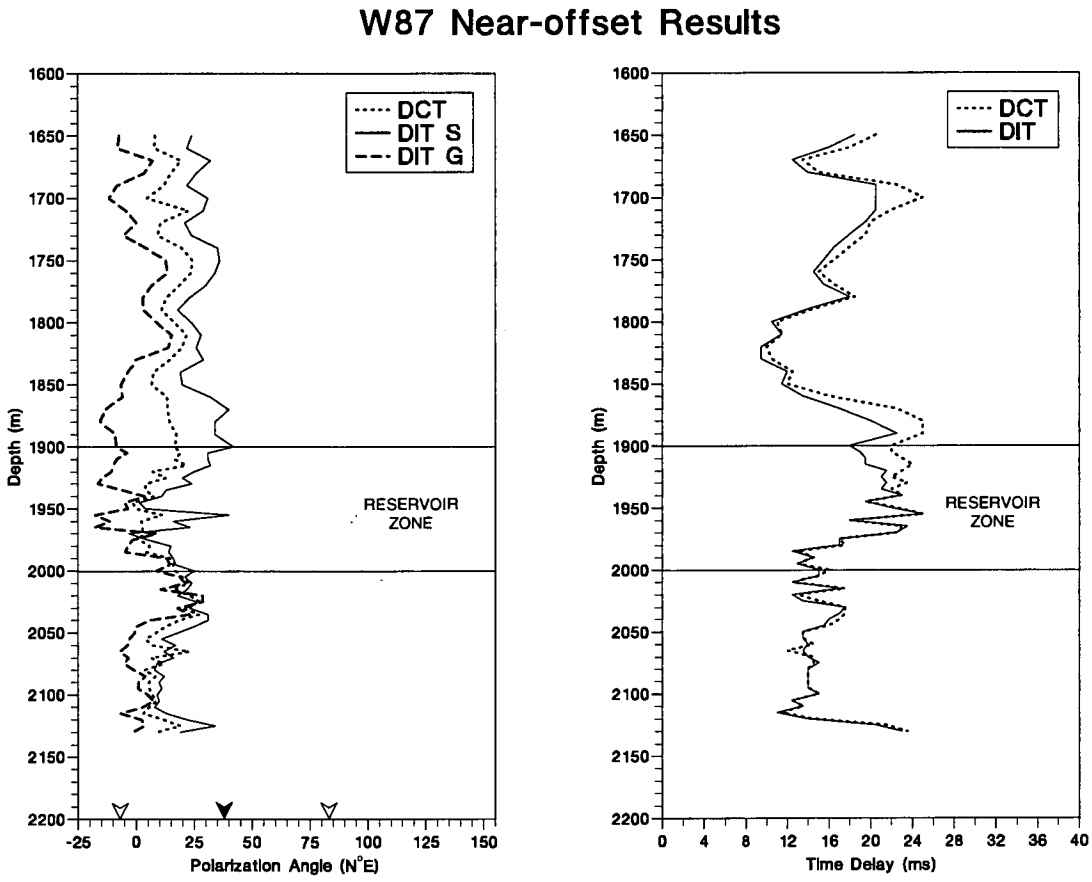

Figure 3.24: Dual-source shear-wave splitting measurements at Well 87. DIT polarization measurements show a difference of up to 25° between the source and geophone estimates. The DCT polarization measurement shows an average of N15° E. The filled and unfilled arrowheads mark the sagittal plane and source polarization directions, respectively. Time delays are scattered about an average of 18 ms for both techniques.

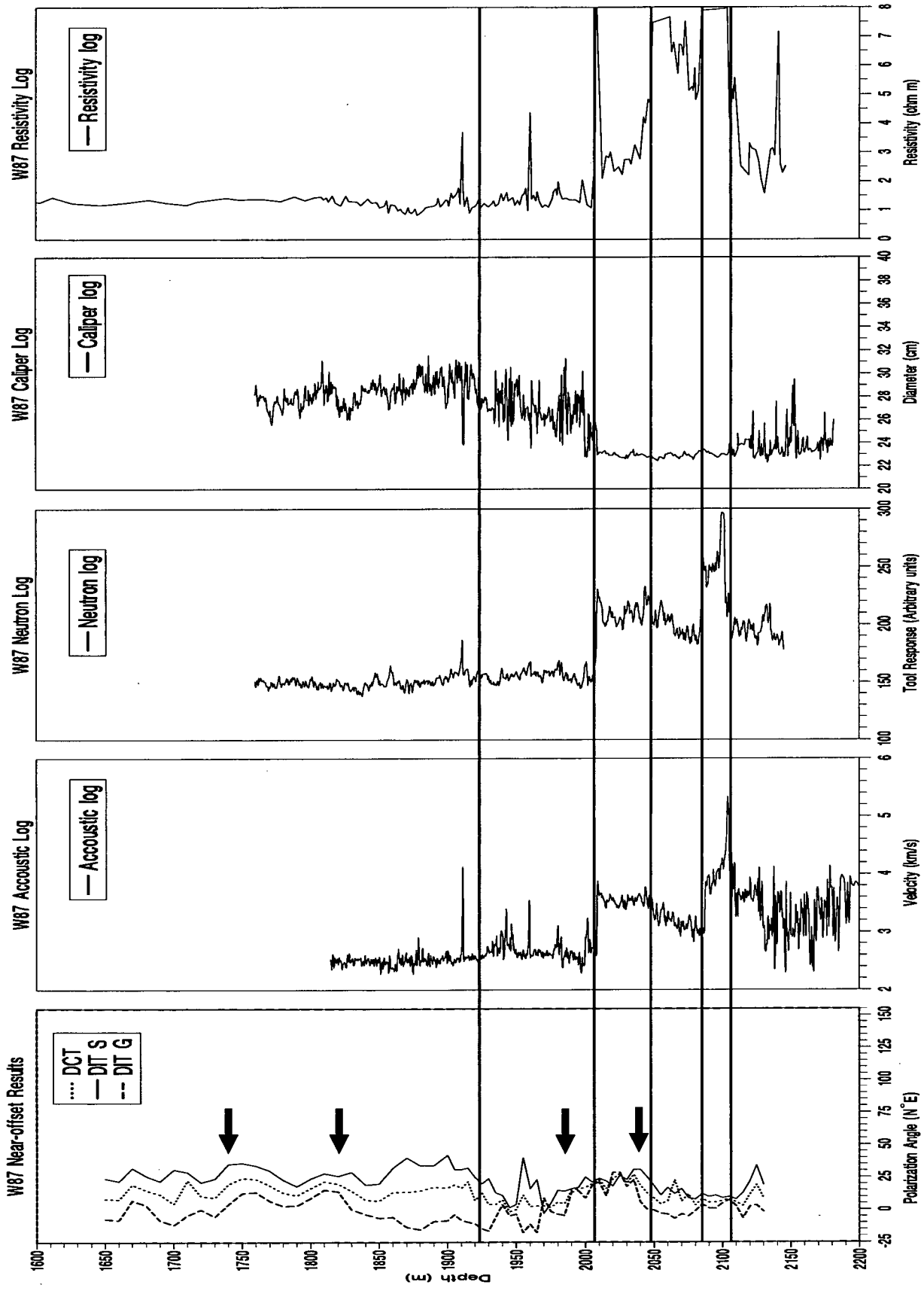

Figure 3.25: Measured qS1 direction and wireline logs at Well 87. Changes in geology are interpreted from the well logs and superimposed onto the qS1 polarization plot. Filled arrows mark the depths at which source trucks were replaced.

correlation between the geological boundaries and the changes in the DIT source and geophone behaviour. The large filled arrows mark the depths at which the sources were replaced. On the other hand, there is an indication of a positive correlation, particularly at 1820 m and 2040 m, between the DIT angles and source replacements (marked by solid arrows in Fig. 3.25). This suggests that deviations in the resultant source polarizations, probably caused by near-surface distortions, may be a significant contributing factor to the separation between DIT source and geophone polarizations.

3.7.3 Well 29

Dual-source methods

Measurements of the *qS1* polarization direction in the three VSPs at Well 29 are made with a 200 ms window containing the direct shear-wave, and the results displayed in Fig. 3.26. Each VSP displays a constant *qS1* direction with depth and, in general, there is an excellent agreement between the DCT and the DIT measurements, particularly for the W29N and W29F1 VSPs. For the near-offset VSP, W29N, the average DCT direction over the interval is N29°E with a mean deviation of 4°. This agrees well with the near-offset measurements at the two other wells, both of which show a NNE-SSW *qS1* direction. The far-offset VSPs, W29F1 and W29F2, have average directions of N124°E and N58°E with mean deviations of 4° and 6°, respectively.

The associated time delays are displayed in Fig. 3.27. The near-offset VSP in Fig. 27a shows a large decrease in time delay from 18 ms to 10 ms between the depths of 2040 m and 2140 m. The far-offset VSPs time delays, however, appear nearly constant with depth at about 12 ms and 14 ms for W29F1 and W29F2, respectively. However, there may possibly be small decreases in both VSPs of around 2 ms.

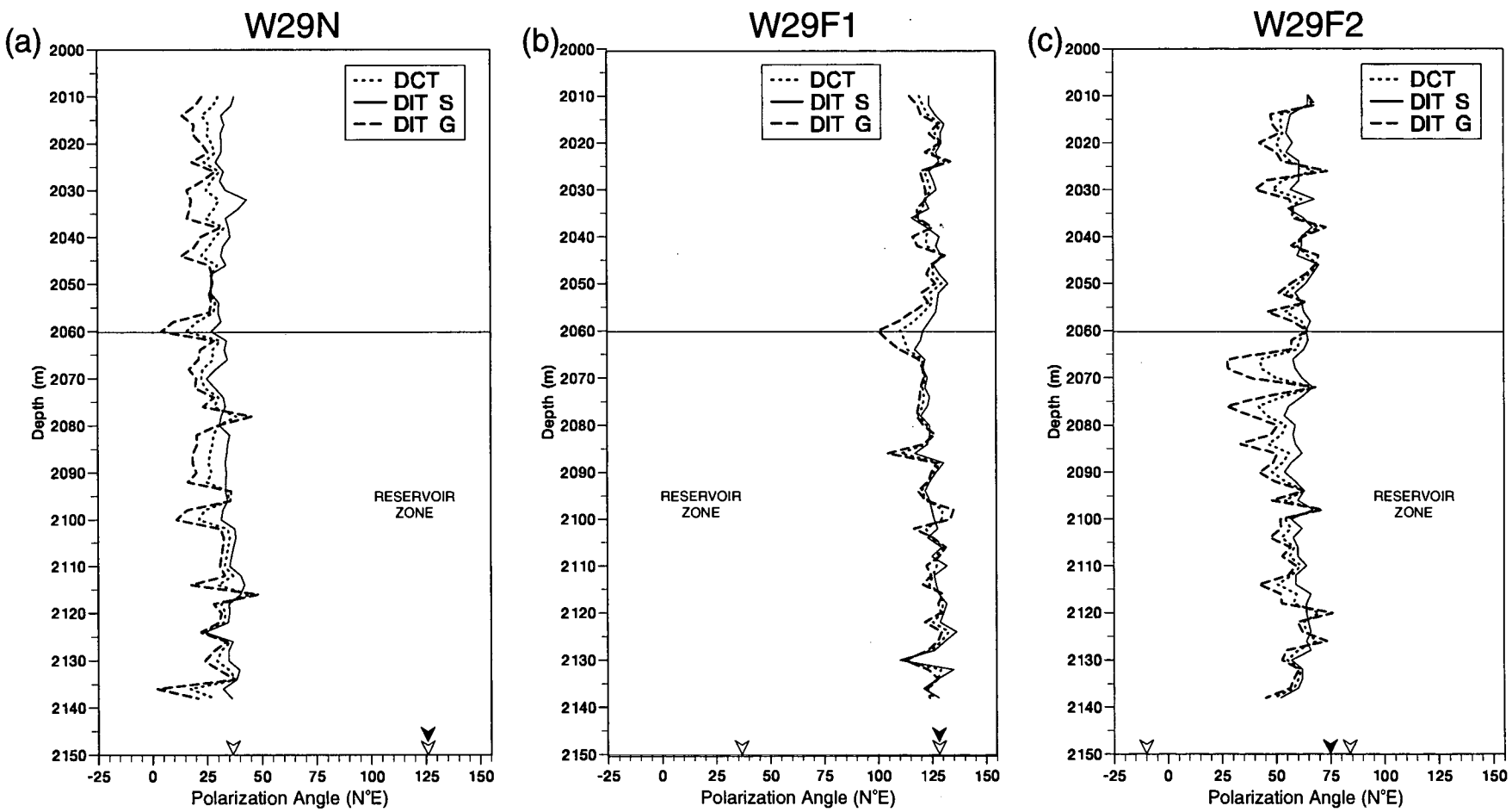

Figure 3.26: Dual-source shear-wave splitting measurements of the qS1 direction at Well 29 from sources positioned at (**a**) near-offset, (**b**) far-offset along N308°E and (**c**) far-offset along N255°E. The offset VSPs, W29F1 and W29F2, display rotations from the near-offset VSP qS1 direction of 90° and 25°, respectively. The filled and unfilled arrowheads mark the sagittal plane and source polarization directions, respectively.

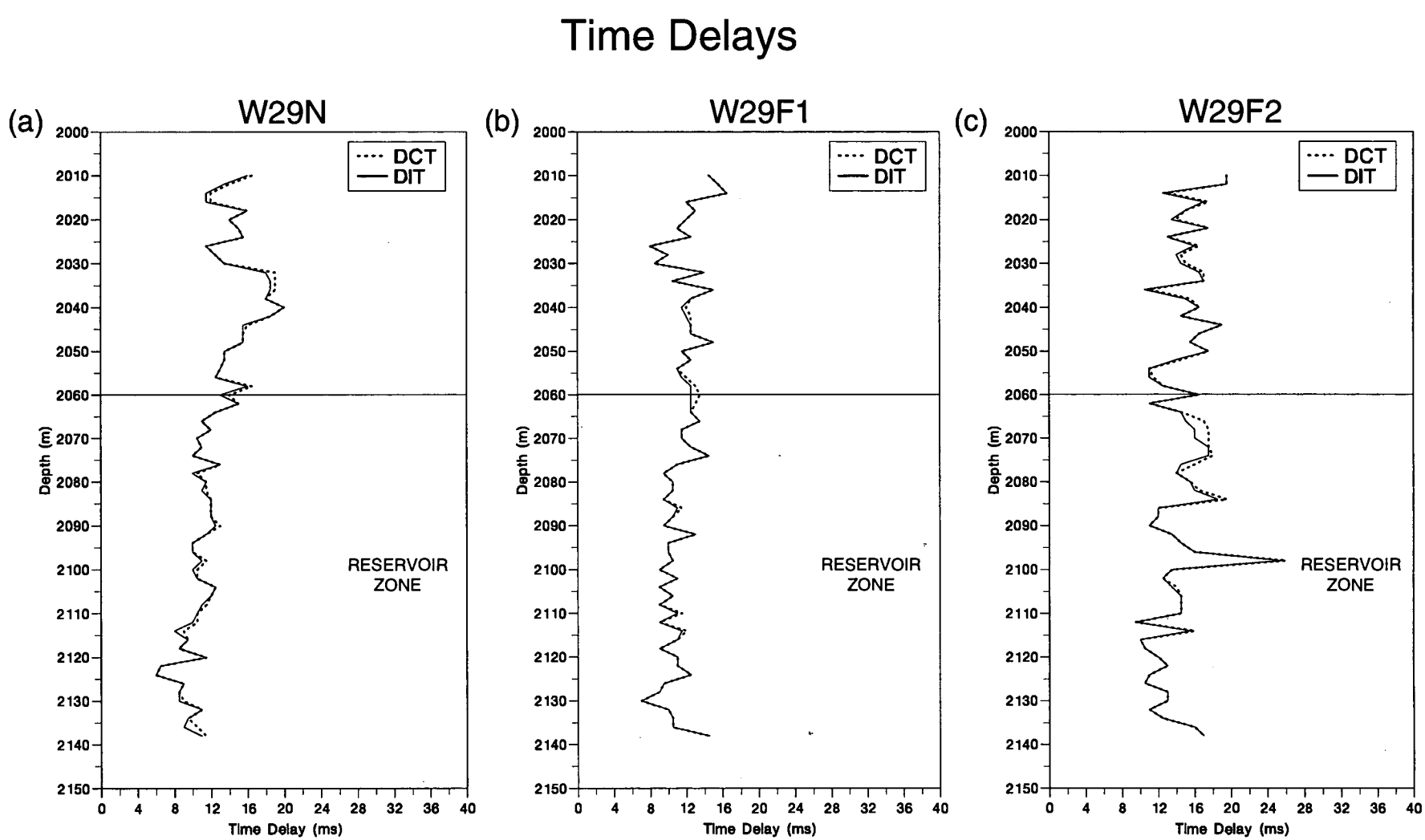

Figure 3.27: Dual-source shear-wave splitting measurements of time-delay at Well 29 from the sources positioned at (**a**) near-offset, (**b**) far-offset along N308°E and (**c**) far-offset along N255°E. The far-offset VSPs, (b) and (c), show constant delay over the interval of about 11 ms and 16 ms respectively. However, the near-offset VSP shows a clear decrease in delay of about 8 ms, from about 18 ms down to about 10 ms, over approximately 100 m.

3.8 SUMMARY AND CONCLUSIONS

Here I summarize the shear-wave splitting measurements obtained in this chapter. Because arrivals at different depths in near-offset VSPs share a common raypath direction, shear-wave splitting measurements in the near-offset VSPs are more straightforward to interpret than those in far-offset VSPs. Therefore, in this summary I shall concentrate on the near-offset VSP results and, in particular, consider whether any changes along the subvertical raypaths indicate significant changes in the anisotropic structure with depth.

The *qS1* polarization variation with depth at each well.

At Well 85 there are two indicators of a constant *qS1* polarization direction with depth: firstly, the close agreement in the near-offset VSP between the DTS measurement in the upper 1 km and the deeper DIT measurements (Figures 3.21 and 3.22); and secondly, the close agreement between the DIT source and geophone measurements in Fig. 3.22, which implies an absence of multiple shear-wave splitting and, therefore, a constant *qS1* direction with depth.

A similar observation is made at Well 29, where the strong agreement between the two DIT estimates implies there is a constant fast shear-wave polarization direction with depth (Fig. 3.26).

At Well 87, however, the significant separation between the DIT estimates in Fig. 3.24 indicates data matrix asymmetry caused by either a change in the fast shear-wave polarization direction with depth, or more likely, differences in the source radiation patterns of the two sources caused by near-surface interactions.

Variation of *qS1* polarization direction between the wells.

Figure 3.28a displays collectively the *qS1* polarization directions at the three wells made using the DCT estimation technique. For comparison, the receiver depths of each VSP are plotted relative to a fixed geological datum, chosen as the base Maikop. There is a high consistency in the polarization direction between the wells in Fig. 3.28a, with the fast shear-wave aligned in a NNE direction subparallel to the regional stress direction inferred from other methods (section 3.2.2). This suggests that the cause of the shear-wave splitting is stress-controlled.

Differential time delay behaviour at the wells

The single-source measurements at Wells 85 and 87 show markedly different behaviour within the uppermost 1 km. However, below this level, the time delays at the two wells are approximately equal, at about 15 ms.

The DCT time delay estimates at greater depths nearer to the reservoir are displayed in Fig. 3.28b for the near-offset VSPs at each of the three Wells. The time delay in Wells 85 and 29 show an agreement down to a depth of about 150 m above the base Maikop. Below this level, though, they appear to diverge steadily. It can be seen in Fig. 3.28b that the reservoir zone appears to be characterized by a decrease in time delay. The decrease seems to start about 20 m above the reservoir zone. At Wells 85 and 87, however, the decreases are questionable. At Well 85, this is because there are few (ten) receiver levels within the reservoir zone and substantial scatter in the measurements. At Well 87, it is because of the large separations between the two DIT polarization estimates (Figure 3.24) which imply poorly resolved data matrices. At Well 29, the time delay decrease is unquestionable and is approximately equal to 8 ms over 100 m. Since the shear-wave velocity through this interval is about 1300 ms^{-1}, this decrease indicates a substantial vertical shear-wave anisotropy of about 9% in the reservoir zone [percentage anisotropy $=100 \times (V_{fast}-V_{slow})/V_{fast}$]. Constant DIT *qS1* polarizations and

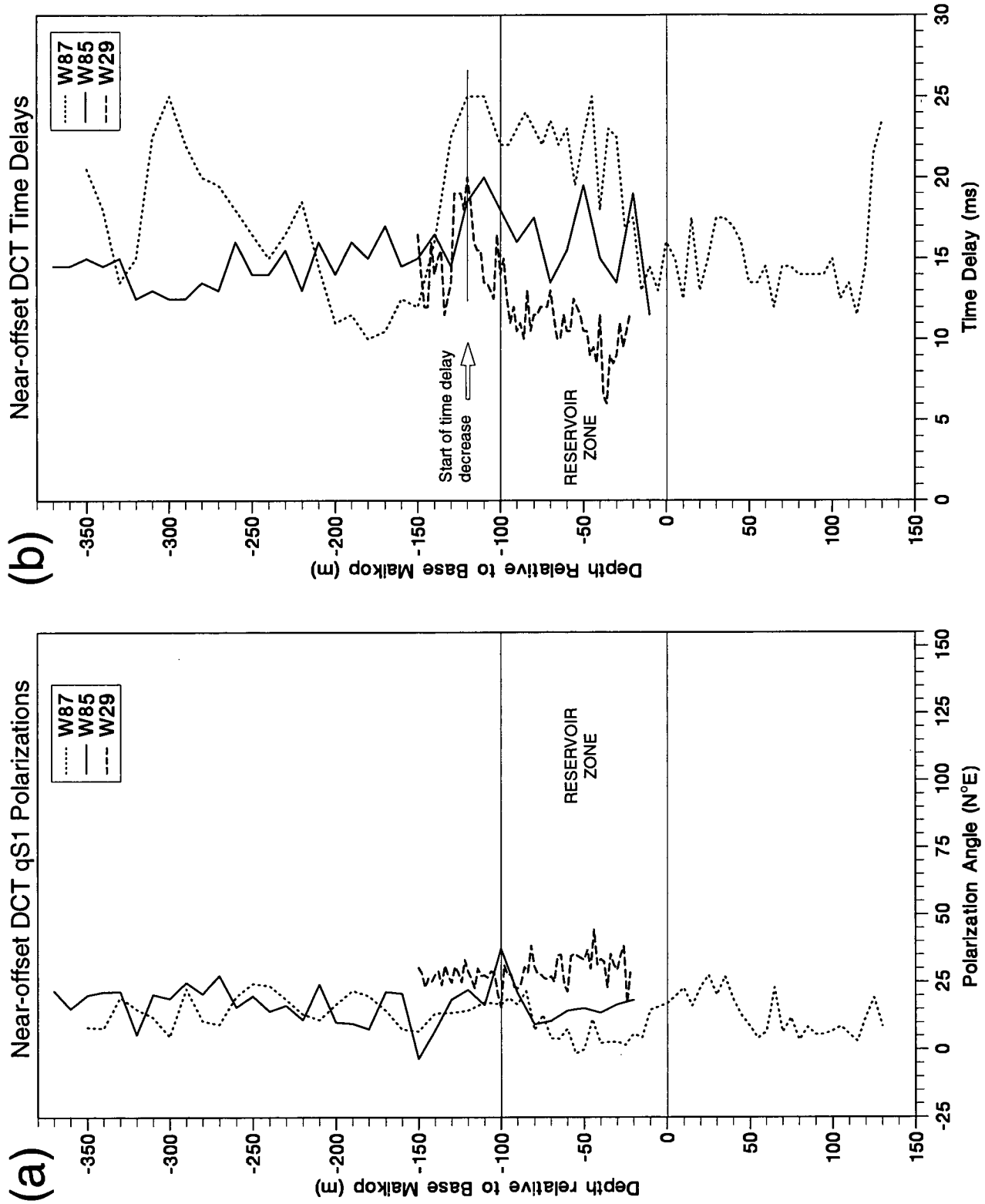

Figure 3.28: Near-offset DCT measurements of (**a**) qS1 polarizations and (**b**) time delay at the three wells. To aid comparison, all depths are displayed relative to a common geological datum, chosen as the base Maikop. The reservoir zone is within the lowermost 100 m of the Maikop. Time delay decreases through this zone at all three wells with the decrease beginning approximately 20 m above the zone.

decreasing time delay with depth implies a 90° rotation of the local *qS1* polarization at a depth just above the start of the decrease.

One of the main conclusions of Galperina and Galperin (1987), discussed in Section 3.4, is that the Maikop clay on the Taman peninsula is characterized by azimuthal isotropy. At the Juravskoe oil field, similar azimuthal isotropy of the 1200m-thick Maikop clay interval is implied by two observations: (1) the single-source measurements of time delay through the Maikop clay interval appear scattered about a constant value (Figures 3.21 and 3.23); and (2) the less-scattered single-source measurements of time delay at the top of the clay interval are very nearly equal to the dual-source measurements near the base of the clays (Fig. 3.22).

An anomaly, however, arises within the reservoir zone near the base of the Maikop clay. There is strong evidence at Well 29 of a decrease in time delay in the reservoir zone and, therefore, the presence of azimuthal anisotropy.

The important conclusions regarding the shear-wave splitting measurements at the wells are summarised below:

1) at Wells 85 and 29 the measured *qS1* polarization direction is constant with depth;
2) in each of the three wells studied there is a high level of consistency of the inferred *qS1* direction;
3) the *qS1* direction in the two oil fields is subparallel to the maximum horizontal stress direction;
4) at Well 29 there is a strong decrease in time delay and no associated deviations in the DIT polarization directions through the reservoir zone. Also, there is an indication of a similar decrease at Well 85.

Due to the three-dimensional variations in shear-wave behaviour in anisotropic materials, interpretation of the measurements from near- and far-offset sources in terms of particular anisotropic structures at each well requires forward modelling. Having established that anisotropy is present in the data, this will be carried out in the following chapter.

CHAPTER FOUR

SHEAR-WAVE SPLITTING AT TWO NORTH CAUCASUS OIL FIELDS: VSP MODELLING

4.1 INTRODUCTION

In this chapter, I model the shear-wave splitting measurements obtained in Chapter Three from the VSPs. The modelling strategy of this chapter is schematically illustrated in Figure 4.1. Firstly, I model the azimuthal anisotropy at Wells 85 and 87. I show that slight changes in the orientation of the symmetry axis of strong TIV (estimated in Chapter Five) cannot match the shear-wave splitting observed at the wells. I then match the shear-wave splitting using models containing aligned cracks. I find that the observations at both the wells can be closely matched with a model which has a low density of cracks in approximately the top 1 km. The cracks are vertical and aligned close to the presumed maximum horizontal stress direction. The top 1 km corresponds to the layering above the near-continuous Maikop clay.

Next, I model the azimuthal anisotropy observed within the reservoir at Well 29. The anisotropy of the reservoir is marked by a strong decrease in time delay along near-vertical raypaths, which suggests that a 90° rotation of the horizontal *qS1* polarization occurs at a depth just above the reservoir. For this well, I base the isotropic velocities and anisotropy parameters of the layers above the reservoir on the models for Wells 85 and 87. I then model the azimuthal anisotropy of the reservoir zone using three different types of cracked reservoir models. The three types were chosen because they give a 90° change in qS1 polarization at vertical incidence. The first model has vertical cracks striking orthogonal to the cracks in the upper 1 km and to the direction of the presumed maximum horizontal stress. The second model has dipping cracks striking parallel to the presumed maximum horizontal stress direction. The third model has a distribution of cracks with significantly high, pore-fluid

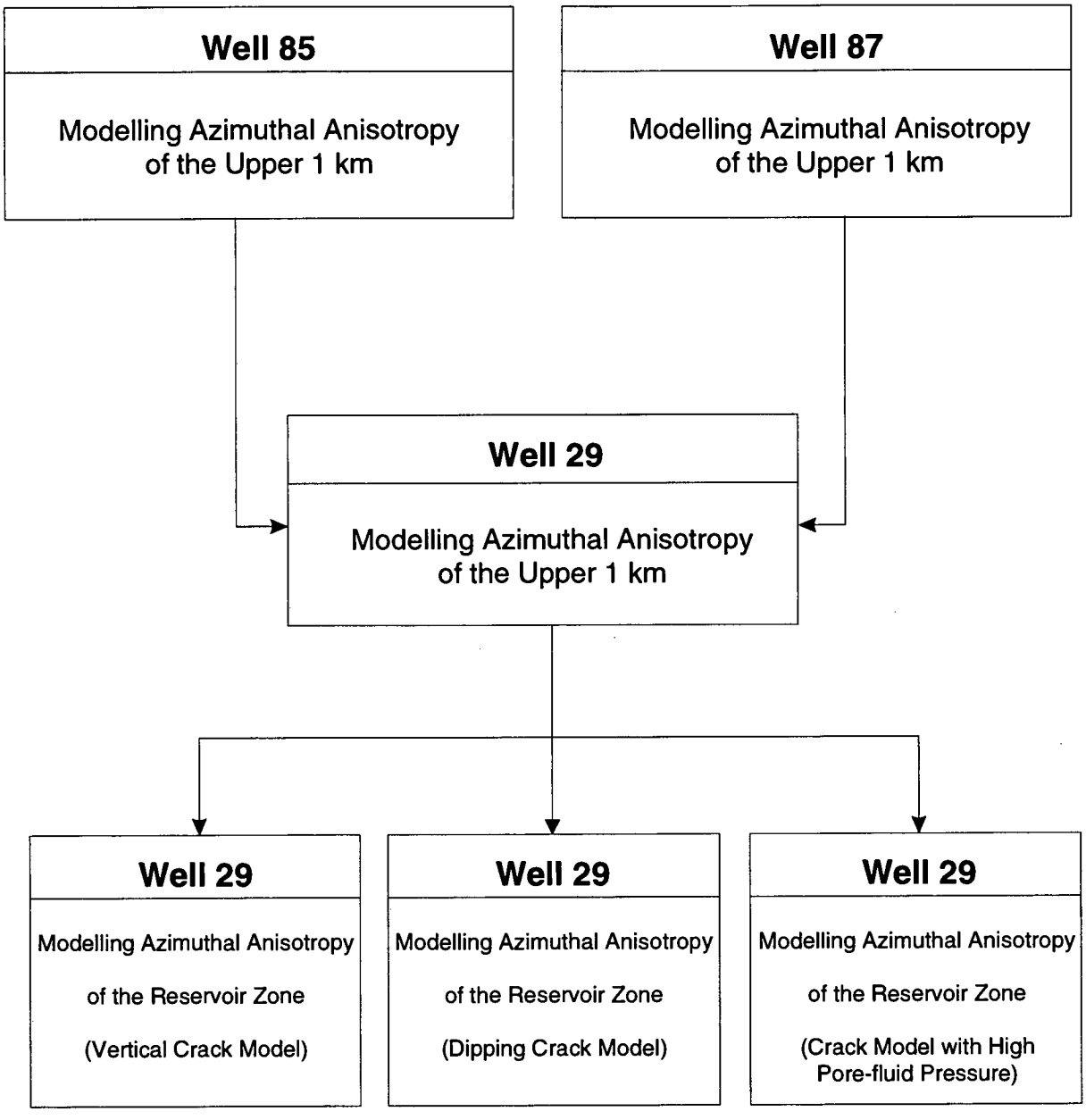

Figure 4.1: Modelling of the shear-wave splitting in the VSPs from the Juravskoe and Vorobievskoe oil fields. At Wells 85 and 87 the models obtained have azimuthal anisotropy in approximately the upper 1 km. These models are then used to estimate an anisotropic model for the layers above reservoir at Well 29. The azimuthal anisotropy of the reservoir at Well 29 is then modelled using three different cracked models.

pressure. I find that a close match to the near-offset observations may be achieved with all the three models. Some of the results from this study were presented at the 58*th* EAGE conference (Crampin *et al.*, 1996).

4.2 MODELLING OF WELL 85 MEASUREMENTS

In the previous chapter, the variations of time delay in Figures 3.21 and 3.22 indicated that at Well 85 azimuthal anisotropy is present in the top 870 m-thick sequence of alternating sandstones, limestones and clays.

In this section, I first test that the isotropic velocity model matches the VSP arrival times. Then I attempt to match the observed *qS1* polarization directions and time delays by introducing azimuthal anisotropy into the top 870 m in two different ways. Firstly, I consider whether the observations can be matched by slightly tilting from vertical the symmetry axis of the TIV which will be estimated in Chapter Five. Secondly, I attempt to match the observations using models containing aligned vertical cracks defined by the Hudson effective medium theory (1986, 1991).

4.2.1 Isotropic Velocity Model

An isotropic velocity structure for Well 85, derived from the near-offset VSP, was provided by Neftegeofizika, Moscow. The structure is shown in Fig. 4.2a and the parameters given in Table 4.1. The density of each layer in Table 4.1 was calculated from the isotropic P-wave velocity using the empirical relationship of Gardner, Gardner and Gregory (1974). Note that, due to poor quality shear-wave data in the near-surface, the shear-wave velocity is calculated for a comparatively-thick top layer. To check the shear-wave isotropic velocity structure, I calculated near-offset VSP arrival times using isotropic ray tracing and compared them with the observed shear-wave signals. Ray tracing arrival times and shear-wave signals recorded on the X-receiver from the X-source at receiver levels selected every 200 m are shown in Fig. 4.3. It can be seen in Fig. 4.3 that, except for a slight disagreement at the 1.8 km level, all first breaks are closely matched by the ray tracing times. This indicates that

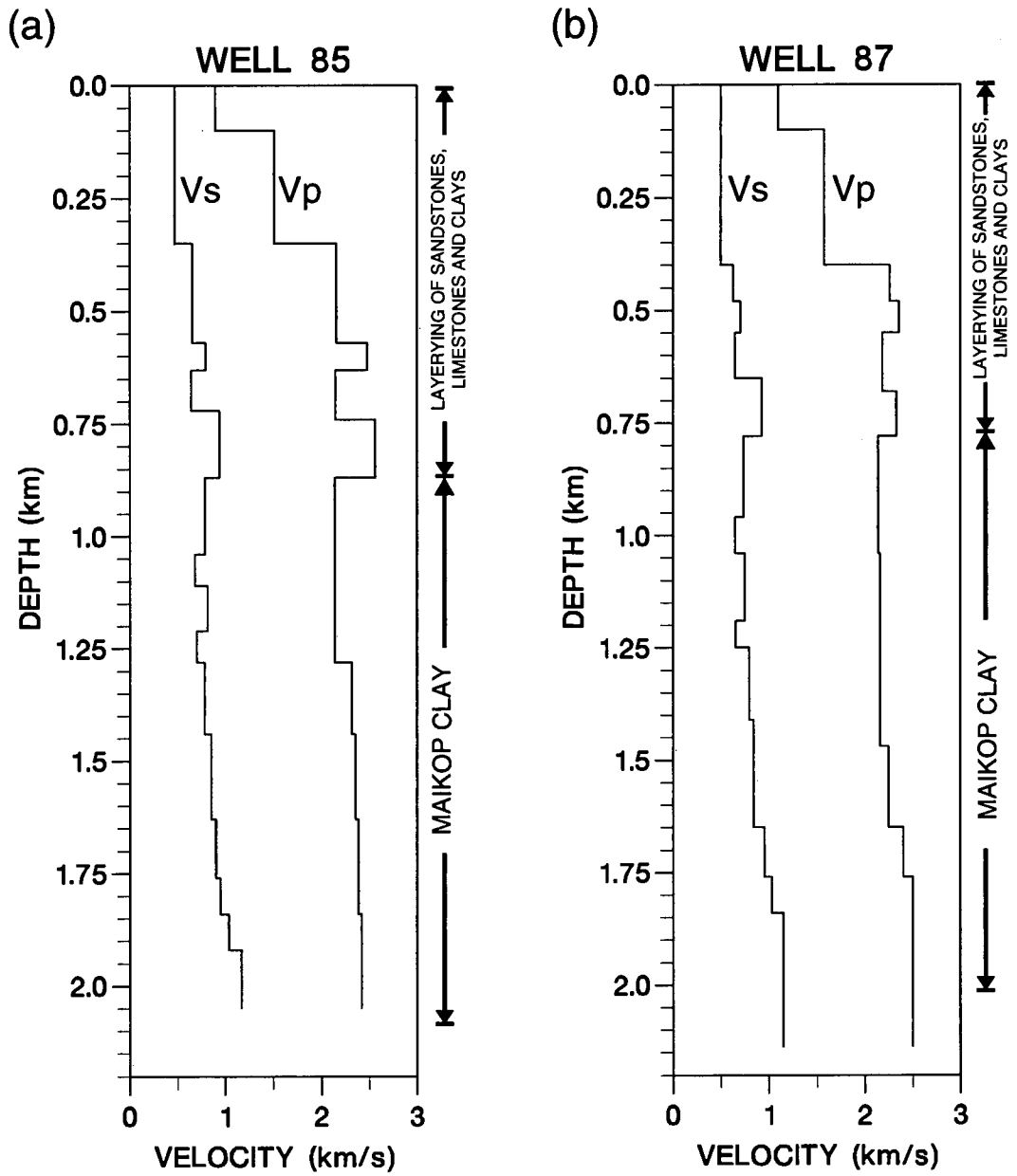

Figure 4.2: Shear- and P-wave velocities at **(a)** Well 85 and **(b)** Well 87 calculated from the near-offset VSPs.

Table 4.1: Isotropic velocity structure at Well 85

Layer Number	Thickness (km)	Density (g/cm^3)	*Vp* (km/s)	*Vs* (km/s)
1	0.10	1.70	0.90	0.448
2	0.25	1.96	1.60	0.448
3	0.22	2.11	2.16	0.654
4	0.06	2.19	2.48	0.795
5	0.09	2.11	2.15	0.645
6	0.15	2.21	2.56	0.944
7	0.17	2.11	2.14	0.789
8	0.07	2.11	2.14	0.680
9	0.10	2.11	2.14	0.815
10	0.07	2.11	2.14	0.702
11	0.16	2.15	2.32	0.781
12	0.19	2.16	2.36	0.852
13	0.13	2.17	2.39	0.904
14	0.08	2.17	2.39	0.947
15	0.08	2.17	2.42	1.037
16	halfspace	2.17	2.42	1.168

Table 4.2: Three selected anisotropic models 85A, 85B and 85C with different crack densities used to match the near-offset VSP shear-wave splitting measurements at Well 85. The TIV parameters are determined in Chapter Five and the vertical velocity in each layer corresponds to the isotropic velocity in Table 4.1.

	Depth Interval (km)	Layers in zone	TIV Parameters			Crack Density ($\epsilon=Nr^3/V$)	Crack Strike (N°E)
			qP (%)	SH (%)	qSV_{45} (%)		
Model 85A							
zone 1	0.00 - 0.87	1 - 6	15	24.6	15	0.005	19
zone 2	0.87 - ∞	7 - 16	15	41	25	0.00	NA
Model 85B							
zone 1	0.00 - 0.87	1 - 6	15	24.6	15	0.01	19
zone 2	0.87 - ∞	7 - 16	15	41	25	0.00	NA
Model 85C							
zone 1	0.00 - 0.87	1 - 6	15	24.6	15	0.015	19
zone 2	0.87 - ∞	7 - 16	15	41	25	0.00	NA

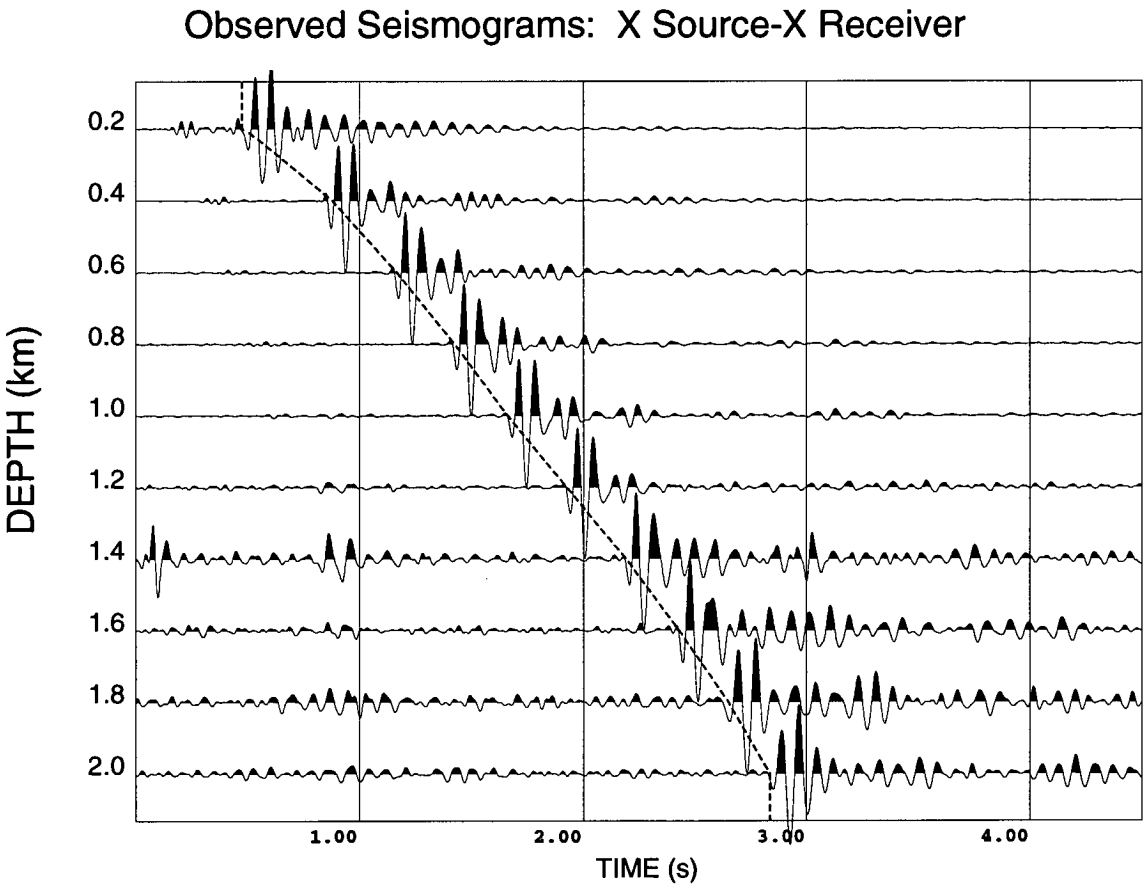

Figure 4.3: Testing the shear-wave isotropic velocity structure for Well 85 shown in Fig. 4.2a. Shear-wave signals recorded by the X receiver from the X source are displayed for receiver levels spaced 200 m apart. Arrival times from ray tracing calculations using the shear-wave velocity model in Fig. 4.2a are indicated by the dashed line, and show a close match to the shear-wave first-breaks.

the isotropic velocity structure is a suitable model on which to base future anisotropic models.

4.2.2 Modelling using Thin-layer or Inherent-Clay Anisotropy

In Chapter Five I will show that at the Juravskoe oil field the anisotropic structure of the top 2 km includes a component of strong TIV. By definition, a TIV medium has a strictly vertical symmetry axis. Consequently, as no shear-wave splitting occurs along vertical raypaths, the TIV model in Chapter Five cannot match the shear-wave splitting observed in the three near-offset VSPs analyzed in Chapter Three. However, if the symmetry axis of the TIV structure is tilted slightly from vertical, shear-wave splitting will occur along vertical raypaths. In this section, I estimate the tilt of the TIV symmetry axis which produces a match to the shear-wave splitting measurements in Fig. 3.21.

In the top 870 m at Well 85 the TIV is strong (about 24% SH anisotropy). However, over this interval the vertical differential shear-wave anisotropy is weak (about 1%). Therefore, it is possible that only a slight tilt of the TIV symmetry axis in the top 1 km would be necessary to match the observed time delays. Note that the observed polarizations in Figures 3.21 and 3.22 can be matched by a tilt of the TIV symmetry axis in a direction approximately perpendicular to the sagittal plane containing the source and receiver.

In Fig. 4.4 I show group velocities of one representative layer from the upper 870 m of the TIV model at Well 85 (described in Table 5.2). All layers within the top 870 m are defined with common anisotropy parameters, therefore, the group velocity variations will be similar in all layers in the top 870 m and conclusions based on examining one layer will be also applicable to all other layers in the upper 870 m. The tilt of the symmetry axis necessary to match the observed shear-wave time delay is estimated by calculating the percentage of differential shear-wave anisotropy $[=100\times(V_{fast}-V_{slow})/V_{fast}]$ at angles of propagation up to 25° from the symmetry axis. The results, shown in Fig. 4.4b, indicate that the symmetry axis of the TIV in the top 870 m must tilt by nearly 18° from vertical to produce a 1% differential shear-wave anisotropy.

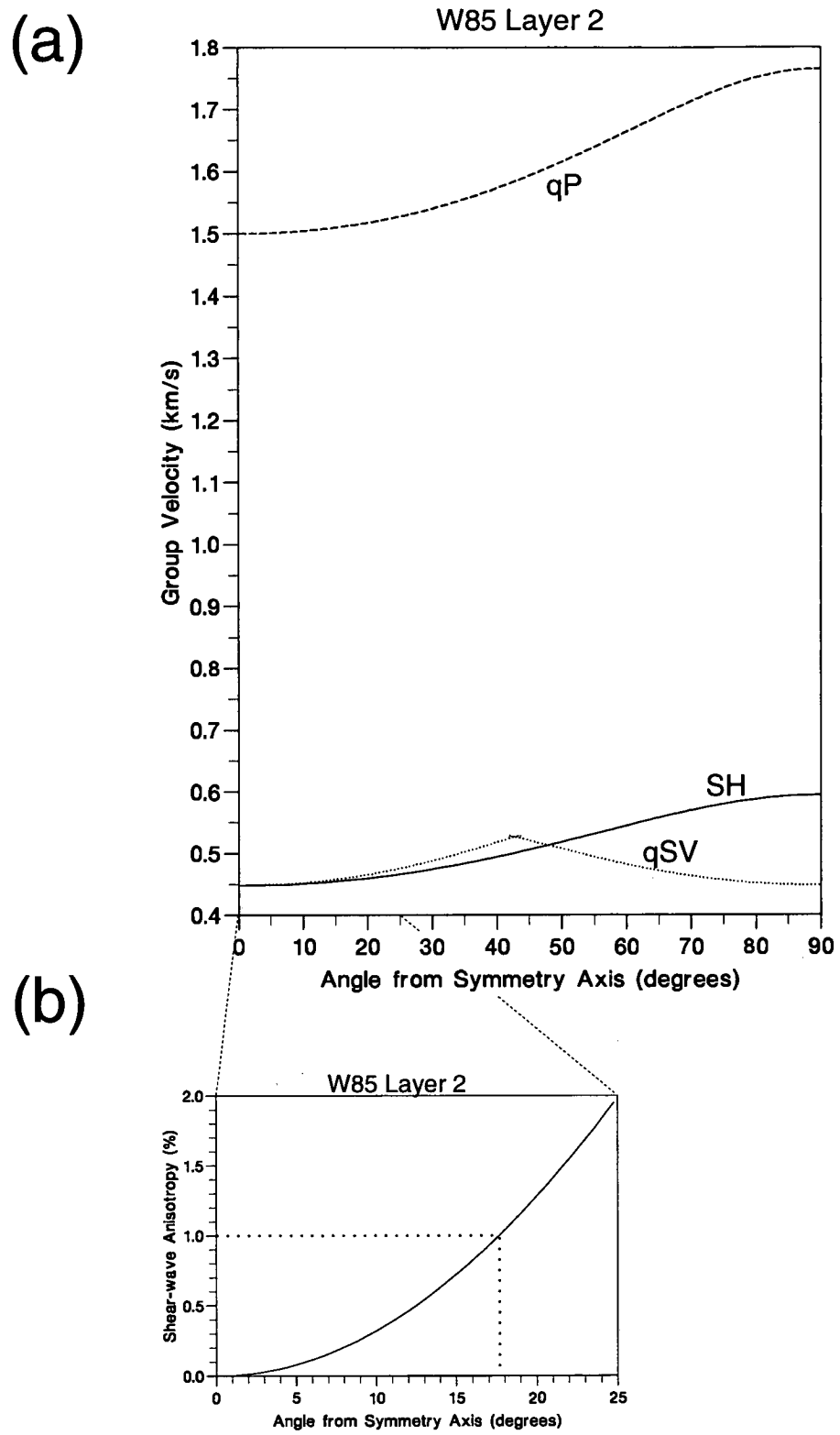

Figure 4.4: Differential shear-wave anisotropy in a TI layer: (**a**) shows the group-velocity sheets of the second uppermost layer at Well 85 for the TIV model; and (**b**) shows the corresponding percentage of differential shear-wave anisotropy for angles of propagation up to 25° from the symmetry axis. The dotted line in (b) indicates that only a tilt of the TIV symmetry axis as large as 18° will yield 1% differential shear-wave anisotropy.

The TIV in the Juravskoe oil field is associated with thin-layer or inherent-clay anisotropy or both. In parallel bedded sedimentary basins, the symmetry axis of thin-layer and inherent-clay anisotropy is normal to the bedding planes (Postma, 1955; Kaarsberg, 1968). In such basins, the beds may be dipping. Consequently, the likely deviation from vertical of the TI(V) symmetry axis may be estimated by measuring the dip of the bedding planes. On the northern side of the North Caucasus foredeep, the dip of the layers is gentle: regional geological surveys in the North Caucasus (Nalivkin, 1973) and seismic reflection profiles crossing the Juravskoe field (L.Y. Brodov, personal communication, Neftegeofizika, Moscow) have shown that the regional structures dip by less than 2°; and high resolution P-wave reflection surveys within the Juravskoe field indicate that internal cross-bedding within the main geological units is characterised by dips of less than 5° (L.Y. Brodov, personal communication, Neftegeofizika, Moscow). As these observed dips are significantly less than 18°, it is unlikely that strong transverse isotropy in the top 870 m causes the observed shear-wave splitting in any of the near-offset VSPs observed in Chapter Three.

The maximum bedding dip of 5° corresponds to a percentage of azimuthal anisotropy which is less than one-tenth of that observed, therefore, in the rest of this chapter I assume that the thin-layering and inherent-clay anisotropy has a strictly vertical symmetry axis and does not directly contribute to the shear-wave splitting observed along near-vertical raypaths. Any further references in this chapter to the model with strong TIV, unless otherwise stated, refers to the model given in Table 5.1.

4.2.3 Modelling using Hudson Cracks

Starting from the TIV model, I attempt to use iterative forward modelling to find simple, azimuthally anisotropic models which match the observed shear-wave splitting observations. First, azimuthal anisotropy is introduced by inserting cracks into the TIV structure using Hudson's formulations (1986, 1991). Next, synthetic seismograms are computed using the full waveform modelling package ANISEIS for source receiver geometries matching the field set-up. Lastly, shear-wave splitting measurement

techniques are applied to the synthetics and the results compared with the observed measurements obtained in Chapter Three.

Modelling single-source measurements

In this section I attempt to match the single source measurements shown in Fig. 3.21. The objective of modelling is to find the simplest model which matches the observed *qS1* polarization direction and the observed increase in time delay over approximately the top 870 m in Fig. 3.21. The simplest cracked model, with layers defined by the isotropic velocity structure in Fig. 4.2a, has parameters such as crack density and crack orientation, equal in all layers in the top 870 m. Consequently, I calculate synthetic seismograms for propagation through azimuthally anisotropic structures by inserting a constant density of Hudson cracks into the top six layers of the sixteen-layer TIV model estimated in Chapter Five (given in Table 5.2).

I assume that the cracks are vertical, thin (aspect ratio=0.01) and water-filled. Considering only vertical cracks means that the cracks must strike at about N19°E to match the *qS1* polarization at near-vertical incidence. No information is available on the likelihood of the presence of cracks or fractures in the top 1 km, but the alignment of the *qS1* polarization direction close to the presumed maximum horizontal stress direction implies that the anisotropy is stress controlled and, therefore, likely caused by aligned (EDA) fractures or microcracks.

I computed seismograms from models with constant crack densities of 0.005 to 0.015, in steps of 0.001. The pulse shape I used for generating the synthetics was chosen to match the fast shear-wave signal in the field data. DTS measurements from three selected models are shown in Fig. 4.5. The three models are labelled 85A, 85B and 85C and correspond to crack densities of 0.005, 0.01, and 0.015, respectively (Table 4.2).

For receiver levels below 350 m, a good match to the observed polarization direction can be seen in Fig. 4.5a for all crack densities. At the shallow receivers above 350 m, the larger crack density matches the polarization angles best, although all models display a similar pattern of variation over this interval.

A greater variation between the three models is seen in the time delay results in Fig. 4.5b, which indicates that, for a constant crack density in the top 870 m, the best model has a crack density of 0.010±0.002.

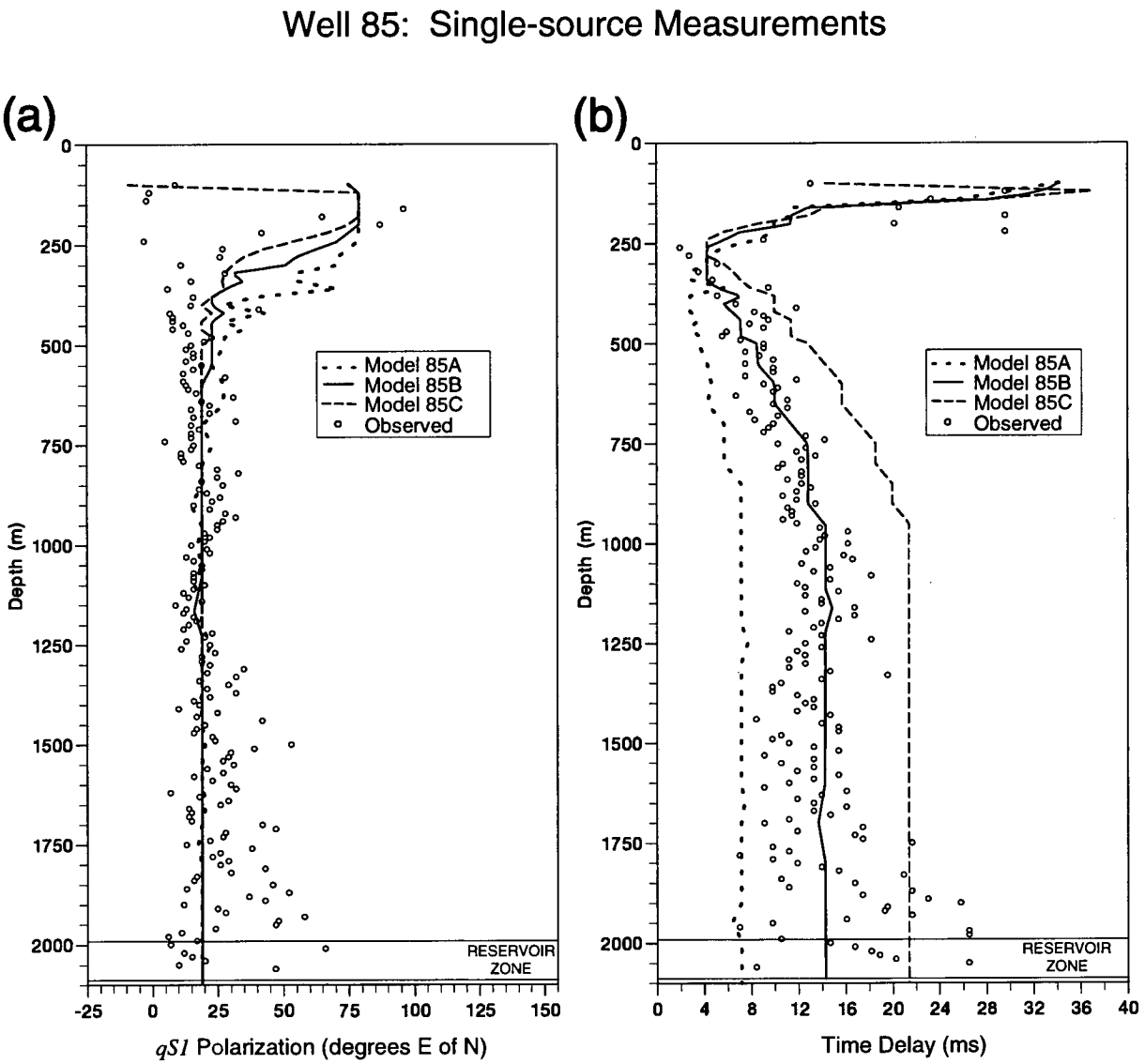

Figure 4.5: Modelling the single-source measurements of (**a**) *qS1* polarization direction and (**b**) time delay in the near-offset VSP at Well 85. The lines indicate DTS measurements made on synthetic seismograms calculated from models with azimuthal anisotropy. The models were created by inserting vertical cracks into the uppermost 870 m of a sixteen-layer structure characterized by strong TIV. The crack strike is N19°E. The models 85A, 85B and 85C have constant crack densities of 0.005, 0.010 and 0.015, respectively. The model parameters are given in Tables 4.1 and 4.2.

Modelling dual-source measurements

The DIT estimation technique is applied to synthetic seismograms calculated using model 85B which closely fits the single-source measurements. This model has vertical cracks with a density of 0.01 inserted in the top 870 m of the TIV structure. The DIT measurements from the synthetics show a close match to the observed polarization directions and also, in general, to the observed time delay (Fig. 4.6). As already pointed out in Section 3.8, there is arguably a slight increase in time delay down to about 1950 m followed by a decrease below this depth. However, I do not attempt to match this as the scatter between levels is comparatively large.

4.3 MODELLING OF WELL 87 MEASUREMENTS

The DTS shear-wave splitting measurements in Fig. 3.23 show an almost constant polarization with depth. They also display a large time delay of 30-40 ms in the near-surface and a decrease to about 15 ms at 800 m depth. In this section I attempt to match the Well 87 shear-wave splitting measurements by inserting vertical Hudson cracks into a layered model which has the same TIV parameters as those estimated for Well 85.

4.3.1 Modelling using Hudson Cracks

Modelling single-source measurements

The large time delay variation above 400 m in Fig. 3.23a, and near-constant delay below this level, suggests that most of the azimuthal anisotropy at Well 87 is present in approximately the upper 400 m. Consequently, after testing the isotropic velocity structure provided by Neftegeofizika, Moscow, (see Fig. 4.2b and Table 4.3), I computed synthetic seismograms from models with a constant density of vertical Hudson cracks, striking N25°E, inserted into the top 400 m of the TIV model with parameters given in Table 5.2. Between models, the crack density was varied from 0.005 to 0.03, in steps of 0.005. The DTS measurements from the synthetics (not shown) demonstrated that a crack density which matches the time delay along the inclined raypaths to the receivers in the top 400 m, produces too small a delay along vertical raypaths to the receivers below 1 km depth. This implied that for a vertically

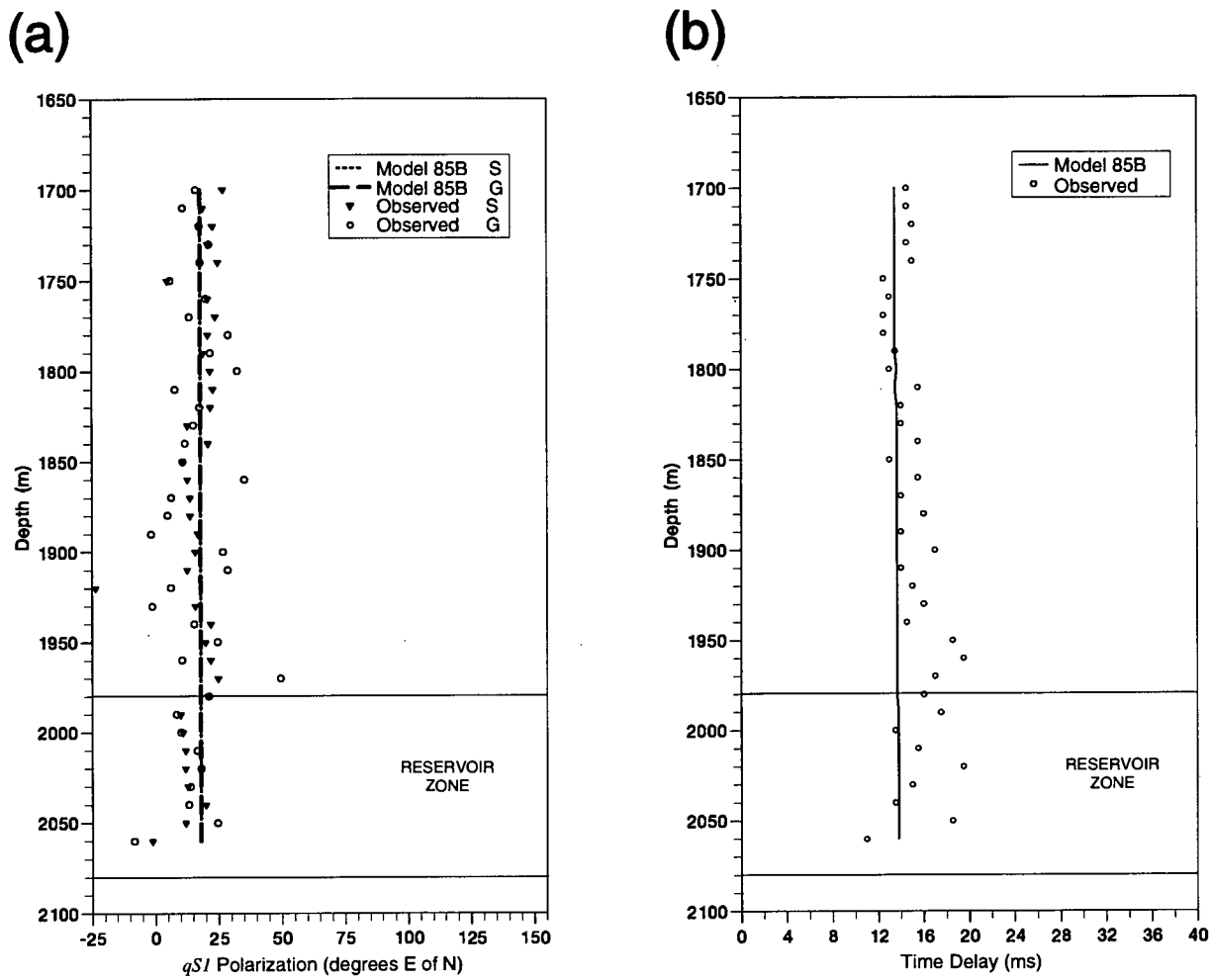

Figure 4.6: Modelling dual-source measurements of (**a**) *qS1* polarization direction and (**b**) time delay in the near-offset VSP at Well 85. The lines indicate DIT measurements made on synthetic seismograms calculated from the model 85B. The model was created by inserting vertical cracks into the uppermost 870 m of a sixteen-layer structure characterized by strong TIV. The crack strike in model 85B is N19°E and the crack density is 0.01. The model parameters are given in Tables 4.1 and 4.2. The source and geophone polarizations measured for model 85B by DIT are plotted as dotted and dashed lines, respectively.

Table 4.3: Isotropic velocity structure at Well 87.

Layer Number	Thickness (km)	Density (g/cm^3)	*Vp* (km/s)	*Vs* (km/s)
1	0.10	1.79	1.10	0.503
2	0.30	1.95	1.58	0.503
3	0.08	2.14	2.26	0.630
4	0.07	2.16	2.36	0.707
5	0.10	2.12	2.19	0.650
6	0.13	2.15	2.33	0.930
7	0.18	2.11	2.14	0.736
8	0.08	2.11	2.14	0.647
9	0.15	2.11	2.16	0.750
10	0.06	2.11	2.16	0.656
11	0.16	2.11	2.16	0.793
12	0.24	2.14	2.25	0.820
13	0.11	2.17	2.40	0.956
14	0.08	2.17	2.40	1.032
15	halfspace	2.17	2.50	1.148

Table 4.4: Three selected anisotropic models 87A, 87B and 87C with different crack densities used to match the near-offset VSP shear-wave splitting measurements at Well 87. The TIV parameters are determined in Chapter Five and the vertical velocity in each layer corresponds to the isotropic velocity in Table 4.3.

	Depth Interval (km)	Layers in zone	TIV Parameters			Crack Density ($\epsilon=Nr^3/V$)	Crack Strike (N°E)
			qP (%)	SH (%)	qSV_{45} (%)		
Model 87A							
zone 1	0.00 - 0.78	1 - 6	15	24.6	15	0.005	25
zone 2	0.78 - ∞	7 - 15	15	41	25	0.00	NA
Model 87B							
zone 1	0.00 - 0.78	1 - 6	15	24.6	15	0.01	25
zone 2	0.78 - ∞	7 - 15	15	41	25	0.00	NA
Model 87C							
zone 1	0.00 - 0.78	1 - 6	15	24.6	15	0.015	25
zone 2	0.78 - ∞	7 - 15	15	41	25	0.00	NA

cracked model, a better match to the shear-wave splitting measurements would be achieved if the cracks were included in an upper zone of significantly greater thickness than 400 m.

The shear-wave splitting observations at Well 85 were successfully matched in Section 4.2.3 using models with vertical Hudson cracks inserted into the 870 m-thick zone of alternating layers overlying the Maikop clay. The geology at Wells 85 and 87 is very similar, as can be seen by the similarity in the velocity structure in Fig. 4.2. Therefore, I attempted to model the Well 87 shear-wave splitting measurements using a similar anisotropic structure to that determined at Well 85, despite the fact that the DTS measurements in the top 1 km at Well 87 are quite different to those at Well 85. The model has constant crack density in all the layers down to the top of the Maikop clay, which at Well 87 is at a depth of 780 m.

I computed synthetic seismograms for fifteen-layer models with thin, water-filled cracks striking N25°E inserted into the top 780 m of the TIV structure. The DTS measurements are shown in Fig. 4.7 from selected models 87A, 87B and 87C with crack densities of 0.005, 0.01 and 0.015, respectively. The model parameters are given in Table 4.4.

Below 250 m, measurements from all three models in Fig. 4.7a show a close match to the observed polarization direction. Above 250 m depth, the fit of the model polarizations varies in a similar way to the observed measurements. The DTS time delays from the three models are shown in Fig. 4.7b. All three models give a large time delay in the near-surface which decreases with depth. The model 87B, which has a crack density of 0.01±0.002, gives the best match to the observations.

Modelling dual-source measurements

I computed synthetic seismograms from model 87B for orthogonally-polarized horizontal sources arranged to match the field acquisition geometry. Model 87B was chosen because it was found to match the single-source measurements best. Shear-wave splitting measurements made on the synthetics using the dual-source DIT technique are shown in Fig. 4.8. In general, there is an agreement between the observed and model results. In contrast to the significantly large separation in the observations, the source and geophone estimates of the *qS1* polarization direction from the synthetics show negligible separation in Fig. 4.8a. The separation between the two

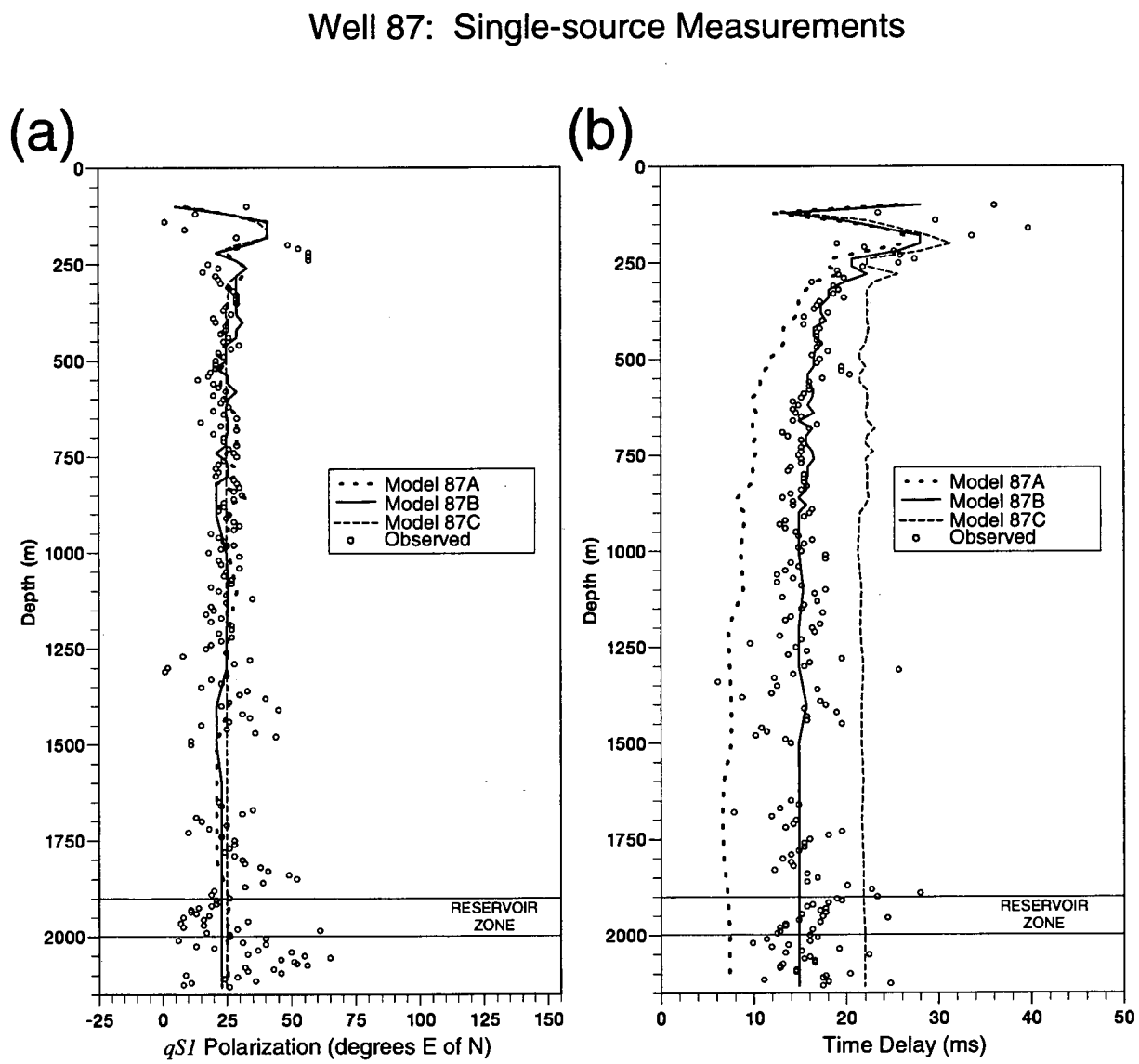

Figure 4.7: Modelling the single-source measurements of (**a**) *qS1* polarization direction and (**b**) time delay in the near-offset VSP at Well 87. The lines indicate DTS measurements made on synthetic seismograms calculated from models with azimuthal anisotropy. The models were created by inserting vertical cracks into the uppermost 780 m of a fifteen-layer structure characterized by strong TIV. The crack strike is N25°E. The models 87A, 87B and 87C have constant crack densities of 0.005, 0.010 and 0.015, respectively. The model parameters are given in Tables 4.3 and 4.4.

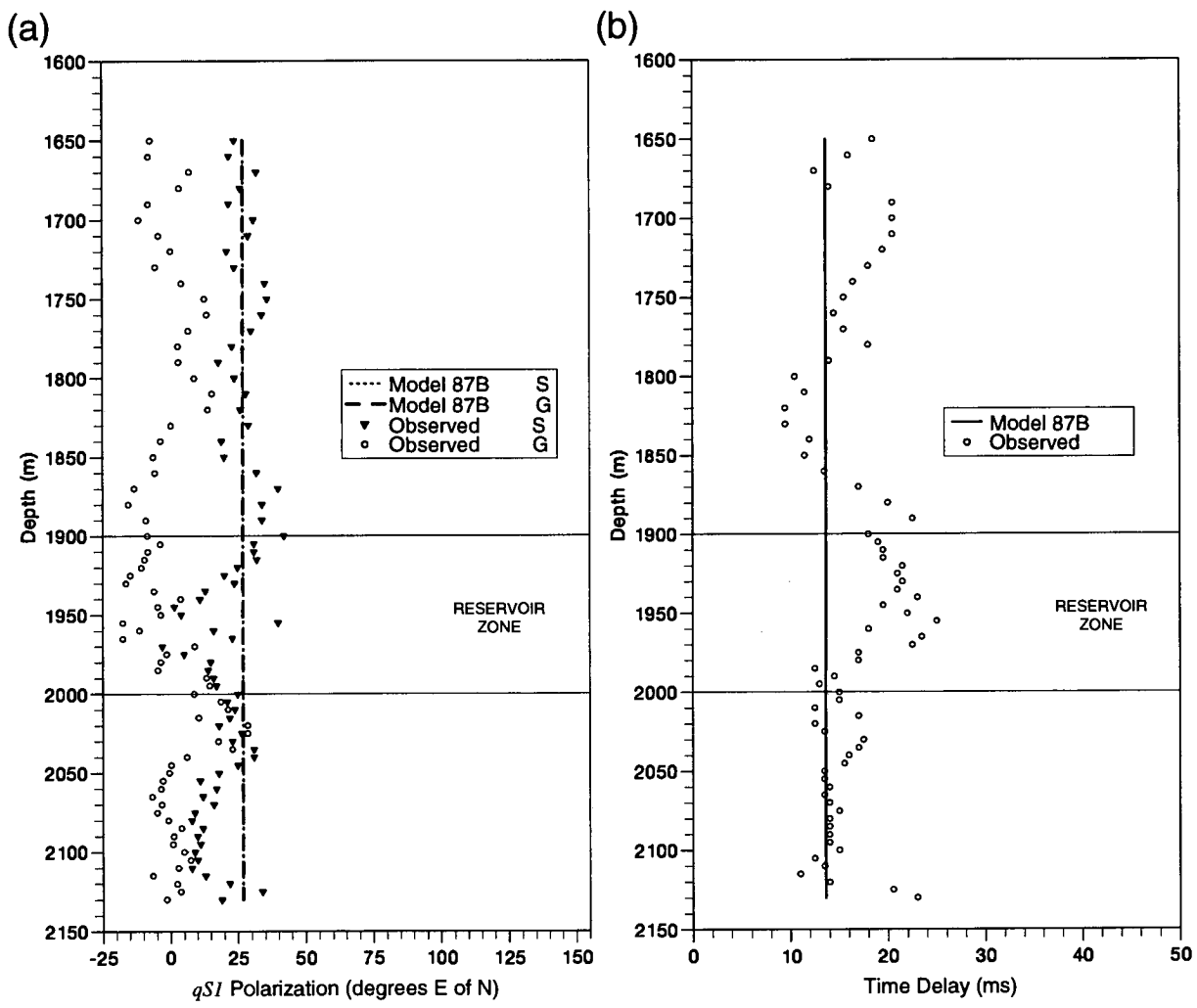

Figure 4.8: Modelling the dual-source measurements of (**a**) *qS1* polarization direction and (**b**) time delay in the near-offset VSP at Well 87. The lines indicate DIT measurements made on synthetic seismograms calculated from the model 87B. The model was created by inserting vertical cracks into the uppermost 780 m of a fifteen-layer structure characterized by strong TIV. The crack strike in model 87B is N25°E and the crack density is 0.01. The model parameters are given in Tables 4.3 and 4.4. The source and geophone polarizations measured for model 87B are plotted as dotted and dashed lines, respectively.

DIT polarization angles is, therefore, unlikely to be an effect from propagation through the upper orthorhombic layers and, consequently, it still remains most likely that the separation is caused by a source coupling problem (Section 3.7.2).

Summary and discussion of the modelling of Wells 85 and 87

The DTS measurements in the top 1 km at Wells 87 and 85 are quite different from one another (Figs 3.21 and 3.23), yet the polarization and time delay measurements at the two wells are closely matched by similar models consisting of a distribution of vertical cracks with the same crack density (=0.01) inserted into similar TIV structures. In general, shear-wave splitting variations in orthorhombic media is complex and sometimes difficult to predict. However, there is a straightforward reason for the difference between the DTS results from the models of Well 85 and 87. The reason is that the inclined raypaths to the upper receiver levels have different azimuthal orientations at the two wells. This is illustrated in Fig. 4.9, which shows equal area plots of the polarization variations of the fast split shear-wave in the orthorhombic upper layers of the models 85B and 87B. The rectangles on the equal area plots indicate the range of straight-line incidence angles for receivers in the orthorhombic layers above the Maikop clay. As Fig. 4.9a shows, the raypaths to the upper receivers at Well 85 are along an azimuth roughly parallel to the measured *qS1* polarization direction, whereas at Well 87, the raypaths are along an azimuth roughly perpendicular to the *qS1* polarization direction. Consequently, in the model for Well 85, the raypaths pass close to an area corresponding to a point singularity in the phase velocity surfaces. However, at Well 87 the raypaths in the model are almost perpendicular to the equivalent point singularity. This causes a rapid variation in time delay and polarization (from transverse to radial polarization) in the model results for the uppermost 300-400 m of Well 85 (Fig. 4.5). [The region associated with the singularity lies at an incidence angle of about 16° in Fig. 4.9a which, for a straight-line raypath, corresponds to a receiver level at about 300 m depth, and explains why there is a minimum in time delay between 250-350 m depth in Fig. 4.5.] In the modelling of Well 87 (Fig. 4.9b), the range of incidence angles does not cross a region associated with a point singularity, and the *qS1* polarization direction is nearly constant for all raypaths. There is no singularity-induced rapid decrease in time delay and, consequently, the time delay decreases slowly with depth in the top 1 km because

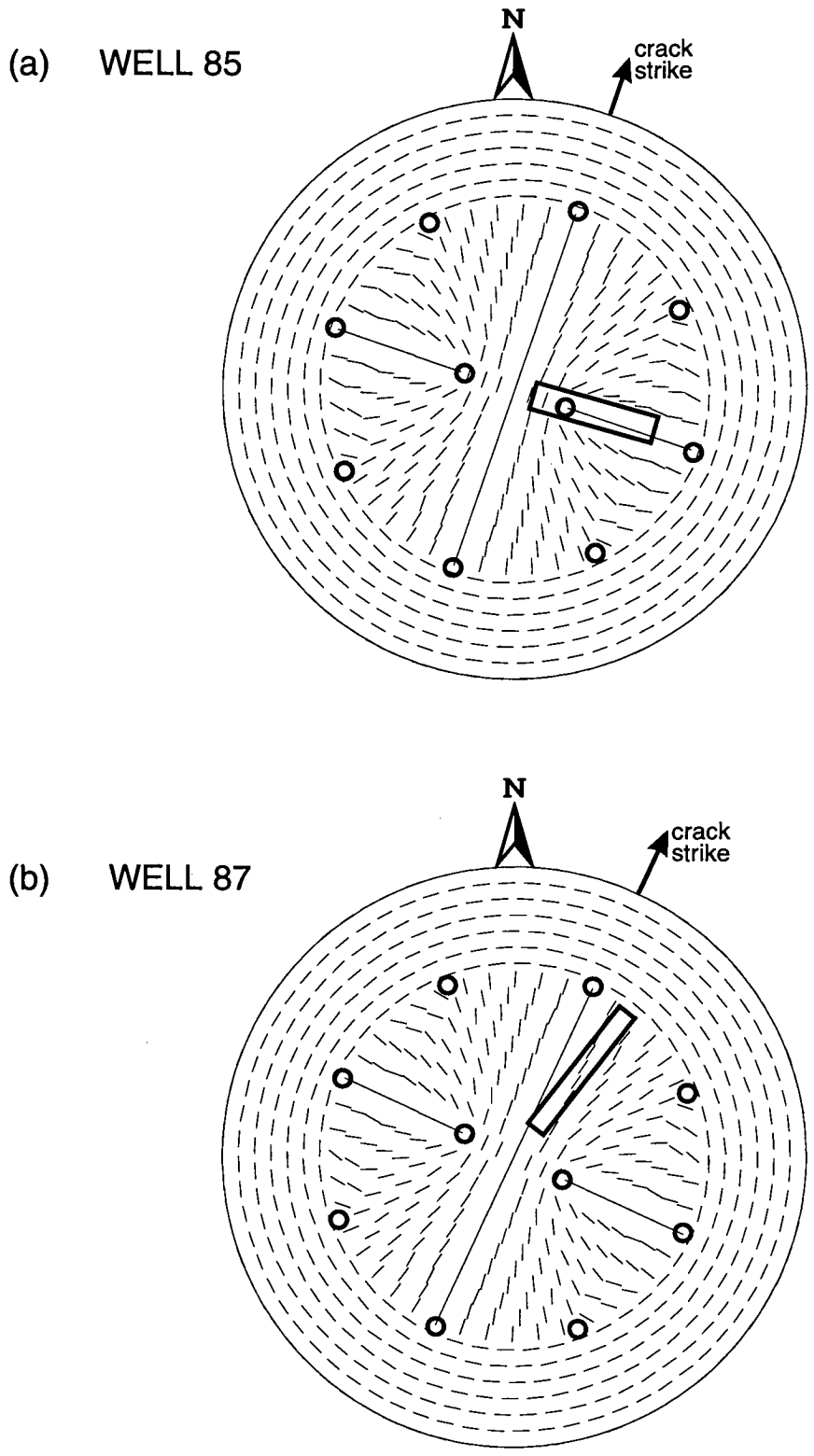

Fig. 4.9: Equal area plots, for incidence angles up to 90°, showing model horizontal plane polarization variations of the fast split shear-wave in the azimuthally anisotropic layers above the Maikop clay for (**a**) Well 85 and (**b**) Well 87. The azimuthal anisotropy at each well was found by matching the near-offset VSP shear-wave splitting parameters. The rectangle in each plot indicates the range of straight-line incidence angles to the receivers in the layers above the Maikop clay, and the open circles schematically indicate the areas of disturbance in the group velocity surfaces associated with point singularities in the phase velocity surfaces.

the shear-wave anisotropy associated with the strong TIV diminishes as the raypaths tend towards vertical orientation.

The observations at Wells 85 and 87 together with the associated modelling provides a clear example of the presence of orthorhombic anisotropy in sedimentary basins, as pointed out by Bush and Crampin (1991).

4.4 MODELLING OF WELL 29 MEASUREMENTS

In this section, I model the dual-source shear-wave splitting observations made in Section 3.7.3. Of the three wells studied in Chapters Three and Four, Well 29 is the only one in which azimuthal anisotropy of the reservoir zone is reliably observed. This is because of the many receiver levels within the reservoir zone (Fig. 3.4), and because of the high quality of the recorded seismograms at Well 29.

In the near-offset VSP (W29N), the measured time delay between split shear-waves decreased substantially in the reservoir zone, while the corresponding two DIT measurements of polarization displayed no significant separation (Fig. 3.26). This implies a 90° rotation (approximately) of the *qS1* polarization direction along the vertical raypath, with the rotation occurring at a depth of about 2.04 km (20 m above the supposed upper limit of the reservoir zone). In this section, after describing the initial isotropic velocity and anisotropic structures of Well 29, I use forward modelling to obtain three models of the reservoir zone which match the orthogonal change of polarization in the W29N VSP. The first reservoir model has vertical cracks, the second has dipping cracks, and the third has a distribution of cracks with high internal pore-fluid pressure.

4.4.1 Isotropic Velocity Model

I have been unable to obtain VSP or wireline log data from which to calculate an isotropic velocity model. Therefore, as an approximation, I assumed initially that the isotropic velocity structure above the shallowest receiver (at depth of 2.01 km) was the same as that at Well 85 shown in Fig. 4.2a. Isotropic ray tracing and synthetic seismograms calculations using this velocity structure showed a good match to the arrival time at 2.01 km depth in the W29N VSP. However, to fine-tune the velocity

structure, I matched arrival times on synthetic seismograms to the fast shear wave arrival time at the 2.01 km deep receiver. I did this by applying a 3% reduction to the velocities of each layer. Additionally, I calculated P- and shear-wave isotropic velocities for the interval spanned by the receivers in Well 29, and obtained values of 2.78 km/s and 1.33 km/s, respectively. The final isotropic velocity model for Well 29 is given in Table 4.5.

4.4.2 Approximate Anisotropic Model above the Reservoir Zone

As there are no receiver levels above 2.01 km, I cannot determine an independent estimate of the anisotropy parameters above the reservoir zone at Well 29. I therefore initially assumed that the anisotropy parameters above the reservoir are similar to the models 85B and 87B which match the near-offset VSP measurements at Wells 85 and 87, respectively. This assumption is supported by two facts: firstly, the geology surrounding the oil fields is essentially horizontally layered and shows little lateral variation; and secondly, the near-offset time delay and polarization measurements at the shallow receiver levels just above the reservoir in Well 29 agree well with those measured at Wells 85 and 87.

Using the isotropic velocity model in Table 4.5, I computed synthetic seismograms for propagation through a model with similar anisotropy parameters as those determined at Well 85 (Section 4.2.3). This model, named 29A, has vertical Hudson cracks, with a crack density of 0.01 within the top 870 m of the strong TIV model estimated in Chapter Five. The crack strike is set to N30°E to match the *qS1* polarization directions in the W29N VSP. The model is described in Table 4.6.

DIT measurements from model 29A are shown in Figures 4.10a to 4.10f. The observed polarization directions in the W29N and W29F1 VSPs are closely matched in Figures 4.10a and 4.10b. However, the W29F2 VSP polarization directions are less well matched in Fig. 4.10c which shows a separation in the two DIT polarization directions. This separation is likely caused by multiple splitting at the 870 m-deep interface between the upper orthorhombic layers and lower TIV Maikop clay. The model 29A time delays in Figures 4.10d to 4.10f generally show a close agreement with the observations, although there are significant differences.

Table 4.5: Isotropic velocity structure at Well 29

Layer Number	Thickness (km)	Density (g/cm^3)	*Vp* (km/s)	*Vs* (km/s)
1	0.10	1.69	0.87	0.435
2	0.25	1.95	1.55	0.435
3	0.22	2.10	2.10	0.634
4	0.06	2.17	2.41	0.771
5	0.09	2.09	2.09	0.626
6	0.15	2.19	2.48	0.916
7	0.17	2.09	2.08	0.765
8	0.07	2.09	2.08	0.660
9	0.10	2.09	2.08	0.791
10	0.07	2.09	2.08	0.681
11	0.16	2.14	2.25	0.758
12	0.19	2.14	2.29	0.826
13	0.13	2.15	2.32	0.877
14	0.08	2.15	2.32	0.919
15	0.08	2.16	2.35	1.006
16	0.09	2.16	2.35	1.133
17	halfspace	2.25	2.78	1.330

Table 4.6: Details of models used to match the shear-wave splitting measurements at Well 29. The vertical velocity of each layer is given in Table 4.5.

	Depth Interval (km)	Layers in zone	TIV Parameters			Crack Density ($\epsilon=Nr^3/V$)	Crack Strike (N°E)	Crack Dip
			qP (%)	SH (%)	qSV_{45} (%)			
Model 29A								
zone 1	0.00 - 0.87	1 - 6	15	24.6	15	0.01	30	0
zone 2	0.87 - ∞	7 - 17	15	41	25	0.00	NA	NA
Model 29B								
zone 1	0.00 - 0.87	1 - 6	15	24.6	15	0.02	30	72° to WNW
zone 2	0.87 - ∞	7 - 17	15	41	25	0.00	NA	NA
Model 29C								
zone 1	0.00 - 0.87	1 - 6	15	24.6	15	0.03	30	68.5° to WNW
zone 2	0.87 - ∞	7 - 17	15	41	25	0.00	NA	NA
Model 29D								
zone 1	0.00 - 0.87	1 - 6	15	24.6	15	0.03	30	68.5° to WNW
zone 2	0.87 - 2.04	7 - 17	15	41	25	0.00	NA	NA
zone 3	2.04 - ∞	18 - 18	15	41	25	0.08	120	90°
Model 29E								
zone 1	0.00 - 0.87	1 - 6	15	24.6	15	0.03	30	68.5° to WNW
zone 2	0.87 - 2.04	7 - 17	15	41	25	0.00	NA	NA
zone 3	2.04 - ∞	18 - 18	15	41	25	0.2	30	39° to ESE

Table 4.7:Details of relative stress parameters used in the APE theory to define cracked materials with different pore-fluid pressures to model the decrease in time delay below a depth of 2.04 km. Above 2.04 km, the layers are defined by the Model 29C.

	s_V	s_H	s_h	p_f
Model 29F				
	20	18	0	10
Model 29G				
	20	18	0	16
Model 29H				
	20	18	0	18

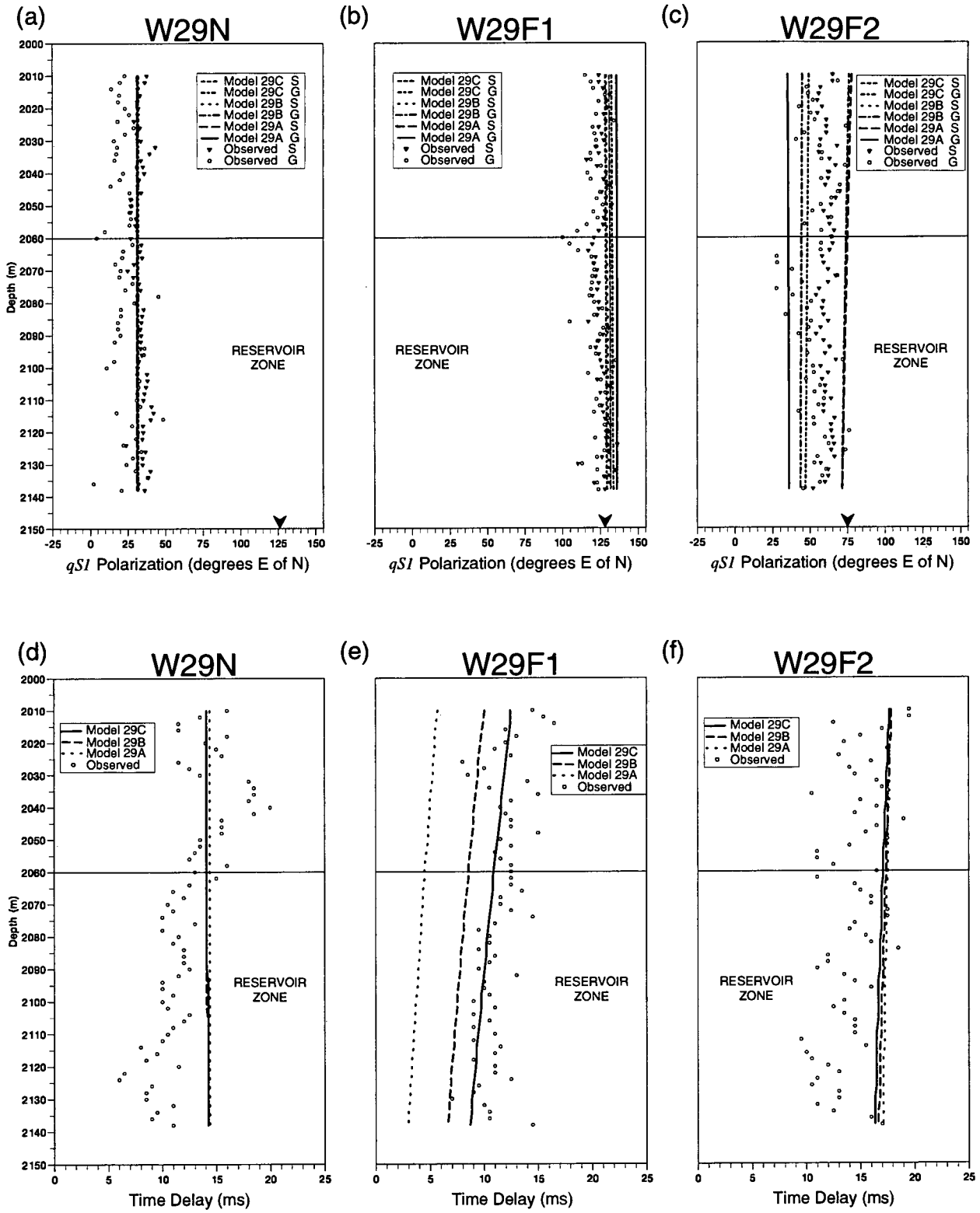

Figure: 4.10: Modelling DIT measurements of *qS1* polarization in the three VSPs at Well 29. The three models, 29A, 29B and 29C are based on the Walkaway and near-offset VSP modelling of Well 85, and consist of Hudson cracks, striking N30°E, inserted into the top 870 m of a sixteen-layer TIV structure with different crack dips. The model parameters are given in Table 4.6. The solid arrowhead marks the azimuth of the sagittal plane.

In summary, this initial structure gives a good general fit to the observed data. However, there are three significant aspects of the field results which the model fails to match: firstly, the decrease in time delay in W29N, secondly, the magnitude of time delay in W29F1 and, lastly, the close agreement in the two polarization estimates in W29F2.

As the raypaths to the receivers in the W29N VSP are vertical, the decrease of time delay below 2.04 km cannot be caused by anisotropy above this depth. Modelling of this decrease is carried out in the following sections.

Increasing the fit of the initial model

The fit of model 29A to the observations in the W29F1 VSP is poor (Fig. 4.10e). For models with cracks inserted into a TIV structure, the fit to the time delay at the shallowest receiver in the W29F1 VSP may be increased (while maintaining the same time delay at vertical incidence in the W29N VSP) by either increasing the qSV_{45} parameter defining the TIV or by altering the dip and density of the cracks. [Varying the content or aspect ratio of the cracks in the W29A model cannot improve the fit to the W29F1 observations].

To model the Well 85 and 87 VSPs (Sections 4.2.3 and 4.3.1), the cracks in the upper 1 km were assumed to be vertical. It is likely, however, that a similarly close fit at Wells 85 and 87 would have been achieved with dipping cracks. Consequently, I attempted to find a closer fit to the W29F1 time delay by dipping the cracks in the upper part of the model.

I used forward modelling to find models which matched the 15 ms time delay in the W29N VSP whilst giving an increased time delay in the W29F1 VSP. (The variation in the W29F2 model results is not explicitly considered because for all the models which matched the W29N measurement, there was no significant change in the W29F2 VSP.) I calculated synthetic seismograms from models with crack density varied between 0.01 and 0.06 and dip between 85° and 60°. The crack strike was constant at N30°E to match the observed W29N polarization direction. I calculated seismograms from a total of 37 different models. Shear-wave splitting measurements from the synthetics indicated that, for combinations of crack density and dip which match the W29N VSP, the greater the crack density, the larger the time delay in the W29F1 VSP. This is illustrated in Figures 4.10d and 4.10e by two models, 29B and

29C, which have crack densities of 0.02 and 0.03 and crack dips of 72° and 68.5° to west-north-west (WNW), respectively. Figure 4.10e shows that the best fit to the W29F1 VSP is found using model 29C.

In the following sections, I attempt to match the 6-8 ms decrease in time delay in the W29N VSP and the 2-3 ms decrease in the W29F1 VSP. The decrease in the W29N begins at a depth of approximately 2.04 km, which is 20 m above the presumed upper limit of the reservoir zone. The model 29C gives a close fit to the time delay above 2.04 km. Consequently, for all other models calculated in the remainder of this chapter parameters of all layers down to 2.04 km are defined by the model 29C.

Two equal area plots of the horizontal *qS1* polarizations in model 29C are shown in Fig. 4.11. The upper plot corresponds to the azimuthally anisotropic layers above the Maikop clay and the lower plot to the TIV reservoir zone. (To highlight the polarizations relevant to the three VSPs, I only plot variations for incidence angles up to 50°.) The rectangular boxes in Fig. 4.11 are centred about the incidence angles of straight-line raypaths to the receivers and schematically indicate the model polarizations along raypaths in the three VSPs.

4.4.3 Modelling the Reservoir Zone using Vertical Hudson Cracks

In this section, I model the decreasing time delay in the W29N VSP by inserting vertical Hudson cracks below a depth of 2.04 km. The cracks are water-filled, thin and strike in an orthogonal direction to the cracks in the upper layers. I calculated DIT estimates from seismograms for a range of models for crack densities between 0.02 and 0.1. The closest match to the time delay decrease in the W29N VSP was obtained with a model with a crack density of 0.08±0.01. The results from this model, named 29D, are shown in Fig. 4.12 and the model parameters are given in Table 4.6. Equal area polar projections of the polarization above 870 m and below 2.04 km are shown in Fig. 4.14a. It should be noted that between 870 m and 2.04 km the layers are characterized by strong TIV.

Model 29D polarization directions in Fig. 4.12 show no significant change from the uncracked reservoir model results in Fig. 4.10, and therefore still give a reasonably close match. On the other hand, the time delay estimates in Fig. 4.12 do

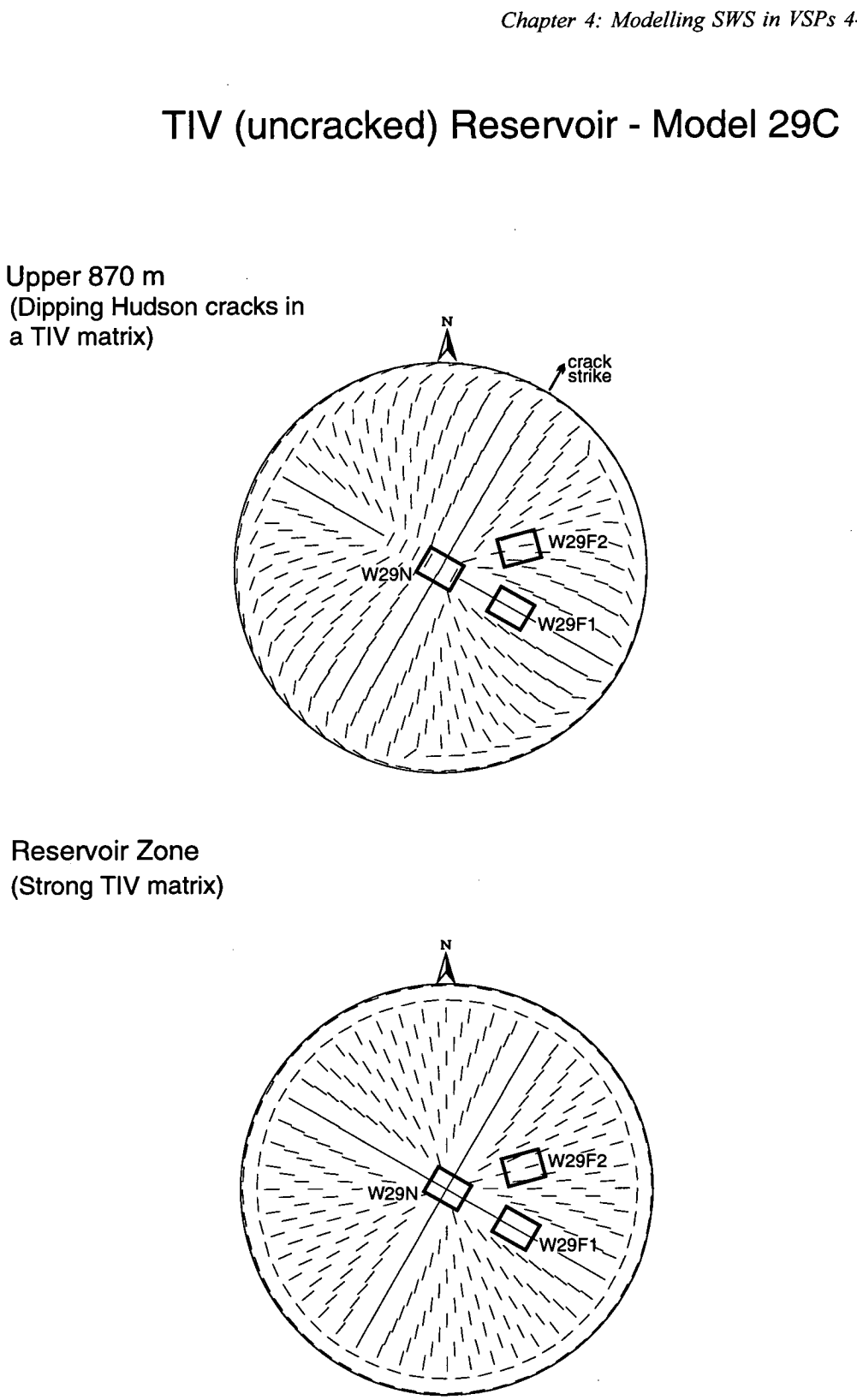

Figure 4.11: Equal area plots of the horizontal *qS1* polarization for incidence angles up to 50° in model 29C. The rectangular boxes indicate schematically the polarizations in each of the three VSPs within the azimuthally anisotropic layers above the Maikop clay, and within the reservoir zone which is characterized by strong TIV. Model parameters are given in Tables 4.5 and 4.6.

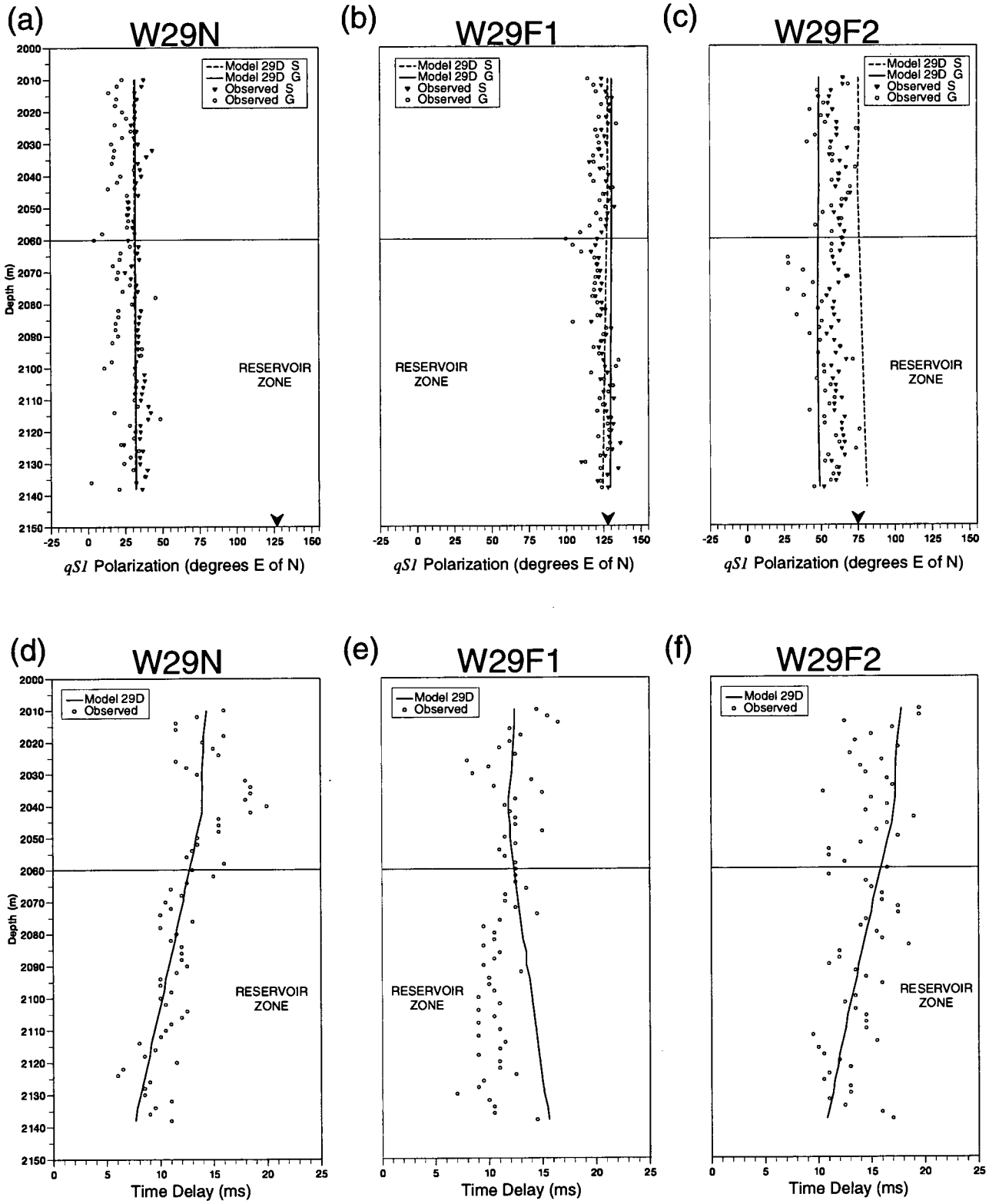

Figure 4.12: Modelling the DIT measurements of shear-wave splitting at Well 29. The model named 29D, described in Table 4.6, has vertical cracks below a depth of 2.04 km striking orthogonally to the cracks in in the upper layers. The solid arrowheads mark the azimuth of the sagittal plane.

show a significant change from Fig. 4.10. Although, the W29N observed time delay is much better matched in Fig. 4.12d, it can be seen in Fig. 4.12e that the time delay of the W29F1 VSP is less well matched. For cracks with this strike direction, no change to the dip, content (wet or dry) or aspect ratio of the cracks can give a better match to the W29F1 observations. The model results for the W29F2 VSP show a significant decrease in Fig. 4.12f. However, because there is a large scatter in the observations, it is not possible to reliably interpret whether this is a better match or not to the W29F2 observations.

4.4.4 Modelling the Reservoir Zone using Dipping Hudson Cracks

To match the observed DIT polarization observations with dipping cracks, the cracks must be parallel to the cracks in the layers above 870 m and the presumed maximum horizontal stress direction. Synthetic seismograms were calculated from 38 cracked reservoir models with crack density between 0.1 and 0.6 and dip between 60° and 37° towards east-south-east (ESE). I found that a reasonable match to the observations could be made for models with a crack density between 0.2 and 0.3. For each density the dip is constrained and equals 39° and 42° for densities of 0.2 and 0.3, respectively. The model results for a density of 0.2 and dip of 39° are shown in Fig. 4.13. The model shows a close fit to the observed polarizations in Fig. 4.13a to 4.13c. Furthermore, it can be seen in Figures 4.13d to 4.13f that the large decrease in the W29N observations is well matched and the slight, 2-3 ms, decrease in the W29F1 VSP is also closely reproduced.

Equal area plots of the horizontal-plane polarization directions of the fast split shear-wave are shown in Fig. 4.14b. The decreases in time delay in Figures 4.13d and 4.13e can be understood by comparing the upper and lower plots in Fig. 4.14b. It can be seen in Fig. 4.14b that the model polarizations in the W29N and W29F1 VSPs have changed by approximately 90°. The model polarization direction in the W29F2 VSP is more or less radial in both plots.

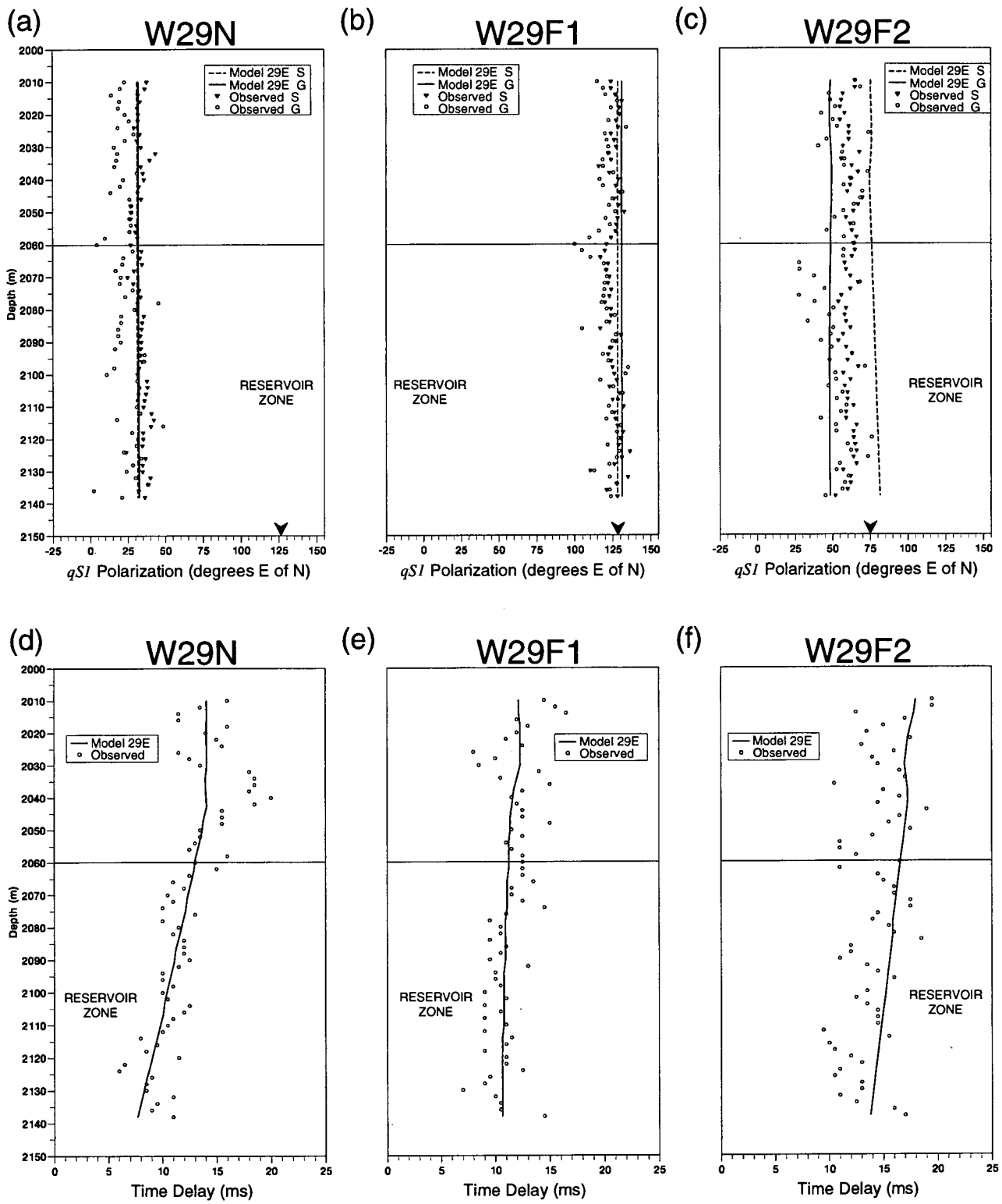

Figure 4.13: Modelling the DIT measurements of shear-wave splitting at Well 29 with dipping cracks in the upper 870 m and dipping cracks in the reservoir. Model 29E, described in Table 4.6, has cracks in the reservoir zone with density=0.2 and and dip=39°, respectively. The solid arrowheads mark the azimuth of the sagittal plane.

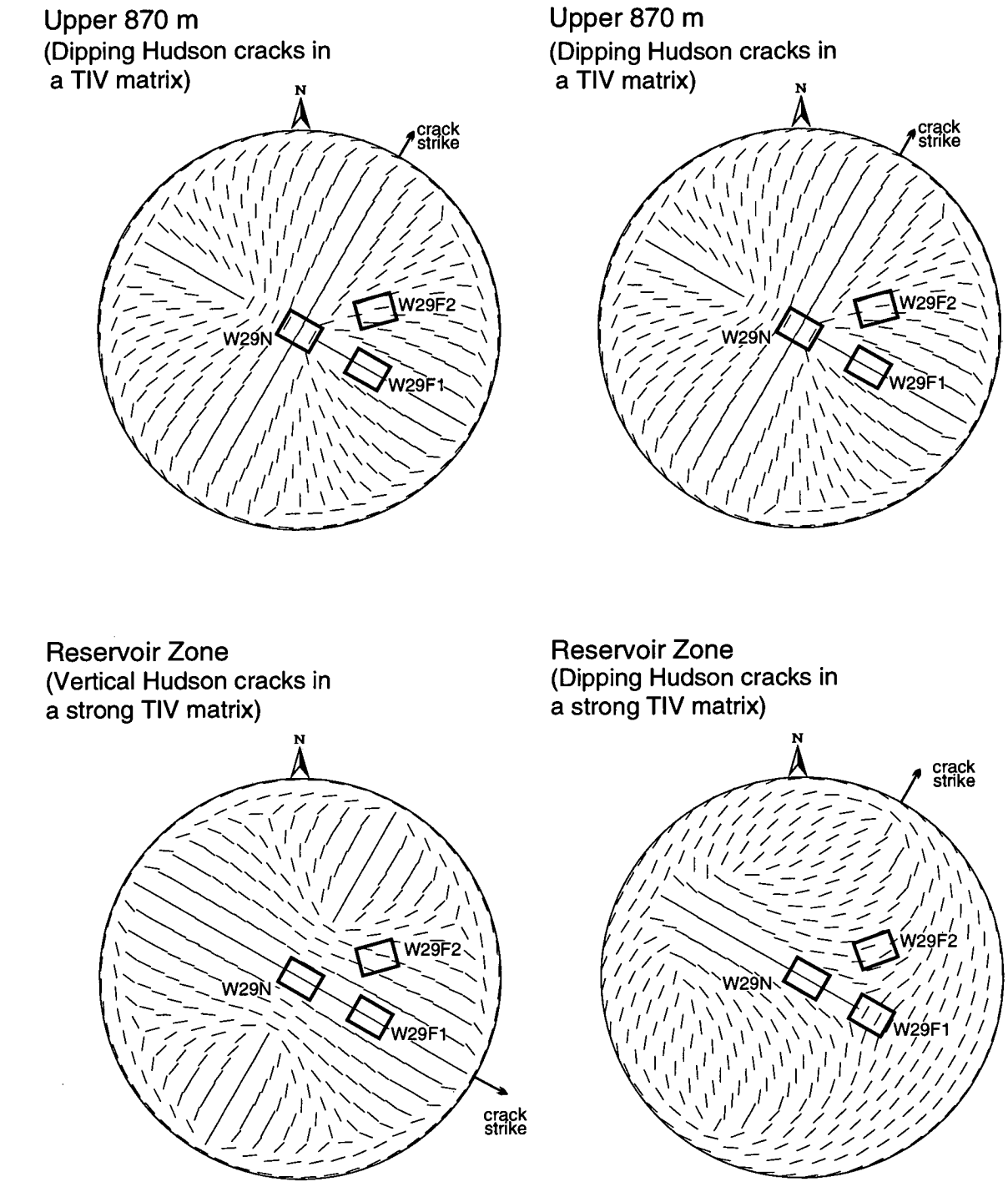

Figure 4.14: Equal area plots of the horizontal *qS1* polarization for angles of incidence up to 50° in (**a**) model 29D and (**b**) model 29E. The rectangular boxes indicate schematically the polarizations in each of the three VSPs. The model parameters are given in Tables 4.5 and 4.6.

4.4.5 Modelling the Reservoir Zone using APE Cracks

In this section, I attempt to match the large decrease of time delay in the W29N near-offset observations using the Anisotropic Poro-Elastic (APE) theory of Zatsepin and Crampin (1995, 1997), which is summarized in Section 2.6. Zatsepin and Crampin (1997) find that the APE theory predicts a distinctive 90° change in *qS1* polarization at near-vertical incidence between models with comparatively low and high pore-fluid pressure. This phenomenon is illustrated in Fig. 4.15, which shows the evolution of shear-wave polarizations for increasing pore-fluid pressure in a constant differential stress field where $s_V \geq s_H \geq s_h$. Figure 4.15 demonstrates that at low pore-fluid pressure the APE theory predicts variations in *qS1* polarization which are similar to those from other formulations for aligned cracks (e.g. Hudson, 1986 and 1991). These formulations predict that the *qS1* polarization at near-vertical incidence will be aligned with the maximum horizontal stress direction. However, at a high pore-fluid pressure the maximum horizontal stress, the APE theory predicts that the *qS1* polarization at near-vertical incidence will be orthogonal to the direction of maximum horizontal stress. This effect is not yet fully understood; however, it appears that the maximum horizontal stress must be greater than approximately half of the overburden stress for the change to occur (S. Crampin, personal communication, University of Edinburgh).

I have no information on the likely pore-fluid pressure, magnitudes of the principal stresses or crack density in the reservoir zone. Therefore, in this study I only intend to investigate what relative stresses and pore fluid pressures may match the observations.

I define the rock matrix of the reservoir zone by the isotropic velocity calculated from the near-offset W29N observations (Table 4.5), and by the TIV parameters estimated in Chapter Five for the Maikop clay at Well 85 (Table 5.2). The gradient of time delay decrease in the W29N measurements is large. Therefore, the crack density is set at a relatively high value of 0.045 (which equals the upper limit of crack density inferred by Crampin (1994) from an extensive review of published field observations).

The normalised differential stresses, s_V, and s_h were held constant at 20 and 0, respectively, and the pore-fluid pressure, p_f, and the maximum horizontal stress, s_H,

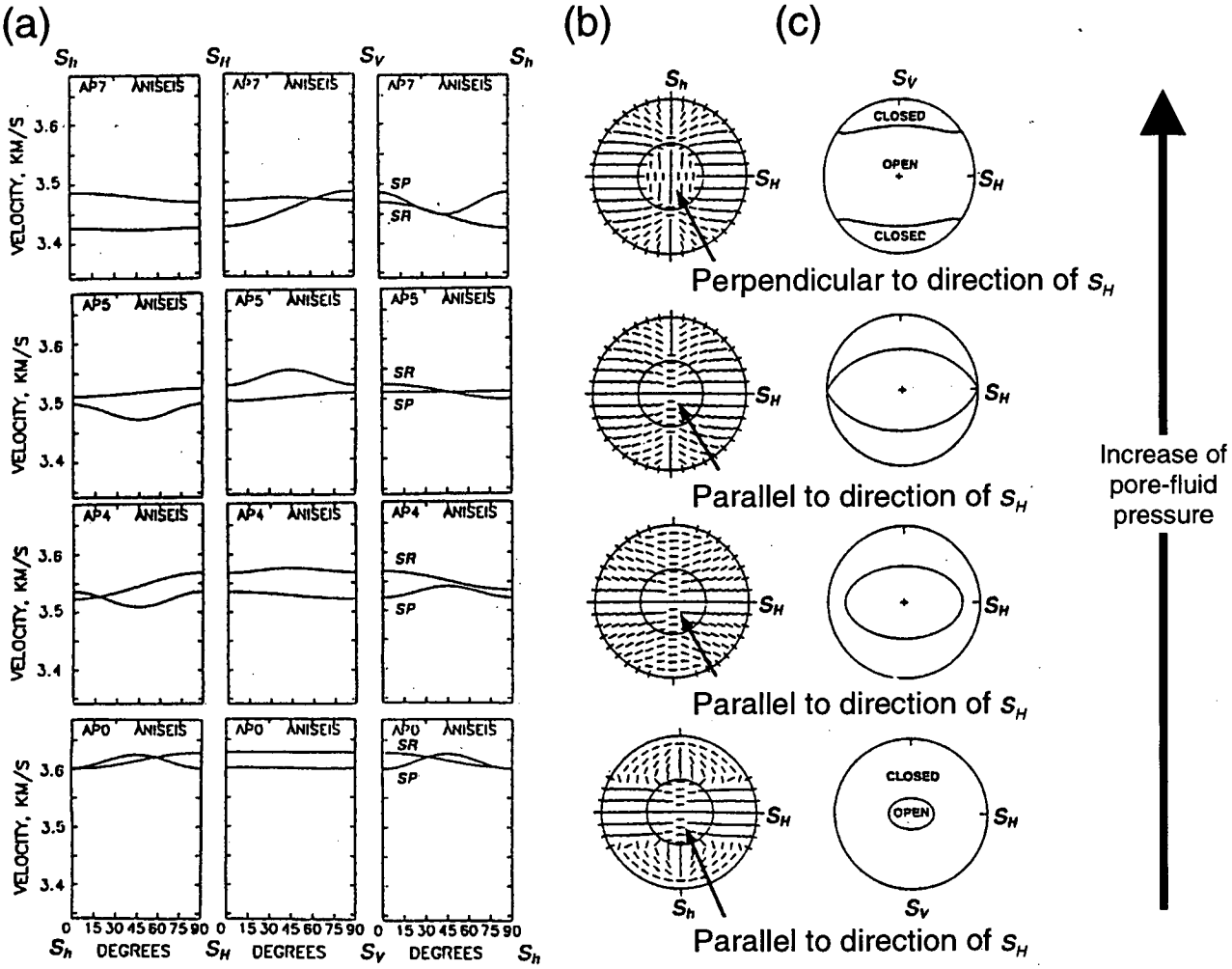

Figure 4.15: Shear-wave polarizations of stress aligned fluid-filled intergranular cracks subjected to increasing pore-fluid pressure in a constant differential stress field with $s_V \geq s_H \geq s_h$. In the bottom row of diagrams the pore-fluid pressure, p_f, is zero and in the top row the pore-fluid pressure equals the maximum horizontal stress ($p_f = s_H$). (**a**) shows quadrants of shear-wave velocity variations between the principal stress directions, (**b**) shows equal-area projections about s_V of the polarization of the fast split shear-wave and (**c**) shows polar projections about s_h of the distribution of crack normals. It can be seen in (b) that the fast split shear-wave polarization about the vertical direction changes by 90° when the pore-fluid pressure is near to the maximum horizontal stress. (after Crampin *et al.*, 1996)

were varied to match the gradient of decrease in the W29N VSP (about 60-70 ms/km). The cracks are water-filled and have an average aspect ratio of 0.01. It was found that the large time delay decrease could only be matched when $s_H \geq 18$. In other words, in the theoretical model the maximum horizontal stress must be nearly equal to the vertical stress. The results of DIT measurements from synthetic seismograms calculated from three models with different pore-fluid pressures for models with s_H=18, are shown in Fig. 4.16. The three models 29F, 29G and 29H have normalised pore-fluid pressures of 10, 16 and 18, respectively. A summary of the model parameters are given in Table 4.7.

In Figures 4.16a to 4.16c, the observed polarizations are well matched for all three models with different pore-fluid pressures. The time delays, however, show a much larger variation in agreement. In Fig. 4.16d it can be seen that increasing the pore-fluid pressure improves the fit to the W29N observations. The best fit to the W29N observations is achieved with a pore-fluid pressure of 18, which is equal to the maximum horizontal stress. Figure 4.16f shows that, for the W29F1 VSP, increases in pore-fluid pressure gives an increase in time delay through the reservoir zone. The best fit to the time delay of the W29F1 observations is with a low pore-fluid pressure model ($p_f \approx 13$). Overall, the model 29G with a pore-fluid pressure of 16 gives the best fit to the observations, although neither VSP is matched fully. However, it should be noted that the modelling using the APE theory was based on finding a match to the near-offset results at Well 29. Therefore, it is possible that the W29F1 far-offset VSP results can also be matched with the APE model by varying some of the model parameters, such as crack density, which were held constant in the models examined.

Equal area plots for the models with the lowest and highest pore-fluid pressures are shown in Fig. 4.17. The 90° change in *qS1* polarization at near-vertical incidence associated with the increase in pore-fluid pressure can be confirmed by comparing the two lower equal area plots.

Summary of the modelling of Well 29

I have shown that no unique model matches the decreasing time delay observed along near-vertical raypaths in the W29N VSP. In particular, three cracked reservoir models have been found to match the decrease in time delay and associated 90° change in *qS1*

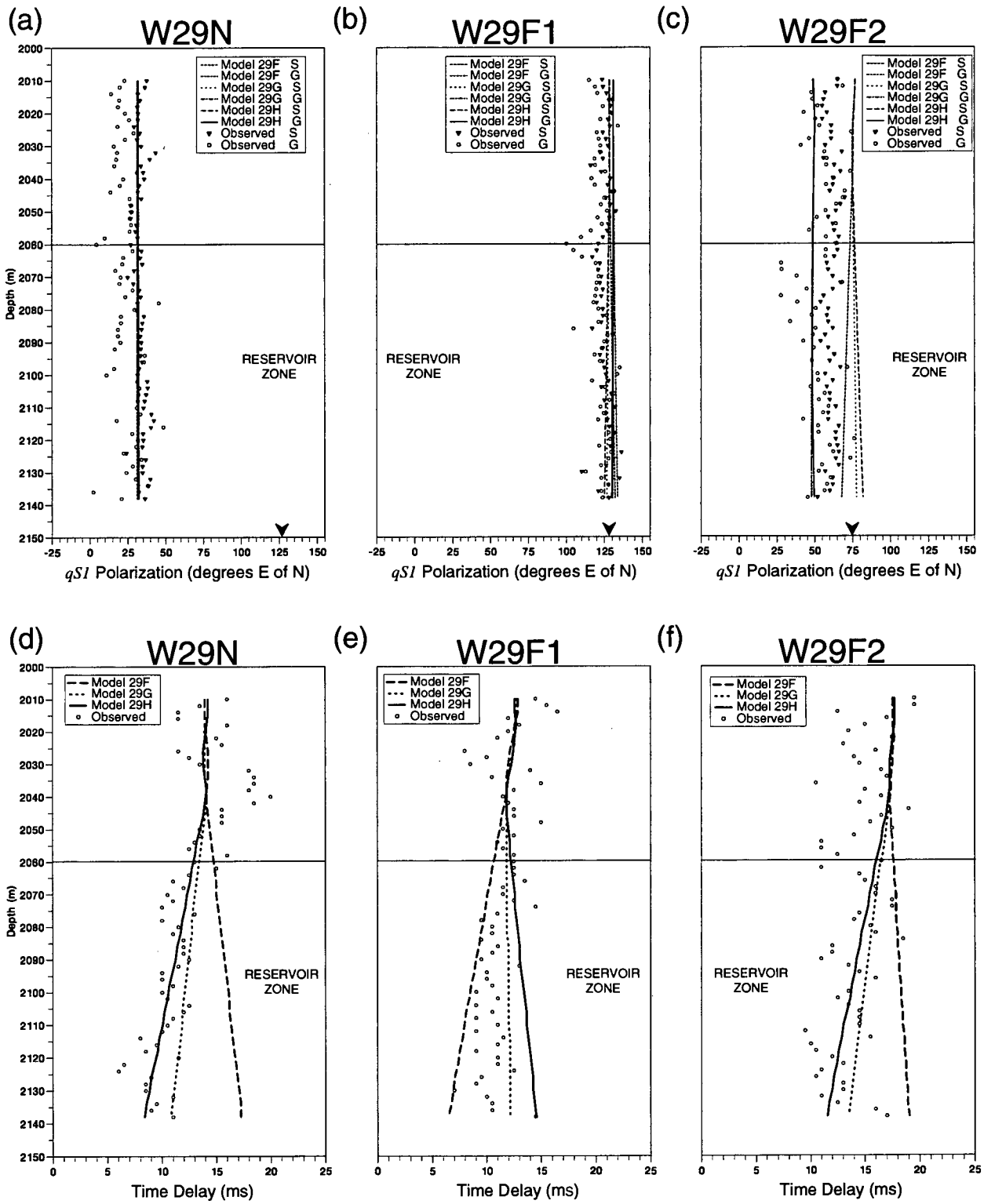

Figure 4.16: Modelling the DIT shear-wave splitting measurements at Well 29 using the APE theory. A distribution of intergranular microcracks is inserted below 2.04 km, with pore-fluid pressure increasing between models 29F, 29G and 29H. The model parameters are given in Table 4.7. The solid arrowheads mark the azimuth of the sagittal plane.

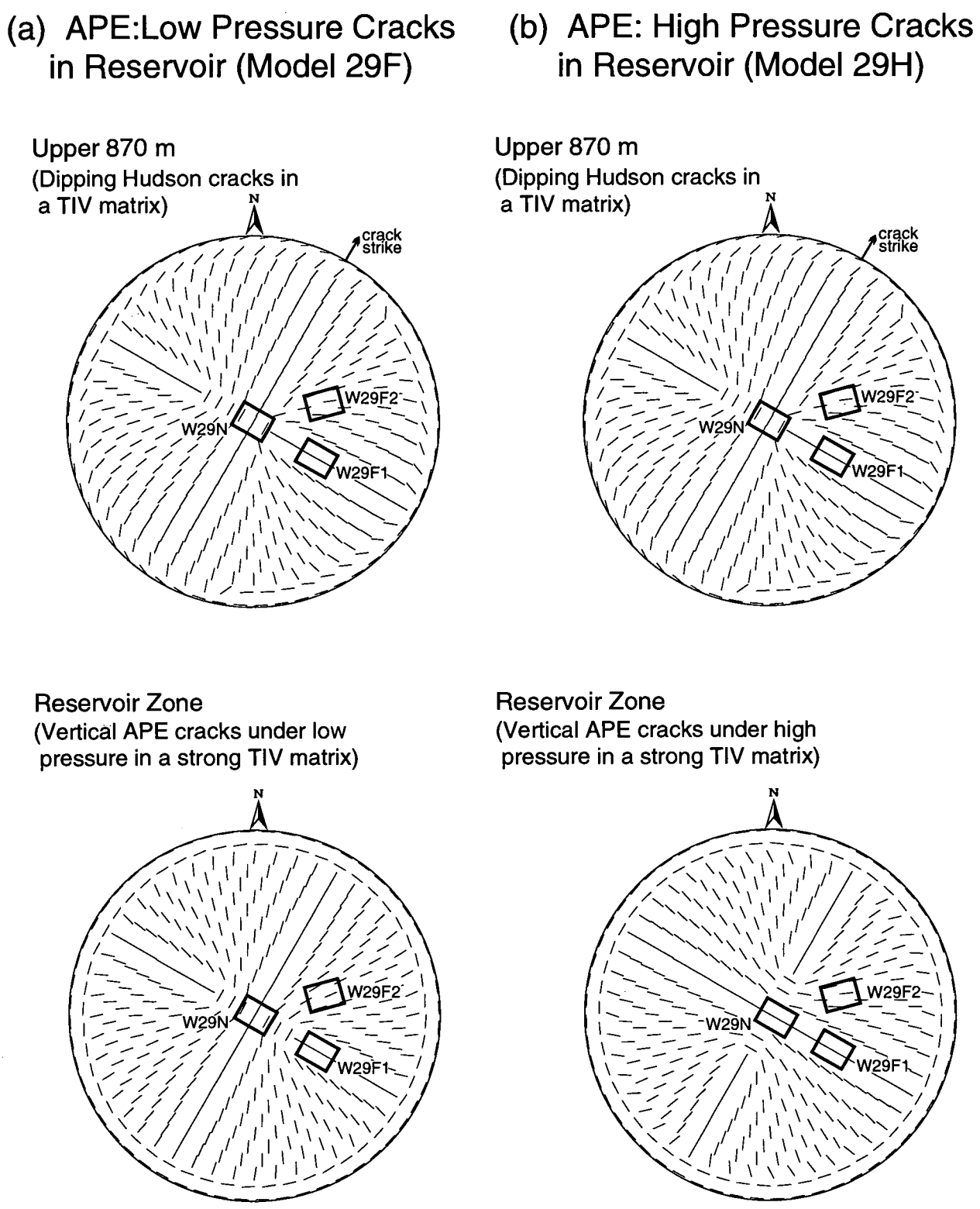

Figure 4.17: Equal area plots of the horizontal *qS1* polarization for incidence angles up to 50° in (**a**) the model 29F and (**b**) the model 29H. The rectangular boxes indicate schematically the polarizations in each of the three VSPs. The model parameters are given in Tables 4.5 and 4.7.

polarization direction. The three different reservoir models are defined by (i) vertical aligned cracks, (i) dipping aligned cracks and (iii) a distribution of cracks.

Further information from far-offset VSPs may help to reduce the non-uniqueness in modelling the reservoir azimuthal anisotropy. I have modelled two far-offset VSPs and the best model I have found has a high density of dipping cracks in the reservoir. However, other interpretations of the reservoir azimuthal anisotropy, such as the distribution of cracks predicted by the APE theory, cannot be excluded. This is because the anisotropic structure overlying the reservoir zone at Well 29 is not fully resolved due to a lack of receiver levels above the reservoir.

4.5 SUMMARY AND CONCLUSIONS

In this chapter, I have obtained models which match shear-wave splitting estimates at three wells from two North Caucasus oil fields. Essentially, this involved first determining anisotropic models of the top 1 km at Wells 85 and 87 and then determining anisotropic models of the reservoir zone at Well 29.

At Wells 85 and 87, I have shown that the shear-wave splitting measured in the near-offset VSPs is unlikely to be caused by an inclination of the strong TIV determined in Chapter Five. Subsequently, using forward modelling, I found that the shear-wave splitting measurements from Wells 85 and 87 can be matched by similar models which have a constant density of Hudson cracks inserted into the layers above the Maikop clay. The cracks are vertical and aligned close to the presumed maximum horizontal stress direction. The layers of sandstones, limestones and clays overlying the Maikop clay have, therefore, orthorhombic or lower anisotropic symmetry.

At Well 29, I have shown that the decrease in time delay along near-vertical raypaths through the reservoir can be matched by three different cracked models. Such non-uniqueness cannot be resolved using only vertically propagating shear waves but requires additional information from other propagation directions obtained, for example, from far-offset VSP experiments. In this chapter, I have also modelled the far-offset VSP observations at Well 29. The best-fitting model I have found to match the shear-wave splitting in the three VSPs has a high density of dipping cracks in the reservoir zone. However, due to the absence of receiver levels above the reservoir zone, other interpretations cannot be excluded.

CHAPTER FIVE

MODELLING OF WALKAWAY VSP DATA FROM THE JURAVSKOE OIL FIELD, NORTH CAUCASUS

5.1 INTRODUCTION

In 1991, Neftegeofizika Geolkom (Moscow), Stavropol-Neftegeofizika (Stavropol), and the Edinburgh Anisotropy Project (British Geological Survey, Edinburgh), collaborated in walkaway VSP experiments in two wells, Well 85 and Well 87, in the Juravskoe oil field in the North Caucasus Foredeep, Russia. The reservoir in the Juravskoe field is in the bottom 100 m of a 1.2 km-thick layer of uniform Maikop clay. Such clay reservoirs are comparatively common in oil fields throughout the Russian Platform and Western Siberia, and are thought to be present in many areas elsewhere. During acquisition of the walkaway experiments anomalously fast SV-wave arrivals were observed on all walkaway profiles and suggested by L.Y. Brodov (Neftegeofizika, Moscow) as being caused by cusps in the SV group-velocity surface.

Cusps are well established theoretically (Musgrave, 1970), but observations of cusps are rare. Jolly (1956) is the only known report suggesting observation of anisotropic cusps in field data. However, as the waveforms observed by Jolly have never been matched by synthetic seismograms, these observations remain unconfirmed.

In this chapter, I confirm by modelling with full waveform synthetic seismograms, that the anomalous arrivals recorded in the Juravskoe oil field are cuspidal phases generated on the SV-wave group-velocity surfaces related to high shear-wave anisotropy. The shear-wave arrival times and polarizations, including the cuspidal arrivals, are matched with synthetic seismograms in a model in which the Maikop clay has strong transverse isotropy with SH-wave and qSV-wave anisotropies equal to 41% and 24%, respectively. This chapter, and its associated publication (Slater *et al.*, 1993), appears to be the only published report of anisotropic cusps in

exploration seismic to be confirmed by matching with full waveform synthetic seismograms.

5.2 BACKGROUND INFORMATION ON TIV AND CUSPS

The purpose of this section is to provide sufficient background information on wave propagation in media displaying TIV so that the following sections may be understood. First, I describe the theoretical phase-velocity variations of TIV media. Then I describe the associated group-velocity variations and the occurrence of cusps in the wave surfaces. Next, I describe published reports relating to experimental observations of cusps and, lastly, I briefly outline the common causes of TIV in sedimentary basins.

5.2.1 Phase-Velocity Variations

Seismic velocity variations of anisotropic media depend on the pattern of elastic constants which define the stiffness tensor, $\boldsymbol{C}$. Only five independent elastic constants are required to define the tensor of TIV media due to the high degree of symmetry of such media. Using the condensed tensor notation described in Section 2.2 (sometimes referred to as the Voigt notation) the tensor of a TIV medium for a vertical x_3 reference axis is:

$$\boldsymbol{C} = \begin{bmatrix} C_{11} & C_{12} & C_{13} & 0 & 0 & 0 \\ C_{12} & C_{11} & C_{13} & 0 & 0 & 0 \\ C_{13} & C_{13} & C_{33} & 0 & 0 & 0 \\ 0 & 0 & 0 & C_{44} & 0 & 0 \\ 0 & 0 & 0 & 0 & C_{44} & 0 \\ 0 & 0 & 0 & 0 & 0 & C_{66} \end{bmatrix}; \qquad (5\text{-}1)$$

where

$$C_{12}=(C_{11}-2C_{66}) .$$

Inserting this tensor into the equations of motion (Eqn. 2-3) and solving for plane-wave propagation yields, in general, three independent solutions for each

propagation direction. These solutions represent three orthogonally polarized body waves travelling with different phase velocities. The three body waves are: a quasi-longitudinal (qP) wave, a quasi-transverse (qSV) wave, and a purely transverse wave (SH), where the qSV and SH waves have polarization vectors strictly in the vertical and horizontal planes, respectively. Daley and Hron (1977) present a clear derivation of the well known equations to describe the directional dependence of the three phase velocities. Using notation similar to Thomson (1986), the equations for propagation at an angle θ to the vertical symmetry axis are:

$$V_P^2(\theta)=\frac{1}{2\rho}\left[C_{33}+C_{44}+(C_{11}-C_{33})\sin^2(\theta)+D(\theta)\right]; \tag{5-2a}$$

$$V_{SV}^2(\theta)=\frac{1}{2\rho}\left[C_{33}+C_{44}+(C_{11}-C_{33})\sin^2(\theta)-D(\theta)\right]; \tag{5-2b}$$

and

$$V_{SH}^2(\theta)=\frac{1}{\rho}\left[C_{66}\sin^2(\theta)+C_{44}\cos^2(\theta)\right]; \tag{5-2c}$$

where ρ is the density of the medium and

$$\begin{aligned} D(\theta)\equiv\Big\{&(C_{33}-C_{44})^2 \\ &+2\left[2(C_{13}+C_{44})^2-(C_{33}-C_{44})(C_{11}+C_{33}-2C_{44})\right]\sin^2(\theta) \\ &+\left[(C_{11}+C_{33}-2C_{44})^2-4(C_{13}+C_{44})^2\right]\sin^4(\theta)\Big\}^{1/2}. \end{aligned} \tag{5-2d}$$

To illustrate the likely velocity variations expected in a TIV medium, I plot phase-velocity variations of a Cretaceous TIV shale in Fig. 5.1a, calculated from the elastic constants of Jones and Wang (1981). The general variations in the phase-velocity surfaces in Fig. 5.1a are geometrically simple and may be easily understood by referring to the approximations of Crampin (1977), which are indicated by the dashed line in Fig. 5.1a. Crampin (1977) has shown that the square of the phase-velocity variations of the qP-wave, even for strong TIV, has an approximately $\sin 2\theta$ variation with angle from the symmetry axis (with a, usually small, $\sin 4\theta$ contribution). Similarly, the squares of the SH- and qSV-wave phase-velocity variations have approximately $\sin 2\theta$, and $\sin 4\theta$, variations, respectively, where the coefficients of the $\sin 4\theta$ variations of the squares of qP- and qSV-wave phase-velocities are equal and opposite in sign.

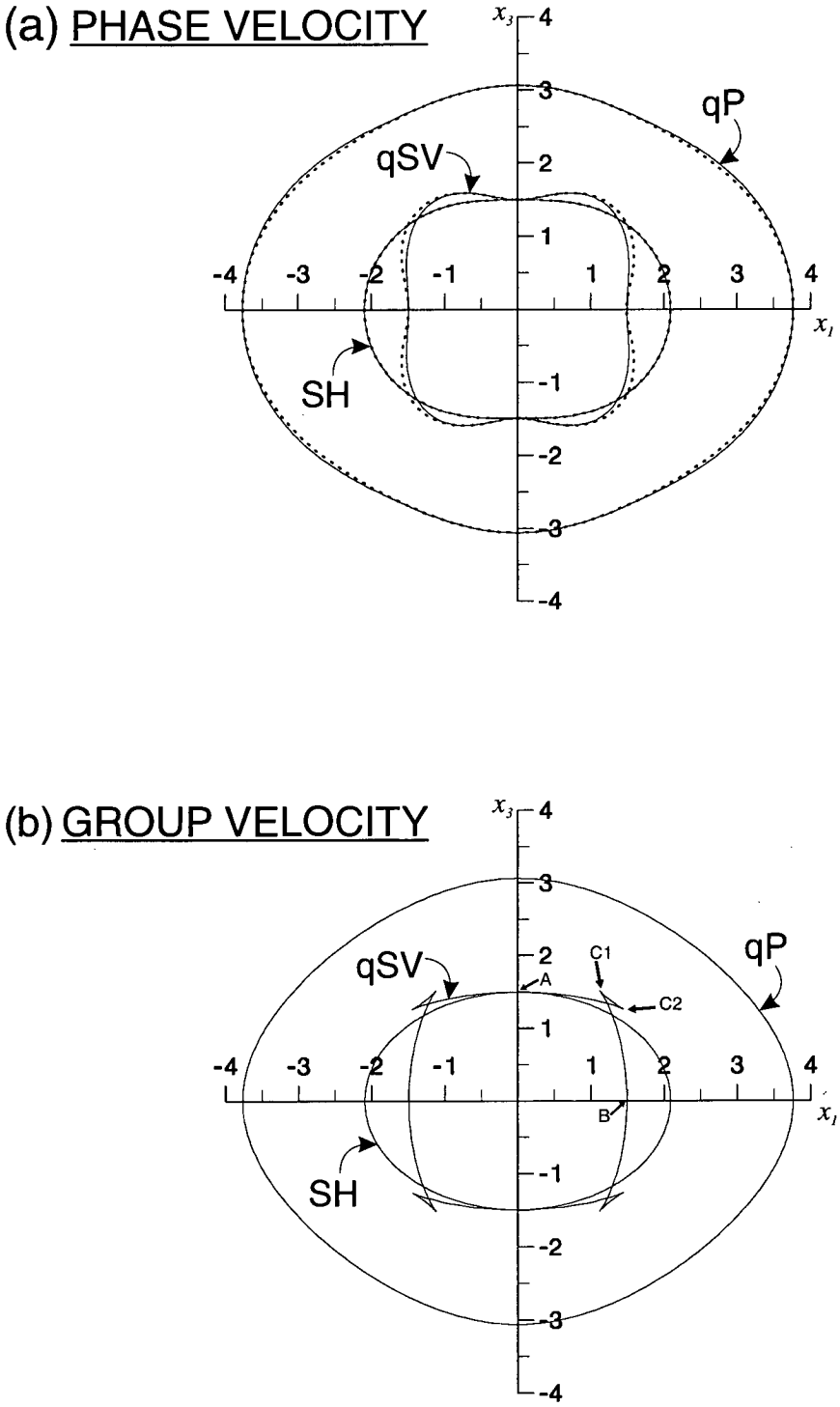

Figure 5.1: The solid line displays variations in (**a**) phase-velocity and (**b**) group-velocity of a transversely isotropic Cretaceous shale (Jones and Wang, 1981). The dashed line in (a) represents the phase-velocity surface calculated using approximations from Crampin (1977). The vertical x_3 axis is an axis of rotational symmetry and cusps can be cleary identified at points marked C1 and C2 on the qSV group- velocity sheet in (b).

5.2.2 Group-Velocity Variations and Cusps

In general, seismic waves propagating at the group-velocity have more complicated surfaces, which may in some circumstances contain cusps. Musgrave (1954) showed theoretically that materials with strong transverse isotropy may have cusps in the qSV-wave group-velocity surface (wave surface) caused by the high curvature of the qSV-wave phase-velocity variations. [A clear illustration of the geometrical relationship between the phase-velocity, slowness, and group-velocity surfaces is given by Helbig (1994, Fig. 4.1).] The group-velocity surfaces in Fig. 5.1b calculated from the phase-velocities in Fig. 5.1a show that the shale studied by Jones and Wang (1981) has a complicated qSV wave surface that displays cuspidal features. In each quadrant of Fig. 5.1b, the qSV group-velocity surface has three branches: two ordinary branches - joining A to C2, and C1 to B; and one reverse branch - joining C2 to C1. These two types of branches meet at points known as cusps which are marked C1 and C2 in Fig. 5.1b. Between the two cusps there is an area of triplication where, for each direction of group-velocity propagation, there are three qSV phases travelling at different velocities.

Theoretically therefore, a cusp is a singular point joining two separate branches of the wave surface. However, due to the finite bandwidth of the signal in field recordings, it is likely that the two leading qSV-phases within the triplication area will overlap, so that identifying three separate arrivals on seismograms may be difficult, particularly for short pathlengths (This is demonstrated on the synthetic seismograms of White (1982), and Kerner, Dyer and Worthington (1989)). For this reason, in the remainder of this thesis I use the term cusp to mean anomalously fast qSV-phases generated within the area of triplication arriving in advance of the slowest (principal) qSV-phase. Although cusps are well established theoretically, observations of them appear to be rare. In the next section I will describe the few reports relating to observations of seismic cusps.

5.2.3 Experimental Observations of Cusps

The only previous publication reporting observations of anisotropic cusps in exploration seismics appears to be Jolly (1956), interpreted by Levin (1979). Jolly

observed abnormally large SV-wave velocities in field observations in Pierre-shale, and suggested these as resulting from a severe near-vertical cusp. Levin (1979) presented an explanation of these observations in terms of general cusp arrival time behaviour, and White (1982) and Kerner, Dyer and Worthington (1989) show general results on cusp amplitudes which help to support Levin's explanation. As far as I am aware, though, the observation of cusps in field seismograms proposed by Jolly (1956) has yet to be confirmed by matching synthetic seismograms to the observed waveforms.

Seismic-waves in rocks with strong TIV can also be studied in the laboratory using ultrasonic propagation through homogeneous core samples. Such experiments can potentially image the wavefront in detail, and thus give direct evidence of anisotropic cusps. However, because the sample-height to transducer-width ratio is typically small, it is the phase velocities and not the group velocities which are measured (Dellinger and Vernik, 1994). Consequently, there have been no reported observations of anisotropic cusps in laboratory ultrasonic experiments.

5.2.4 Causes of TIV in Sedimentary Basins

Riznichenko (1949) and Postma (1955) showed theoretically that effective transverse isotropy could be caused by sequences of thin isotropic layers (layering-anisotropy) with layer thicknesses smaller than the seismic wavelengths. Lithological-anisotropy of aligned clay platelets in shale and clay rocks may also cause such transverse isotropy (Kaarsberg, 1968; Johnston and Christensen, 1995; Sayers, 1994) and, since layering-anisotropy and lithological-anisotropy have very similar patterns of elastic constants, it is difficult to separate the cause from their effects on seismic waves.

5.3 GEOLOGY OF JURAVSKOE OIL FIELD

A description of the local geology surrounding Well 85 and Well 87 is given in Chapter Three. In summary, the geology consists of a 600 m-thick near-horizontal sequence of Neogene clays, sandstones, and limestones overlying the Maikop Series of Middle Oligocene to Lower Miocene rocks (Fig. 3.3). The uppermost 200 m of the Maikop in the area of the wells is an alternating sequence of sandstones and clays,

overlying 1.2 km of uniform clay with the reservoir in the lowest 100 m. The velocity structure shown in Fig. 5.2a is derived from a near-offset VSP. Below 870 m in Fig. 5.2a, the Maikop clay layers have a small gradient in P-wave velocity, a slightly larger gradient in shear-wave velocity and large Vp/Vs ratios between 2.1 and 3.0 which is characteristic of clay beds (Castegna, Batzle and Eastwood, 1985). The increase of Vs and decrease in Vp/Vs below 1.95 km in the clay reservoir is thought to be caused by the presence of organic-rich material in the clay (L.Y. Brodov, Neftegeofizika, Moscow, personal communication).

The study by Galperina and Galperin (1987), described in Section 3.4, is the only known previous work on the seismic anisotropy of Maikop clays. Their main conclusion is that the near-surface Maikop clays are characterized by TIV with a horizontal velocity ratio (SH/SV) of 1.2.

5.4 DATA ACQUISITION

Walkaway VSPs at Well 85 and Well 87 were acquired, as suggested by MacBeth *et al.*, (1993), with two source polarizations along two azimuths with geophones at two levels. In this study I examine the dataset from the upper geophone level at Well 85, but all walkaway profiles from both wells show similar features. The walkaways at Well 85 were acquired along azimuthal directions N355°E, labelled WA1, and along N55°E, labelled WA2, 30° either side of the presumed direction of maximum horizontal stress. The geophone levels spanned the 100 m-thick reservoir zone near the bottom of the 1200 m-thick clay layer of uniform clay. Figure 5.3 shows a plan view of the acquisition geometry at Well 85, which is summarized in Table 3.1.

Shear waves were generated on the surface by an impulsive electrodynamic source, the VEIP-40 (Fig. 3.5), aligned in-line and cross-line to the direction of the wellhead. Since the walkaways were not parallel to the presumed stress (symmetry) directions, such source orientations excited both split shear-wave polarizations. Each truck had three baseplates producing a horizontal force giving impulsive signals with, in this experiment, an effective peak frequency of 16 Hz. The source signals were stacked, up to 32 times for the farthest offset, with left and right source polarizations at each geophone level. This arrangement allows P-wave signals to be cancelled and shear-wave signals to be enhanced by subtracting seismograms made with opposite

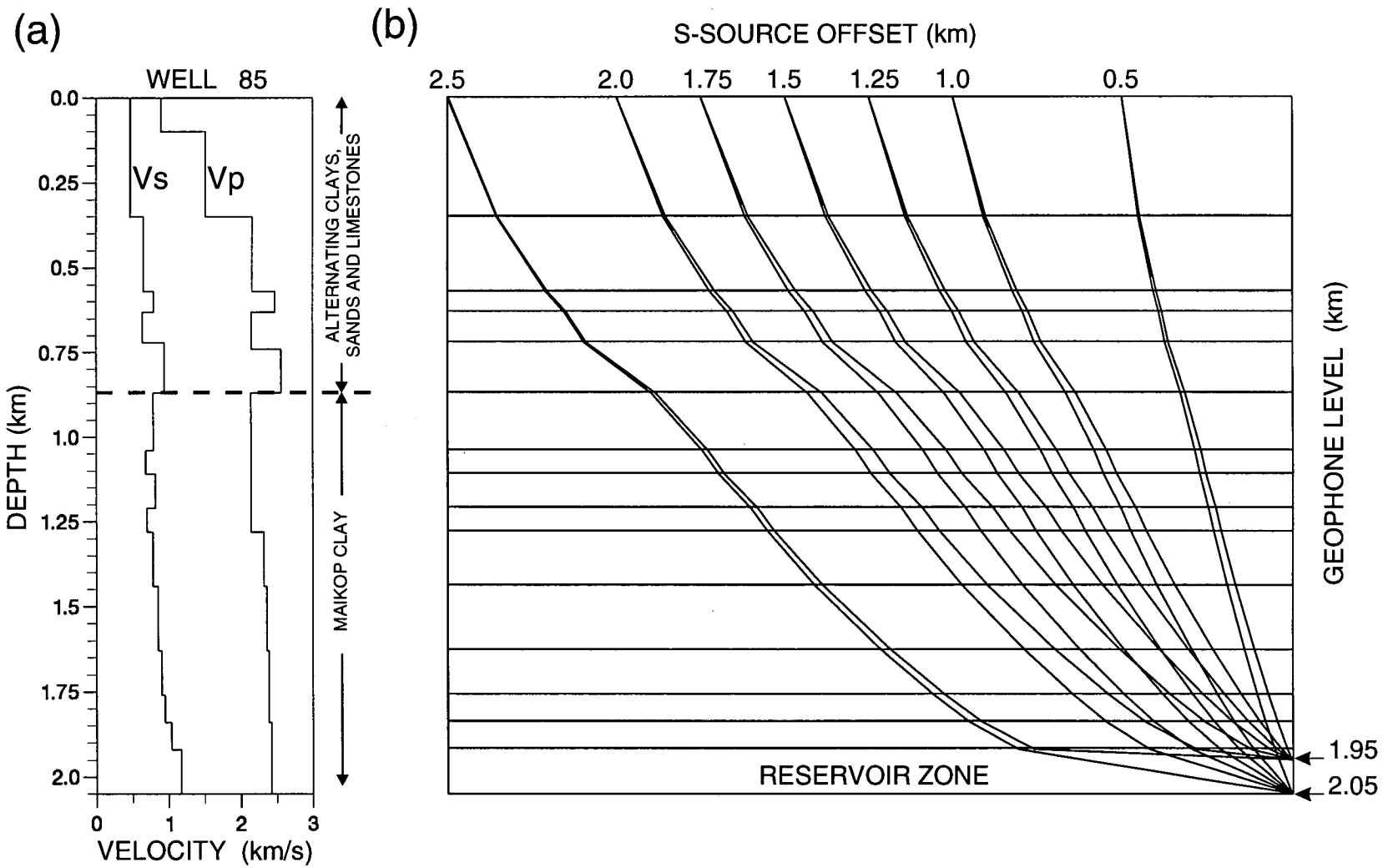

Figure 5.2: (**a**) Isotropic velocity structure ; and (**b**) ray paths of shear waves through the isotropic velocity stucture in (a). The dashed line in (a) at 870 m indicates a sharp decrease in velocities. At this level lithology changes from alternating clays, sands and limestones above, to thick Maikopian clays below.

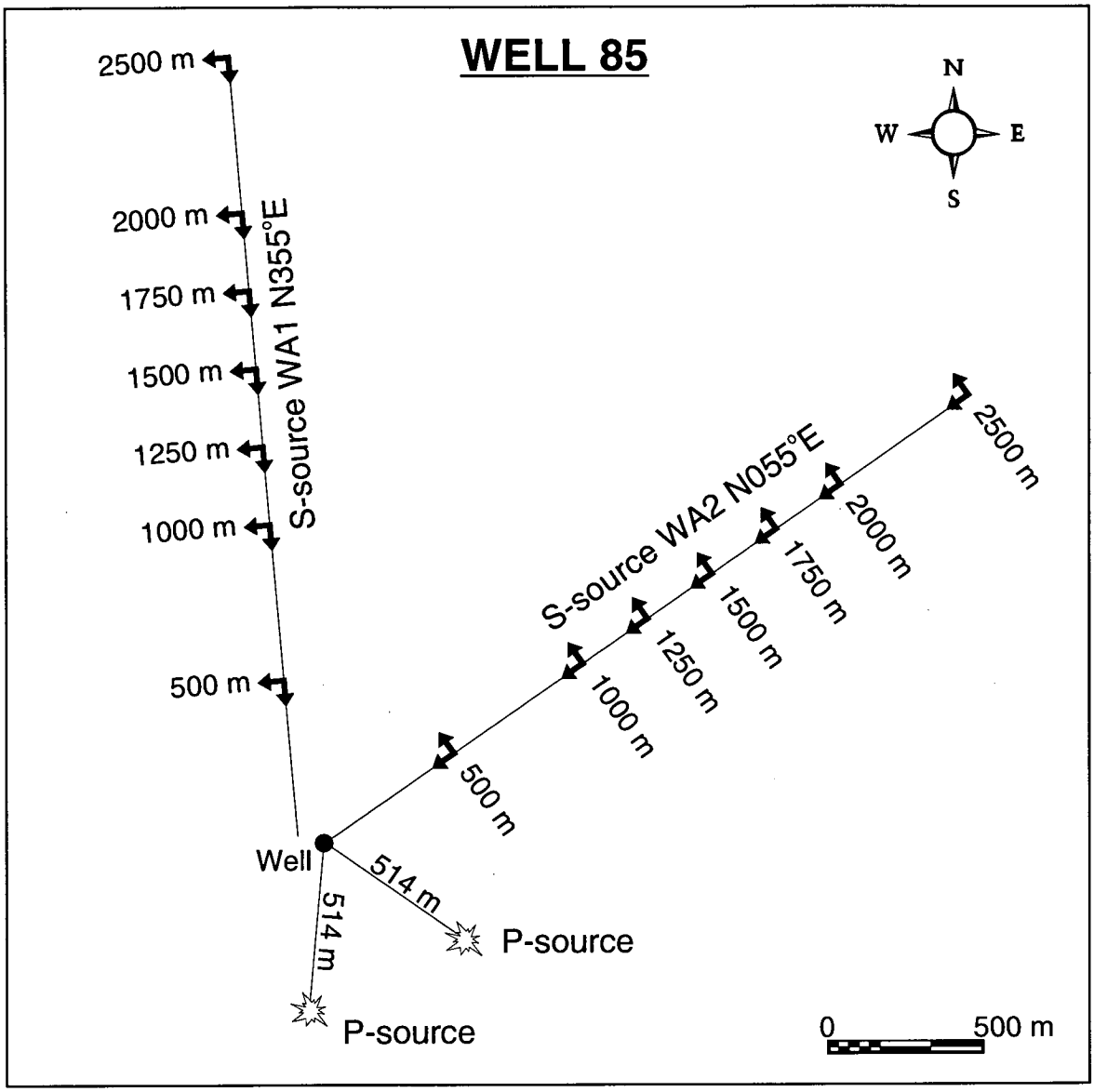

Figure 5.3: Plan view of acquisition geometry of the walkaway profiles at Well 85. The VEIP-40 shear-wave sources indicated by arrows are located 500 m to 2500 m from the borehole along two azimuths separated by 60°. The three-component receiver is locked at depths of 1950 m and 2050 m.

source-polarizations (Puzirev and Brodov, 1969). Correspondingly, P waves can be enhanced and shear waves cancelled by summing seismograms of opposite polarizations. To determine orientations of the downwell geophones, high-energy P waves were generated by explosives in shallow boreholes at offsets of 514 m.

5.5 PROCESSING

5.5.1 Processing Summary

I apply the following principal processing procedures to the data:

(i) subtraction and summation of records from oppositely polarized sources. This preferentially enhances shear and P waves, respectively;

(ii) rotation of the two horizontal receiver components into directions in-line (radial) and cross-line (transverse) to the sagittal-plane containing source and receiver. I calculate the azimuthal orientation of the horizontal components from compressional arrivals generated by the far-offset explosive sources (Fig. 5.3);

(iii) static time shifting of the signals on some traces by -50 ms to correct for a source triggering delay. The walkaway source offsets affected by the delay for the 1950 m-geophone level in Well 85 are:

WA1 - 0.5, 1.0, 1.25, 1.5 and 2.0 km

WA2 - 0.5, 1.25, 1.5, 1.75, and 2.5 km

at each offset position, recordings from both in-line and cross-line source polarizations were equally effected because the source was the same for both polarizations;

(iv) bandpass filtering from 3-40 Hz to remove high frequency noise interference.

5.5.2 Observed Seismograms

In Figures 5.4 and 5.5 the three-component seismograms display shear-wave arrivals from two sources along two walkaways with the geophone at the 1950 m-level in Well 85. Since the relative arrival times of phases on different components of the seismic traces, important for this study, are usually well-separated, displays of polarization diagrams (hodograms) are not informative. Instead, I prefer to display these shear-wave walkaway records as three-component record sections. The direct P-wave arrivals recorded in WA1 and WA2 from the VEIP-40 source are shown in Fig. 5.6. [Note that the offsets along each walkaway are 250 m apart except for the first and last offsets which are 500 m apart.]

The datasets from the two walkaways show many similarities with the largest differences occurring between the relative amplitudes of the three-component signals. All eight walkaways show very similar features, and most of the following comments and modelling results, including observations of cuspidal arrivals, apply equally to all walkaways. There are many anomalous features in Fig. 5.4, particularly the multiple shear-wave arrivals with different velocities (leading to different arrival times) and different polarizations. These multiple arrivals have similar arrival times at the corresponding offsets and geophone levels along the different walkaways, but the relative three-component amplitudes vary substantially between offsets and geophone levels and between walkaways (compare the seismograms for the two walkaways in Figures 5.4 and 5.5).

5.6 OUTLINE OF MODELLING

In this section I outline the different types of model structure I use to match the principal shear- and P-wave arrival times and amplitude features observed in WA1 (Figures 5.4 and 5.6a, respectively). As the seismograms in Fig. 5.4 are complicated, with several different shear-wave arrivals, I first describe which particular shear-wave arrivals I attempt to match.

The shear-wave arrivals in Fig. 5.4 I try to model are: the principal shear waves, marked by solid triangles at each offset; and the anomalous fast arrivals at the 1.5 km and 2.5 km offsets, marked by open triangles. The anomalous arrivals also

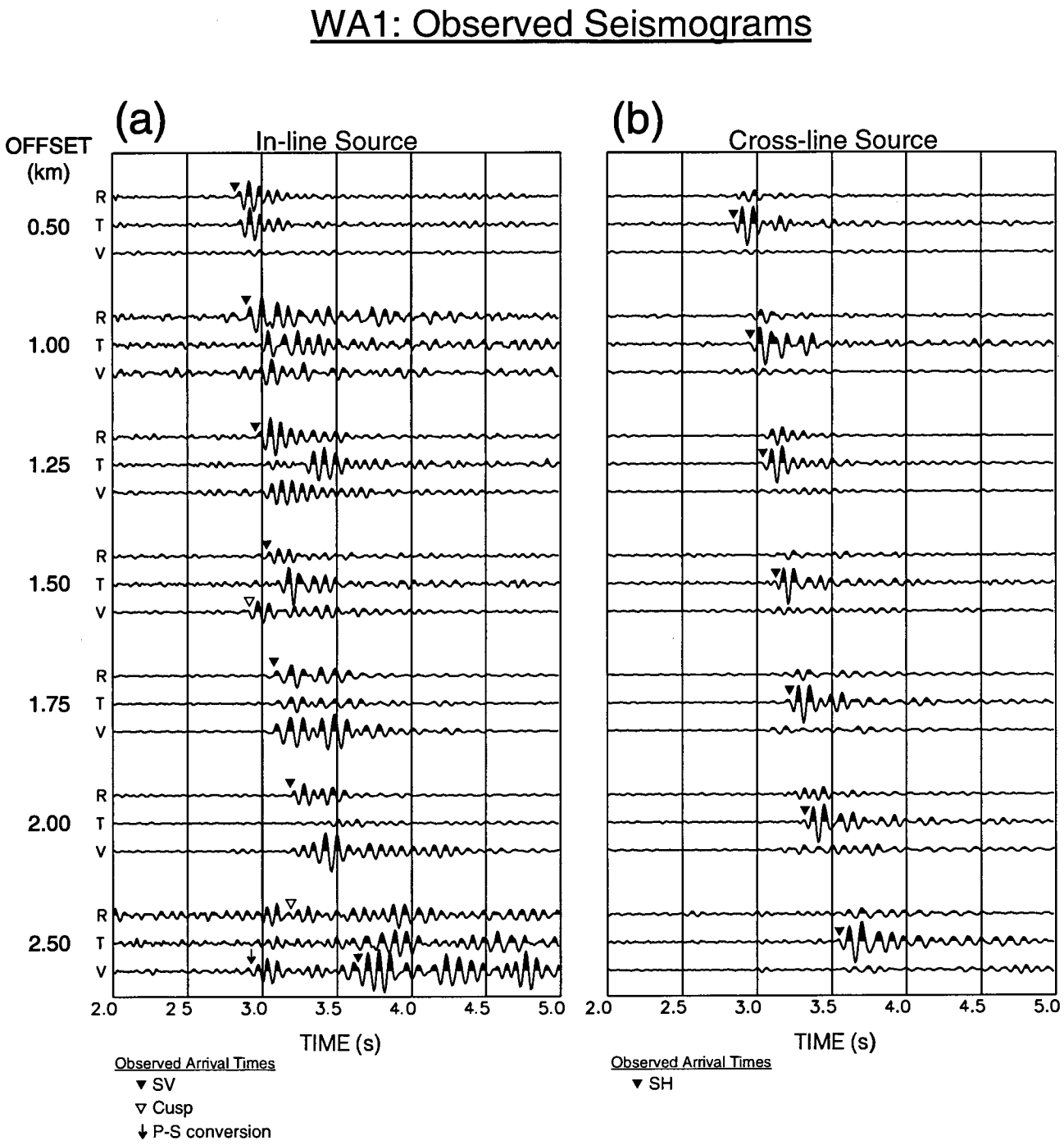

Figure 5.4: Three-component seismograms recorded by geophone at 1950-m level for walkaway WA1 for **(a)** in-line and **(b)** cross-line source orientations at Well 85. Seismograms are (V)ertical and horizontal (R)adial (in-line) and (T)ransverse (cross-line) and each three-component seismogram is normalized separately. The solid triangles mark the arrival times of the main shear-wave phases used to estimate the transverse isotropy and the open triangles mark anomalous arrivals which synthetic seismograms show are generated by cusps. The arrow (2.5 km offset) marks an arrival which synthetic seismograms show is generated by a shallow P-S conversion.

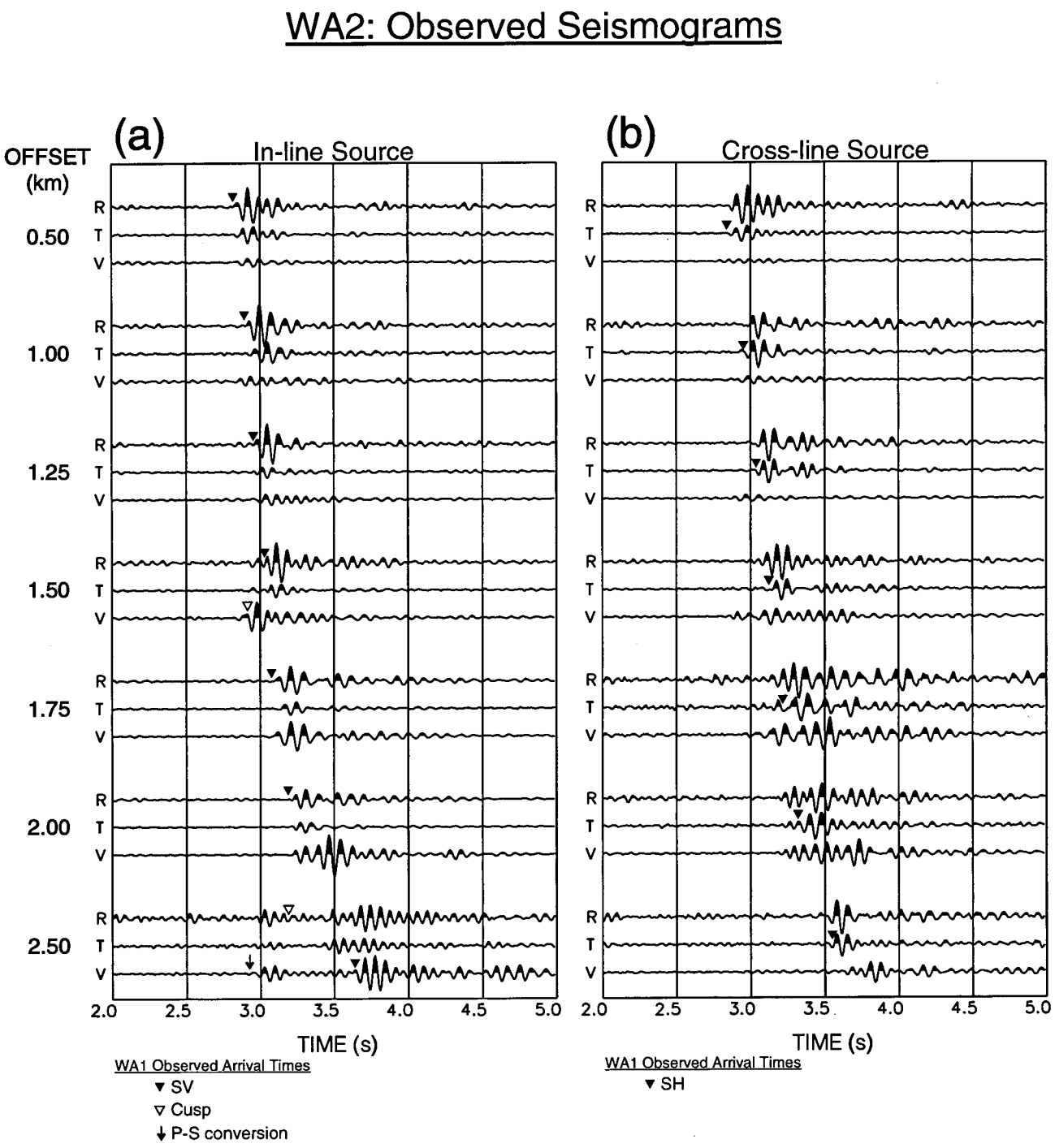

Figure 5.5: Three-component seismograms recorded by a geophone at the 1950-m level of walkaway WA2 for **(a)** in-line and **(b)** cross-line source orientations at Well 85. Seismograms are (V)ertical and horizontal (R)adial (in-line) and (T)ransverse (cross-line) and each three-component seismogram is normalized separately. The arrival times marked in Fig. 5.4 for WA1 are plotted for comparison.

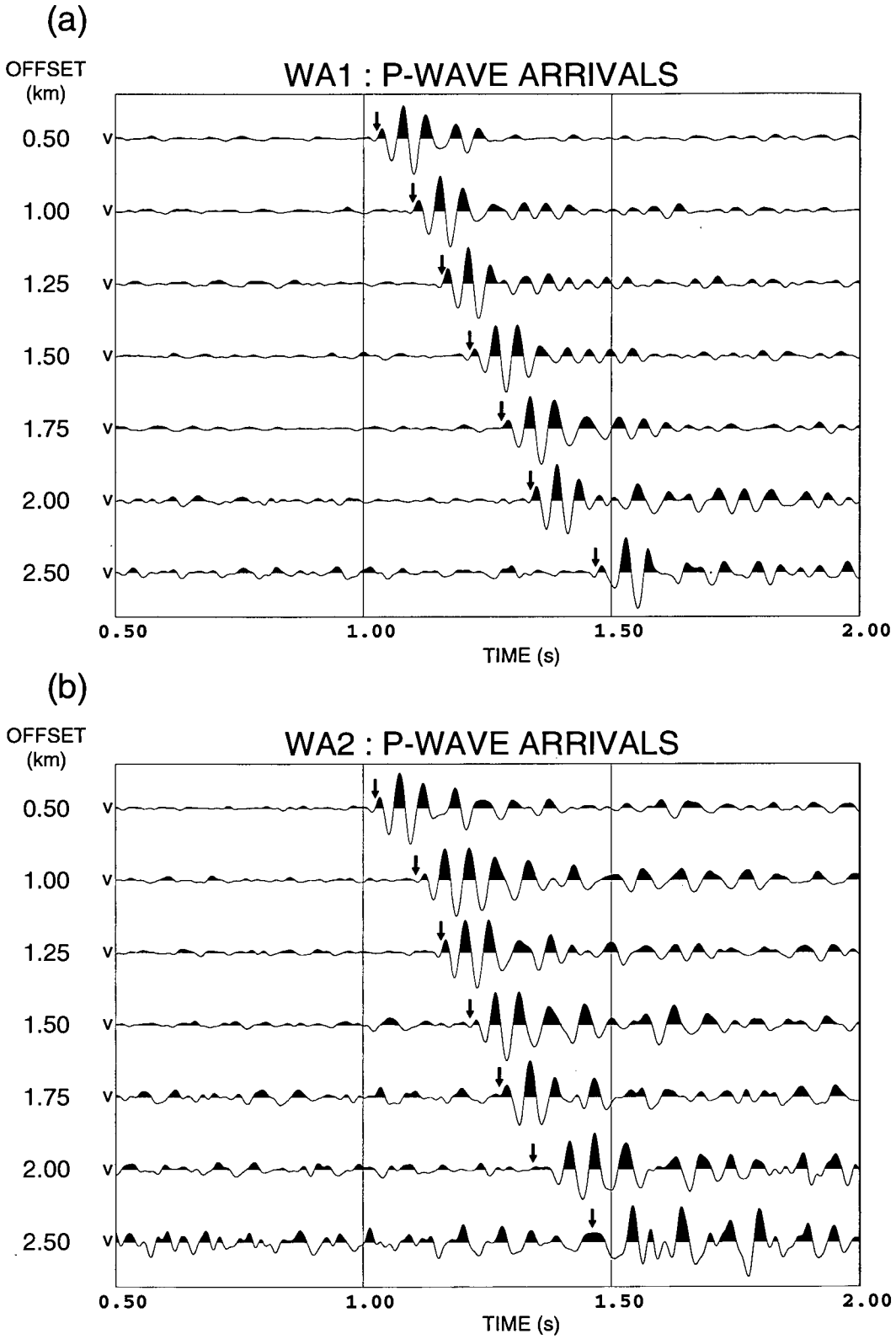

Figure 5.6: P-waves recorded by the vertical receiver component at a depth of 1950 m from in-line sources located on the surface 0.5 km to 2.5 km along two walkaway profiles **(a)** WA1 and **(b)** WA2 at Well 85. The solid arrows in (a) mark the arrival times of the main phase used to estimate the transverse isotropy, and are repeated in (b) as an indicator of the similarity in arrival times along the two profiles.

appear on the record sections of WA2 (as shown in Fig. 5.5), and on the other walkaways to the deeper geophone level at Well 85 and on all walkaways at Well 87. Similarly, the cross coupling between arrivals on the sagittal plane and the transverse horizontal direction that would not be expected in a flat-layered isotropic or azimuthally isotropic structure is observed on all walkaways. The arrival marked on the 2.5 km offset by an arrow is also observed on other walkaways and is confirmed by later modelling as a shear-wave originating from a P-S conversion at one of the larger impedance contrasts above the top of the clay interval (870 m). The P-wave arrivals I attempt to match are marked by solid arrows in Fig. 5.6a

The flowchart shown in Fig. 5.7 outlines the general sequence of models I use in attempting to match arrival times and amplitudes recorded by the 1950 m-level geophone in WA1. I match the field seismograms with synthetic seismograms by proceeding from isotropic models to TIV models to azimuthally anisotropic models. The next five main sections of this chapter deal successively with the five different types of model outlined in the right-hand side of Fig. 5.7. The synthetic seismograms are computed by a reflectivity technique (Booth and Crampin, 1983) using the ANISEIS full waveform modelling package (Taylor, 1987, 1990).

5.7 MODELLING USING A LAYERED ISOTROPIC MODEL

So that observed arrival times may be easily compared with arrivals on synthetic seismograms, I interactively pick shear- and P-wave arrival times observed along WA1 from the seismograms shown in Figures 5.4 and 5.6a, respectively. The arrival times are given in Table 5.1 and are indicated by triangle and arrow symbols in Figures 5.4 and 5.6. [Note that, as the source coordinate system was left-handed and the receiver system was right-handed, the polarity of the SV waveform in Fig. 5.4a recorded from the in-line source is opposite to the SH waveform in Fig. 5.4b recorded from the cross-line source. Consequently, first-break picks were made at the zero-crossings of the SV and SH arrivals just at the start of the first peak and trough, respectively.] The WA1 arrival times are repeated on the WA2 seismograms in Figures 5.5 and 5.6b and all the following synthetic seismograms to help identify relevant phases and easily judge the match of model arrival times to the observed times.

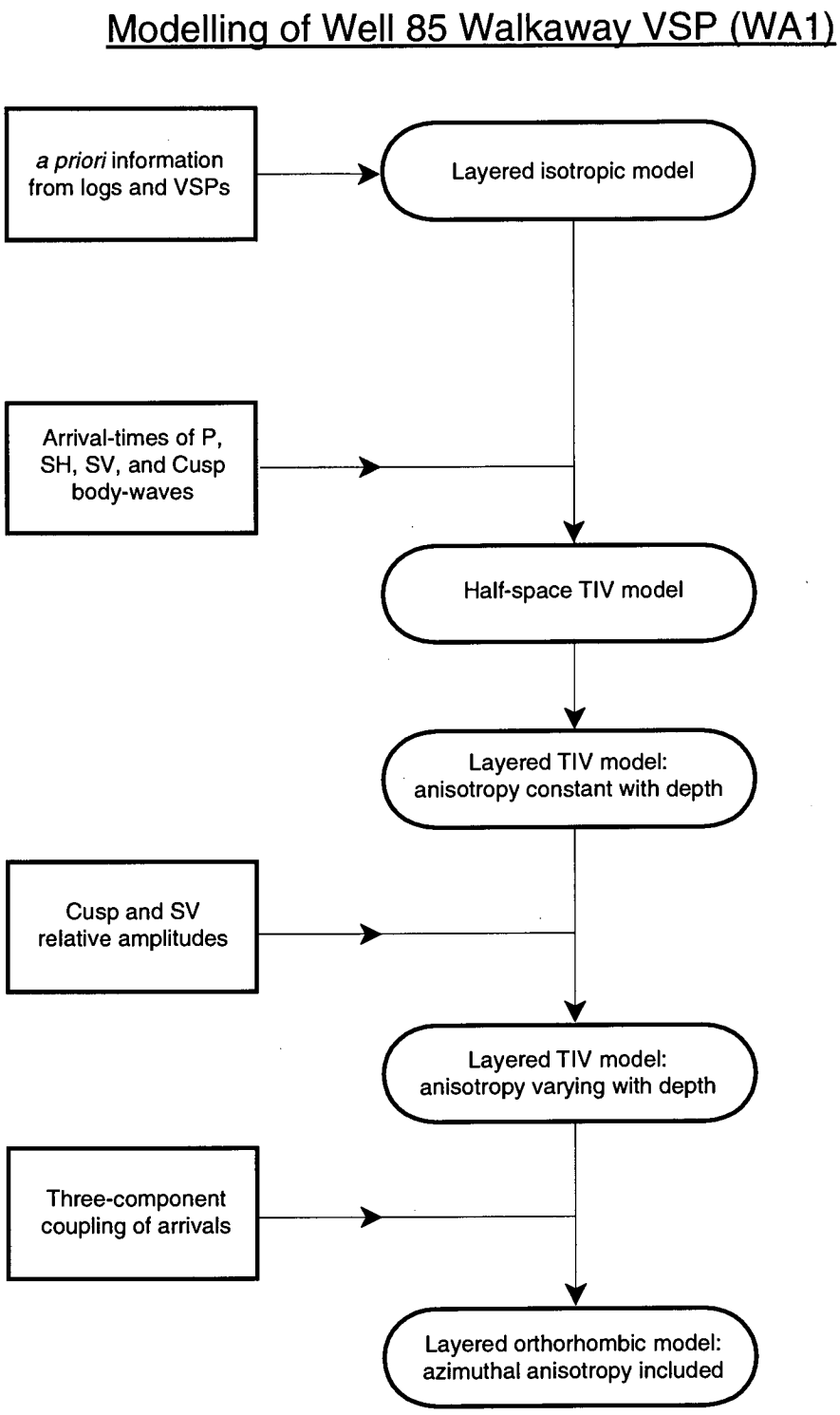

Figure 5.7: Flowchart outlining the sequence of models used to match arrival-times and amplitudes recorded by the 1950 m-deep geophone in WA1 at Well 85. Each square box on the left-hand side represents the inclusion of additional information to be matched by the successive model structures represented by the oblong boxes on the right-hand side.

Table 5.1: WA1 Main Body-phase Arrival Times at the 1950-m geophone inWell 85

Offset (km)	ARRIVAL TIME (ms)			
	P-phase	SH-phase	SV-phase	Cusp-phase
0.50	1023 ± 4	2838 ± 6	2815 ± 8	-
1.00	1104 ± 4	2956 ± 6	2892 ± 8	-
1.25	1158 ± 4	3046 ± 6	2954 ± 8	-
1.50	1212 ± 4	3123 ± 6	3027 ± 30	2912 ± 6
1.75	1277 ± 4	3212 ± 6	3077 ± 8	-
2.00	1335 ± 4	3315 ± 6	3181 ± 8	-
2.50	1462 ± 4	3550 ± 6	3642 ± 30	3212 ± 15

Figure 5.2a shows the isotropic velocity structure obtained from a near-offset VSP survey. The velocities in each layer are given in Table 4.1. Using these velocities I calculate synthetic seismograms for in-line and cross-line walkaway source orientations to the 1950 m-level geophone (shown in Figures 5.8 and 5.9). Density was derived using the P-wave velocities in Fig. 5.2a from the algorithm of Gardner, Gardner and Gregory (1974). There are large differences in arrival times between the field data in Fig. 5.4 and the synthetic seismograms in Figures 5.8 and 5.9. Although the model gives approximately correct arrival times for near-vertical propagation at the 0.5 km offset, the differences in traveltime increase with offset, reaching about 95 ms and 700 ms at the 2.5 km offset for P- and shear-wave arrivals, respectively. Since the geology is known to be extremely flat-lying and the velocity structure in the vertical direction known in detail, it is unlikely that an unknown lateral or vertical velocity variation causes the differences between model and observed arrival times. I suggest it is more likely that the extremely large differences imply horizontal velocities substantially greater than vertical velocities indicating some form of anisotropy. Comparing the main arrivals of WA2 in Fig. 5.5 with the picked WA1 arrivals times (plotted on the same figure), it can be seen that an equal velocity increase is apparent on the two walkaway VSPs. Such azimuthally invariant velocity variations are characteristics of TIV structures.

5.8 MODELLING USING A HALF-SPACE TIV MODEL

In the previous section a strong velocity increase for ray paths towards horizontal was implied which is characteristic of strong TIV structures. In this section, I attempt to match group-velocities of a TIV half-space to observed velocities approximated using straight-line ray paths between sources and receivers. I then calculate synthetic seismograms of the best-fitting half-space model to help with interpreting the observed seismograms.

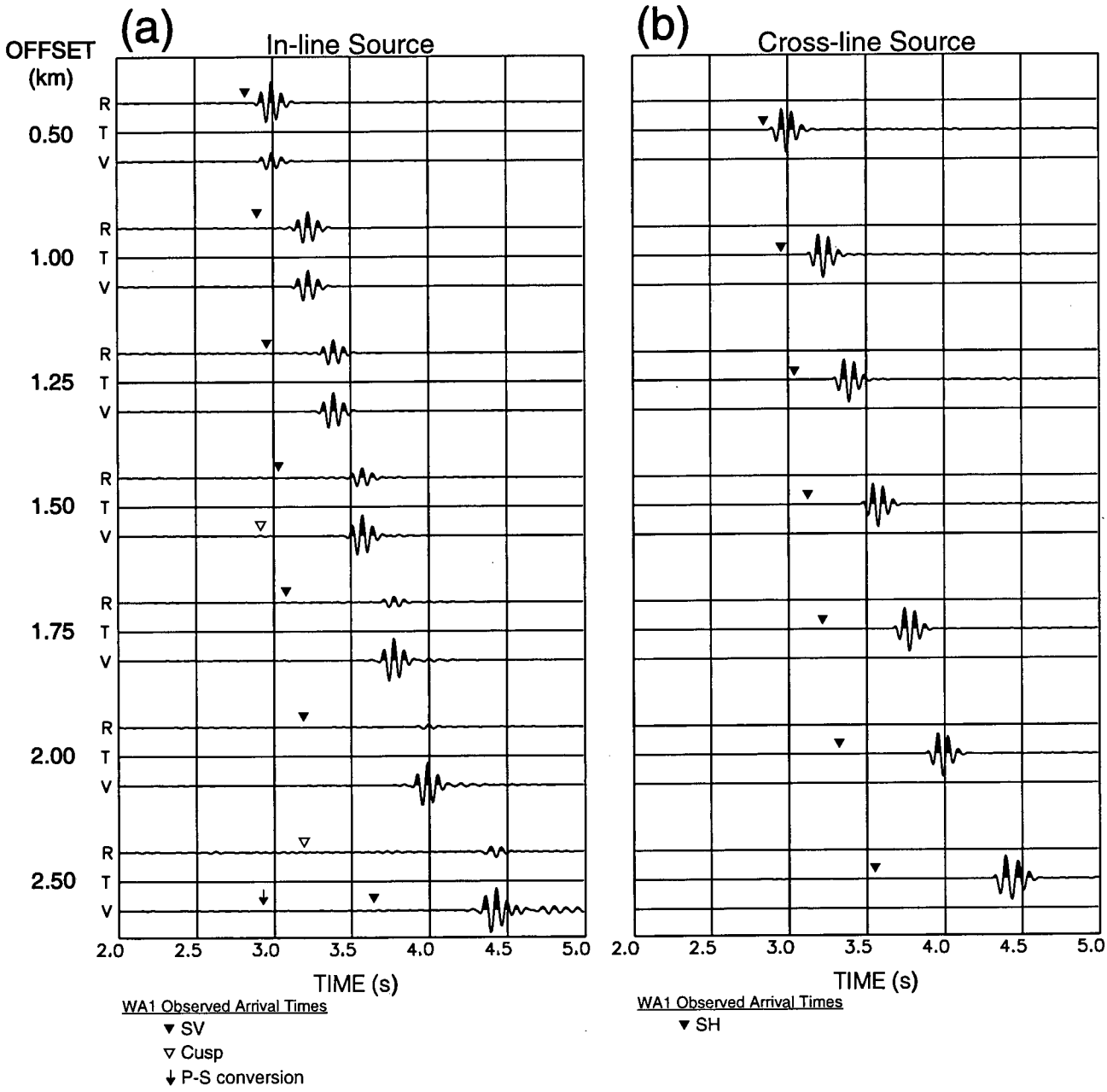

Figure 5.8: Three-component synthetic seismograms for a walkaway profile to a geophone at 1950-m depth through the multilayered isotropic structure in Fig. 5.2a for **(a)** in-line and **(b)** cross-line source orientations. Notation as in Figure 5.4 : the triangle and arrow symbols mark the arrival times of the main shear-wave phases in Figure 5.4.

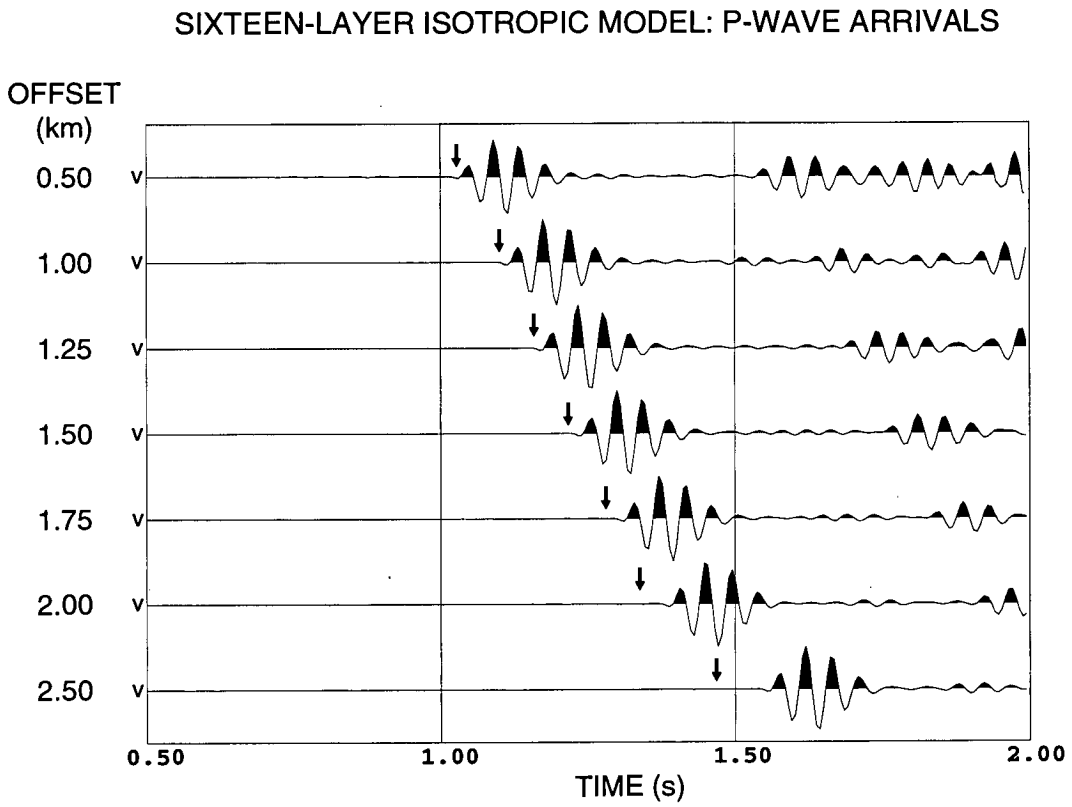

Figure 5.9: P-wave arrivals on the vertical component of synthetic seismograms for a walkaway profile to a geophone at 1950-m depth for propgation through the multilayered isotropic structure in Fig.5.2a. The solid arrows, used to estimate the transverse isotropy, indicate the arrival times of the P-waves in the field seismograms of Figure 5.6a.

5.8.1 Straight-line Approximation to Velocities

Firstly, I use ray tracing to establish if a straight-line is a reasonable approximation to the walkaway ray paths. Figure 5.2b shows shear-wave ray paths through the isotropic velocity structure in Fig. 5.2a for the seven walkaway offsets of WA1. The ray tracing shows that, except for the 2.5 km offset, the ray paths are quite close to straight lines, particularly through the clay from 870 m to 1.9 km. Although straight-lines to the geophone are different from the ray paths in Fig. 5.2b, the deviations of the ray paths are comparatively small, and source to geophone straight lines are likely to be a good first order approximation to the true ray paths. This suggests that a simple half-space TIV model may provide an approximate first order match to the arrival times observed in Figures 5.4 and 5.6.

Figure 5.10 shows the approximated qP-, qSV- and SH-wave (group) velocity variations derived from the arrival-time picks in Table 5.1. The velocities are plotted against incidence angle assuming straight-line ray paths for walkaway WA1. A pronounced increase of velocity with ray path incidence angle is indicated. Also, an increasing separation between the SH and SV velocities can be seen - by itself an indicator of possible TIV. However, approximating the curved ray paths by (shorter) straight lines will introduce an increase to the calculated velocity which increases with incidence angle.

To test the effect of the approximation, I calculate apparent velocity increases for an isotropic sixteen-layer model based on the velocities in Fig. 5.2a. These velocity increases are plotted as dashed lines in Fig. 5.10 and indicate that the increase introduced by the approximation is likely to be relatively small and is not the cause of the observed large increases in velocity.

Before determining the half-space TIV model which best matches the observed straight-line velocities I first describe the parameterization which I adopt for defining TIV materials.

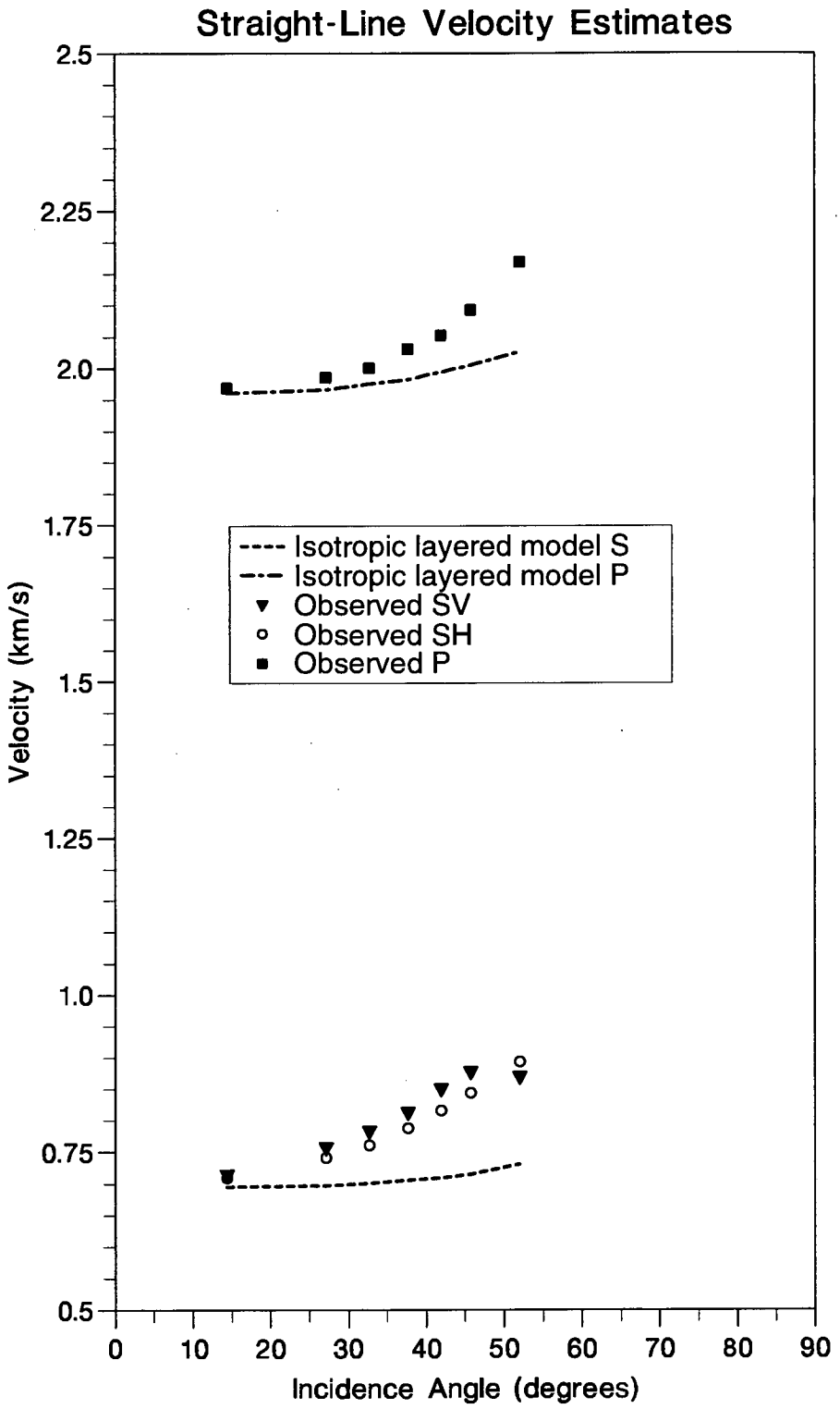

Figure 5.10: Estimates of group-velocity from the observed arrival times of Figures 5.4 and 5.6 (given in Table 5.1) using a straight-line approximation for the raypaths. A large increase in velocity with incidence angle of the straight-line raypath is observed. Dashed lines show an apparent increase caused by approximating raypaths with straight lines for the sixteen-layer isotropic model shown in Fig. 5.2a.

5.8.2 TIV Model Parameterization

Defining a TIV material requires assigning a material density, ρ, and five independent elastic constants of the stiffness tensor (Eqn. 5-1). It is straightforward to show, using Equations 5-2, that four of the five elastic constants are directly related to the horizontal and vertical velocities of the material. [Note that in TIV media, the group and phase velocities are equal along horizontal and vertical propagation directions, therefore the equations are identical for either phase- or group-velocity.] The relationships are:

$$C_{33}=\rho\, V_{P_{vert}}^2 \; ; \tag{5-3a}$$

$$C_{11}=\rho\, V_{P_{horz}}^2 \; ; \tag{5-3b}$$

$$C_{66}=\rho\, V_{SH_{horz}}^2 \; ; \tag{5-3c}$$

and

$$C_{44}=\rho\, V_{S_{vert}}^2 \; ; \tag{5-3d}$$

where the subscripts *vert* and *horz* refer to vertical and horizontal propagation, respectively, and $V_{S_{vert}}$ in Eqn. 5-3d is the shear-wave velocity along the vertical symmetry axis. No qualification is required for the polarization of the shear-wave in the vertical direction because along the symmetry axis the velocities of the two shear-waves are equal and any transverse polarization is possible (Crampin, 1986).

From Eqn. 5-2b, the fifth elastic constant, C_{13}, may be defined using the qSV phase-velocity at an angle of 45° to the symmetry axis, giving:

$$C_{13}=-C_{44}+\left[4\rho^2(V_{SV45})^4-2\rho(V_{SV45})^2(C_{11}+C_{33}+2C_{44})+(C_{11}+C_{44})(C_{33}+C_{44})\right]^{1/2} \; ; \tag{5-3e}$$

where V_{SV45} is the qSV phase-velocity at 45° to the vertical symmetry axis. [Note that this is close to the maximum qSV phase-velocity due to the approximate sin4θ nature of the qSV phase-velocity surface (Crampin, 1977).] The C_{33} and C_{44} constants of each TIV layer used to model the walkaway VSP at Well 85 are constrained by the vertical P- and shear-wave velocities calculated from the arrival times of the near-offset VSP in the same well (Chapter Three). This leaves three elastic constants, C_{11}, C_{66} and C_{13}, which may be varied, subject to stability constraints (Helbig, 1994), to match the observations. However, describing each layer by the three elastic constants

directly gives no immediate information regarding the velocity variations in the layer. Instead of defining the elastic constants directly, I define them indirectly using the following percentage measures of anisotropy:

$$\Delta_P = 100 \times \frac{V_{P_{horz}} - V_{P_{vert}}}{V_{P_{horz}}} ; \tag{5-4a}$$

$$\Delta_{SH} = 100 \times \frac{V_{SH_{horz}} - V_{S_{vert}}}{V_{SH_{horz}}} ; \tag{5-4b}$$

and

$$\Delta_{SV45} = 100 \times \frac{V_{SV45} - V_{S_{vert}}}{V_{SV45}} . \tag{5-4c}$$

These definitions using percentage anisotropy allow an immediate intuitive understanding of the velocity variations in the particular TIV model. Additionally, when further complexity is added by the inclusion of *a priori* information, the use of percentage anisotropy as a definition is an efficient way to produce models which remain simple in terms of the overall anisotropic structure. An example of such *a priori* information is velocity layering determined from near-offset VSPs. Incorporating such layering into a TIV model greatly increases the number of variable elastic constants in the model. By using percentage anisotropy to define the layers, however, it is straightforward to create layered TIV models which are relatively simple in terms of anisotropy by assigning common anisotropic properties over many layers. For example, one may define a five-layer model with equal qP-anisotropy in all layers (where each layer is defined by a different vertical-velocity). This simplification is particularly useful for modelling thick sequences of similar rock type which display a regular vertical-velocity gradient, such as the 1.2 km of clay which overlies the walkaway receiver level in the walkaway VSPs studied in this chapter.

5.8.3 Determination of Best-fit Model

A grid search is made for the halfspace TIV model with group velocities closest to the observed straight-line velocities in Fig. 5.10. The elastic constants, C_{33} and C_{44}, of all half-space TIV models are constrained by the average vertical-velocities down to the 1950 m-level as measured in a near-offset VSP (Chapter Three). The average P- and

shear-wave vertical-velocities are 1.97 km/s and 0.70 km/s, respectively. I calculate SH velocities for 28 models with Δ_{SH} varying by 1% between 25% and 52%. The qP and qSV velocities depend on both the Δ_{SV45} and Δ_P parameters, therefore, I calculate qP and qSV velocities for models over a grid of variations in the two parameters. The grid is formed by varying Δ_P between 11% and 29% in 2% increments and Δ_{SV45} between 18% and 34% in 2% increments, giving a total of 90 models.

To perform the search I first determine the phase-velocities of each TIV model from computed eigenvalue solutions to the Kelvin-Christoffel equation (Crampin, 1981) over a range of propagation vectors with a 0.5° spacing in the vertical plane. Next, I compute the corresponding grid of group velocities and group-velocity vectors from the phase velocities using the envelope of wave fronts method (Musgrave, 1970). I then compute the group-velocities for propagation angles equal to the incidence angles in Fig. 5.10 by linear interpolation between the two group-velocity vectors closest to each desired incidence angle. Finally, I calculate a least-squares misfit, M_V, between model (V_{model}) and observed (V_{obs}) velocities for each model using:

$$M_V = \sum_{i=1}^{N} \frac{(V_{obs} - V_{model})^2}{(\delta_{obs} + \delta_{model})^2} \; ; \qquad (5\text{-}5)$$

where N is the number of observations and δ_{obs} and δ_{model} represent error estimates of the observed and model velocity values, respectively. δ_{obs} is calculated from the arrival time errors given in Table 5.1 and δ_{model} is set at 5 m/s, which is equal to one-quarter of the maximum difference between any two velocities used in the group-velocity interpolation for all models.

The misfit of the SH model velocities are considered independently due to the complete decoupling of the SH-wave at oblique incidence angles which exists in all TIV models. The SH velocity misfit values (with N=7) are shown in Fig. 5.11a and shows a well defined minimum, indicating a best-fitting model with 38% SH-anisotropy. Because the velocity variations of the qP and qSV arrivals at oblique incidence angles in TIV media are mutually dependent on the other two anisotropy parameters, Δ_P and Δ_{SV45}, I search for the best estimate of Δ_P and Δ_{SV45} by calculating the total misfit of all qP and qSV arrivals (N=14). This combined misfit function is shown in Fig. 5.11b, and indicates that the best-fitting model has around

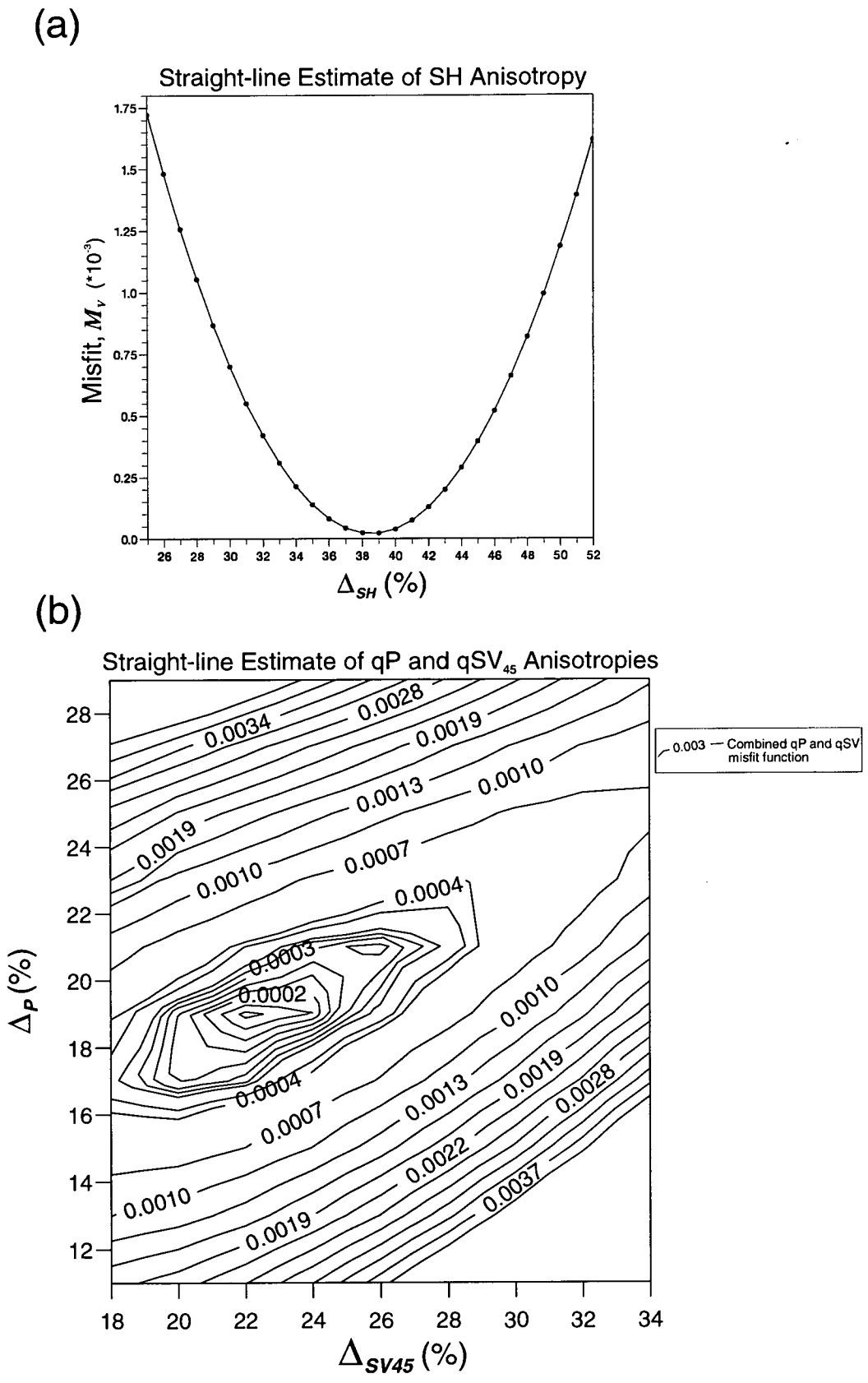

Figure 5.11: Estimate of percentage anisotropy using a least-squares misfit function (M_v) between a simple half-space model velocities and straight-line observed velocities for **(a)** SH and **(b)** P and SV body-phases in TIV structures. The qP and qSV phases in TIV media are coupled and therefore estimated together in (b).

19% qP and 22% qSV_{45} anisotropy. [Note that for clarity of display the contour step is increased in the areas distant from the minimum.]

The group-velocity surfaces of the half-space with the best-fitting anisotropy parameters described above are shown in Fig. 5.12 along with the observed velocities. A close match between observed and model velocities is achieved, with the most significant feature of the model velocity surfaces being the presence of large cusps near the middle of the qSV surface. This is the first indication that the anomalous arrivals in the observed seismograms in Fig. 5.4 may be cusp arrivals.

The model velocities in Fig. 5.12 fit the observations well. However, due to the ray path approximations in the velocity calculations, it is unlikely that seismograms calculated using the half-space model will closely match the features of the observed seismograms in Fig. 5.4. Nevertheless, inspecting synthetic seismograms for propagation through a simple half-space may help the interpretation of the complicated arrivals observed in Fig. 5.4a. Therefore, in the next section I calculate full waveform synthetic seismograms to compare with the observations.

5.8.4 Seismograms

Full waveform synthetic seismograms for a point source were calculated using the best-fit half-space model in Fig. 5.12 which has the three anisotropy parameters, Δ_P, Δ_{SH} and Δ_{SV45} equal to 19%, 38% and 22%, respectively. The source-receiver geometry is the same as WA1. The synthetic seismograms are plotted in Fig. 5.13.

The SH arrivals times in Fig. 5.13b show a much closer match to the observed arrival times than those from the the isotropic model, however, there is still a deviation between the arrival times which increases with offset to about 80 ms at 2.5 km. The qSV arrival times in Fig. 5.13a, although significantly better than those obtained from the isotropic model, are still poorly matched. To better understand the different arrivals present in the synthetic seismograms of Fig. 5.13a, I plot synthetic seismograms in Fig. 5.14 recorded from an in-line source at offsets every 100 m from 1.0 to 2.5 km. The form of the wave surface can be easily seen in Fig. 5.14 and confirms that all fast arrivals recorded on the synthetics in Fig. 5.13a are cuspidal arrivals, although the cuspidal arrivals at the 1.75 km and 2.0 km offsets in Fig. 5.13a

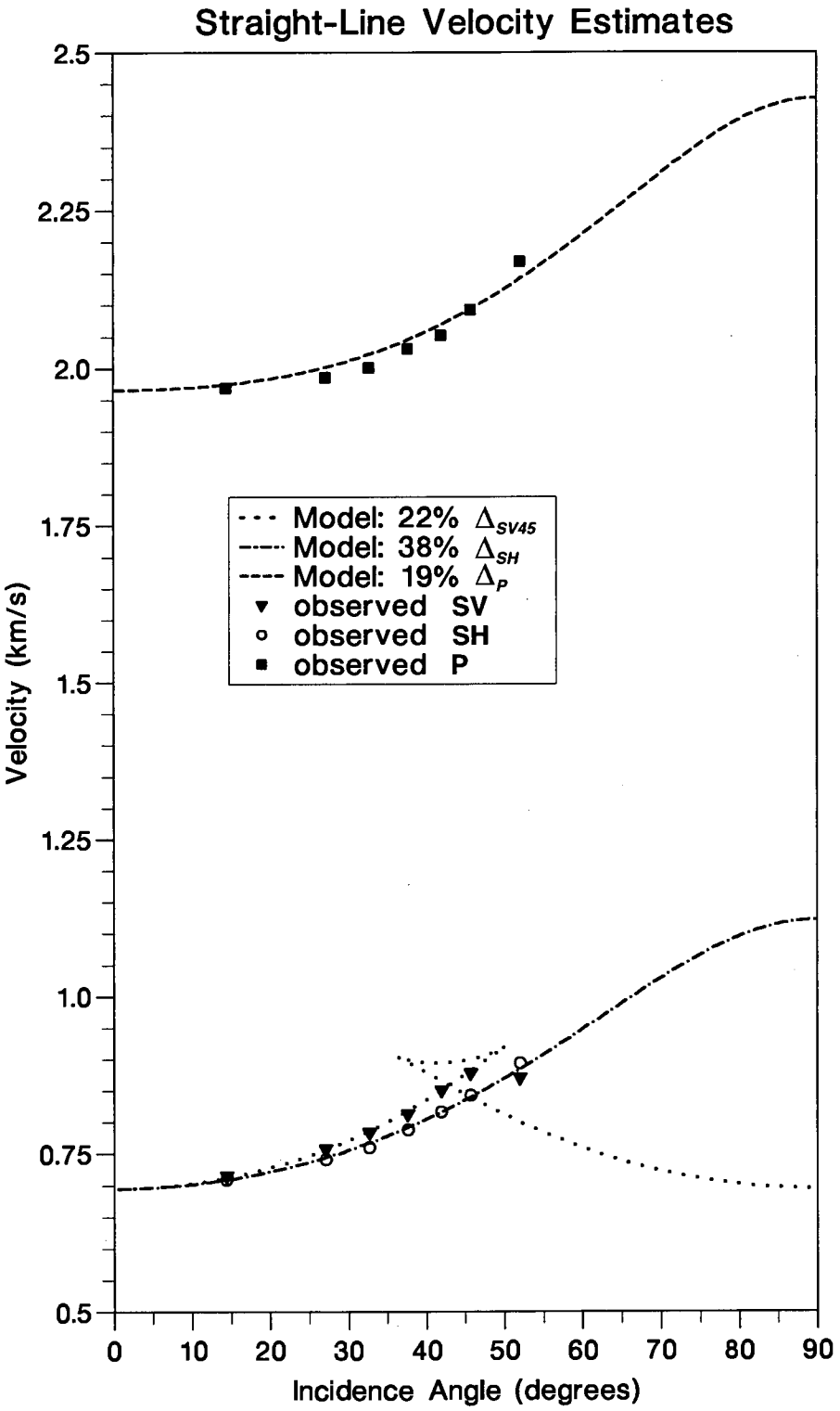

Figure 5.12: Group velocities of the best-fitting model in Fig. 5.11 estimated from Figures 5.4 and 5.6a assuming straight-line raypaths. The solid squares, solid triangles, and open circles mark the straight-line velocity estimates.

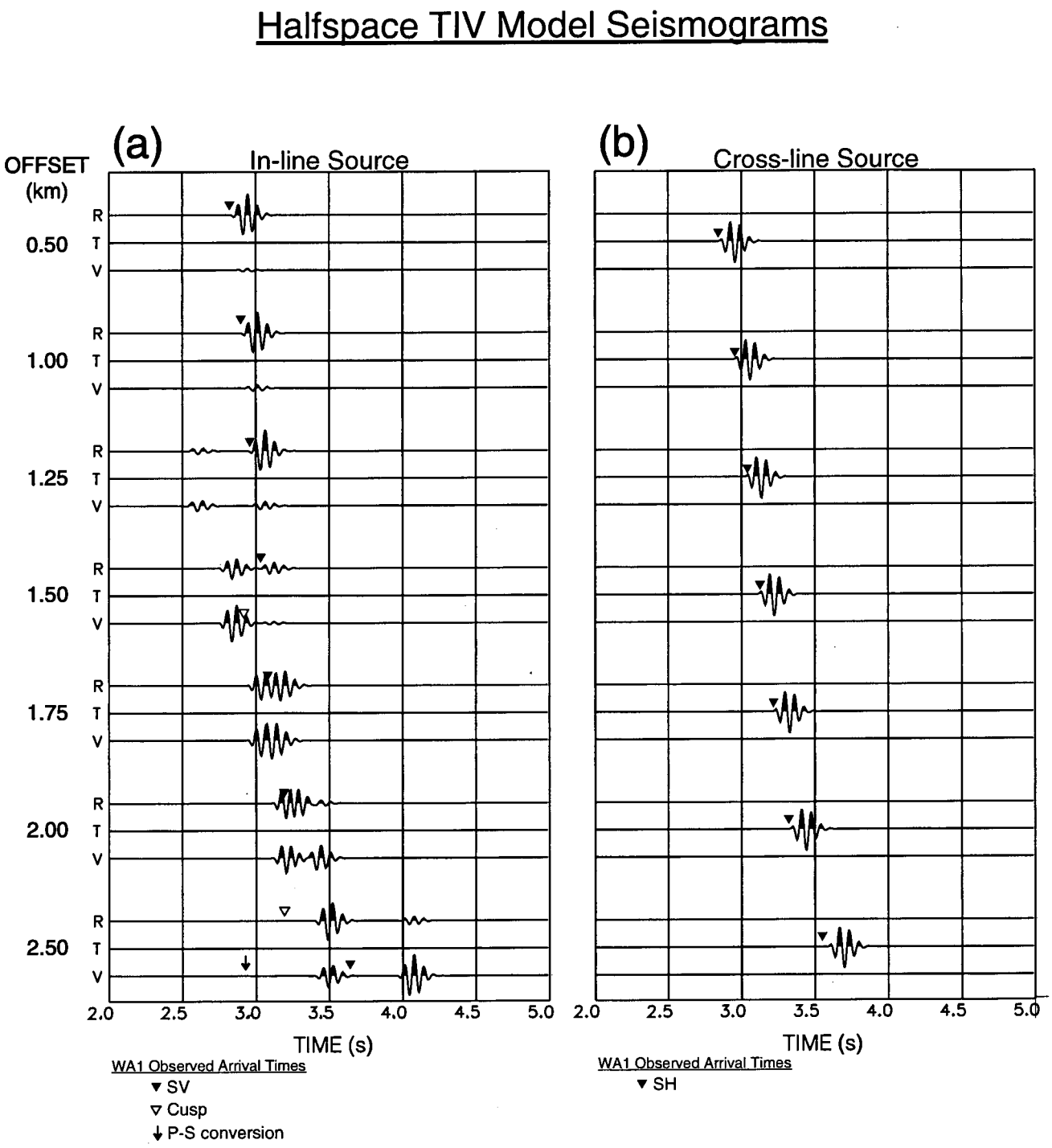

Figure 5.13: Three-component synthetic seismograms for a walkaway profile to a geophone at 1950-m depth through a halfspace TIV structure with velocities as shown in Fig. 5.12 for **(a)** in-line and **(b)** cross-line source orientations. Notation as in Figure 5.4 : the triangle and arrow symbols mark the arrival times of the main shear-wave phases in Figure 5.4.

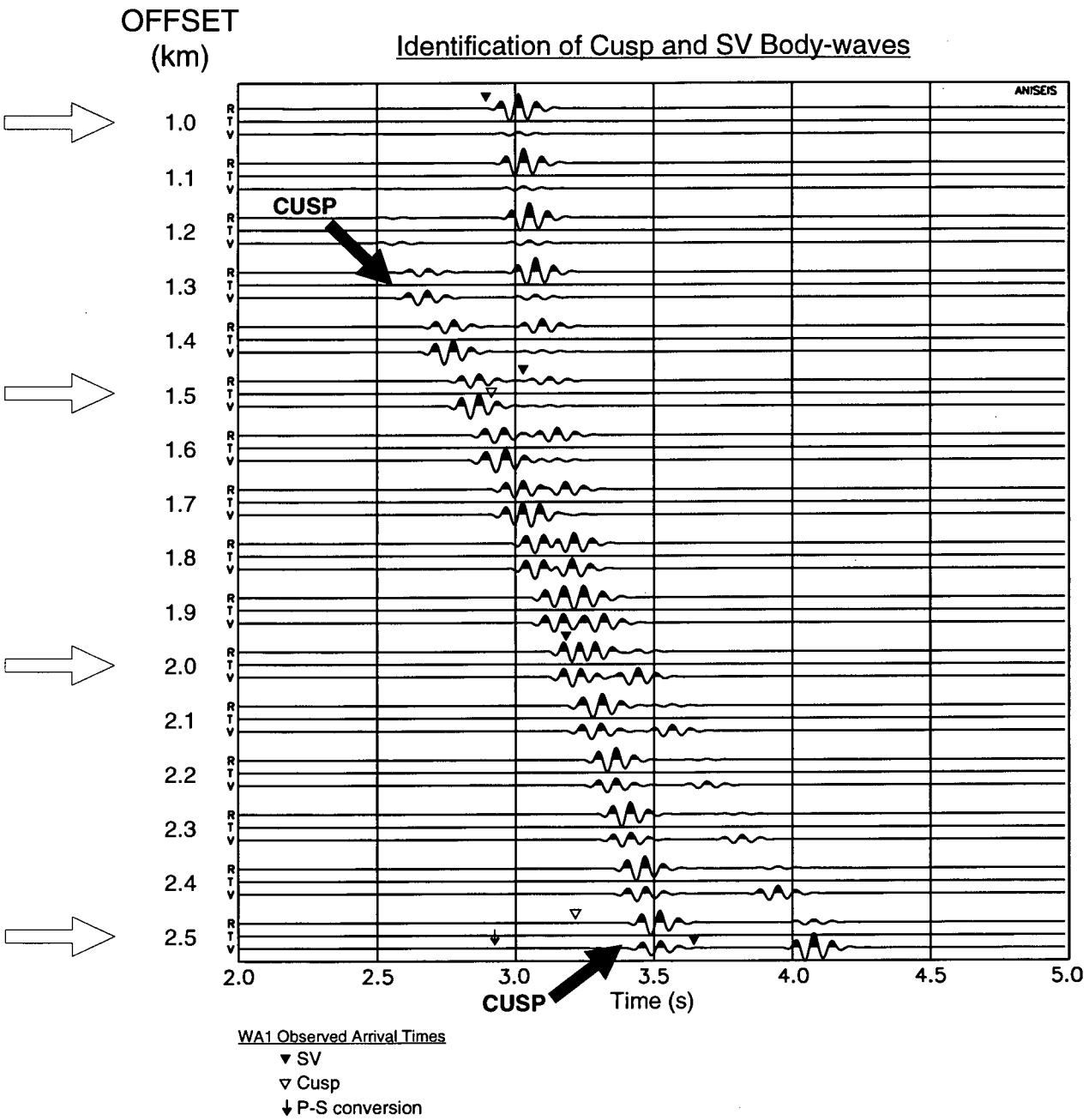

Figure 5.14: Synthetic seismograms modelling WA1 from 1.0 km-offset to 2.5 km-offset at 100 m intervals, through the best TIV half-space model (as in Figure 5.12). Open arrows in the left margin indicate offsets for which there are field observations.

are not sufficiently separated in time from the main shear-wave arrivals to be clearly identified.

Even though the arrival times are not satisfactorily matched, it is useful to compare qualitatively the synthetic and observed seismograms (Figures 5.4a and 5.13a) in order to note some similarities. The main similarities between are:

(i) the multiple phases in the waveforms at the 1.5 km and 2.5 km offsets, and;

(ii) the complicated phases of apparently superimposed arrivals in the waveforms at 1.75 km and 2.0 km offsets.

Similarity (i) suggests that the anomalously fast arrivals on the field seismograms, marked by open triangles in Fig. 5.4a at 1.5 km and 2.5 km offsets, are cuspidal arrivals. It is arrival times and amplitudes of these cuspidal arrivals, in addition to the principal body-wave arrivals, which I attempt to match in the following sections. At the intermediate offsets of 1.75 km and 2.0 km, the arrivals on the field seismograms in Fig. 5.4a appear to be a superposition of phases originating from near the centre of the triplication area. Thus resulting in a long complicated recorded arrival. As a result, it is impossible to pick accurately the separate later arrival times of the different phases at these offsets. Therefore in the later modelling, I use the arrival times at the beginning of the complicated wavelets. These arrival times are already picked and displayed on the field seismograms in Fig. 5.4a.

The best-fitting half-space TIV model found in this section provides a good starting point for constructing layered TIV models which conform to the geological structure indicated by the vertical velocity variations in Fig. 5.2a. In the next section I attempt to match the observations using layered TIV models with anisotropy equal in all layers.

5.9 MODELLING USING A LAYERED TIV MODEL: CONSTANT ANISOTROPY WITH DEPTH

In the previous section I determined the TIV half-space model which best matched observed velocities along ray paths approximated by straight lines. This model was found to give a close first-order match to the observed seismograms. In this section I attempt to improve the fit of the synthetic seismograms by modelling with layered TIV structures. Layered models with TIV arbitrarily defined in each layer are, in terms of anisotropy, complex structures with many free parameters (elastic constants). I reduce the complexity of the layered models by holding anisotropy constant through the layers. The models are based on a sixteen layer velocity structure derived from the velocities shown in Fig. 5.2a.

5.9.1 Least-Squares Fit of Model Parameters

Full waveform synthetic seismograms are calculated for models with anisotropy parameters, Δ_P, Δ_{SH} and Δ_{SV45}, constant through all the layers. Δ_P is varied from 11% to 27%, Δ_{SV45} from 14% to 30%, and Δ_{SH} from 30% to 46%. The discretization interval of the parameters between models is 2%, giving a total of nine models used for matching the independent SH arrivals, and 81 for matching the coupled qP and qSV arrivals. The elastic constants, C_{33} and C_{44}, of each model layer are defined by the velocities which were measured along near vertical ray paths in a near-offset VSP (Fig. 5.2a). The wavelet shapes in the synthetic seismograms were interactively matched to the observed P- and shear-wave signals in Figures 5.4b and 5.6a.

The arrival times of all relevant phases on the synthetic seismograms, including cusps, are interactively picked for each model. The misfit between the observed arrival times, τ_{obs}, (given in Table 5.1) and the model arrival times, τ_{model}, is then calculated using:

$$M_\tau = \sum_{i=1}^{N} \frac{(\tau_{obs} - \tau_{model})^2}{(\delta_{obs} + \delta_{model})^2} \; ; \qquad (5\text{-}6)$$

where N is the number of observations and δ_{obs} and δ_{model} represent the error estimates of the observed and model arrival times, respectively. δ_{obs} is taken from the arrival-time errors given in Table 5.1 and δ_{model} is set at 3 ms for all arrivals except the cusp arrivals which were set at 9 ms and 15 ms for the 1.5 km and 2.5 km offsets, respectively.

The SH misfit as a function of Δ_{SH} is shown in Fig. 5.15. It indicates a minimum close to Δ_{SH}=36%, which is only 2% from the half-space estimate. Separate misfits for the qP, qSV and cusp phases, as functions of Δ_P and Δ_{SV45}, are shown in Figures 5.16a, 5.16b and 5.16c, respectively. The qP misfit in Fig. 5.16a varies with Δ_{SV45} and Δ_P. [The Δ_{SV45} parameter controls the sin4θ nature of the qP phase-velocity surface.] This means that the qP arrivals on their own do not constrain either the qP or qSV_{45} values of anisotropy. The qSV and cusp misfit functions in Figures 5.16b and 516c are relatively independent of Δ_P and have minima for Δ_{SV45} between 18% and 20% for all values of Δ_P. Figure 5.16d show that the total misfit of all three arrivals converges to a solution near a model with Δ_P=15% and Δ_{SV45}=20%.

5.9.2 Seismograms of Best-fitting Model

The best-fitting sixteen-layer TIV model with constant anisotropy through all layers has parameters Δ_P=15%, Δ_{SV45}=20%, and Δ_{SH}=36%. I now check whether the synthetic seismograms corresponding to the best model are a satisfactory match to the observed seismograms. Synthetic seismograms corresponding to the best-fitting constant anisotropy model are shown in Figures 5.17 and 5.18 for P- and shear-wave arrivals, respectively. Figure 5.17 shows that a satisfactory fit has been made to the P-wave arrival times. The improvement over the isotropic model is seen by comparing with Fig. 5.9.

The shear-wave arrivals in Figures 5.18a and 5.18b are from in-line and cross-line source orientations, respectively. The triangle symbols mark the arrival times observed in WA1. It can be seen that a satisfactory fit has been achieved to the SH and qSV arrival times (marked by solid triangles) and the large improvement over the isotropic model may be seen by comparing with Fig. 5.8.

The separate cusp arrivals can be identified in Fig. 5.18a at about 2.9 s for the 1.5 km offset and 3.4 s for 2.5 km offset. The observed cusp arrival-time is closely

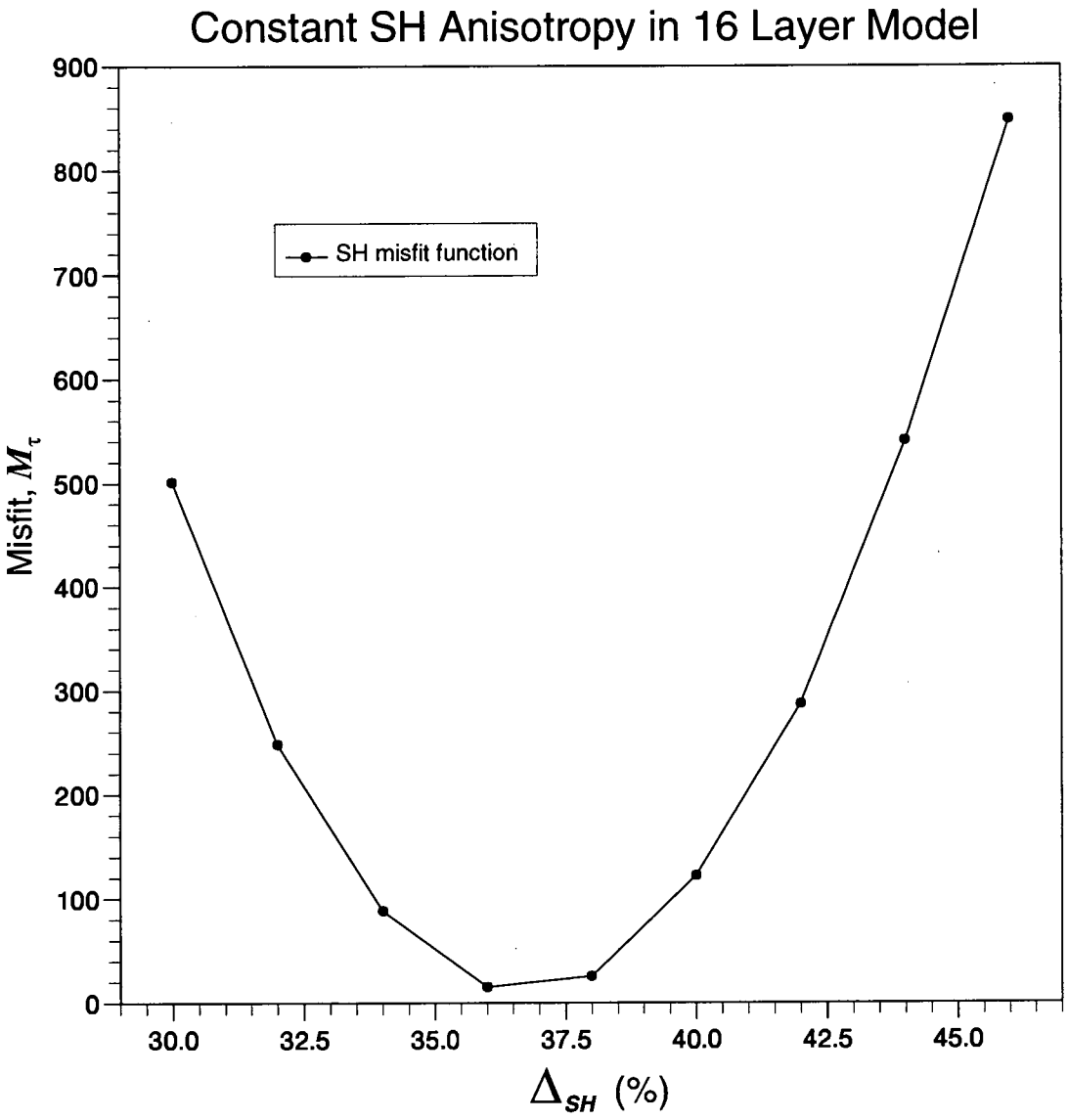

Figure 5.15: Least-squares misfit (M_τ) between observed and model arrival times of the SH body-wave for models with different maximum SH velocity anisotropy. Each model has sixteen layers and equal SH anisotropy (Δ_{SH})in all layers.

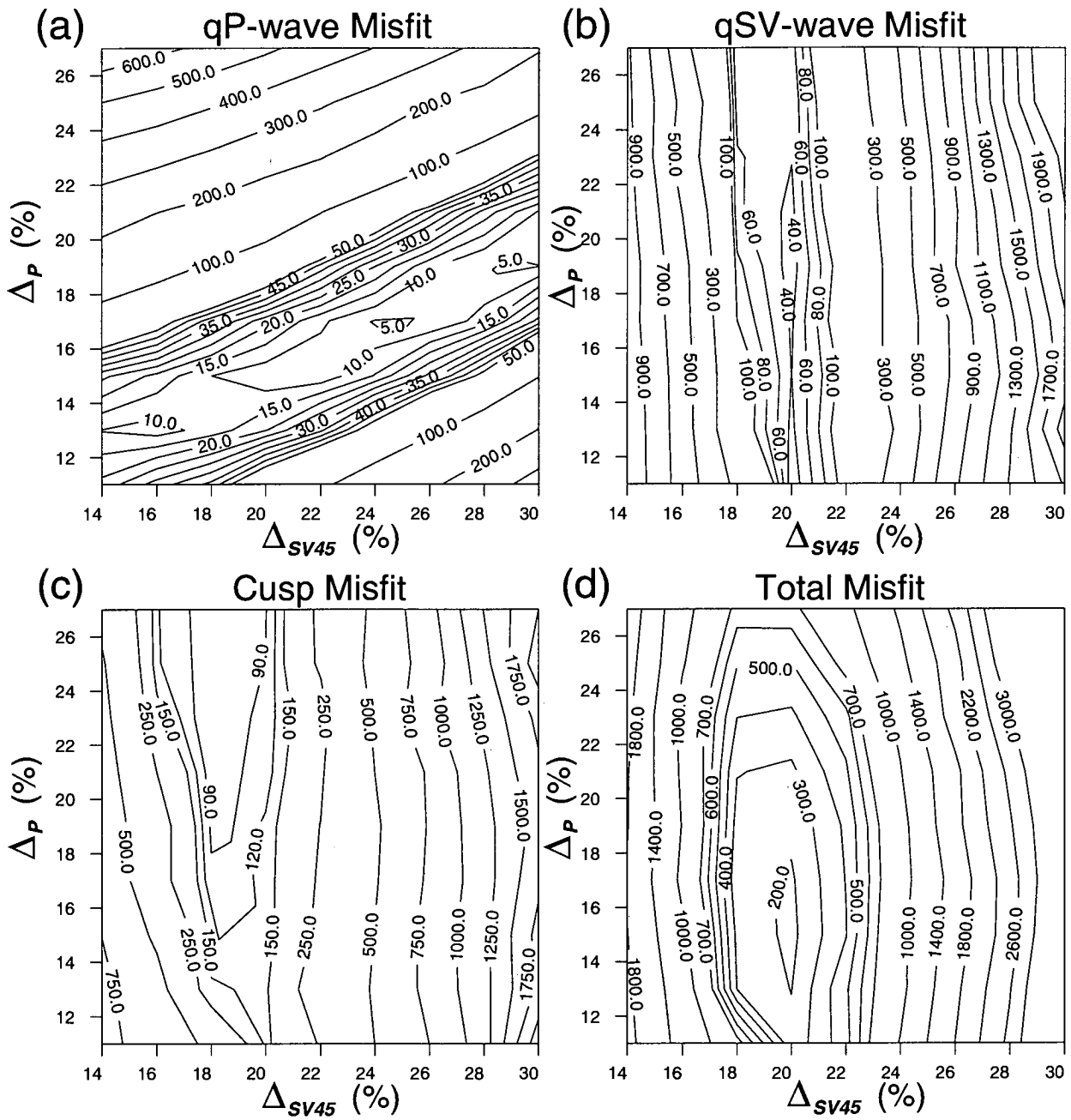

Figure 5.16: Least-squares misfit (M_τ) between observed and model arrival times for **(a)** P **(b)** SV and **(c)** cusp body-wave phases. The misfit functions in (a), (b) and (c) are summed to give a total misfit function shown in **(d)**. Each model comprises sixteen layers with equal qP and qSV_{45} anisotropy in all layers.

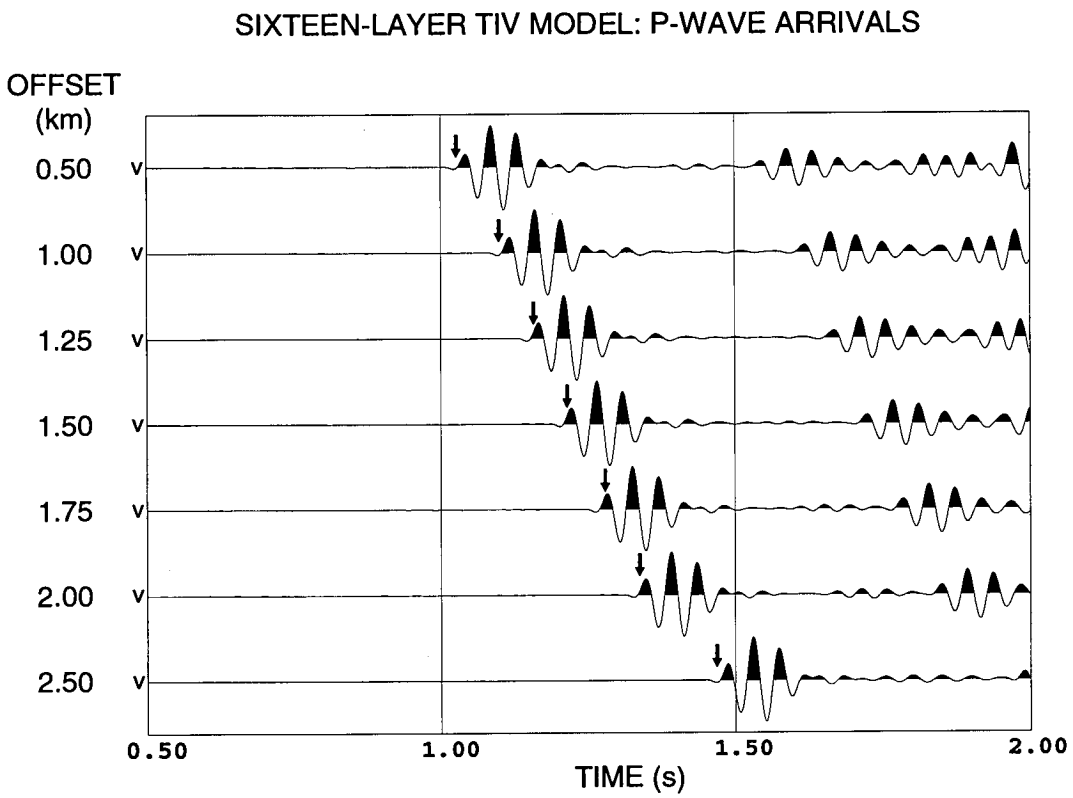

Figure 5.17: P-wave arrivals on the vertical component synthetic seismograms for a walkaway profile to a geophone at 1950 m depth through the best-fitting sixteen-layer TIV model in Fig. 5.16d. The solid arrows, used to estimate the transverse isotropy, indicate the arrival times of the P-waves in the field seismograms of Figure 5.6a.

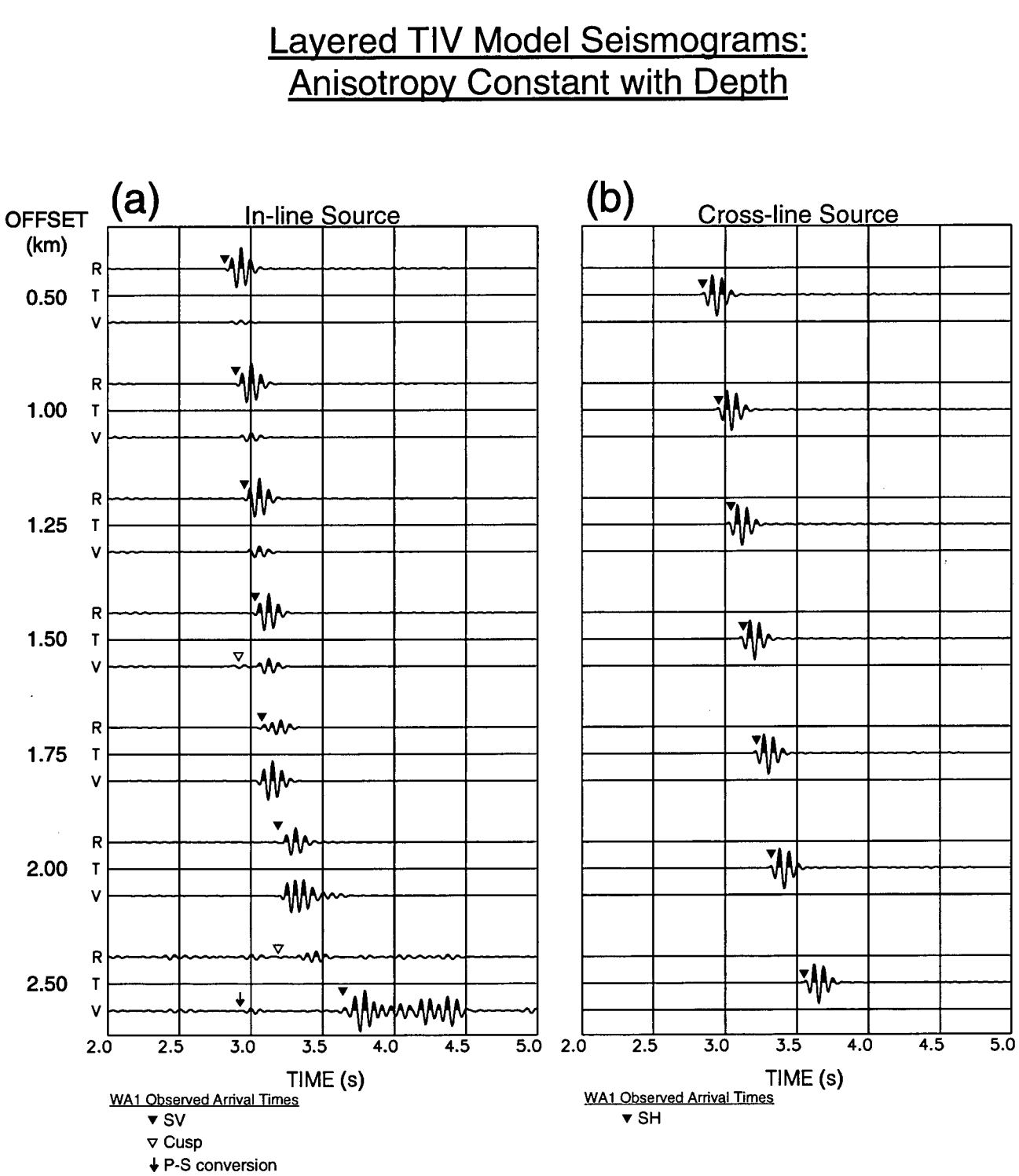

Figure 5.18: Three-component synthetic seismograms for a walkaway profile to a geophone at 1950-m depth through the best-fitting sixteen-layer TIV model with constant maximum velocity anisotropy (Δ_P=15%, Δ_{SV45}=20% and Δ_{SH}=36%) in all layers for **(a)** in-line and **(b)** cross-line source orientations. Notation as in Figure 5.4 : the triangle and arrow symbols mark the arrival times of the main shear-wave phases in Figure 5.4.

matched at 1.5 km, though the 2.5 km cusp arrival-time is less well matched and arrives about 200 ms later than the observed phase.

The match of observed arrival times is extremely good in Figures 5.18a and 5.18b and the interpretation of the anomalous arrivals as cusps is reinforced. However, the match of the cusp amplitude at 1.5 km is far from satisfactory. The amplitude of the cusp relative to the slower main qSV arrival is much larger in the observations than in the synthetic seismograms (Figures 5.4a and 5.18a). In the next section I attempt to improve the amplitude of the modelled cusp arrivals.

5.10 MODELLING USING A LAYERED TIV MODEL: ANISOTROPY VARYING WITH DEPTH

When matching geophysical data with predications from hypothetical models, it is usual to try to find the simplest possible model which gives a satisfactory match to the data. In the previous section, after the inclusion of *a priori* velocity information into the model, I attempted to match the walkaway seismograms using TIV models which were as simple as possible given my TIV parameterization. These models were simple because anisotropy parameters were constant with depth. However, the best-fitting model to the arrival times does not accurately match the observed cusp amplitudes. Any attempt to improve the fit of the cusp amplitudes requires an increase in complexity of the anisotropic structure in the models, this may be justifiably accomplished by the input of additional *a priori* geological or geophysical information. In this section, I use knowledge on lithology to slightly increase the model complexity and subsequently match observed cusp amplitudes. Model complexity is increased by separating the previous models with constant anisotropy model into models with two zones of unequal anisotropy.

The resistivity log in Fig. 3.3 is an indicator of the geology at Well 87. The lithology described in Fig. 3.3 is typical of the area surrounding the Juravskoe oil field and is similar at Well 85. The geology at Well 85 may be divided into two zones. The geology in the upper zone, from the surface down to 870 m, is characterized by thin alternating layers of sandstone, clays, and limestones. The second lower zone is a near-continuous sequence of Maikop clays which extends downwards to the base of the well. It is, therefore, likely that in the top 870 m layering-anisotropy and

lithological-anisotropy contribute to the observed TIV. On the other hand, below 870 m it is likely that only lithological anisotropy causes the TIV. This boundary, therefore, represents a likely depth at which the TIV anisotropy changes, and indicates a depth to subdivide the TIV model to create two zones of unequal anisotropy. In the next section I attempt to find a two zone model to improve the match of the cusp amplitudes, in particular the cusp arrival at 1.5 km offset in Fig. 5.18a.

5.10.1 Effect of Increasing qSV_{45} Anisotropy in the Layering or Clays

In Fig. 5.2a the level dividing the upper thin layering and the lower continuous clays is represented by the sharp velocity decrease at 870 m. Dividing the model into these two lithologically different zones I test whether increasing the relative anisotropy in either of the two zones effects the cusp amplitudes in the synthetic seismograms. Two ratios of upper zone to lower zone anisotropy are tried: 1.25 and 0.8, representing a 25% relative increase of anisotropy in the layering and Maikop clays, respectively.

To determine the effect of creating two anisotropy zones on cusp amplitudes, I must first find the anisotropic models with the prescribed ratios which best fit the observed arrival times. This is done in a similar manner to that used in Section 5.9. The seismograms calculated in Section 5.9 show negligible variation of cusp (and qSv) arrival times and amplitudes for changes in the Δ_P parameter. Therefore, in this section I restrict the search to changes in the Δ_{SV45} parameter (Δ_P is held constant at 15% in all layers of each model). Furthermore, Fig. 5.16a shows that the qP arrival time misfit does not help to constrain Δ_{SV45}, therefore only misfit functions of the qSV and cusp phases are considered. Each model is identified by the value of Δ_{SV45} in the zone in which it has the largest value, using the symbol Δ_{SV45}^{upper} for anisotropy increased in the overlying layering and Δ_{SV45}^{lower} for anisotropy increased in the Maikop clay interval.

Separate qSV and cusp arrival-time misfits are calculated using Eqn. 5-6 for models with anisotropy increased in either the layering or the clay and shown in Figures 5.19a and 5.19b, respectively. In general, these functions show minimum misfit values close to that of the best-fit model with constant anisotropy with depth. Thus, indicating that a close match to the arrival times in Figures 5.19a and 5.19b. Comparing Figures 5.19a and 5.19b in detail shows that the minima of the cusp and

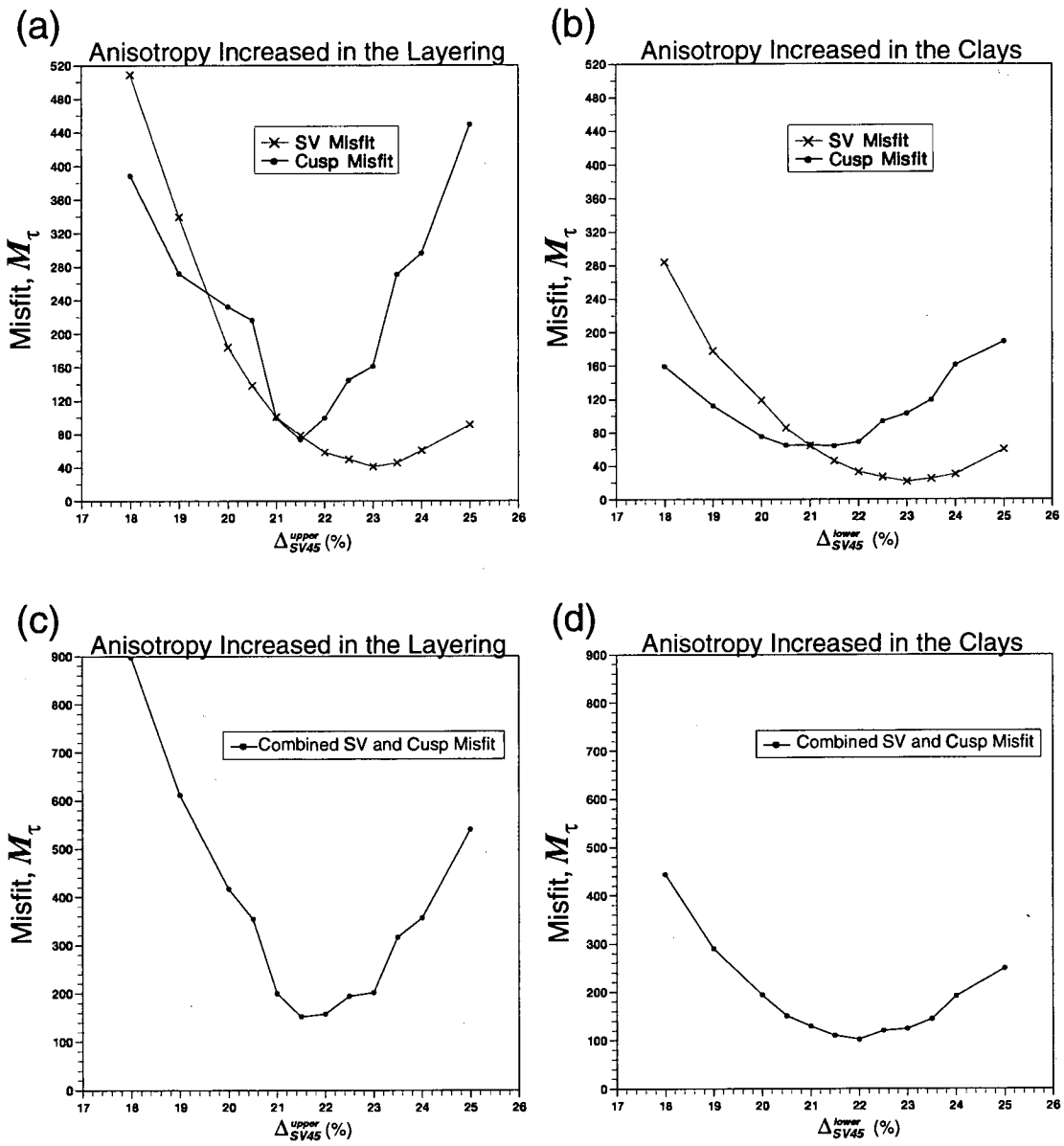

Figure 5.19: Misfit (M_τ) of qSV and cusp arrival times for 16 layer models with the qSV_{45} anisotropy ratio of the upper to lower anisotropy zones equal to (**a**) 1.25, and (**b**) 0.8. The combined misfit of the SV and cusp arrivals are shown in (**c**) and (**d**).

qSV misfits are lower for the model with stronger anisotropy in the clay. The corresponding combined (qSV and cusp) misfit values are displayed in Figures 5.19c and 5.19d and also indicate a slightly lower minimum for stronger anisotropy in the clay. The seismograms corresponding to the best models in Figures 5.19c and 5.19d are shown in Figures 5.20 and 5.21, respectively. Visual comparison of the arrival times in Figures 5.20 and 5.21 with the observed WA1 arrival times confirms that both these models are in very good agreement. The reason for dividing the model into two anisotropic zone, however, is to attempt to match better the cusp amplitude at 1.5 km.

Consequently, I now check if the cusp amplitude in either model has increased relative to the model with anisotropy constant in all layers, shown in Fig. 5.18a. Comparing the 1.5 km offset in Fig. 5.20 to the same offset in Fig. 18a it can just be seen that in the model with anisotropy stronger in the layering there is a decrease of the cusp amplitude in the synthetics. On the other hand, comparing the 1.5 km offsets in Figures 5.21 and 5.18a it is clear that the cusp amplitude is significantly larger in the seismograms from the model with increased anisotropy in the clay. [The amplitude of the cusp arrival at 2.5 km is not significantly altered.] Therefore, I conclude that preferentially increasing qSV_{45} anisotropy within the lower anisotropic zone of Maikop clay results in an improved match of the cusp amplitude at 1.5 km. In the next section this conclusion is confirmed by showing that larger relative increases of anisotropy in the clays produces further increases to the relative amplitude of the cusp at 1.5 km and which results in a further improvement to the observed amplitudes.

5.10.2 Matching Cusp Amplitudes

Results from the previous section indicated that preferentially increasing the qSV_{45} anisotropy in the clays gives a better fit to the cusp amplitudes. In this section I attempt to determine which qSV_{45} anisotropy ratio between the clay and layering zones best matches the observed cusp amplitudes.

Misfit functions of the qSV and cusp arrival times were computed for synthetic seismograms calculated from models with qSV_{45} anisotropy ratios equal to 0.7, 0.6, 0.5, 0.4, and 0.3. The misfit functions are shown in Fig. 5.22 and include the results

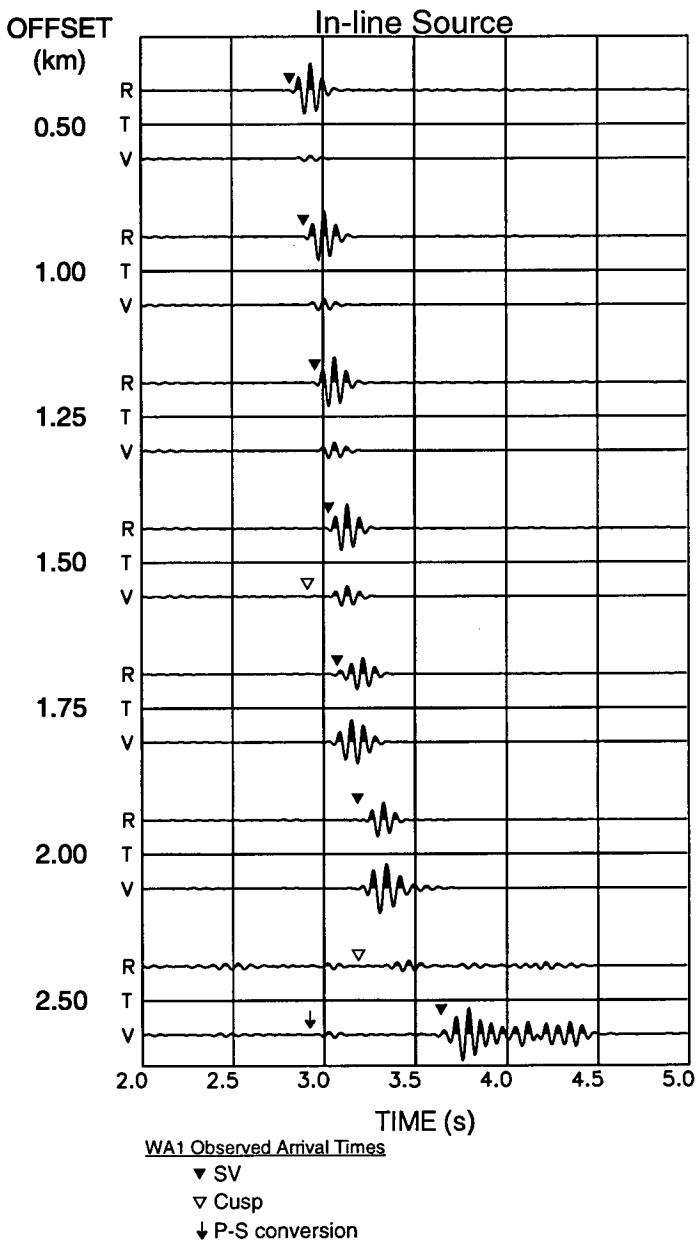

Figure 5.20: Three-component synthetic seismograms from an in-line source for a walkaway profile to a geophone at 1950-m depth through the best-fitting sixteen-layer TIV models with anisotropy relatively increased in the (overlying) layering. The layering to clay anisotropy ratio is 1.25 and the model has Δ_{SV45}^{upper}=21.5%. Notation as in Figure 5.4a : the triangle and arrow symbols mark the arrival times of the main shear-wave phases in Figure 5.4a.

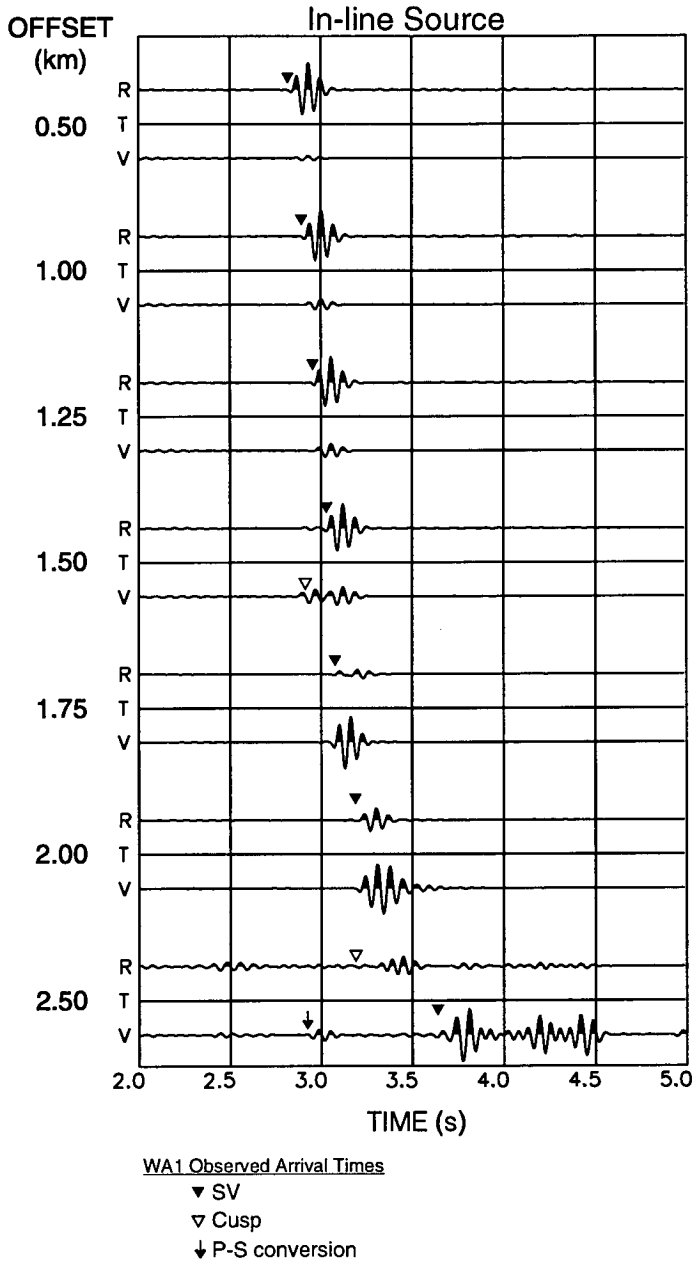

Figure 5.21: Three-component synthetic seismograms from an inline source for a walkaway profile to a geophone at 1950-m depth through the best-fitting sixteen-layer TIV models with anisotropy relatively increased in the near-continuous clay interval. The layering to clay Δ_{SV45} ratio is 0.8 and the model has Δ_{SV45}^{lower}=22%. Notation as in Figure 5.4a : the triangle and arrow symbols mark the arrival times of the main shear-wave phases in Figure 5.4a.

computed in the previous section using a ratio of 0.8. There are a number of interesting features to these misfit functions:

(i) the minimum value of the qSV misfit shows little variation with changes in the anisotropy ratio, particularly between ratios of 0.7 and 0.4 where the minima are almost equal;

(ii) the minimum value of the cusp misfit decreases steadily with decreasing ratio of anisotropy, implying that possibly a best fit to the cusp arrival times may be found using a model with all the anisotropy concentrated in the lower clay zone;

(ii) for large and small anisotropy ratios the minima of the cusp and qSV misfit functions do not correspond to the same value of Δ_{SV45}^{upper}. At the larger anisotropy ratios, the cusp arrival times are best fit by a Δ_{SV45}^{upper} value smaller than that required to best fit the qSV arrivals. As the ratio decreases the difference in Δ_{SV45}^{upper} between the two minima gets smaller until, at ratios between about 0.6 to 0.5, the two minima coincide, meaning that a single model can be found which is the best-fit of both SV and cusp phases, for these particular ratios. At the smaller anisotropy ratios, the cusp arrival times are best fit by a value of Δ_{SV45}^{upper} larger than that required to best fit the qSV arrivals.

To calculate the ratio of anisotropy which best matches the observed cusp amplitudes I first select the model representing the minimum of the combined (qSV and cusp) misfit function for each anisotropy ratio. For each of these models I calculate the amplitude of the cusp phase relative to the qSV phase on the synthetic seismograms at 1.5 km and 2.5 km offsets. I then calculate the squared misfit between the cusp amplitudes from the model and those measured from the observed seismograms in Fig. 5.4a using:

$$M_A = \sum_{i=1}^{N} (A_{obs} - A_{model})^2 \; ; \tag{5-7}$$

where A_{obs} is the observed cusp amplitude and A_{model} is the model cusp amplitude. The cusp amplitude misfit as a function of anisotropy ratio for arrivals at the 1.5 km and 2.5 km offsets are shown in Figures 5.23a and 5.23b, respectively. Both misfit

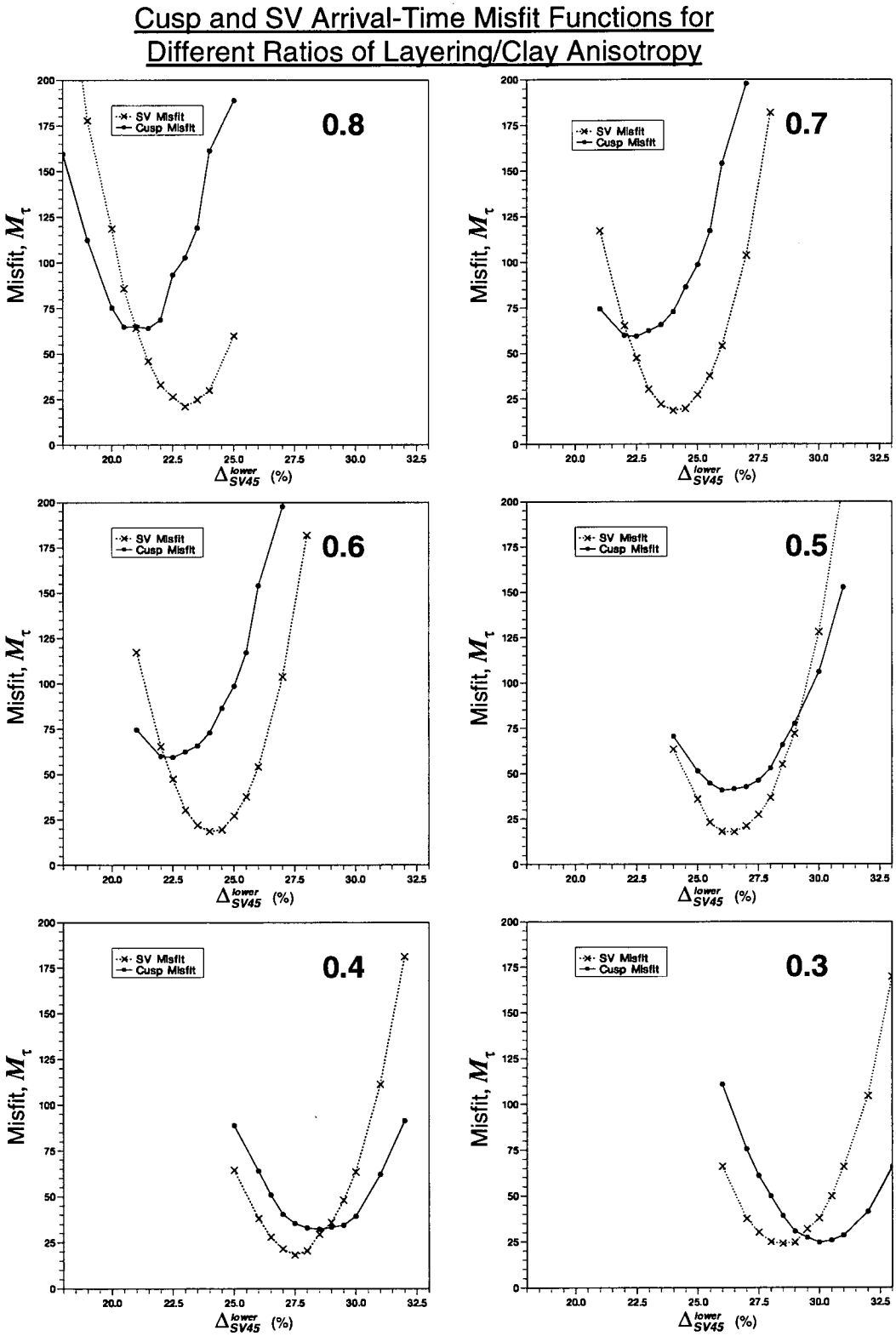

Figure 5.22: Determination of best-fitting sixteen-layer TIV models for qSV and Cusp arrival-times of WA1 at the 1950 m-deep geophone for models with different ratios of SV_{45} anisotropy in the overlaying layering and deeper clays. The ratio of the qSV_{45} anisotropy of the layering, relative to the clays, ranges from 0.8 to 0.3, and is printed in the top right-hand corner of each graph.

functions show a clear minimum at an anisotropy ratio of 0.6. This indicates that the best match to the observed cusp amplitude at both the 1.5 km and 2.5 km offsets occurs for the same ratio of qSV_{45} anisotropy between the two anisotropic zones.

5.10.3 Seismograms of Best-fitting Model

Seismograms for an in-line and cross-line source propagating through the best-fitting sixteen-layer TIV model with qSV_{45} anisotropy varying between two zones are shown in Figures 5.24a and 5.24b respectively. The best-fitting model has SH, and qP anisotropy in each layer equal to 36% and 15%, respectively (the seismograms in Fig. 5.24b are identical to the seismograms in Fig. 5.18b). The qSV_{45} anisotropy has a ratio of anisotropy of 0.6 between the upper layering zone and the lower clay zone. The specific values are 14.4% qSV_{45} anisotropy in the layering zone and 24% in the clay zone.

A comparison of Fig. 5.24a with Fig. 5.4a shows that most of the features in the field data are reproduced, except for the (variable) sagittal to transverse coupling. The arrival times and amplitudes of all of the main phases are similar, and in particular the arrival times and amplitudes of the anomalous phases at offsets of 1.5 km and 2.5 km marked by open triangles are similar (although the arrival at 2.5 km is still a little too late).

To confirm the interpretation of the arrivals I calculate synthetic seismograms at 100 m-interval offsets between 1.0 km and 2.5 km in the TIV structure. The seismograms are shown in Fig. 5.25. The anomalous phases at 1.5 km- and 2.5 km-offset marked by open triangles in Fig. 5.4a are seen to be entirely determined by the cusp. The cuspidal arrivals at the intervening 1.75 km- and 2.0 km-offsets from the in-line source orientation are not sufficiently separated in time from the main shear-wave arrivals to be clearly identified in Fig. 5.4a, but the general form of the arrivals are well reproduced by the synthetic seismograms in Fig. 5.24a. The first anomalous arrival at the 2.5 km-offset, marked by an arrow in Fig. 5.4a and matched by the synthetic seismograms, is a shear-wave generated from a P-to-S conversion at the larger impedance contrasts above the top of the clay (above 870 m).

These models confirm that anomalously fast arrivals at offsets of 1.5 km and 2.5 km are generated by cusps. However, a characteristic feature of the field records

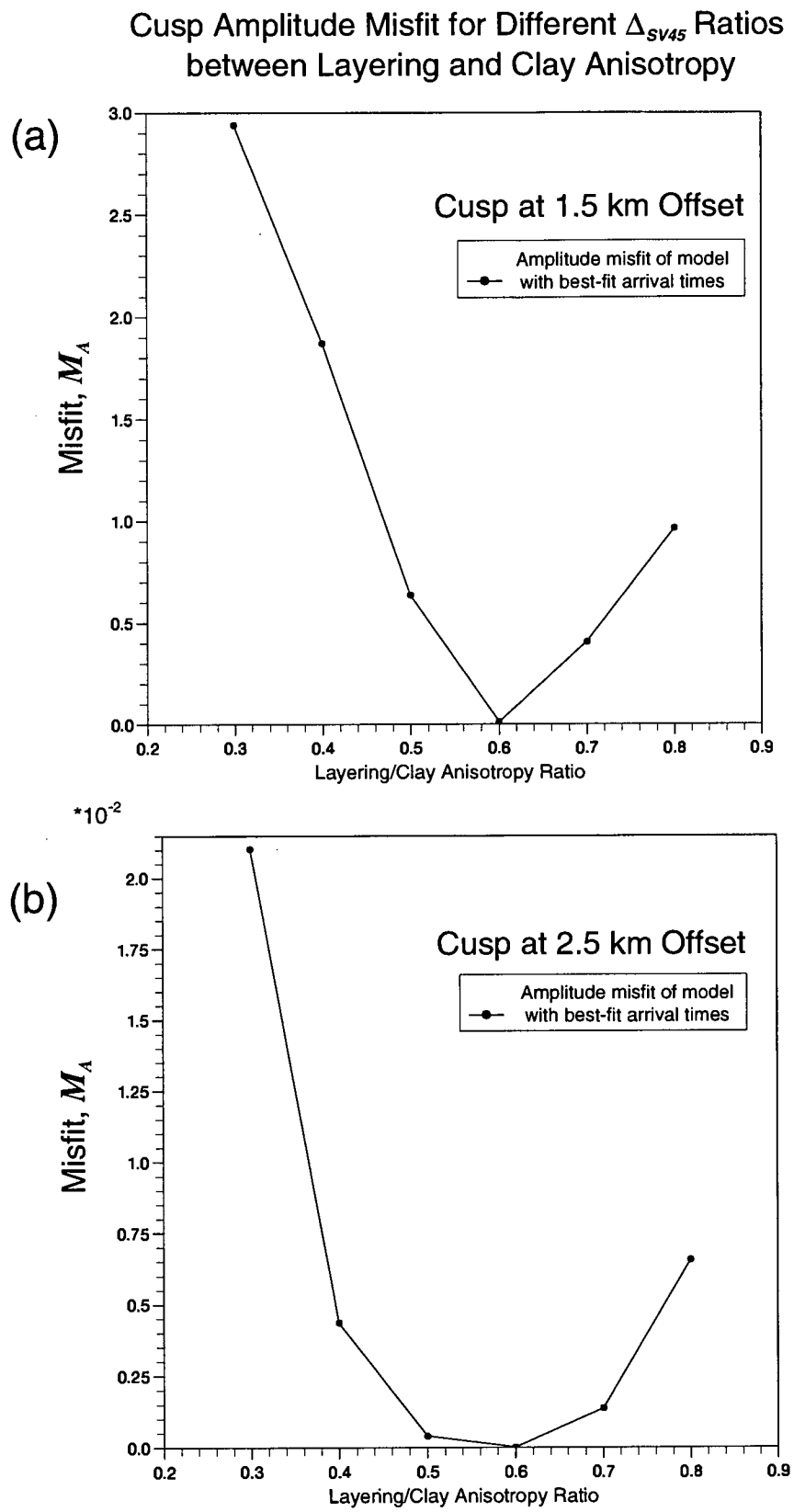

Figure 5.23: Amplitude misfit (M_A) of the cusp phases at (**a**) the 1.5 km and (**b**) the 2.5 km source offset for variation of the qSV_{45} anisotropy ratio between the layering and the clays. For each ratio, the model chosen corresponds to the minimum in the combined qSV and cusp travel-time misfit function (calculated from Fig 5.22). The minima of the two functions coincide at a ratio of 0.6.

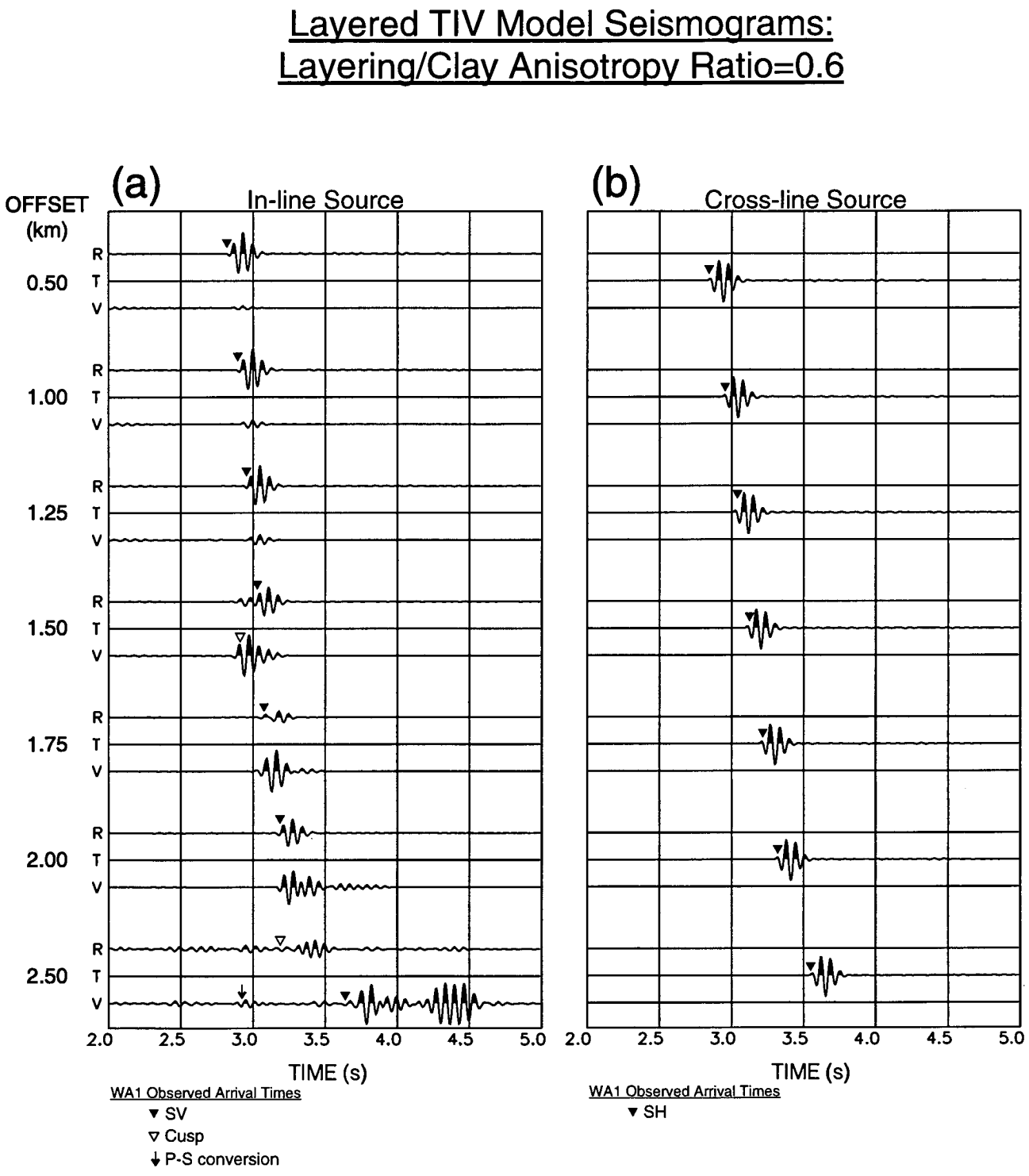

Figure 5.24: Three-component synthetic seismograms for a walkaway profile to a geophone at 1950-m depth through the best-fitting sixteen-layer TIV model with an anisotropy ratio of 0.6 between the upper layering and the lower continuous clays for **(a)** in-line and **(b)** cross-line source orientations. Notation as in Figure 5.4 : the triangle and arrow symbols mark the arrival times of the main shear-wave phases in Figure 5.4.

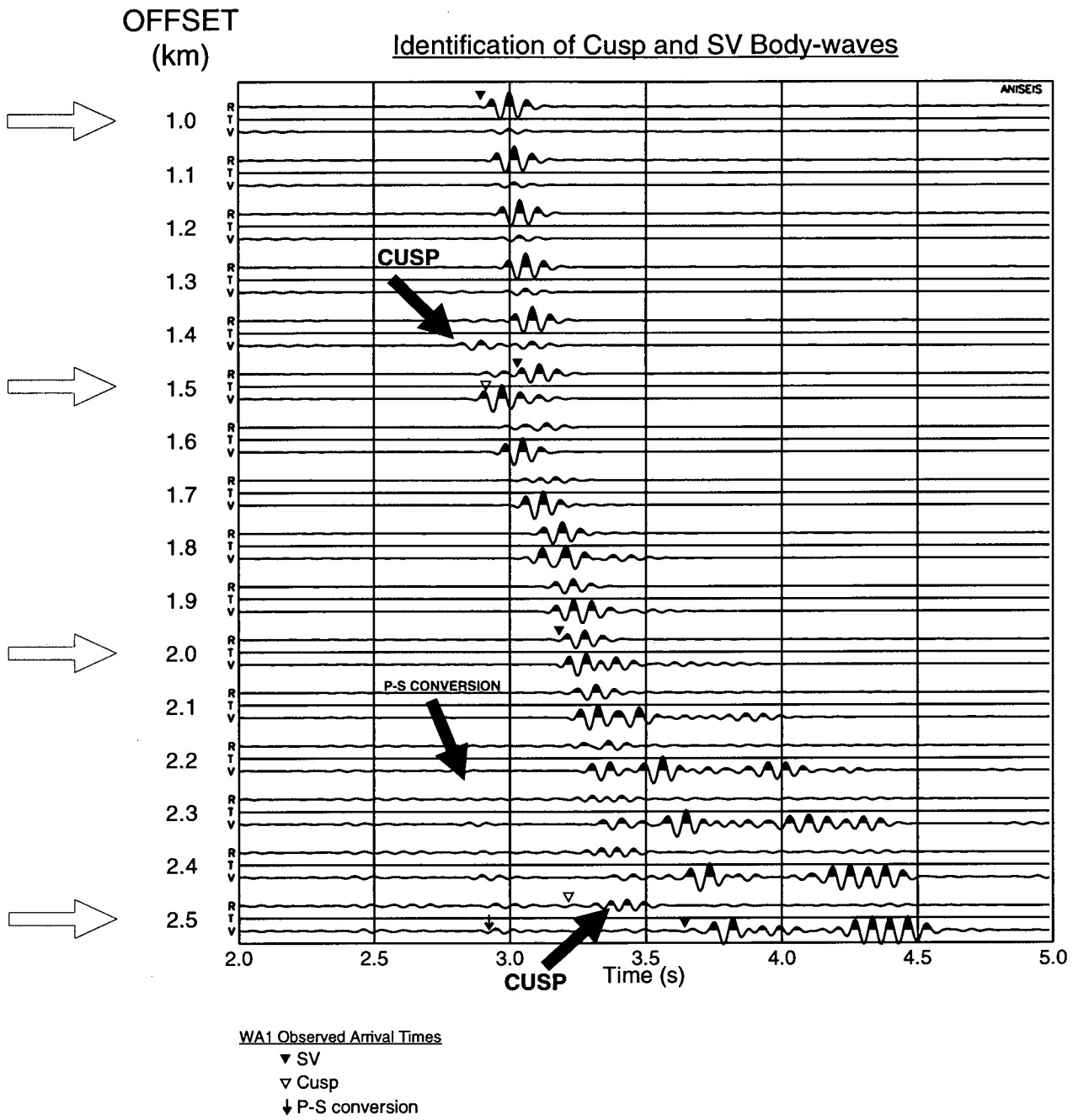

Figure 5.25: Synthetic seismograms from an inline source modelling WA1 from 1.0 km-offset to 2.5 km-offset at 100 m-intervals, through the best-fitting sixteen-layer model with a layering/clay anisotropy ratio of 0.6. Open arrows in the left margin indicate offsets at which there are field observations.

not matched by the seismograms from a transversely isotropic model (Figures 5.24a and 5.24b) is the coupling between motion in the sagittal plane and the transverse direction. This is a strong feature of the field seismograms in all eight walkaways, and such coupling is a characteristic of the azimuthal anisotropy of aligned vertical cracks (Crampin and Lovell, 1991).

5.11 MODELLING USING A LAYERED ORTHORHOMBIC MODEL

The presence of azimuthal anisotropy must be invoked to model the observed sagittal to transverse coupling, however, a full discussion of the azimuthal anisotropy is unnecessary in this chapter as it is covered in Chapters Three and Four. In summary, the near-offset VSPs at Well 85 and Well 87, both display evidence of different near-surface azimuthal anisotropy in the horizontally-layered stratigraphy. Well 87 shows a 20 ms delay between split shear waves at a depth of 300 m, whereas Well 85 shows a steady increase in splitting to about 18 ms at a depth of 1000 m. It is likely that this azimuthal anisotropy is the reason why the field data in Fig. 5.4 show strong coupling for near vertical incidence at the 0.5 km offset. The near-offset VSP measurements at Well 85 can be modelled by introducing vertical cracks (Hudson, 1986, 1991) into the top 870 m with crack density ε=0.01 and strike N19°E (Chapter Four).

Inserting the vertical cracks into the upper 870 m of a sixteen-layer TIV model with a qSV_{45} anisotropy ratio of 0.6 between the upper and lower anisotropic zones produces a reasonable match to the coupling between the sagittal and transverse motion. However, a better match to the coupling on the far-offset seismograms is obtained by dividing the SH anisotropy between the two zones with the same ratio as found for the qSV_{45} anisotropy. Division of the qP anisotropy into two zones produces no significant variation in shear-wave amplitudes therefore it remains unchanged in each layer. The final TIV parameters of the model, which has an SH anisotropy of 41% within the TIV Maikop clays, is listed in Table 5.2. Figure 5.26 shows synthetic seismograms modelling WA1 through the orthorhombic structure. Comparison with the field data in Fig. 5.4 shows that most of the previous similarities in the sagittal plane and the transverse motion are preserved and that many features of the coupling between the sagittal and transverse motion are also reproduced. In

Table 5.2: Final TIV Parameters for Well 85.

Anisotropy Zone	Depth Interval (km)	Number of Layers	TIV Parameters		
			qP (%)	SH (%)	qSV_{45} (%)
1	0.00 - 0.87	6	15	24.6	15
2	0.87 - ∞	10		41	25

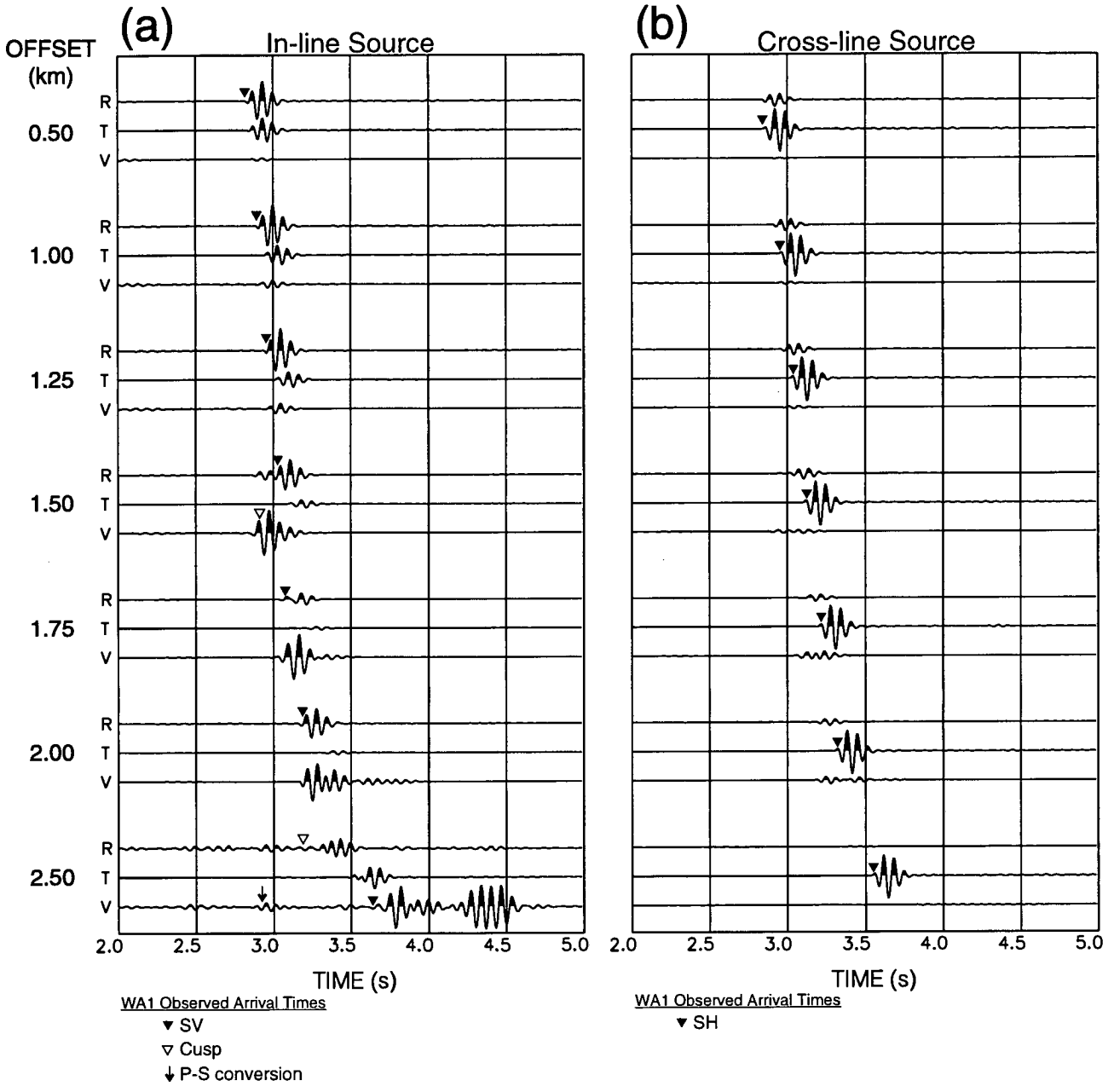

Figure 5.26: Three-component synthetic seismograms for a walkaway profile to a geophone at 1950-m depth through an orthorhombic model with the SH and qSV_{45} anisotropy ratio between the layering and clays set at 0.6 for (**a**) in-line and (**b**) cross-line source orientations. Notation as in Figure 5.4 : the triangle and arrow symbols mark the arrival times of the main shear-wave phases in Figure 5.4.

particular, some features of the multiple shear-wave arrivals with different arrival times and polarizations as well as reverberatory shear-wave coda (which could easily be mistaken for instrumental noise) also appear in the synthetic seismograms in Figures 5.26a and 5.26b. However, many details are not explained, particularly the relative amplitudes of the three-component signals which sometimes vary substantially between offsets in Fig. 5.4a. These anomalies may be caused by near-surface effects at the various source offsets. Such anomalies in the source radiation pattern from orthogonal sources has been recognised in Russia where it is known as Natural Directivity (Puzirev, Trigubov and Brodov, 1985, L.Y. Brodov, Neftegeofizika, Moscow, personal communication). Variations in Natural Directivity can sometimes be correlated with varying consolidation in poorly consolidated sediments and may vary substantially over distances of metres (Puzirev, Trigubov and Brodov, 1985). Natural Directivity may also be caused by multiple reflections from inclined interfaces and near-surface bedding. A brief discussion of Natural Directivity in regard to the field data in this chapter and field data presented by others can be found in Slater *et al.* (1993).

5.12 SUMMARY AND CONCLUSIONS

Anomalously fast arrivals on seismograms recorded from an in-line source were identified during the acquisition of walkaway VSP profiles across the Juravskoe oil field in the North Caucasus foredeep. In this chapter I have demonstrated by forward modelling that plane layered isotropic models based on well VSP velocity measurements cannot match the arrival-time behaviour observed in the walkaways. Using simple straight-line ray path approximations I estimated an increase of velocity towards horizontal. I determined the half-space TIV model which best-fits these velocities. The seismograms from this model show that the anomalously fast phases and the complicated waveforms on the far-offset field seismograms are likely to be caused by a strong TIV structure.

Subsequently, I have shown using forward modelling that a layered TIV structure with equal anisotropy in each layer can model arrival times closely, and I have confirmed that the anomalous recorded phases are generated near cusp in the qSV wave surface. This appears to be only the second published report of field

observations of seismic cusps, and the first to confirm the interpretation by matching with full waveforms.

Although a multi-layered model with constant anisotropy closely matches the observed arrival times, I found that the amplitude of the cusp phase on the 1.5 km-offset seismograms was poorly matched. To match the amplitudes I divided the anisotropic structure into two zones based on general lithology and found that the cusp amplitude was better matched using models with the anisotropy relatively increased in the lower zone which comprises continuous Maikop clays. Azimuthal anisotropy modelled by vertical cracks in Chapter Four, with crack density ε=0.01 and strike N199°E in the top 870 m, was then included to reproduce the sagittal to transverse coupling of the three-component recordings. The final orthorhombic model has 41% SH and 25% qSV_{45} anisotropy within the 1.2 km thick Maikop clay.

The possible importance of exciting cuspidal arrivals for field studies, is that if properly identified they can provide additional signals along some ray paths and place further constraints on interpretation without acquiring additional datasets. Although triplications in the wave surface of media with hexagonal symmetry may also occur parallel and perpendicular to the symmetry axis (Musgrave, 1970), the estimated velocity variations of the clays in this study and laboratory experiments on shales (Jones and Wang, 1981) indicate that triplications generated in argillaceous rocks are most likely to occur at 45° to the symmetry axis. Wide-angle reflection and crosshole shear-wave surveys in addition to walkaway VSPs sample ray paths at large angles from the vertical direction are therefore likely to be sensitive to the cusp phases generated in argillaceous rocks. Moreover, if wrongly identified, they could possibly lead to severe misinterpretations of the fast shear-wave polarization typically used to infer *in-situ* fracture parameters.

CHAPTER SIX

CONCLUSIONS

6.1 INTRODUCTION

In this thesis, my aim was to investigate the seismic anisotropy of a reservoir zone which displays a strong lateral variation productivity. In particular, my aim was to determine whether shear-wave splitting could be used to provide information about the orientation and density of the oil-filled inclusions within the reservoir zone. I have measured shear-wave splitting parameters from VSPs at three locations in two oil fields and successfully modelled the results. I have also successfully modelled Walkaway VSPs from one of the oil fields and confirmed, for the first time, the existence of anisotropic cuspidal arrivals in field seismograms. In this chapter, I summarize my conclusions and make suggestions for future work on the anisotropy of the oil fields.

6.2 CONCLUSIONS

6.2.1 Shear-wave Splitting Measurements in the Oil Fields

Single-source measurements above the reservoir zone

Determination of azimuthal anisotropy in the layers overlying the Maikop clay reservoir was only possible at Wells 85 and 87. This was done using a single-source method to determine shear-wave splitting. Such single-source measurements are generally less reliable than those made from dual-source data. Nevertheless, the single-source VSPs acquired using the VEIP-40 source at Wells 85 and 87 yield shear-wave splitting measurements which are consistent between levels, particularly in the top 1 km. The DTS measurements of *qS1* polarization direction from the two wells

agree closely, and indicate a *qS1* polarization direction of NNE which is subparallel to the direction of maximum compressive stress as indicated by earthquake focal mechanisms (described in Section 3.2.2). This suggests that the cause of the shear-wave splitting in the top 1 km is stress controlled. The time delay from the DTS measurements at Wells 85 and 87 show quite different behaviour in the top 1 km, though an average vertical shear-wave anisotropy of about 1% over the top 1 km.

Dual-source measurements in the reservoir zone

In general, the measurements from the dual-source techniques have been found to agree with the those from the single-source technique. Also, dual-source measurements indicate a constant *qS1* polarization with depth and a high degree of consistency of the *qS1* direction between the three wells.

At Well 87, the resolution of the reservoir anisotropy is impeded by lack of reproducibility of the shear-wave signals and asymmetry of the data matrix. At Well 29 a strong decrease in time delay has been identified which indicates an orthogonal rotation of the *qS1* polarization at a depth just above the reservoir and a vertical shear-wave anisotropy of about 9% in the reservoir zone. At Well 85 there is an indication of a similar decrease but there are too few observations in the reservoir zone to allow a reliable interpretation. Because the reservoir anisotropy could not be resolved at two wells and because the productivity is unknown at one well the main aim of this thesis could not be achieved. Therefore, definite conclusions regarding the relationship between azimuthal anisotropy and productivity at the wells were not achievable with these data.

6.2.2 Modelling Azimuthal Anisotropy

I have shown that the azimuthal anisotropy in the top 1 km at Wells 85 and 87 is unlikely to be caused by a slight rotation to the strong TIV estimated in Chapter Five. I have subsequently modelled the shear-wave splitting from the single-source technique at Wells 85 and 87 using models containing aligned cracks. At both wells, the polarization and time delay parameters in the top 1 km can be matched by similar models with cracks inserted into the TIV structure determined in Chapter Five. The cracks are vertical, have a low density of 0.01, are aligned close to the presumed

maximum horizontal stress direction, and are inserted into the layers above the Maikop clay.

I have found three different cracked models to match the strong decrease of time delay for vertical propagation in the reservoir zone at Well 29. The three models are defined by (i) a set of vertical fractures aligned orthogonal to the presumed maximum horizontal stress direction (ii) a set of dipping cracks or fractures striking parallel to the stress direction and (iii) a distribution of intergranular cracks with a high internal pore-fluid pressure. I have also modelled the far-offset VSP data which is best matched by the model with dipping cracks in the reservoir zone, however, due to a lack of receiver levels above the reservoir zone, other interpretations of the reservoir anisotropy cannot be excluded.

6.2.3 Modelling of Walkaway VSPs

I have shown that the sedimentary rocks overlying the reservoir in the Juravskoe oil field are characterized by strong TIV. In addition, I have demonstrated, by forward modelling with full waveform synthetics, that anomalously-fast SV arrivals recorded at wide-offsets are associated with cusps in the SV group-velocity surface of the strong TIV. I match closely the arrival times and relative amplitudes of most phases recorded in the Walkaway VSP by synthetics calculated from a model with a total of sixteen layers contained in two anisotropic zones. The upper zone, representing an alternating sequence of clays, sandstones and limestones, has qP-, qSV_{45}- and SH-anisotropy equal to 15%, 15% and 25%, respectively. The lower zone of near continuous Maikop clay has qP-, qSV_{45}- and SH-anisotropy equal to 15%, 25% and 41%, respectively. This appears to be the first observation of anisotropic cuspidal phases to be confirmed with full waveform synthetics.

6.3 FUTURE WORK

If more shear-wave VSPs are to be acquired in the North Caucasus oil fields, I recommend the following be carried out:

(i) acquisition of fewer receiver levels above the reservoir zone because the *qS1* polarization direction appears to be consistent with depth;

(ii) acquisition from far-offset shear-wave sources at all receiver levels to allow the anisotropic structure above and, consequently, within the reservoir to be more fully resolved;

(iii) acquisition of densely spaced receiver levels, for example every 2 m, within and just above the reservoir zone to allow a high degree of confidence in the interpretation of reservoir anisotropy;

(iv) a series of experiments aimed at increasing the reproducibility of the shear-wave signal which is variable between well sites and therefore most probably due to irregular source coupling.

(v) in this study, it has been shown that anomalous shear-wave behaviour may be associated with the reservoir at the base of the Maikop clay. Recent numerical modelling has indicated that such anomalous shear-wave behaviour may be related to changes in pore-fluid pressure (Zatsepin and Crampin, 1997; Crampin *et al.*, 1996). To determine whether shear-wave splitting in this reservoir zone is sensitive to changes in pore-fluid pressure requires detailed correlations between shear-wave splitting and downhole pressure measurements.

APPENDIX A

MULTI-OFFSET VSP STUDY OF NEAR-SURFACE ANISOTROPY AT THE GAVRILOV-YAM TEST SITE, RUSSIA

A.1 INTRODUCTORY NOTE

When I was given this dataset, I was told that the twelve shear-wave VSPs were acquired from sources at offsets of 10 m, 30 m, 70 m, 140 m, 205 m, and 207 m along two radial profiles. I processed all the VSPs, measured shear-wave splitting for the six nearest offset VSPs and I matched the measurements using models containing vertical cracks in a TIV matrix. These results were subsequently presented at the UKGA, Liverpool, in 1994 (Slater and Crampin, 1994). Shortly after the UKGA, I visited the test site and inspected the well-site at which the data were supposed to have been acquired. However, it was found that the acquisition geometry previously described to me could not have been acquired at this well because of surface obstructions at some of the supposed source locations. (I was subsequently told that the data from these supposed source locations were actually repetitions of the VSPs on the other profile.) Consequently, because of these and other inconsistencies, and the fact that this study is not directly relevant to the rest of the work in this thesis, I include this study only as an appendix. Nevertheless, it should be noted that these multi-offset VSPs contain high quality shear waves which could, if further information is forthcoming, yield definite conclusions.

A.2 INTRODUCTION

In many shear-wave VSP experiments, anisotropy parameters have been observed to be highly variable within the uppermost 1 km or less of the subsurface. However, as

the target zone is often much deeper, this shallow interval usually contains few receiver levels and is, therefore, poorly resolved. There have been a few reports of VSP experiments to specifically study near-surface anisotropy, for example: Liu *et al.* (1991), Douma, Den Rooijen and Schokking (1990); and Lynn (1991).

In this appendix, near-surface multi-offset VSPs from a field test site are examined for anisotropy. Firstly, I describe the location and geology of the test site. Then I describe the acquisition and processing of the VSPs. Next I demonstrate that there is probably a strong TIV component of anisotropy in the near-surface at the site. Finally, I investigate azimuthal anisotropy of the near-surface by measuring shear-wave splitting in the VSPs.

A.3 LOCATION AND GEOLOGY

The field test site is situated immediately south of Gavrilov-Yam, approximately 200 km to the north-east of Moscow within the Yaroslavl region (Fig. A.1a). The site covers an area of 16 km^2 and is extremely flat (differences in elevation are less than 1 m between wellheads 500 m apart). The site is used mainly to test new seismic sources and receivers (both surface and downhole), and therefore, contains many shallow, intermediate and deep wells drilled to depths of 50 m, 500 m and 3 km, respectively. The data analysed in this appendix come from an intermediate well called Well 23.

The geology at Well 23, from the surface to the depth of the deepest VSP receiver level, is indicated in Fig. A.2. Essentially, the geology consists of a 54 m-thick cover of poorly-consolidated Quaternary glacial clays and sands overlying a sequence of Upper Permian to Upper Jurassic clays, which contain occasional thin layers of sandstone and limestone. As is typical of the central Russian platform, the Permian and Jurassic clay layers are undeformed and flat lying (Nalivkin, 1973), which should help to simplify any interpretation and modelling. However, the overlying Quaternary clays have a comparatively complex structure: within a few metres of the surface there are many infilled channels which may produce lateral variability in velocity and possibly distort the shear-wave source radiation patterns.

(a)

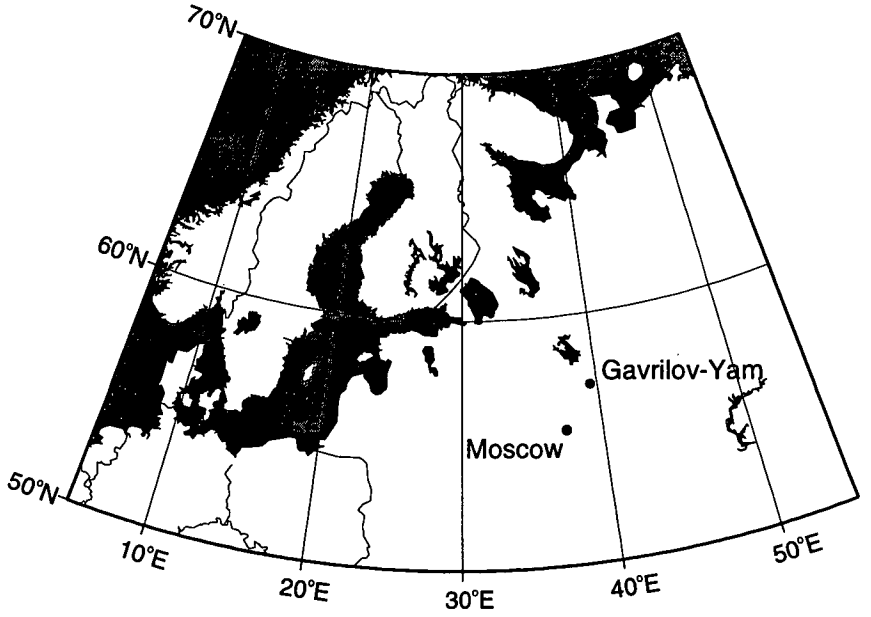

(b)

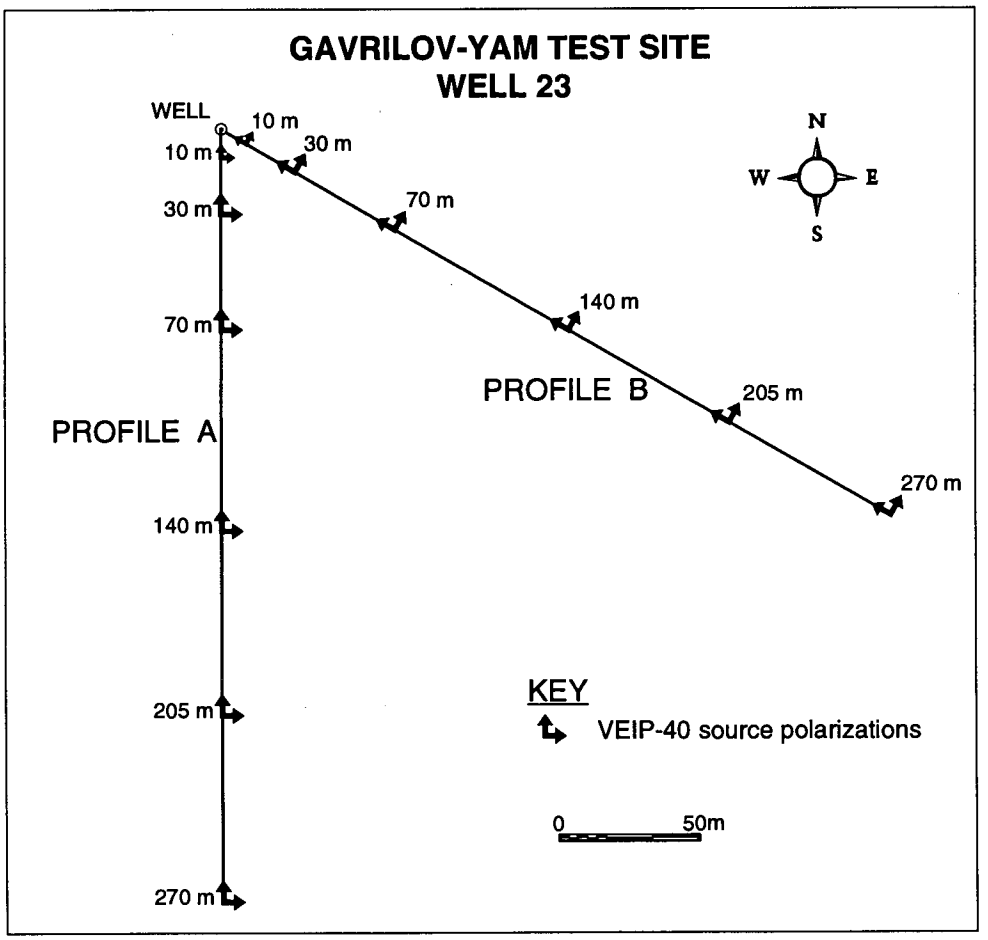

Figure A.1: (a) Location of Gavrilov-Yam; and (b) acquisition geometry of the multi-offset VSP experiment at the 500 m-deep Well 23 within the Gavrilov-Yam field test site. The solid arrows indicate the locations and polarizations of the VEIP-40 source.

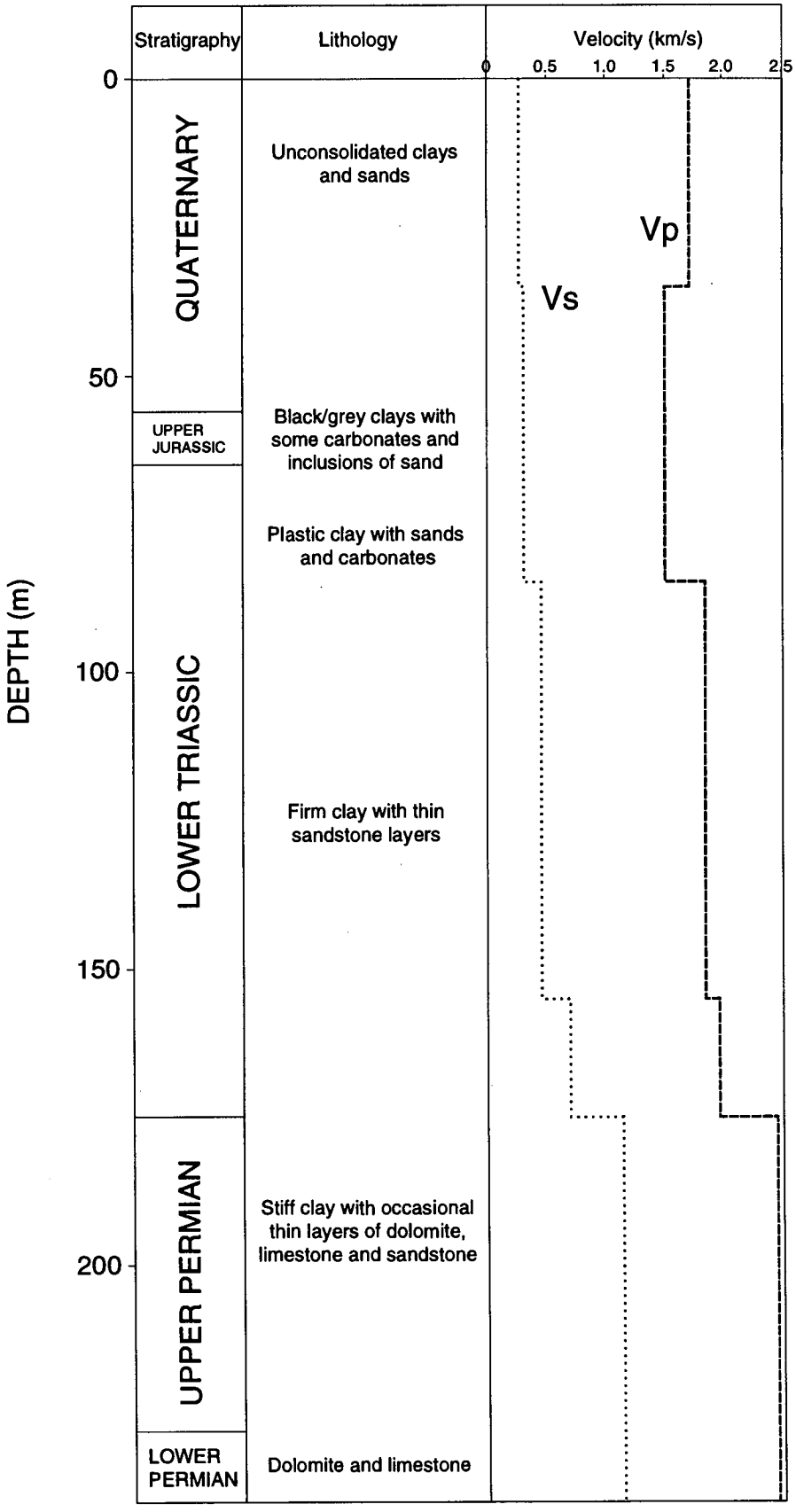

Figure A.2: Summary of the near-surface geology at Well 23.

Azimuthal anisotropy measurements are often compared with estimates of the stress field to help interpret the cause of the anisotropy. However, in this study I have been unable to obtain any information on the local or regional stress field.

A.4 DATA ACQUISITION AND PROCESSING

A.4.1 Acquisition

There are some errors and inconsistencies in the descriptions I have received about the acquisition of these multi-offset VSPs. I will first give a description of the acquisition as I was told initially and then describe the main problem.

Figure A.1b shows the acquisition geometry supplied with the tape containing the data. The data were acquired by Neftegeofizika (Moscow) in the Autumn of 1992. According to Fig. A.1, sources were located at six offset distances along two radial profiles, Profile A and Profile B, which were oriented N180°E and N120°E, respectively. P-wave and shear-wave sources were fired at each source position and recorded by a downhole three-component receiver. The receiver was located between depths of 15 m and 230 m with a sampling interval of 5 m.

However, on a visit to the test site, I inspected the well location and it was apparent that, if the well I inspected was the correct well, no shear-wave sources could have been located 10 m, 30 m and 70 m along Profile B. The test-site manager offered the explanation that some of the Profile B data are actually repetitions of the VSPs along Profile A. However, as no observer's logs have been made available, I cannot verify this. Consequently, in the rest of this appendix I will refer to these VSPs by their location in Fig. A.1, but will show results for both cases of acquisition along Profile A or B.

Two types of sources were used to generate compressional and shear waves at each of the source positions marked in Fig. A.1b: compressional waves were generated by an air gun submerged within a water-filled shallow pit; and shear waves were generated by VEIP-40 source trucks (for a description of the VEIP-40 source see Section 3.4). At each source location, the VEIP-40 sources were oriented inline and crossline to the direction of the well. In order to determine the orientation of the

downhole three-component receiver, P-waves were recorded at each receiver level from one of the far-offset source positions.

Knowing the relative polarities of the horizontal receiver components is important to properly apply the DIT technique. The relative polarities of the receiver components are described as follows: if the vertical component is assigned to be positive up, then the second (H2) horizontal component is oriented, when looking downwards, at an angle of 90° in a clockwise direction from the first (H1) horizontal component (V.M. Kuznetsov, personal communication, Neftegeofizika, Moscow). I could not verify the relative polarities using P-wave arrivals because P-waves were recorded from only one azimuth for each receiver depth (c.f. Section 3.6.1 and Fig. 3.10).

A.4.2 Processing

The processing and analysis of the shear-wave VSP data are schematically shown in Fig. A.3. The data were supplied by Neftegeofizika, Moscow, in SEGY format with a sample rate of 1 ms and a record length of 2 seconds. The accompanying tape description (no observer's logs are available), indicated that both inline and crossline VEIP-40 sources were recorded with negative and positive polarities. This is a common procedure for acquiring shear waves as it allows during processing the enhancement of shear waves and the cancellation of P-waves by subtracting, from each other, the seismograms from opposite source polarities. However, after sorting the records, I found that, for the inline source, both the P- and shear-wave arrivals had the same polarity on traces from oppositely polarized source shots. The traces from the two supposedly opposite-polarity shots were not identical, so the problem was not that of a simple error in tape copying and or tape reading. It appears as though the inline source was recorded twice with the same source polarity. Consequently, subtraction of opposite polarity traces, to reduce P-wave energy, was impossible for data from the inline source.

Later in this appendix, I apply the DIT technique to estimate shear-wave splitting. This technique assumes identical source functions from orthogonally polarized sources. Therefore, to maintain as much similarity between the signals from

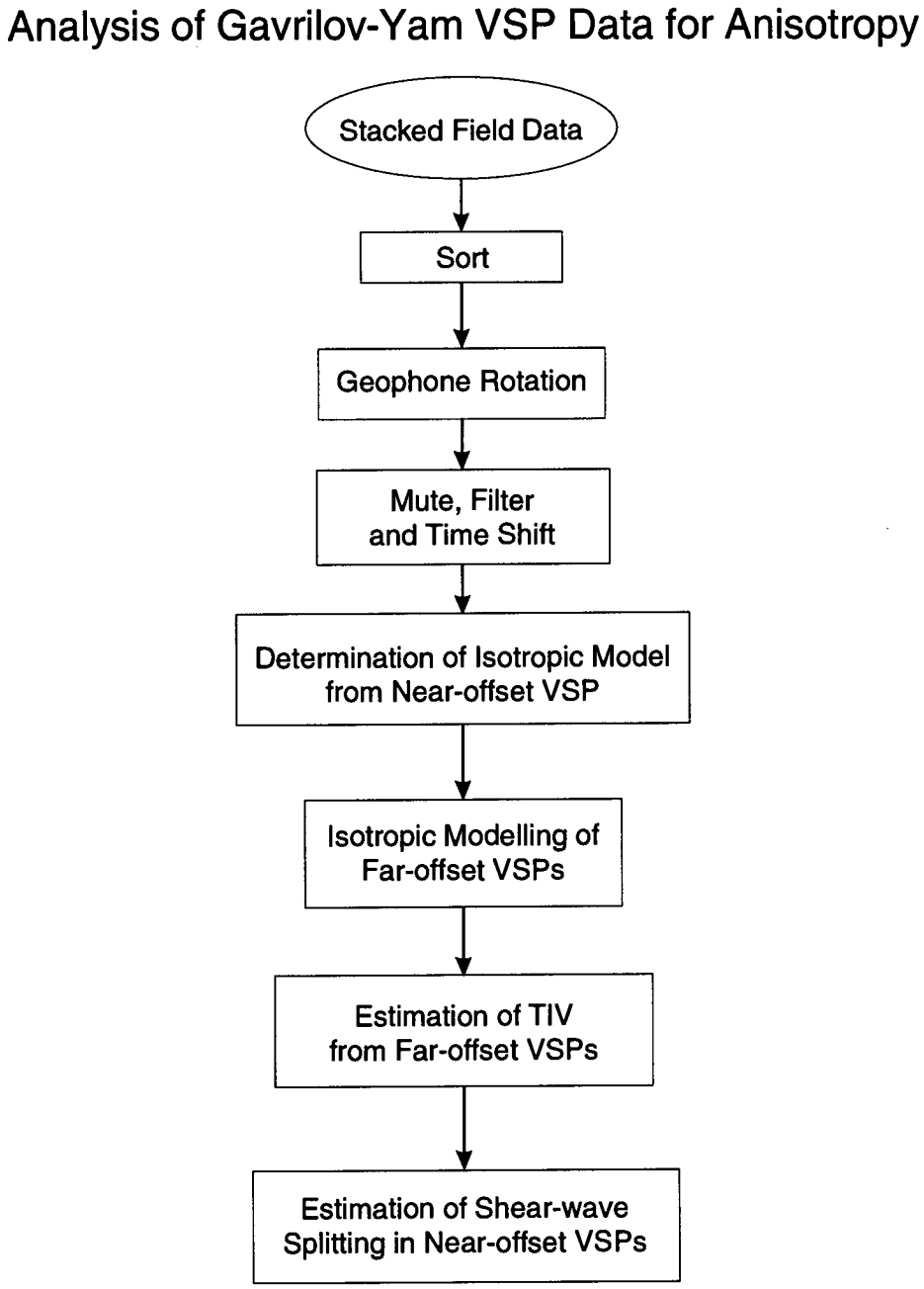

Figure A.3: Schematic flowchart showing the processing and modelling of the Gavrilov-Yam VSP data.

the inline and crossline sources, I analysed only the traces from the sources marked as positive in the tape description.

I determined the orientation of the horizontal receiver components at each receiver level in each VSP using the P-waves recorded from the air gun sources. The seismograms containing the P-waves were filtered from 3 Hz to 150 Hz and a window enclosing the first initial cycle of the arrival was interactively picked. Over this window, receiver orientations were then calculated using a covariance matrix method (Kanasewich, 1981). I then rotated the receiver components to the inline and crossline directions, muted out noise spikes, and bandpass filtered the traces between 3 Hz and 45 Hz.

I was told that time static delays associated with source triggering problems affect the VEIP-40 and air gun sources with magnitudes of 50 ms and 38 ms, respectively (L.Y. Brodov, Neftegeofizika, Moscow). In Fig. A.4 I compare P-wave arrival times from both types of sources offset 30 m from the well. The crosscorrelation in Fig. A.4 shows that there is no relative static difference between the two sources at this offset. Neftegeofizika insist that they understand the cause of the VEIP-40 delay and are confident that it is equal to 50 ms (L.Y. Brodov, Neftegeofizika, Moscow). Therefore, I time shifted all seismograms from the VEIP-40 source by -50 ms. If this shift is incorrect then shear-wave velocities and TIV estimates I obtain later will be in error, however, the shear-wave splitting measurements will remain valid.

A.4.3 Seismograms

Processed seismograms are shown in Figs. A.5 to A.13. The 10 m-, 30 m- and 70 m-offset VSP seismograms from both Profile A and B are displayed. However, to preserve space, I only show the 140 m-, 205 m- and 270 m-offset VSPs from Profile A (the seismograms along Profile B are similar). It can be seen in Figures A.5 to A.13 that shear-wave arrivals with a high signal-to-noise ratio are evident from all source offsets. In each VSP, consistency of shear-wave signal between receiver levels indicates a high degree of source reproducibility and reliability of the rotations of the receivers. The main shear-wave signal is approximately two cycles in length and is followed by lower amplitude short-pathlength multiples. It should be noted that for

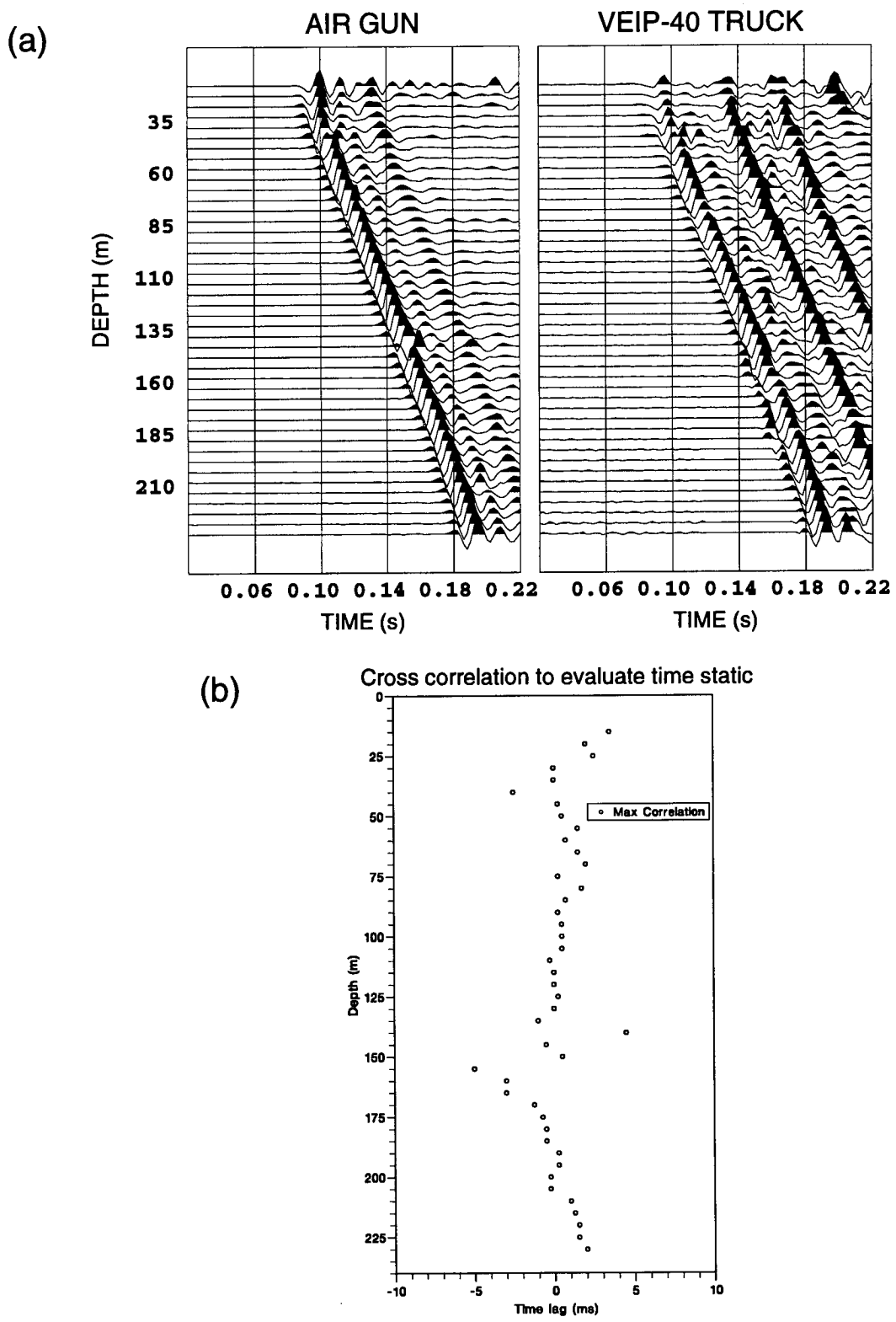

Figure A.4: Evaluating the relative difference in the static timing errors. (**a**) P-wave arrivals from the 30 m-offset air gun and VEIP-40 source, (**b**) Relative time lag of the air gun source found by cross-correlation of the seismograms in (a). It can be seen in (b) that there is no consistent relative difference in the static timing errors.

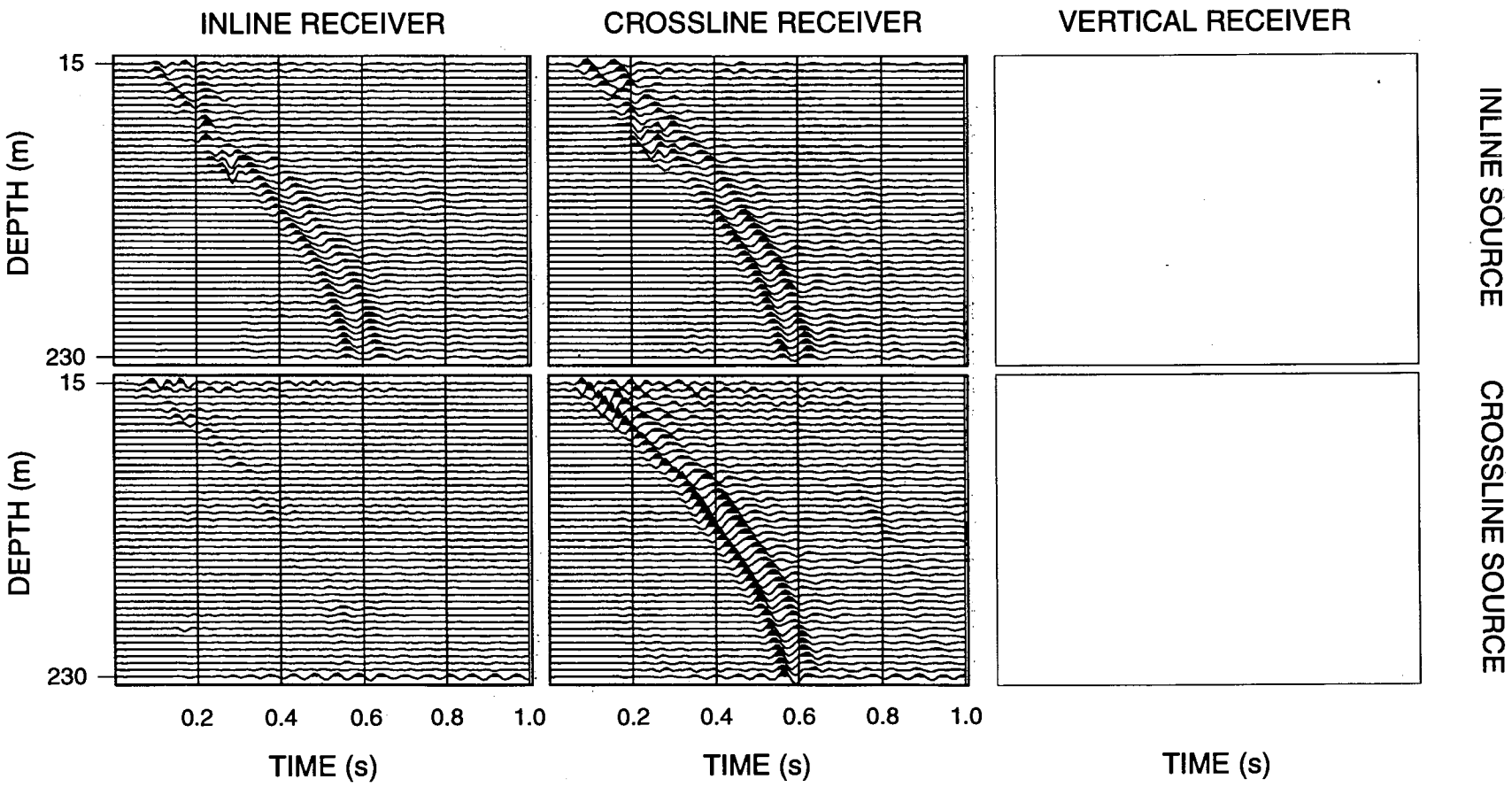

Figure A.5: The processed 10 m-offset VSP from Profile A. Shear waves can be clearly seen on the horizontal components. The vertical components for this offset are badly affected by noise spikes and are therefore not displayed. Note that asymmetry of the data matrix is apparent in the four horizontal components.

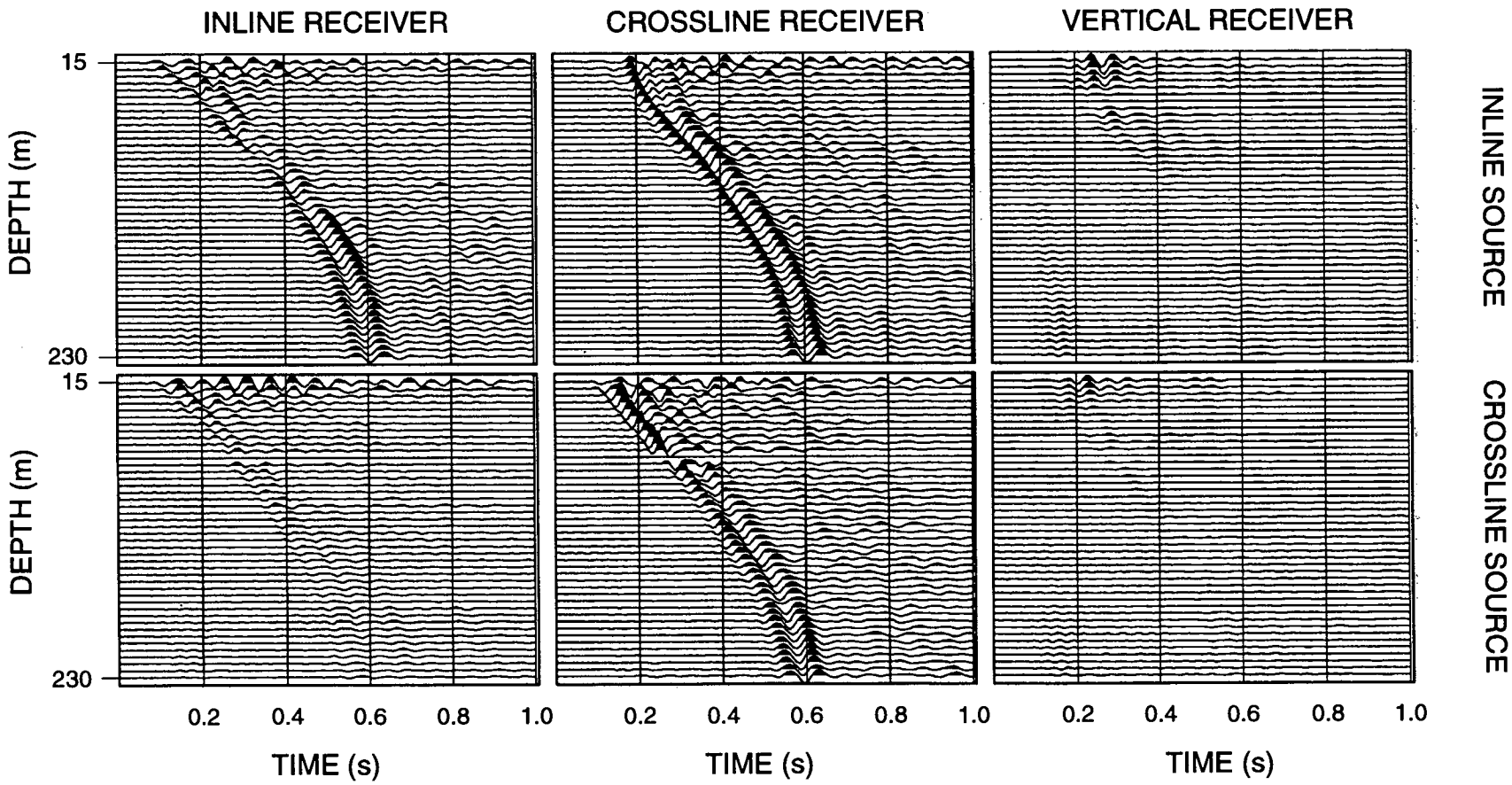

Figure A.6: The processed 30 m-offset VSP from Profile A. Shear waves can be clearly seen on the horizontal components. The vertical components for this offset are badly affected by noise spikes and are therefore not displayed. Again, note that asymmetry of the data matrix is apparent in the four horizontal components.

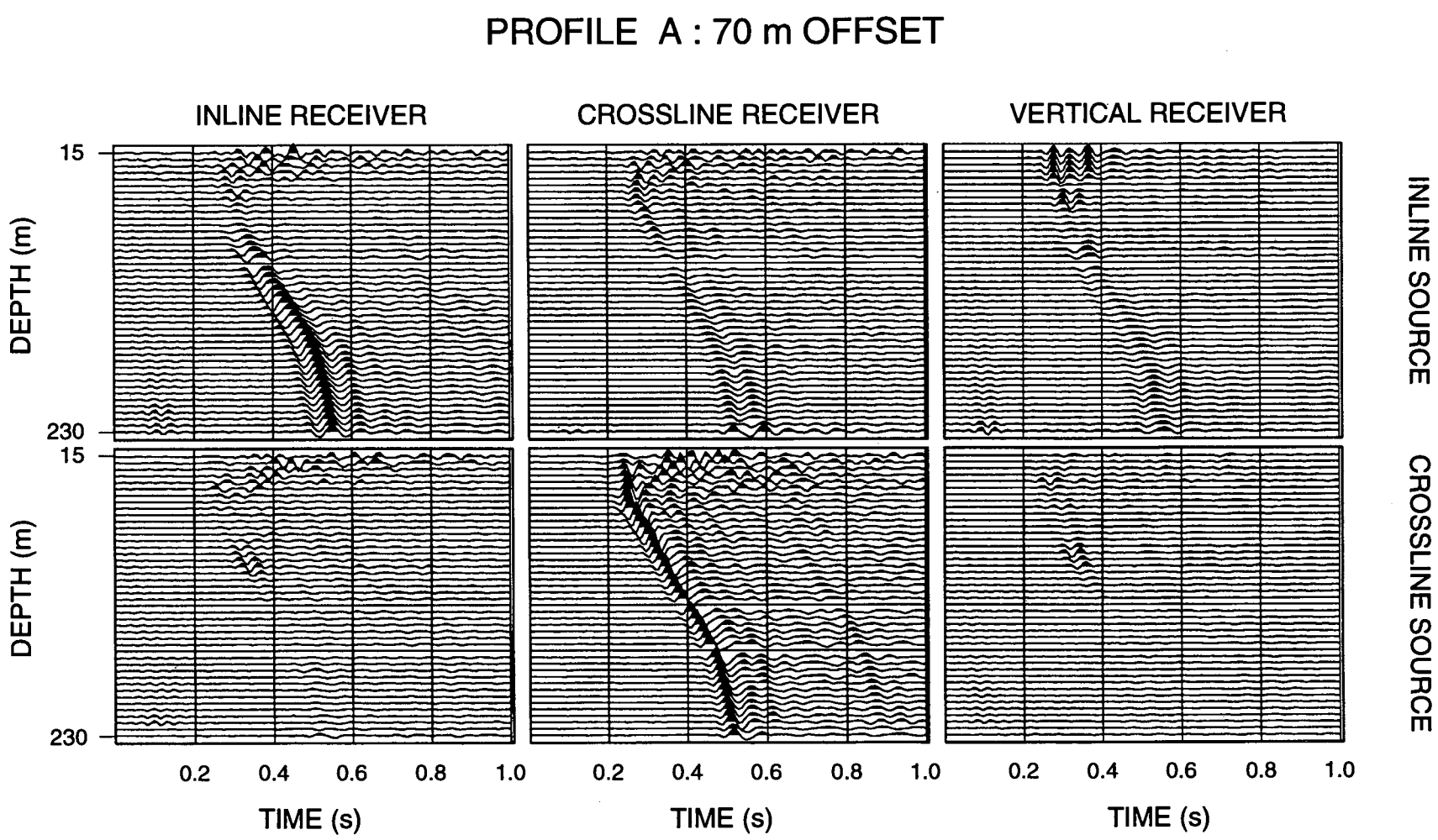

Figure A.7: The processed 70 m-offset VSP from Profile A. Shear waves can be clearly seen on the horizontal components.

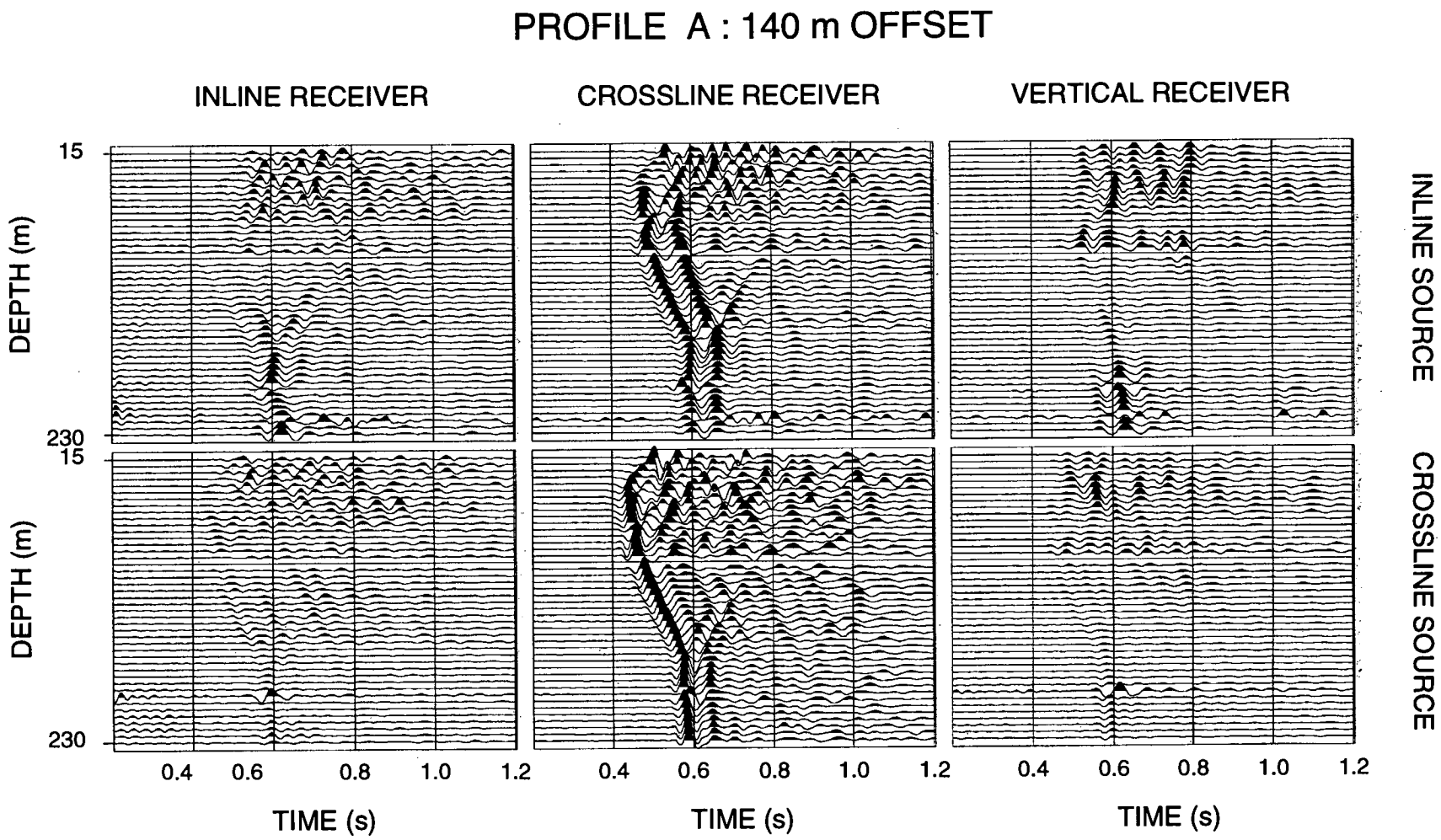

Figure A.8: The processed 140 m-offset VSP from Profile A. Shear-waves can be clearly seen on the horizontal components. Note the lack of energy on the inline receiver from the inline source.

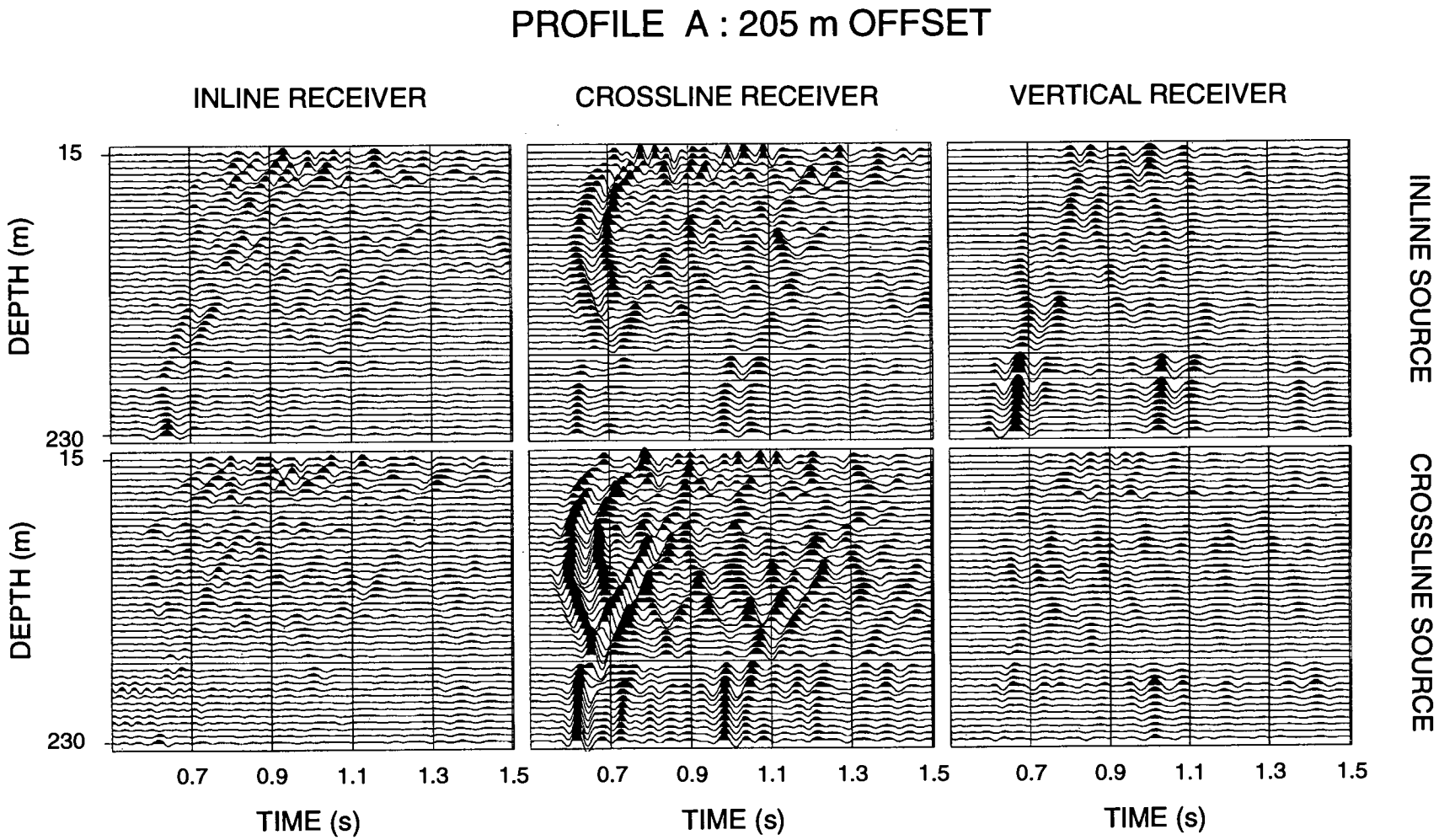

Figure A.9: The processed 205 m-offset VSP from Profile A. Shear waves can be clearly seen on the horizontal components.

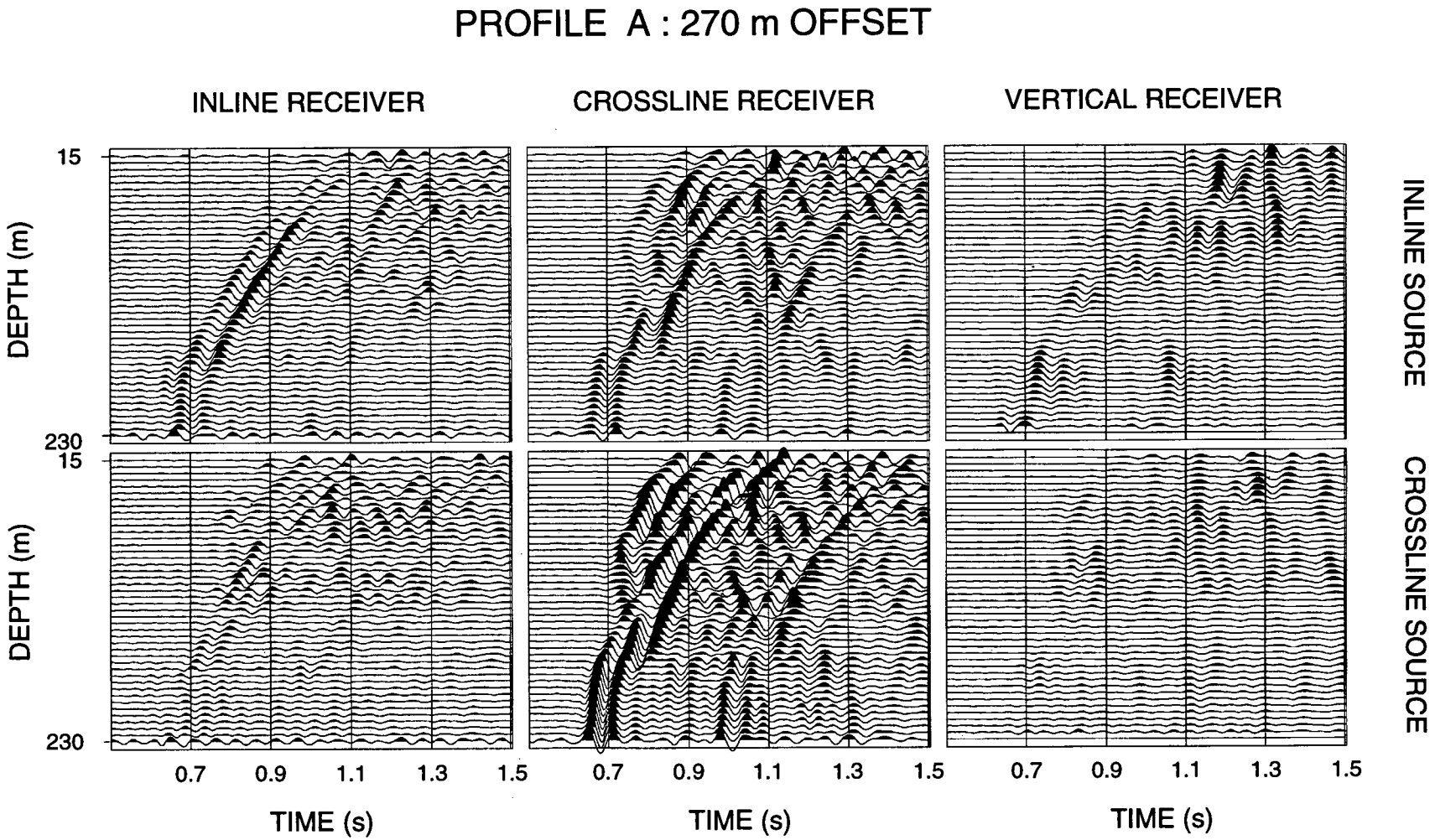

Figure A.10: The processed 270 m-offset VSP from Profile A. Shear-wave can be clearly seen on the horizontal seismograms. Note that almost all the observable shear-wave energy is upgoing.

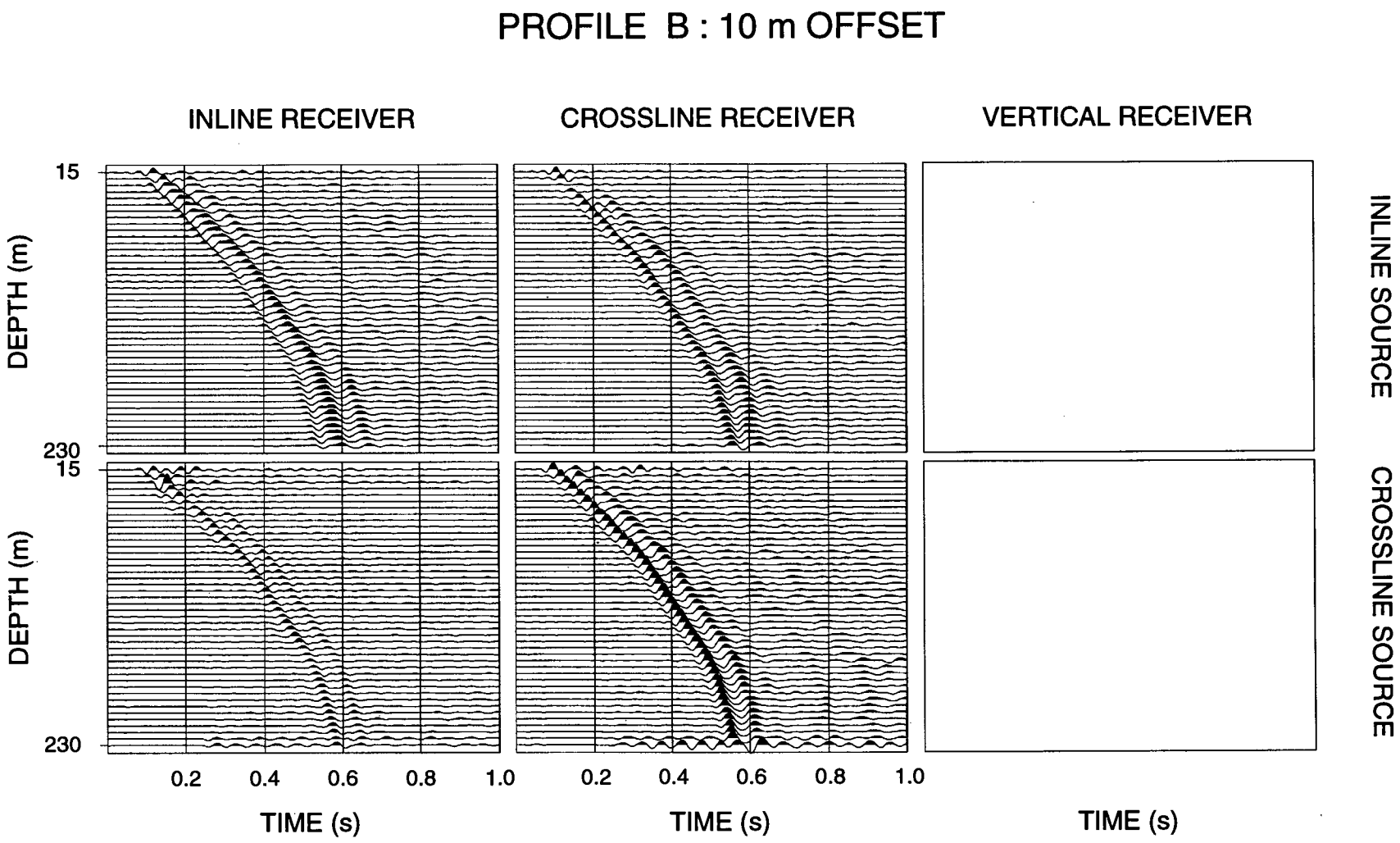

Figure A.11: The processed 10 m-offset VSP from Profile B. Shear waves can be clearly seen on the horizontal components. The vertical components for this offset are badly affected by noise spikes and are therefore not displayed. Note the apparent polarity difference difference between the two main diagonal components.

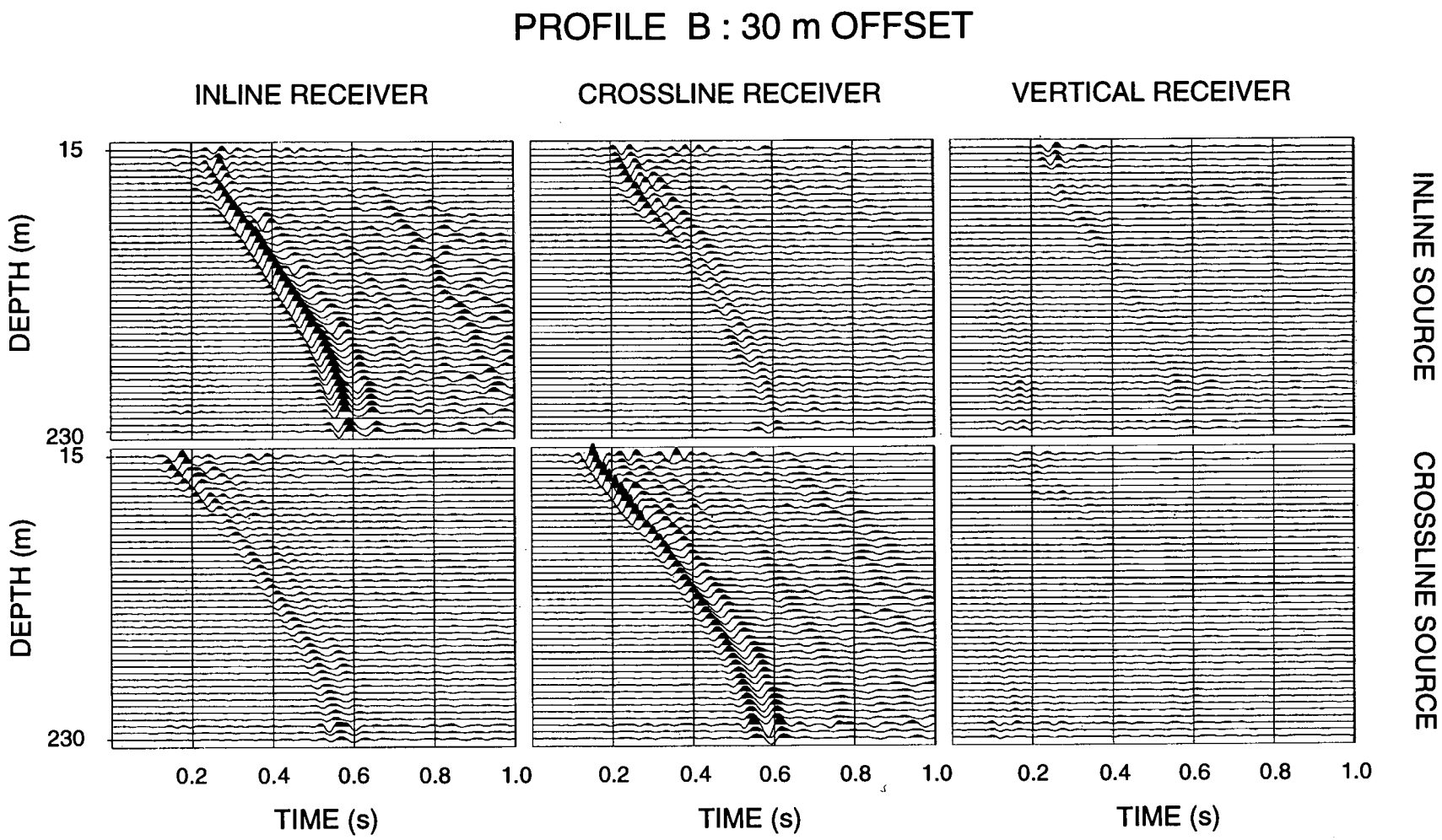

Figure A.12: The processed 30 m-offset VSP from Profile B. Shear waves can be clearly seen on the horizontal components. Very little shear-wave energy is present on the vertical components.

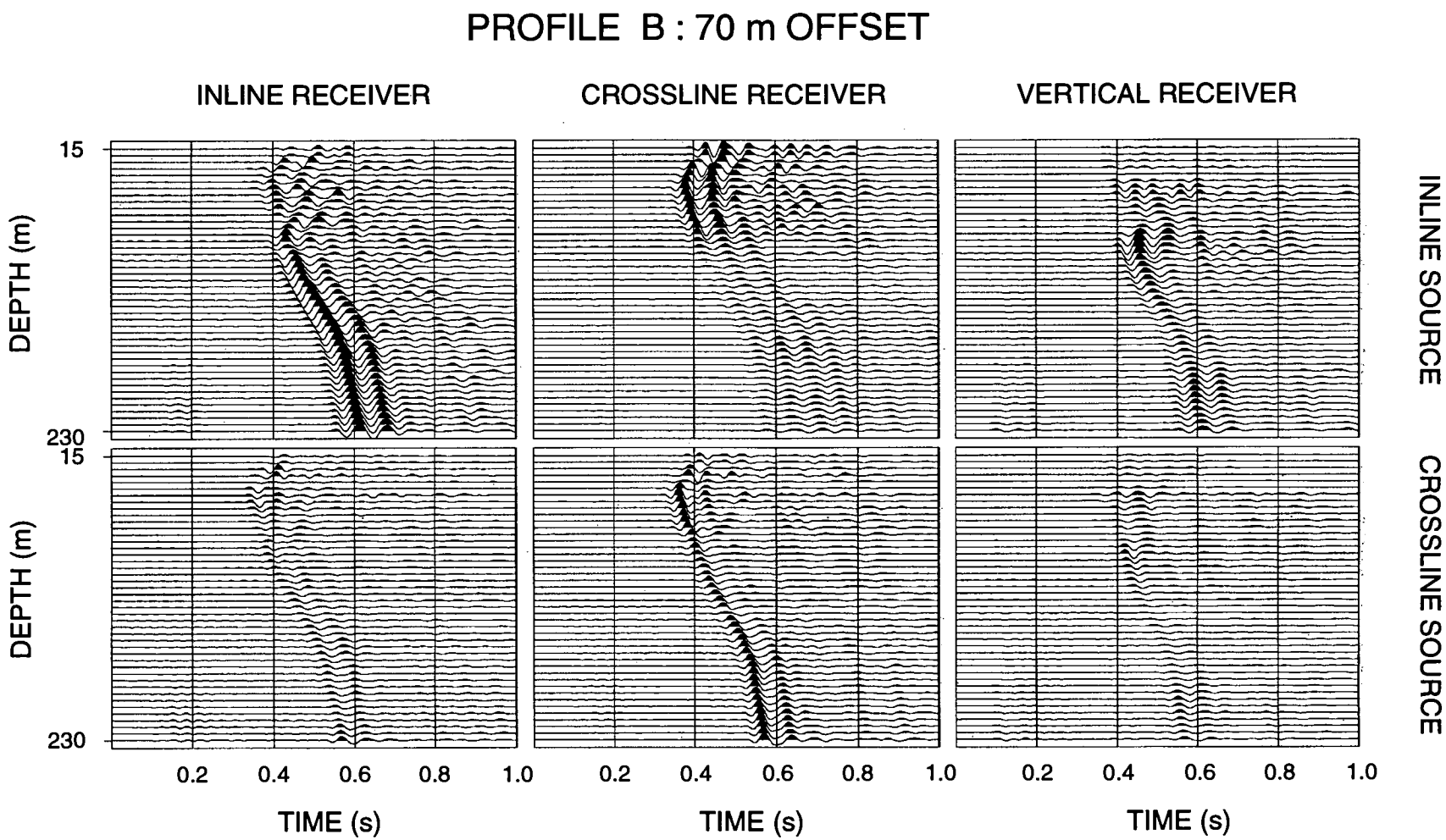

Figure A.13: The processed 70 m-offset VSP from Profile B. Shear-waves can be clearly seen on the horizontal components. The vertical components contain some shear-wave energy, particularly from the inline source. Note the apparent polarity difference between the two main diagonal components.

the near-offset VSPs along Profile B (Figures A.11 to A.13), the arrivals on the inline-inline and crossline-crossline components have opposite polarities, although along Profile A (Figures A.5 to A.7) they have the same polarity. This may indicate that the sources and receivers do not share the same coordinate system for Profile B and, therefore, a switch of the "handedness" of either sources or receivers may be necessary when applying the DIT technique in Section A.6.

A.5 IDENTIFICATION OF TIV ANISOTROPY

Sedimentary rocks have been found to display seismic anisotropy with orthorhombic or lower symmetry (Bush and Crampin, 1991). This is commonly believed to be caused by a combination of subvertical cracks (aligned by the stress field) embedded in a TIV structure (which results from thin-layering or aligned clay platelets). In this section, I investigate whether there is a component of TIV in the near-surface at the test site. I do this by obtaining an isotropic (vertical) velocity model from the 10 m-offset VSP and then modelling arrival times in one of the far-offset VSPs.

A.5.1 Isotropic Velocity Structure

I calculated an isotropic shear-wave velocity structure from the arrival times in the 10 m-offset VSP along Profile B using the method described by Pujol, Burridge and Smithson (1985). The depths of layer boundaries where chosen by examining the arrival-time depth gradient in the VSPs and also by identifying the depths at which significant reflections were generated in the far-offset VSPs. The velocity structure I obtained is shown in Fig. A.2 and ray tracing of direct shear waves through this structure is shown in Fig. A.14.

Using the isotropic velocity model and densities calculated from the empirical relationship of Gardner, Gardner and Gregory (1974), I calculated synthetic seismograms for the 140 m-offset VSP for a crossline source which produces SH arrivals. The observed and synthetic seismograms are shown in Figures A.15a and A.15b. The isotropic model produces a large misfit to the observations, with a maximum difference of about 150 ms. A similar difference in arrival-time was observed along the second profile. This suggests that the shear-wave velocity is

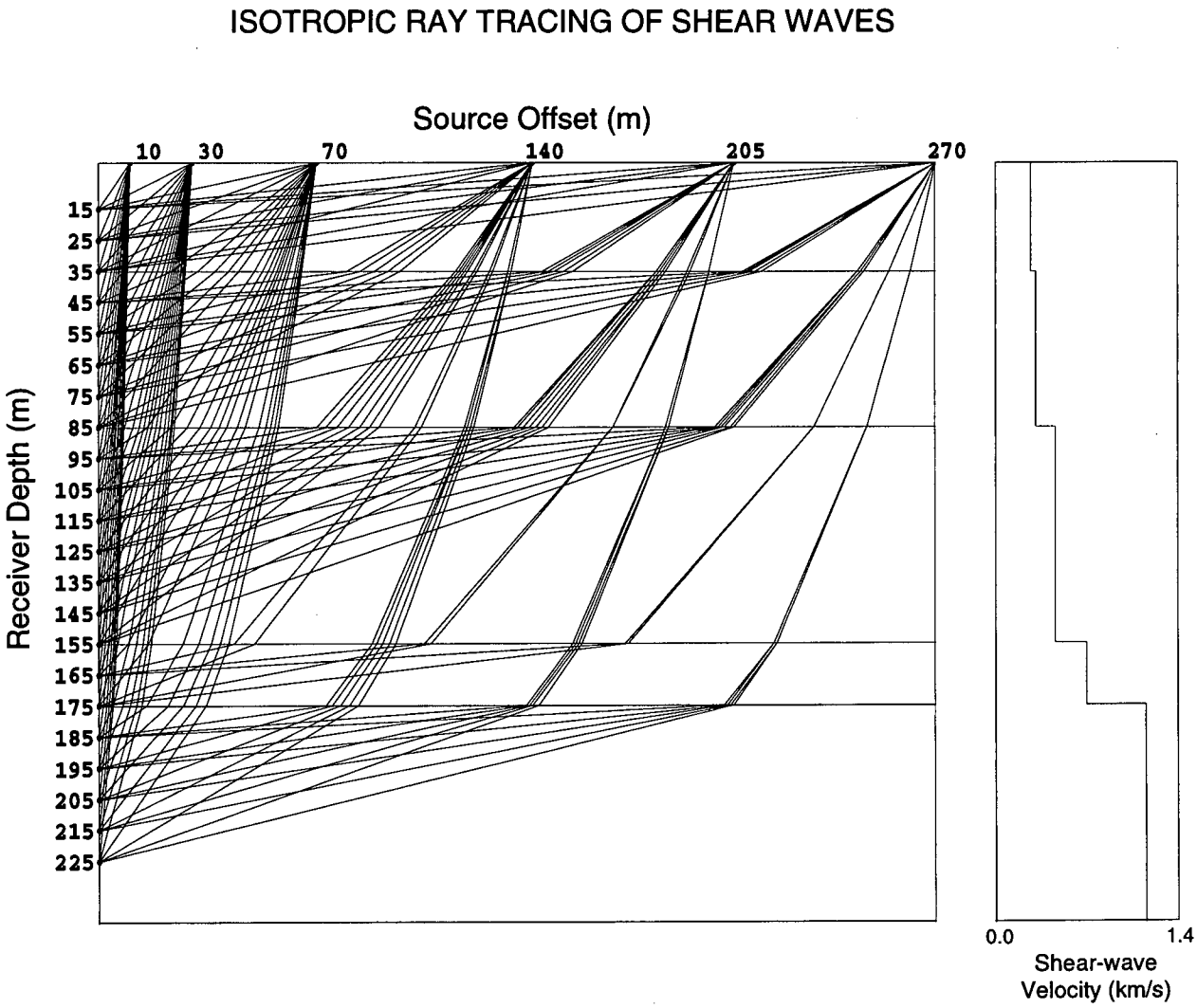

Figure A.14: Isotropic ray tracing of shear-waves through the velocity structure determined from the 10 m-offset VSP. For clarity of display, only raypaths to every second receiver are shown.

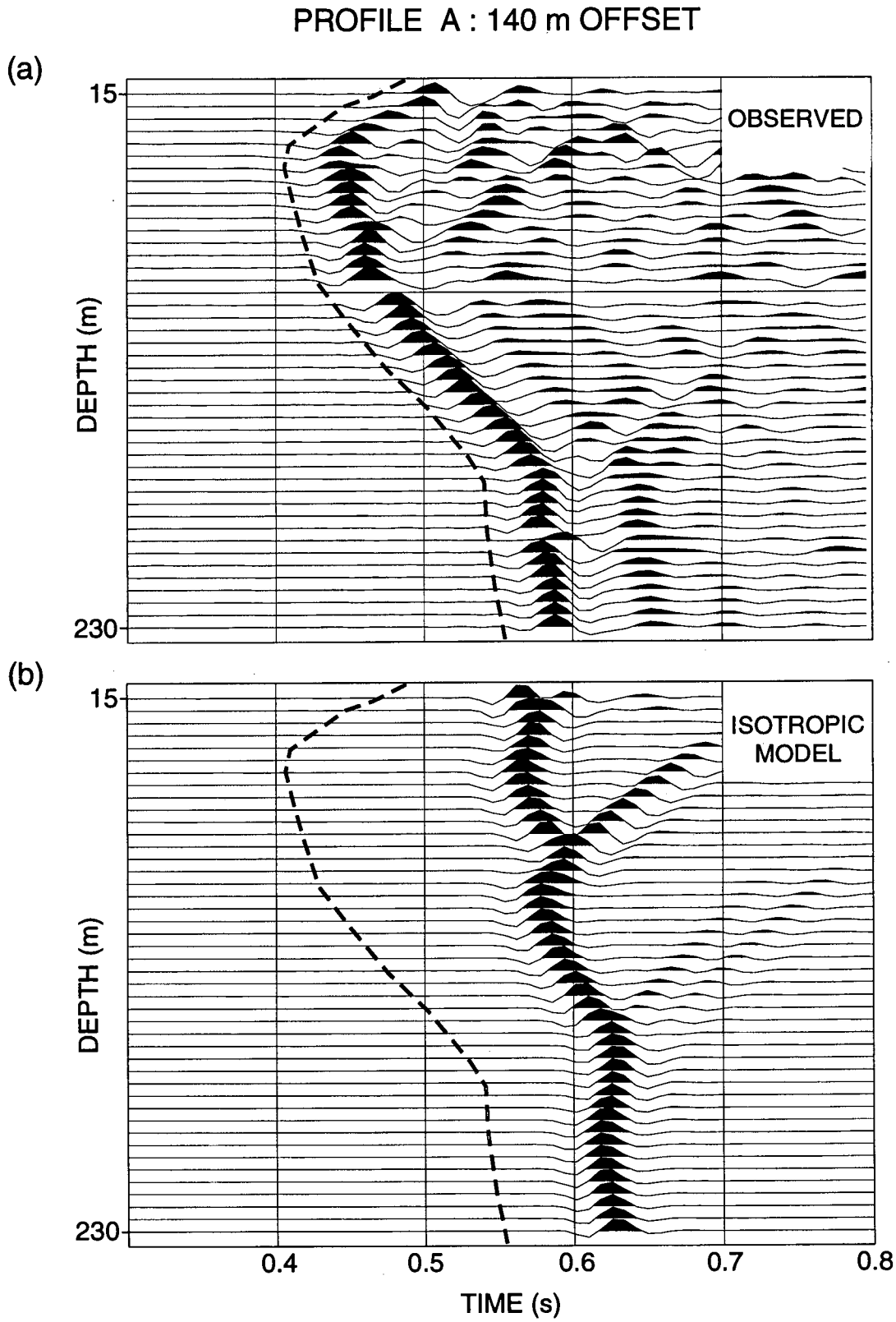

Figure A.15: Testing the isotropic model for the 140 m-offset VSP along Profile A: (**a**) observed shear-wave arrivals recorded by the crossline receiver from the crossline source and (**b**) synthetic seismograms computed using the isotropic velocity structure in Fig. A.2. For comparison of arrival times, the dashed lines indicate the approximate onset of the first trough in (a).

significantly greater along high incidence raypaths than along vertical raypaths and that the near-surface clays have a significant strong component of TIV. In the next section I attempt to model the arrival times using a structures characterized by TIV.

A.5.2 TIV Anisotropy

I could not estimate any qP-wave anisotropy. This is because errors in arrival-times estimation are relatively large for the faster qP-wave velocities. Also, I could not estimate the qSV parameters of the TIV because at large offsets the SV signal-to-noise ratio is too small. However, in a TIV medium the SH wave is completely decoupled from the qP and qSV waves, therefore, it is possible to demonstrate that TIV exist using the comparatively high amplitude SH arrivals, although not all parameters of the TIV model are constrained.

Starting with the uppermost layer of the isotropic velocity model in Fig. A.2 and working downwards, I increased the SH anisotropy in each layer until a reasonable match was found to the 140 m-offset VSP observations in that layer. I found that a good fit to the observed SH arrival times is observed for models with SH anisotropy equal to 20% in the top layer, 32% in the second layer, and 44% in the three lowest layers. The synthetic seismograms from this TIV model are shown in Fig. A.16 and give a close fit to the observed arrival times.

A.6 ESTIMATION OF SHEAR-WAVE SPLITTING PARAMETERS

In this section, I attempt to detect and quantify azimuthal anisotropy by applying the shear-wave splitting estimation technique, DIT, to the VSP seismograms. It can been seen in the ray tracing diagram in Fig. A.14, that the shear waves from the three farthest offsets are likely to have large incidence angles for all receiver depths. Consequently, I restrict the application of DIT to the 10 m-, 30 m- and 70 m-offset VSPs on Profiles A and B. Results will be shown for estimation within the horizontal plane, however, measurements were also made in the dynamic plane, but there was insignificant improvement due to the lack of shear-wave energy on the vertical components.

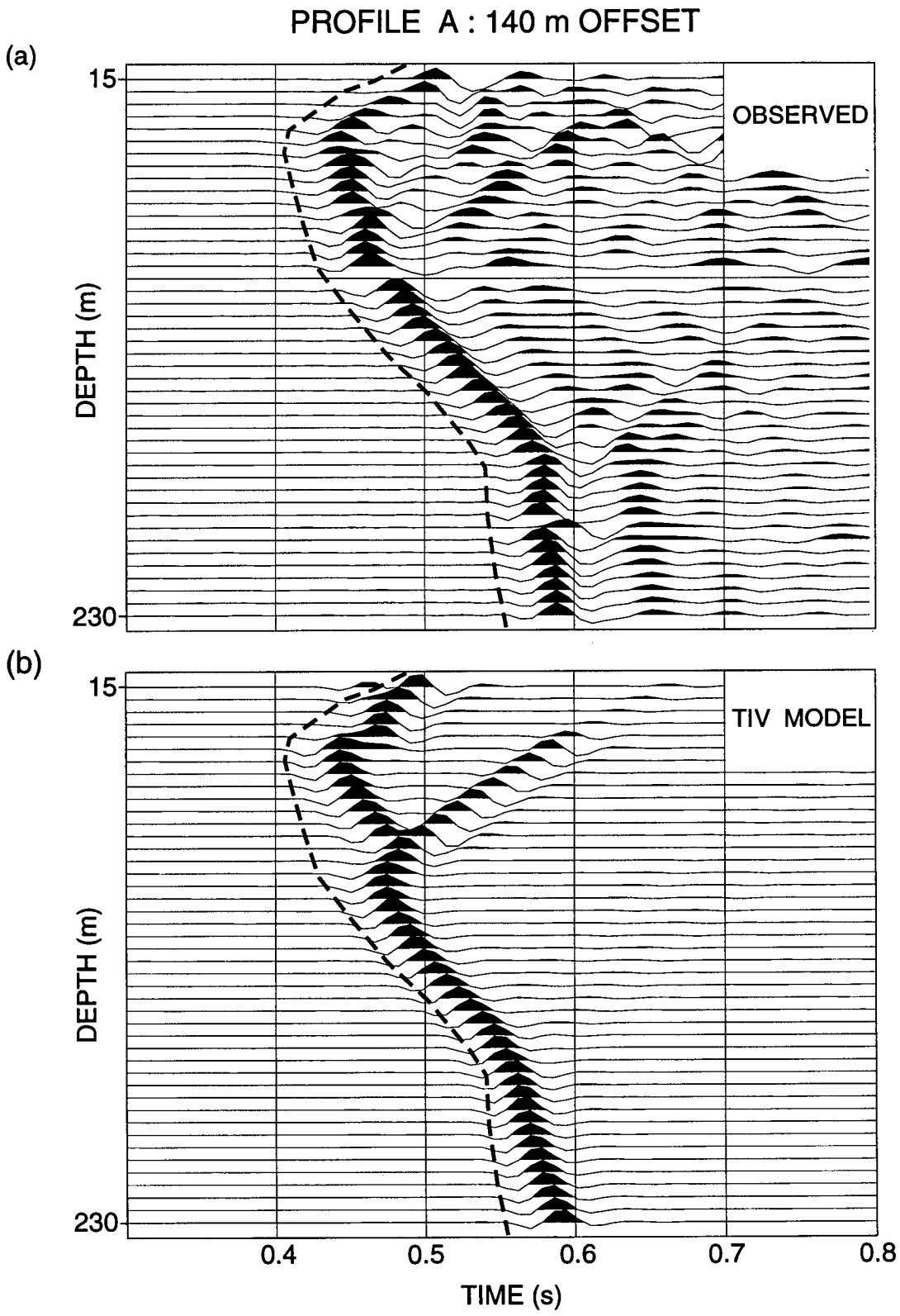

Figure A.16: Matching of SH arrival times in the 140 m-offset VSP from Profile A: (**a**) observed shear-wave arrivals recorded by the crossline receiver from the crossline source and (**b**) synthetic seismograms calculated from a TIV model which has up to 44% SH anisotropy. For comparison of arrival times, the dashed lines indicate the onset of the first trough in (a)

The measured *qS1* polarization direction and differential time delay from the VSPs along Profile A are shown in Fig. A.17. In general, the measurements show a reasonable consistency with depth, although in the 10 m- and 30 m- offset VSPs there is a large separation between the two DIT estimates of *qS1* polarization. This separation arises from the strong asymmetry of the horizontal components observed in Figures A.5 and A.6. The cause of the asymmetry is not known, though it may be caused by the near-source inhomogeneity associated with the infilled channels immediately below the surface. The measurements in Fig. A.17 from the 70 m-offset VSP are extremely consistent with depth and show a close agreement between the two estimates of *qS1* polarization direction. The average *qS1* polarization direction in the 70 m-offset VSP is about N90°E. This is perpendicular to the profile and suggests that the source polarizations are aligned with the natural anisotropy directions. In this case the differential time delay is between two shear waves with polarizations parallel to the two sources. Consequently, it could be argued that differences in arrival-time between inline and crossline sources (and, therefore, the "splitting") may be attributed to slight differences in source offset distances or in the triggering delay. However, in the first case this would produce a decrease in time delay with depth. This is clearly not the true for the 70 m-offset VSP results in Fig. A.17. In the second case, a difference in triggering between sources trucks would most likely be a static delay and likewise would not reproduce the increase of time delay observed in the 70 m-offset VSP.

The measurements from Profile B are shown in Fig. A.18. For the VSPs from Profile B, it was found that the DIT source and geophone estimates of polarization agreed if the "handedness" of the sources was flipped, which is compatible with the source-receiver polarity differences identified in Section A.4.2. The measurements from all three source offsets are remarkably consistent with depth. For near-vertical propagation in the 10 m-offset VSP the measurements indicate a *qS1* polarization direction of about N70°E. The time delay increase of approximately 10 ms between the depth of 50 m and 230 m in the 10 m-offset VSP corresponds to a vertical shear-wave anisotropy of about 4%. The shear-wave splitting measurements in the 30 m- and 70 m-offset VSPs of Profile B are also remarkably consistent. It may be observed that as the source offset distance is increased, the measured *qS1* polarization direction moves closer to north. In the 70 m-offset VSP along Profile B the *qS1* polarization

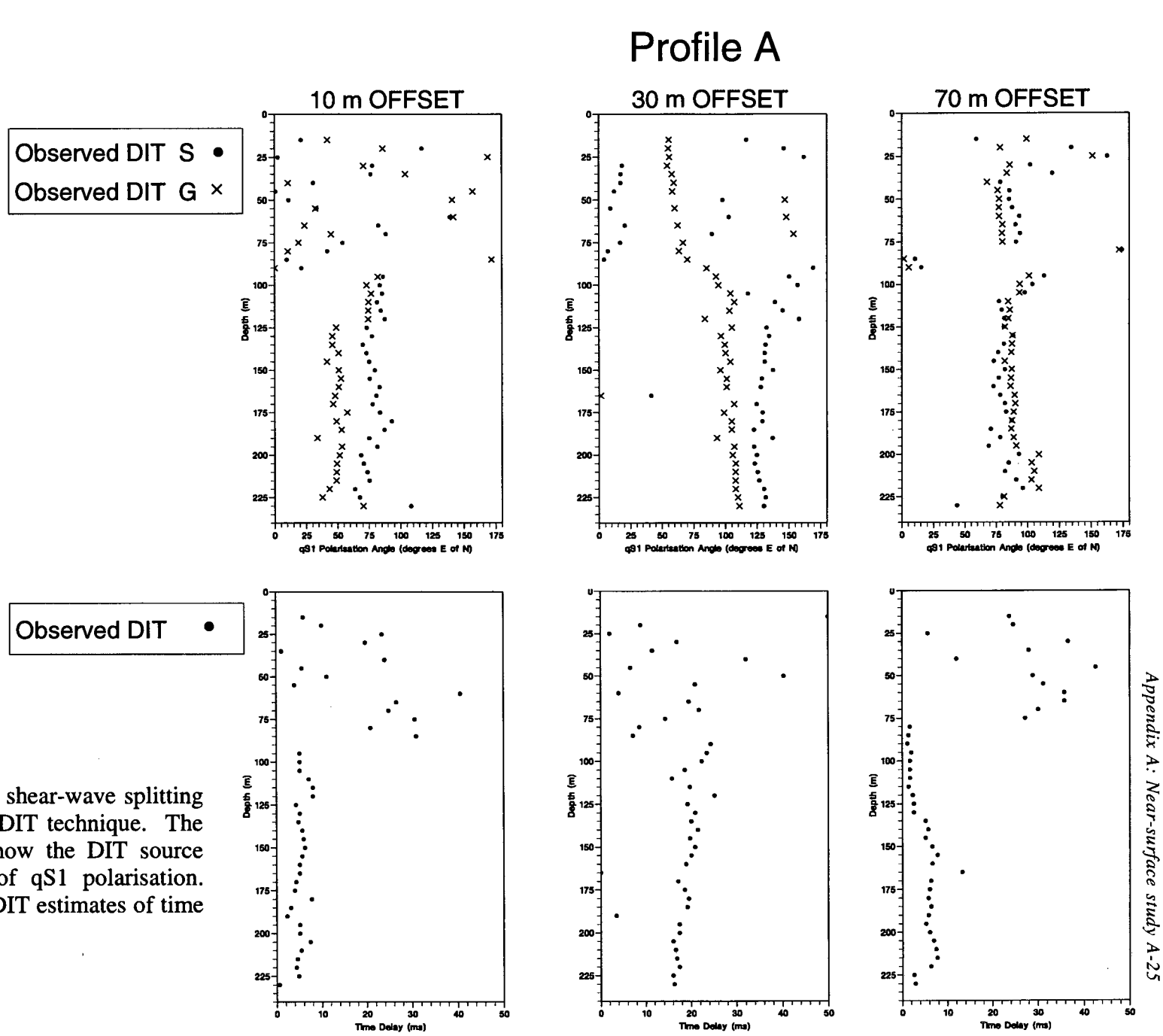

Figure A.17: Estimation of shear-wave splitting along Profile A using the DIT technique. The upper row of diagrams show the DIT source and geophone estimates of qS1 polarisation. The lower row shows the DIT estimates of time delay.

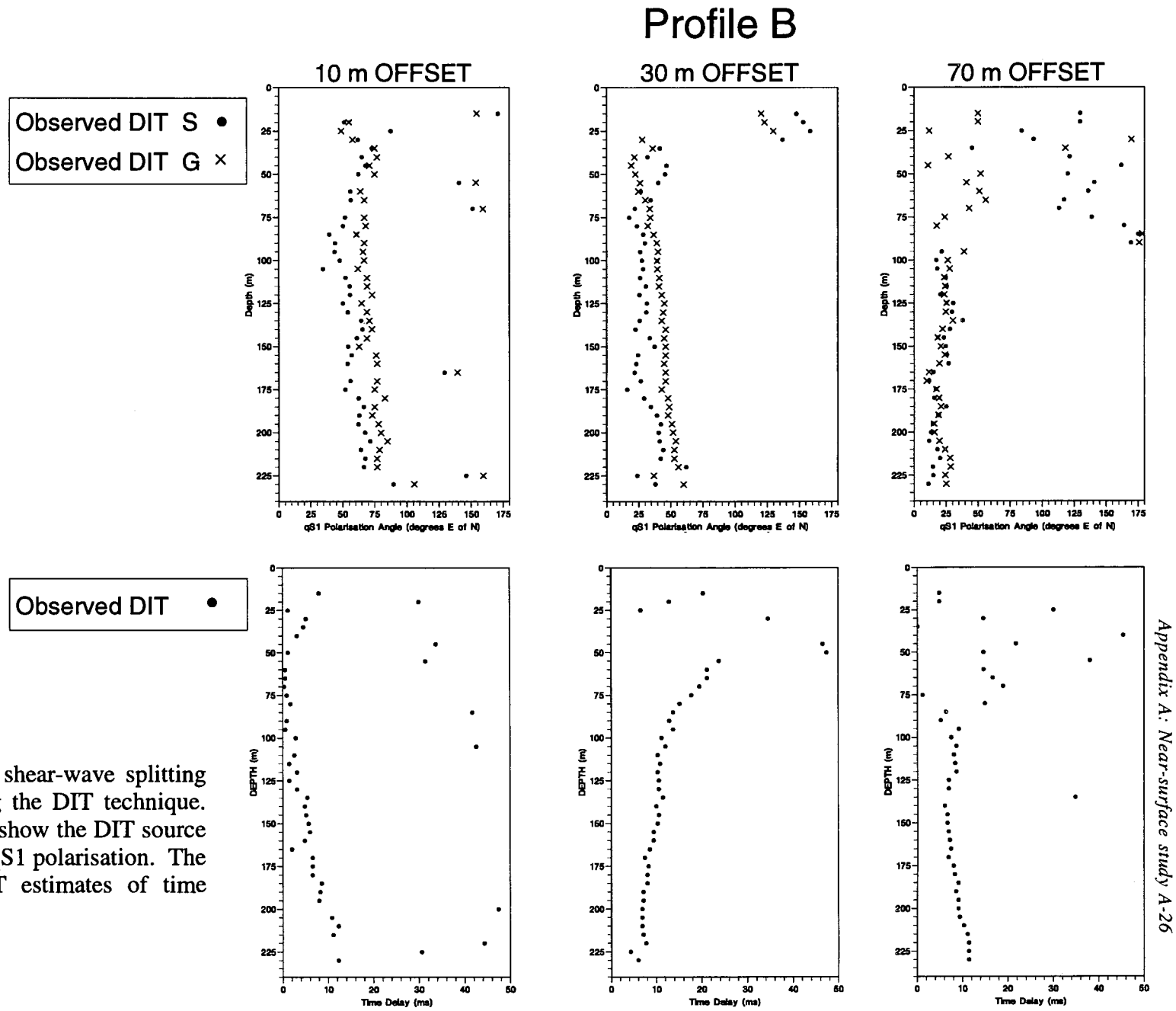

Figure A.18: Estimates of shear-wave splitting from along Profile B using the DIT technique. The upper row of diagrams show the DIT source and geophone estimates of qS1 polarisation. The lower row shows the DIT estimates of time delay.

direction is about 70° from the direction estimated from the 70 m-offset VSP along Profile A.

If the 10 m-, 30 m- and 70 m-offset VSPs from Profile B were actually acquired along Profile A, then the correct *qS1* polarization directions will be different from those shown in Fig. A.18. In Fig. A.19 I compare the measured *qS1* polarizations from Profile A against those from the measurements from Profile B adjusted to acquisition along Profile A, which I denote as Profile A'. If Profile A' is a repeat of Profile A and the data were of good quality the measurements from both profiles should be equal. The polarizations in the 30 m- and 70 m-offset VSPs in Fig. A.19 do show a close agreement below a depth of about 100 m, whereas the 10 m-offset VSPs show significant differences. However, the strong asymmetry in the horizontal components of the 10 m- and 30 m-offset VSPs along Profile A' horizonal components means that this comparison is probably unreliable for these offsets.

A.7 SUMMARY AND CONCLUSIONS

In this study I have processed twelve shear-wave VSPs and obtained shear-wave splitting estimates from six of these VSPs. The differential time delays between split shear waves indicate that within the near-surface at the test site there is azimuthal anisotropy with a velocity anisotropy of about 4% in the vertical direction. However, the inconsistencies in reported acquisition geometry means that no definite conclusions can be made regarding the *qS1* polarization directions.

I have shown that an isotropic layered model, with velocities obtained from vertical propagation in a near-offset VSP, cannot match the arrival-time behaviour in the far-offset VSPs. I interpreted this as an indication of TIV associated with the near-surface clays. Using forward modelling I have shown that TIV models with up to 44% SH anisotropy can match the arrival times. However, it should be noted that, due to inconsistencies in reported source timing statics, the velocities and the SH anisotropy parameters may be inaccurate, although it is unlikely that this would alter the conclusion that there is strong TIV in the near-surface.

The shear-wave splitting measurements and TIV estimation results indicate that the near surface at this well is likely to have orthorhombic or lower symmetry. However, the many acquisition inconsistencies and unknown parameters, such as

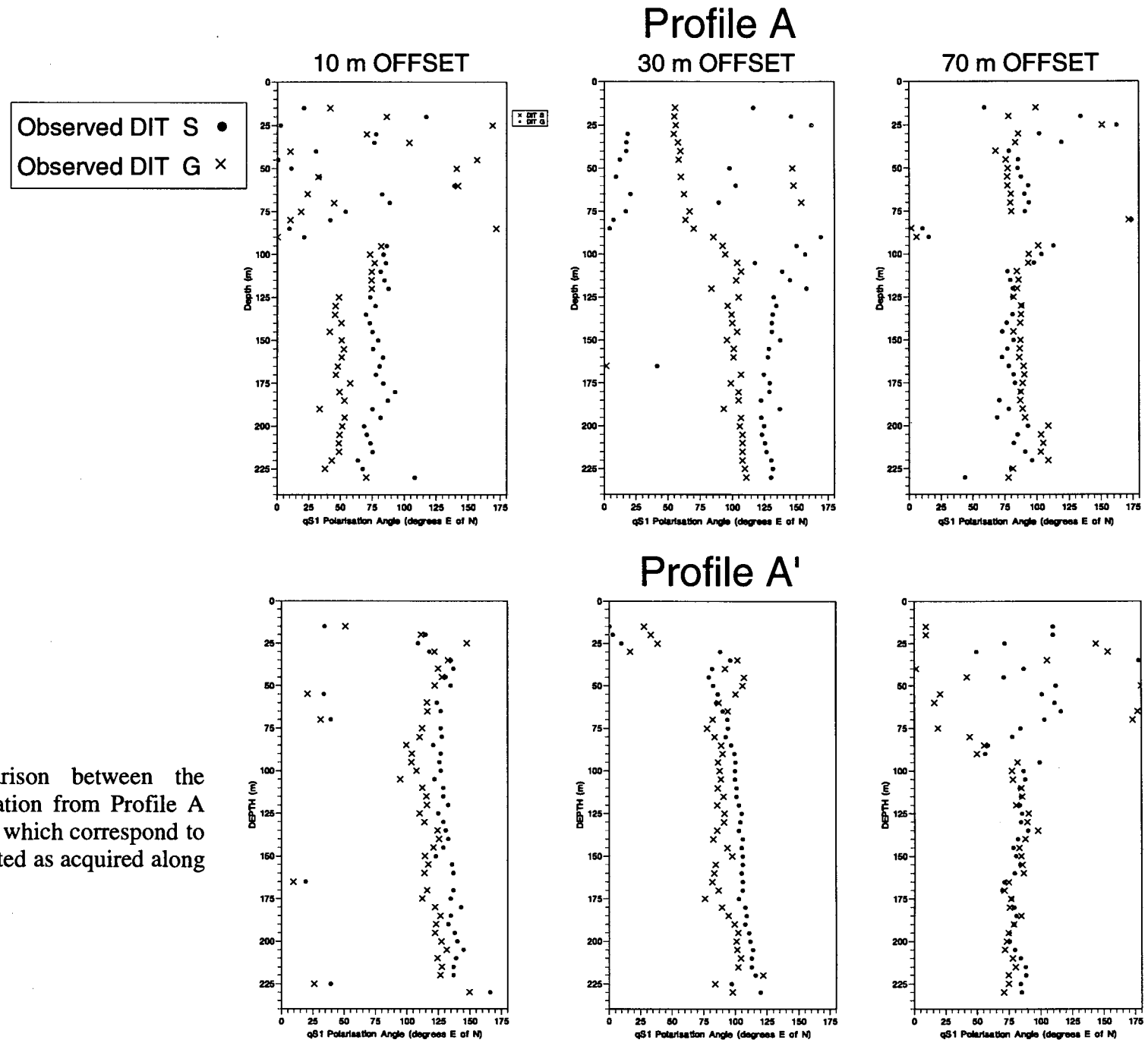

Figure A.19: Comparison between the estimates of qS1 polarization from Profile A and those from Profile A' which correspond to the VSPs originally reported as acquired along Profile B.

source and receiver polarities, means that no definite conclusions can be made from these data at the moment. It appears, however, that the shear-wave source and borehole conditions at the test site are favourable for determining anisotropy of the near-surface. Given the high quality of data, it is probable that, if additional information from say observer's logs were available, firm conclusions could be obtained from these data in the future.

REFERENCES

Adamia, SH.A., Chkhotua, T., Kekelia, M., Lordkipanidze, M. and Shavishvili, I., 1981, Tectonics of the Caucasus and adjoining regions: implications for the evolution of the Tethys ocean: *Journal of Structural Geology*, **3**, 4, 437-447.

Aguilera, R., 1980, *Naturally fractured reservoirs*: PennWell Publishing Company, Tulsa, Oklahoma.

Alford, R.M., 1986, Shear data in the presence of azimuthal anisotropy, Dilley, Texas: *56th Annual SEG Meeting, Houston, Expanded Abstracts*, 476-479.

Backus, G., 1962, Long-wave elastic anisotropy produced by horiontal layering: *Journal of Geophysical Research*, **67**, 4427-4440.

Banik, N.C., 1984, Velocity anisotropy of shales and depth estimation in the North Sea basin: *Geophysics*, **49**, 1411-1419.

Bochkarev, A.V., and Yevik, V.N., 1990, Anomalies in Lower Maikopian bituminous clays of the central Precaucasus: *Lithology and Mineral Resources (U.S.S.R.)*, **25**, 46-54.

Booth, D.C. and Crampin, S., 1983, The anisotropic reflectivity technique: theory: *Geophysical Journal of the Royal Astronomical Society*, **72**, 755-766.

Brodov, L.Y., Evstifeyev, V.I., Karus, E.V. and Kulichikhina, T.N., 1984, Some results of the experimental study of sedimentary rocks using different types of waves: *Geophysical Journal of the Royal Astronomical Society*, **76**, 191-200.

Brodov, L.Y., Zatsepin, S.V. and Tertychniyi, V.V., 1992, Kinematic inversion of seismic data for determination of crack and pore structure in anisotropic reservoir rock, *Presented at 5th Int.Workshop on Seismic Anisotropy, Banff, 1992*, Abstract No.22.

Bush, I., 1990, Modelling shear-wave anisotropy in the Paris basin: *Ph.D Thesis*, University of Edinburgh.

Bush, I. and Crampin, S., 1991, Paris Basin VSPs: case history establishing combinations of matrix- and crack-anisotropy from modelling shear wavefields near point singularities, *Geophysical Journal International*, **107**, 433-447.

Campden, D.A., 1990: Analysis of multicomponent VSP data for shear-wave anisotropy: *Ph.D. Thesis*, University of Edinburgh.

Castagna, J.P., Batzle, M.L. and Eastwood, R.L., 1985, Relationships between compressional-wave and shear-wave velocities in clastic silicate rocks: Geophysics **50**, 571-581.

Chepak, G.N., Shaposhnikov, V.M., Naryzhnyy, P.S., Markov, V.F., and Goshokov, K.I., 1983, Oligocene petroliferous clay series in eastern Cis-Caucasia [in Russian]: *Geologiya-Nefti-i-Gaza*, **8**, 36-40.

Cliet, Ch., Brodov, L., Tikhonov, A., Marin, D. and Michon, D., 1991, Anisotropy survey for reservoir definition: *Geophysical Journal International*, **107**, 415-427.

Crampin, S., 1977, A review of the effects of anisotropic layering on the propagation of seismic waves: *Geophysical Journal of the Royal Astronomical Society*, **49**, 9-27.

Crampin, S., 1981, A review of wave motion in anisotropic and cracked elastic-media: *Wave Motion*, **3**, 343-391.

Crampin, S., 1983, Shear wave polarizations: A plea for three-component recording: *53rd SEG Annual Meeting, Expanded Abstracts*, 425-428.

Crampin, S., 1985, Evaluation of anistropy by shear-wave splitting: *Geophysics*, **50**, 141-152.

Crampin, S., 1986, Anisotropy and Transverse Isotropy: *Geophysical Prospecting*, **34**, 94-99.

Crampin, S., 1987, Geological and industrial implications of extensive dilatancy anisotropy: *Nature*, **328**, 491-496.

Crampin, S., 1989, Suggestions for a consistent terminology for seismic anisotropy: *Geophysical Prospecting*, **37**, 753-770.

Crampin, S., 1990, Alignment of near-surface inclusions and appropriate crack geometries for geothermal hot-dry-rock experiments: *Geophysical Prospecting*, **38**, 621-631.

Crampin, S., 1993a, A review of the effects of crack geometry on wave propagation through aligned cracks: *Canadian Journal of Exploration Geophysics*, **29**, 3-17.

Crampin, S., 1993b, Arguments for EDA: *Canadian Journal of Exploration Geophysics*, **29**, 18-30.

Crampin, S., 1994, The fracture criticality of crustal rocks: *Geophysical Journal International*, **118**, 428-438.

Crampin, S., Bush, I., Naville, C. and Taylor, 1986, Estimating the internal structure of reservoirs with shear-wave VSP's: *The Leading Edge*, **5**, 35-39.

Crampin, S., Chesnokov, E.M. and Hipkin, R.G., 1984, Seismic anisotropy - the state of the art: II, *Geophysical Journal of the Royal Astronomical Society*, **76**, 1-16.

Crampin, S., Evans, R. and Atkinson, B.K., 1984, Earthquake prediction: a new physical basis: *Geophysical Journal of the Royal Astronomical Society*, **76**, 147-156.

Crampin, S. and Lovell, J.H., 1991, A decade of shear-wave splitting in the Earth's crust: what does it mean? what use can we make of it? and what should we do next?: *Geophysical Journal International*, **107**, 387-407.

Crampin, S., Stephen, R.A. and McGonigle, R., 1982, The polarization of P-waves in anisotropic media: *Geophysical Journal of the Royal Astronomical Society*, **68**, 477-485.

Crampin, S., and Zatsepin, S.V., 1995, A new understanding of shear-wave splitting: *57th Annual EAGE Meeting, Abstracts, Glasgow*, C041.

Crampin, S., Zatsepin, S.V., Slater, C. and Brodov, L.Y., 1996, Abnormal shear-wave polarizations as indicators of pressures and over pressures: *58th Annual EAGE Meeting, Abstracts, Amsterdam*, X038.

Daley, P.F. and Hron, F., 1977, Reflection and transmission coefficients for transversely isotropic media: *Bulletin of the Seismological Society of America*, **67**, 661-675.

Dellinger, J. and Vernik, L., 1994, Do traveltimes in pulse-transmission experiments yield anisotropic group or phase velocities?: *Geophysics*, **59**, 1774-1779.

Douma, J., Den Rooijen, H. and Schokking, F., 1990, Anisotropy detected in shallow clays using shear-wave splitting in a VSP survey: *Geophysical Prospecting*, **38**, 983-998.

Eshelby, J.D., 1957, The determination of the elastic field of an ellipsoidal inclusion and related problems: *Proceedings of the Royal Society of London*, **A**, 241, 376-396.

Evans, R., 1984, Effects of the free surface on shear wavetrains: *Geophysical Journal of the Royal Astonomical Society*, **76**, 165-172.

Galperina, R.M. and Galperin, E.I., 1987, Experimental study of shear-waves from shots in anisotropic media: *Geophysical Journal of the Royal Astronomical Society*, **91**, 517-533.

Gamkrelidze, I.P., 1986, Geodynamic evolution of the Caucasus and adjacent areas in Alpine time: *Tectonophysics*, **127**, 261-277.

Gardner, G.H.F., Gardner, L.W. and Gregory, A.R., 1974, Formation velocity and density - the diagnostic basics for stratigraphic traps: *Geophysics*, **39**, 770-780.

Hardage, B.A., 1985, Vertical seismic profiling Part A: Principles: In *Handbook of Geophysical Exploration, Section I. Seismic Exploration, Volume 14A*, K.

Helbig and S. Treitel (eds), Geophysical Press.

Helbig, K, 1994, *Foundations of anisotropy for exploration seismics*: Elsevier Science Ltd, Oxford.

Hornby, B.E., Schwartz, L.M. and Hudson, J.A., 1994, Anisotropic effective-medium modeling of the elastic properties of shales: *Geophysics*, **59**, 1570-1583.

Hudson, J.A., 1986, A higher order approximation to the wave propagation constants for a cracked solid: *Geophysical Journal of the Royal Astronomical Society*, **87**, 265-274.

Hudson, J.A., 1991, Crack distributions which account for a given seismic anisotropy: *Geophysical Journal International*, **104**, 517-521.

Igel, H. and Crampin, S., 1990, Extracting shear wave polarizations from different source orientations: synthetic modelling: *Journal of Geophysical Research*, **95**, 11283-11292.

Johnston, J.E. and Christensen, N.I., 1995, Seismic anisotropy of shales: *Journal of Geophysical Research*, **100**, 5991-6003.

Jolly, R.N., 1956, Investigation of shear waves: *Geophysics*, **21**, 905-938.

Jones, L.E.A, and Wang, H.F., 1981, Ultrasonic velocities in Cretaceous shales from the Willistin basin: *Geophysics*, **46**, 288-297.

Kaarsberg, E.A., 1959, Introductory studies of natural and artificial argillaceous aggregates by sound-propagation and X-ray diffraction methods: *Journal of Geology*, **67**, 447-472.

Kaarsberg, E.A., 1968, Elasticity studies of isotropic and anisotropic rock samples: *Transactions of the Society of Mining Engineers*, **241**, 470-475.

Kanasewich, E.R., 1981, *Time series analysis in geophysics*: The University of Alberta Press, Edmonton, Alberta.

Kerner, C., Dyer, B. and Worthington, M., 1989, Wave propagation in a vertical transversely isotropic medium: field experiment and model study: *Geophysical Journal*, **97**, 295-309.

Klubova, T.T., 1991, Argillaceous reservoirs of oil and gas: *Petroleum Geology*, **25**, 148-167.

Kunin, N.Ya., Kosova, S.S. and Blokhina, G.Yu., 1990, Seismic-Stratigraphic analysis of sedimentary cover in the eastern Precaucasus: *Lithology and Mineral Resources (U.S.S.R.)*, **24**, 545-557.

Levin, F.K., 1979, Seismic velocities in transversely isotropic media: *Geophysics*, **44**,

918-936.

Lewis, C., Davis, T.L. and Vuillermoz, C., 1991, Three-dimensional multicomponent imaging of reservoir heterogeneity, Silo Field, Wyoming: *Geophysics*, **56**, 12, 2048-2056.

Liu, E. and Crampin, S., 1990, Effects of the internal shear-wave window: comparison with anisotropy induced splitting: *Journal of Geophysical Research*, **95**, 11275-11281.

Lui, E., Crampin, S. and J.H. Queen, 1991: Fracture detection using crosshole surveys and reverse vertical seismic profiles at the Conoco Borehole Test Facility, Oklahoma: *Geophysical Journal International*, **107**, 3, 571-583.

Liu, E., MacBeth, C.D., Pointer, T., Hudson, J.A. and Crampin, S., 1996, The effective elastic compliance of fractured rock: *66th SEG Annual Meeting, Expanded Abstracts, Denver*, 1842-1845.

Love, A.E.H., 1892, *A treatise on the mathematical theory of elasticity*: Cambridge University Press, Cambridge.

Lynn, H.B., 1991, Field measurements of azimuthal anisotropy: First 60 meters, San Francisco Bay area, CA, and estimation of the horizontal stresses' ratio from V_{s1}/V_{s2}: *Geophysics*, **56**, 822-832.

MacBeth, C., 1991, Inverting shear-wave polarizations for anisotropy using three-component offset VSPs: synthetic seismograms: *Geophysical Journal International*, **107**, 3, 571-583.

MacBeth, C., 1993, How can anisotropy be used for reservoir characterization?: *First Break*, **13**, 1, 31-37.

MacBeth, C. and Crampin, S., 1991, Processing of seismic data in the presence of anisotropy: *Geophysics*, **56**, 1320-1330.

MacBeth, C. and Yardley, G.S., 1992, Optimal estimation of crack strike: *Geophysical Prospecting*, **40**, 849-872.

MacBeth, C., Zeng, X., Yardley, G.S. and Crampin, S., 1994, Interpreting data matrix asymmetry in near-offset, shear-wave VSP data: *Geophysics*, **59**, 2, 176-191.

Majer, E.L., McEvilly, T.V., Eastwood, F.S. and Myer, L.R., 1988, Fracture detection using P-wave and *S*-wave vertical seismic profiling at the Geysers: *Geophysics*, **53**, 76-84.

McGonigle, R., and Crampin, S., 1982, A fortran program to evaluate the phase- and group-velocity surface in an anisotropic solid: *Computers and Geoscience*, **8**, 221-226.

Mueller, M.C., 1991, Prediction of lateral variablity in fracture intensity using multicomponent shear-wave surface seismics as a precursor to horizontal drilling in the Austin Chalk: *Geophysical Journal International*, **107**, 3, 409-416.

Musgrave, M.J.P., 1970, *Crystal Acoustics*: Holden Day, San Fransisco.

Musgrave, M.J.P., 1954, On the propagation of elastic waves in aeolotropic media II. Media of hexagonal symmetry: *Proceedings of the Royal Society of London*, **A226**, 356-366.

Nalivkin, D.V., 1973, *Geology of the U.S.S.R.*: Oliver and Boyd, Edinburgh.

Naryzhnyy, P.S., 1986, Forecasting productive reservoir rocks in the Oligocene-Miocene clays of the Caucasus Foreland: for example, in the Zhurav area [in Russian]: In *Forecasting of a geologic profile and explorations of complexly shielded traps*, A.G. Aleksin (ed), Izd. Nauka, Moscow, 126-131.

Nikolayev, P.N., 1979, The stress state and mechanism of deformation of the crust of the Alpine fold region: *International Geology Review*, **21**, 1168-1178.

Nowroozi, A.A., 1971, Seismo-tectonics of the Persian Plateau, eastern Turkey, Caucasus, and Hindu-Kush regions: *Bulletin of the Seismological Society of America*, **61**, 317-341.

Peacock, S., and Crampin, S., 1985, Shear-wave vibrator signals in transversely isotropic shale: *Geophysics*, **50**, 1285-1293.

Philip, H., Cisternas, A., Gvishiani, A. and Gorshkov, A., 1989, The Caucasus: an actual example of the initial stages of continental collision: *Tectonophysics*, **161**, 1-21.

Postma, G.W., 1955, Wave propagation in a stratified medium: *Geophysics*, **20**, 780-806.

Pujol, J., Burridge, R. and Smithson, S.B., 1985: Velocity determination from offset vertical seismic profiling data: *Journal of Geophysical Research*, **90**, 1871-1880.

Puzirev, N.N. and Brodov, L.Y., 1969, Efficient SH-wave generation, *Geologika Geofizika*, **5**, 81-88.

Puzirev, N.N.,Trigubov, A.V. and Brodov, L.Y., 1985, *Seismic prospecting methods in shear and converted waves (in Russian)*: Nedra, Moscow.

Riznichenko, Y.V., 1949, On seismic quasi-anisotropy (In Russian), Izv. Akad. Nauk. USSSR, Series Geografika Geofizika, **13**, 518-544.

Robertson, J.D. and Corrigan, D., 1983, Radiation of a shear-wave vibrator in near-

surface shale, *Geophysics*, **48**, 19-26.

Sayers, C.M., 1994, The elastic anisotropy of shales: *Journal of Geophysical Research*, **99**, 767-774.

Schoenberg, M. 1980, Elastic wave behaviour across linear slip interfaces: *Journal of the Accoustical Society of America*, **68**, 1516-1521.

Schoenberg, M. and Douma, J., 1988, Elastic wave propagation in media with parallel fractures and aligned cracks: *Geophysical Prospecting*, **36**, 571-590.

Slater, C., Crampin, S., Brodov, L.Y., and Kuznetsov, V.M., 1993, Observations of anisotropic cusps in transversely isotropic clay: *Canadian Journal of Exploration Geophysics*, **29**, 216-226.

Slater, C. and Crampin, S., 1994. Modelling near-suface shear-wave anisotropy in clays near Yaroslavl, Russia. *18th UKGA, Liverpool.*

Slater, C, Crampin, S. and Brodov, L. Y., 1994, Near-surface shear-wave anisotropy study using VPS's, Yaroslavl, Russia: *56th Annual EAEG Meeting, Expanded Abstracts, Vienna,*

Taylor, D.B., 1987, Double contour integration for transmissions from point sources through anisoropic layers as used in ROCPAC software: *Geophysical Journal of the Royal Astronomical Society*, **91**, 373-381.

Taylor, D.B., 1994, *ANISEIS MANUAL*, version 5.2, Applied Geophysical Software Inc., Houston, Texas.

Teslenko, P.F. and Korotkov, B.S., 1967, Effect of arenaceous intercalations in clays on their compaction: *International Geology Review*, **9**, 5, 699-701.

Thomsen, L., 1986, Weak elastic anisotropy, *Geophysics*, **51**, 1954-1966.

Uhrig, L.F. and Van Melle, F.A., 1955, Velocity anisotropy in stratified media: *Geophysics*, **20**, 774-779.

Wild, P., and Crampin, S., 1991, The range of effects of azimuthal isotropy and EDA anisotropy in sedimentary basins: *Geophysical Journal International*, **107**, 3, 513-529.

White, J.E., 1982, Computed waveforms in transversely isotropic media: *Geophysics*, **47**, 771-783.

White, J.E., Martineau-Nicoletis, L. and Monash, C., 1983, Measured anisotropy in Pierre shale: *Geophysical Prospecting*, **31**, 709-725.

Yardley, G., 1994, Processing and modelling of shear-wave VSPs in anisotropic structures: case studies: *Ph.D. Thesis*, University of Edinburgh.

Yardley, G. and Crampin, S., 1993, Shear-wave anisotropy in the Austin Chalk, Texas, from multioffset VSP data: case studies: *Canadian Journal of Exploration Geophysics*, **29**, 1, 163-176.

Zatsepin, S.V. and Crampin, S., 1995, Modelling the compliance of in-situ rock- a new formulation for the equation of state: *57th Annual EAGE Meeting, Abstracts*, Glasgow, C042.

Zatsepin, S.V. and Crampin, S., 1997, Modelling the compliance of crustal rock: I-response of shear-wave splitting to differential stress: *Geophysical Journal International*, **129**, in press.

Zeng, X., 1994, Shear-wave VSP data processing for anisotropy: *Ph.D. Thesis*, University of Edinburgh.

Zeng, X. and Macbeth, C., 1993a, Accuracy of shear-wave polarization estimates from near-offset VSP data: *Canadian Jounal of Exploration Geophysics*, **29**, 246-265.

Zeng, X. and Macbeth, C., 1993b, Algebraic processing techniques for estimating shear-wave splitting in near-offset VSP data: theory: *Geophysical Prospecting*, **41**, 1033-1066.

Zoback, M.L., 1992, First- and second-order patterns of stress in the lithosphere: The World Stress Map Project: *Journal of Geophysical Research*, **97**, 11703-11728.

Zonenshain, L.P. and Le Pichon, X., 1986, Deep Basins of the Black Sea and Caspian Sea as remnants of Mesozoic back-arc basins: *Tectonophysics*, **123**, 181-211.

PUBLICATIONS

Slater, C., Crampin, S., Brodov, L.Y. and Kuznetsov, V.M., 1993. Observations of anisotropic cusps in transversely isotropic clays. *Can. J. Expl. Geophys.*, **29,** 227-235.

PRESENTATIONS

Slater, C. and Crampin, S., 1992. Shear-wave anisotropy in the Caucasus oil field, Russia. *Fifth International Workshop on Seismic Anisotropy, Banff, Canada.*

Slater, C. and Crampin, S., 1992. Anisotropy case study: Caucasus oil field, Russia. *European Geophysical Assembly, Edinburgh.*

Slater, C., Crampin, S., Brodov, L.Y. and Kuznetsov, V.M., 1993. Observations of anisotropic cusps in Walkaway VSP's in a clay reservoir in the Juravskoe oil field. *SEG/Moscow '93, Expanded Abstracts.*

Bordov, L.Y., Kuznetsov, V.M., Slater, C. and Crampin, S., 1993. Observations of anisotropic cusps in a clay reservoir. *55th EAEG Meeting, Stavanger, Expanded Abstracts.*

Slater, C. and Crampin, S., 1994. Modelling near-suface shear-wave anisotropy in clays near Yaroslavl, Russia. *18th UKGA, Liverpool.*

Slater, C., Crampin, S. and Brodov, L.Y., 1994. Near-surface shear-wave anisotropy study using VSP's, Yaroslavl area, Russia. *56th EAEG Meeting, Vienna, Expanded Abstracts.*

Crampin, S., Zatsepin, S.V., Slater, C. and Brodov, L.Y., 1996. Abnormal shear-wave polarizations as indicators of high pressures and over pressures. *58th EAGE Meeting, Amsterdam, Expanded Abstracts.*

POSTER PRESENTATIONS

Slater, C., Crampin, S. and Brodov, L.Y., 1994. Near-surface shear-wave anisotropy in clay near Yaroslavl, Russia. *Sixth International Workshop on Seismic Anisotropy, Trondheim, Norway.*

FAX MESSAGE

British Geological Survey
Murchison House
West Mains Road
Edinburgh, EH9 3LA

TEL: +44 (0)131 667 1000
FAX: +44 (0)131 667 1877
EMAIL: c.slater@bgs.ac.uk

ATTENTION: C.J.E.G Editor

FAX NO: 001 403 262 7383
DATE: 24th March, 1997

FROM: Colin Slater

PAGES TO FOLLOW:0

SUBJECT: Permission to Reproduce a Paper

Dear Editor,

please could you grant me permission to reproduce a paper published in the special issue of CJEG for the Fifth International Workshop on Seismic Anisotropy. I would like to attach this paper to my Ph.D. thesis for submission to the University of Edinburgh, U.K.

The paper is:
Slater, C., Crampin, S., Brodov, L.Y. and Kuznetsov, V.M., 1993, Observations of anisotropic cusps in transversely isotropic clay: Canadian Journal of Exploration Geophysics, 29, 216-226.

Yours sincerely,

Colin Slater

Permission Granted 03/24/97
Please make reference to reprinted by per
Heather Bryne
CSEG Office Mgr.

CANADIAN JOURNAL OF EXPLORATION GEOPHYSICS
VOL. 29, NO. 1 (JUNE 1993), P. 216-226

OBSERVATIONS OF ANISOTROPIC CUSPS IN TRANSVERSELY ISOTROPIC CLAY

COLIN SLATER[1], STUART CRAMPIN[1], LEONID Y. BRODOV[2] AND VASILIY M. KUZNETSOV[2]

ABSTRACT

Three-component seismograms from two shear-wave source orientations in eight walkaway VSPs to two wells in the Juravskoe Oil Field in the Caucasus Basin display anisotropic cusps. These are caused by strong transverse isotropy with a vertical axis of symmetry in a 1200 m-thick layer of uniform clay. The arrival times and polarizations of the shear waves, including the cuspidal arrivals, can be matched by full-wave synthetic seismograms in a model with the clay having transverse isotropy with 41% *qSH*-wave and 27% *qSV*-wave anisotropy. These appear to be the first published reports of anisotropic cusps in exploration seismics to be confirmed by matching with synthetic modelling. Techniques for exploring clay reservoirs have not yet been established and such cuspidal arrivals may be useful as they provide additional new signals with new properties for examining structures and tracing the *qSV* wavefront. These experiments are the first to use new techniques designed to optimize acquisition geometry for recording seismic anisotropy.

The experiments also show strong azimuthal variations of anisotropy (affecting source radiation, shear-wave source polarization, traveltime and wavelet shape), known as natural directivity (ND), in the top few hundred metres of the uniform horizontal structure.

INTRODUCTION

In 1991, Neftegeofizika Geolkom, Moscow, Stavropol-Neftegeofizika, Stavropol, and the Edinburgh Anisotropy Project, British Geological Survey, Edinburgh, collaborated in walkaway VSP experiments in two wells, Nos. 85 and 87, in a clay reservoir in the Juravskoe Oil Field in the Caucasus Basin of Russia. Such clay reservoirs are comparatively common in oil fields throughout the Russian Platform and western Siberia and are thought to be present in many areas elsewhere. Clay reservoirs are often characterized by production rates varying from hundreds of tons per day to zero over comparatively short distances. The reservoir we investigate is in the bottom 100 m of a 1200 m-thick layer of uniform clay, and the distribution, orientation and internal structure of the oil-bearing inclusions are clearly crucial to productivity. Techniques for exploring such reservoirs are not yet established, and the primary aim of the collaboration is to use shear waves and shear-wave splitting to extract information about the orientation and characteristics of the oil-filled inclusions in the clay reservoir layer (Brodov et al., 1992) where Well No. 85 is producing and Well No. 87 is not producing. This preliminary report analyzes anisotropic cusps observed in record sections of shear-wave walkaways through the thick clay layer above the reservoir.

The behaviour of shear-wave splitting and anisotropy varies with the azimuth and angle of incidence of the raypath in three dimensions. Consequently, the information about anisotropy that can be extracted from any particular experiment depends critically on the three-dimensional geometry of the source-to-geophone raypaths (Brodov et al., 1992). Depending on the structure and orientation of the anisotropic symmetry, particular record sections may or may not contain the information required, or may possibly duplicate information along other (expensively acquired) record sections. This makes it important to optimize acquisition geometry in relation to what is known about the geological structure and the stress directions and orientation of the anisotropy in order to maximize the information content at minimal cost. Making minimal assumptions about the form of the inclusions, the recording geometry for these VSP walkaways in the Caucasus was optimized using a data-based inversion scheme for anisotropic parameters (MacBeth et al., 1993). These are the first field experiments where acquisition geometry has been optimized for anisotropic information using this technique. Essential features of such geometry, as has long been recognized (Crampin, 1987), are walkaways in directions which are not parallel to the supposed symmetry (stress) directions and source orientations that generate both split shear-wave polarizations.

During the course of the experiment with the optimized geometry anomalously fast *SV*-wave arrivals were identified on all walkaway profiles and recognized as being caused by cusps. This paper confirms, by modelling with full-wave

[1]Department of Geology and Geophysics, University of Edinburgh, Grant Institute, West Mains Road, Edinburgh EH9 3JW; also, Edinburgh Anisotropy Project, British Geological Survey, Murchison House, West Mains Road, Edinburgh EH9 3LA

[2]Neftegeofizika Geolkom, Chernyshevsky Str.22, Moscow 101000

We thank Gareth Yardley and geophysicists from Neftegeofizika and Stavropol-Neftegeofizika for their contributions (and their good company) during the field work. Synthetic seismograms were calculated with the ANISEIS package of Applied Geophysical Software Inc., Houston, and Macroc Ltd., Edinburgh. This research was supported by Neftegeofizika Geolkom, Stavropol-Neftegeofizika, the Sponsors of the Edinburgh Anisotropy Project and the Natural Environment Research Council and is published with the approval of the Director of the British Geological Survey (NERC).

synthetic seismograms, that these anomalous phases are generated by cusps on the *SV*-wave group-velocity surfaces caused by the high differential shear-wave anisotropy. Although cusps are well established theoretically, and are expected in strong anisotropy, there appears to be no reports synthetically modelling cusps in field observations before this study. Previously, Jolly (1956) observed abnormally large *SV*-wave velocities in field observations in (Pierre) shale and offered these, qualitatively, as observations of cusps. Later Levin (1979) presented an explanation of these observations in terms of general cusp arrival time behaviour and White (1982), although not discussing Jolly or Levin's work, shows results on cusp amplitudes which support Levin. The possible importance of exciting cuspidal arrivals for field studies is that they can provide additional signals along raypaths through zones of interest and place further constraints on interpretation of the fluid-filled inclusions without acquiring additional data sets. The terminology we use for describing anisotropy is that suggested by Crampin (1989).

Transverse Isotropy and Cusps

Velocities of both *P*- and *S*-waves propagating obliquely in sedimentary sequences may differ substantially from vertical velocities. This is characteristic of hexagonal anisotropic symmetry, that is transverse isotropy about a vertical symmetry axis leading to azimuthal isotropy. Uhrig and Van Melle (1955) report anisotropy factors as large as $K = 1.4$ for *P*-waves, where $K = V_{horiz}/V_{vert}$, and Brodov et al. (1984) report anisotropy factors for shear waves as large as $K = 1.5$. Brodov et al. note that most argillaceous sediments are transversely isotropic with clays having particularly pronounced shear-wave anisotropy.

Riznichenko (1949) and Postma (1955) showed that such effective transverse isotropy could be caused by (P)eriodic sequences of (T)hin isotropic (L)ayers (PTL anisotropy) with layer thicknesses smaller than the seismic wavelengths. Lithological anisotropy of aligned grains may also cause such transverse isotropy (Kaarsberg, 1968) and, since lithological anisotropy and PTL anisotropy have very similar patterns of elastic constants, it is difficult to separate the cause from their effects on seismic waves. Clays typically display little bedding and the observed transverse isotropy is believed to be caused by the lithology of preferentially aligned grains.

Musgrave (1954) showed theoretically that materials with strong transverse isotropy may have cusps in the *SV*-wave group-velocity surfaces, caused by the high curvature of the *SV*-wave phase-velocity variations. One of the clearest indications of cusps on record sections is anomalously fast arrivals. The only previous publication reporting observations of anisotropic cusps in exploration seismics appears to be Jolly (1956), interpreted by Levin (1979).

Geology of Juravskoe Oil Field

Wells Nos. 85 and 87 are located in the foredeep, north of the Caucasus Mountains, 5 km and 10 km southwest of the village of Blagodarnyy, 100 km east of Stavropol (Figure 1). The flat-lying geology, determined previously by well logs, seismic reflection and VSP surveys, consists of an almost horizontal sequence, about 600 m thick, of Neogene clays, sandstones and limestones overlying the Maikop Series of Middle Oligocene to Lower Miocene rocks (Nalivkin, 1973). The uppermost 200 m of the Maikop in the area of the wells is an alternating sequence of sandstones and clays overlying 1200 m of uniform clay with the reservoir in the lowest 100 m. The velocity structure in Figure 2a, derived from a near-offset VSP, indicates continuous clay below 870 m with a small gradient in *P*-wave velocity and a slightly larger gradient in shear-wave velocity, with V_p/V_s ratios between 2.1 and 3.0. High V_p/V_s ratios between 1.8 and 3.0 are characteristic of clay beds (Castagna et al., 1985). The increase of V_s and decrease in V_p/V_s below 1950 m in the clay reservoir is thought to be caused by the presence of organic-rich material in the clay.

Data Acquisition

The walkaway profiles suggested by the acquisition optimization procedure (MacBeth et al., 1993) were two source polarizations along two azimuths with geophones at two levels in two cased vertical wells, Nos. 85 and 87. We examine the data set from Well No. 85 in this study but all walkaway profiles from both wells show similar features. The geophone levels spanned the 100 m-thick reservoir zone near the bottom of the 1200 m-thick clay layer of uniform clay. Figure 1 shows the layout of the acquisition geometry and Table 1 lists details of the field experiment at Well No. 85.

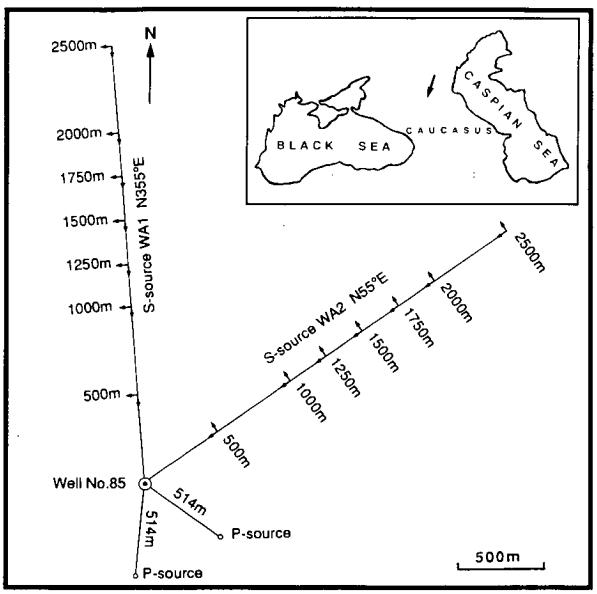

Fig. 1. Location of Caucasus region with arrow marking study area and acquisition geometry for Well No. 85 showing walkaway shear-wave offsets.

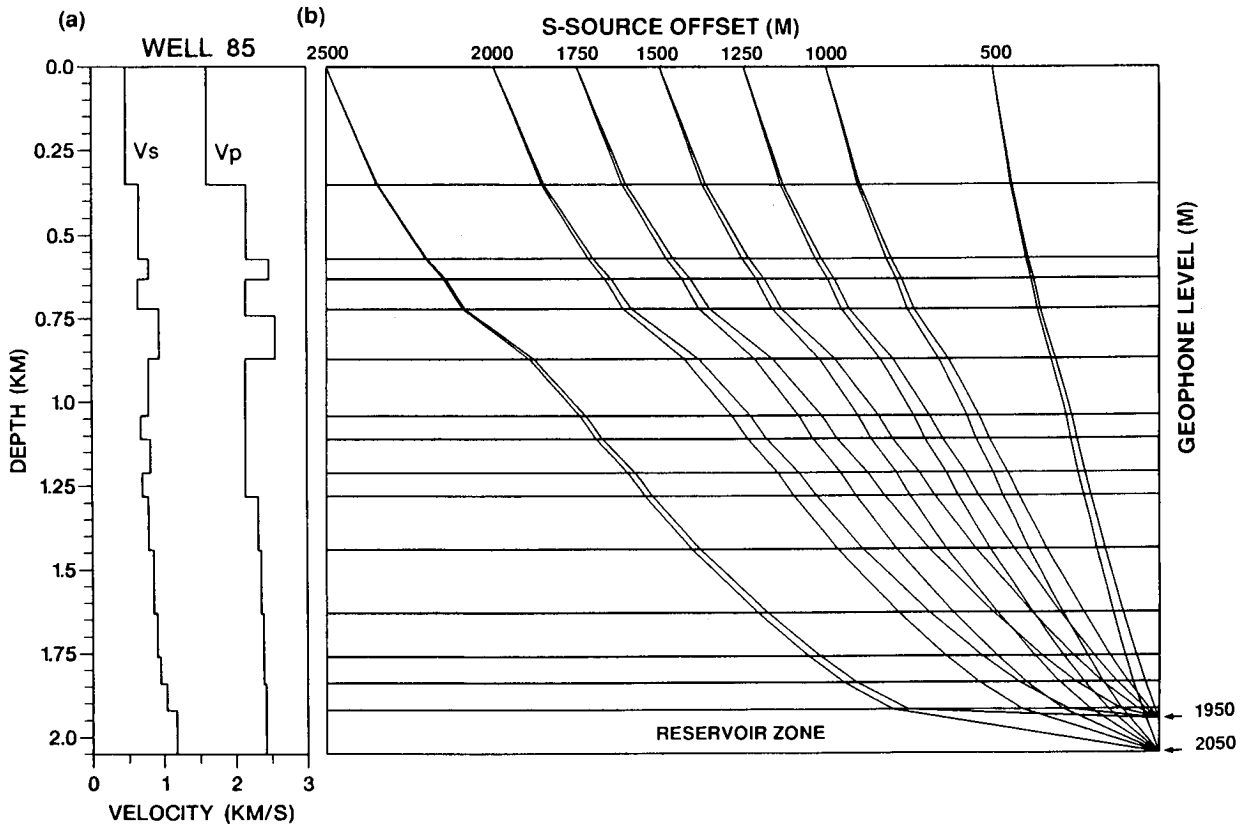

Fig. 2. **(a)** Isotropic velocity structure derived from a near-offset VSP, and **(b)** ray tracing shear waves through the isotropic velocity structure in (a).

Table 1. Details of the field experiment at Well No. 85.

EQUIPMENT AND LAYOUT	
S-wave source	Electrodynamic VEIP-40 truck
Peak frequency	16 Hz
Offset from wellhead	500-2500 m
Azimuth of walkaways	1) N355°E, 2) N55°E
P-wave source	400-g blocks of explosive
Peak frequency	100 Hz
Offset from wellhead	514 m
Azimuth	1) N125°E, 2) N185°E
Geophone system	Orthogonal 3-component, moving coil
Geophone levels	1950 and 2050 m
Field filters	10 Hz low-cut, 50 Hz Notch
Sample rate	1 ms
Record length	6 s

Shear waves were generated with an impulsive electrodynamic source, the VEIP-40 (Table 1), aligned in-line and cross-line to the direction of the wellhead. Since the walkaways were not parallel to stress/symmetry directions such source orientations excited both split shear-wave polarizations. Each truck had three baseplates producing a horizontal force giving impulsive signals with, in this experiment, an effective centre frequency of 16 Hz. The source signals were stacked (up to 32 times for the widest offset with a 3200-m raypath) with left and right source polarizations at each geophone level allowing *P*-wave signals to be cancelled and shear-wave signals enhanced by subtracting seismograms of opposite source polarizations (Puzirev and Brodov, 1969). Correspondingly, *P*-waves were enhanced and shear waves cancelled by adding opposite polarizations. To determine orientations of the downwell geophones, high-energy *P*-waves were generated by explosives in shallow boreholes at offsets of 514 m.

Analysis

Figure 3 shows three-component seismograms for two sources along two walkaways with the geophone at the 1950-m level in Well No. 85. (Note that the offsets along each walkaway are 250 m apart except for the first and last offsets which are 500 m apart.) Since the relative arrival times of phases on different components of the seismic traces, important for this study, are usually well separated displays of polarization diagrams (hodograms) are not informative. We prefer to display these walkaway records as three-component record sections (Figure 3), rather than four-, six- or nine-component matrix displays as has become conventional in

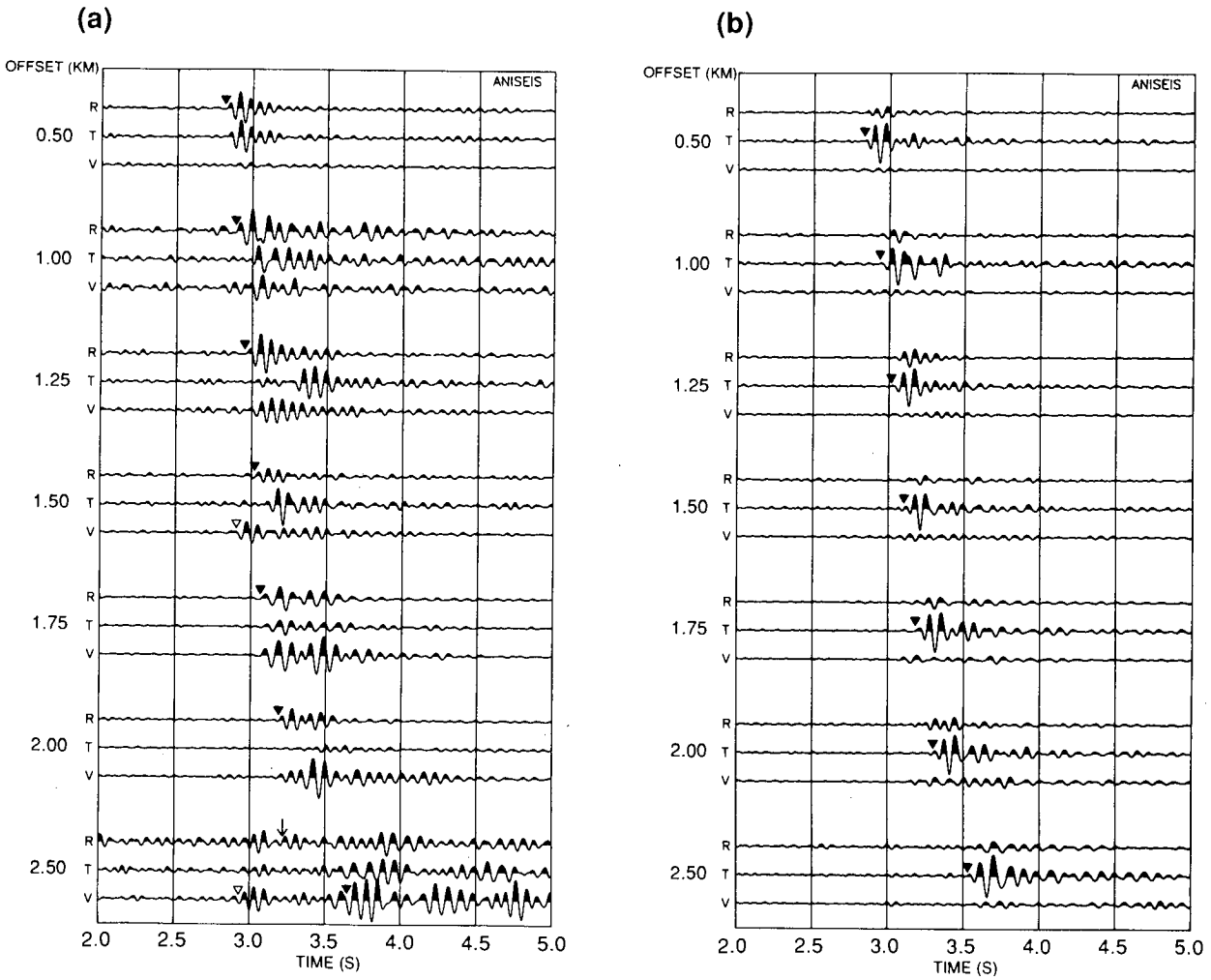

Fig. 3. Three-component seismograms recorded by geophone at 1950-m level for walkaway WA1 at an azimuth of N355°E for **(a)** in-line, and **(b)** cross-line source orientations and for walkaway WA2 at an azimuth of N55°E for **(c)** in-line, and **(d)** cross-line source. Seismograms are (V)ertical and horizontal (R)adial (in-line) and (T)ransverse (cross-line) and time is from origin. Each three-component seismogram is normalized separately. The small solid triangles mark arrival times of the main body-wave phases used to estimate the transverse isotropy and the open triangles mark anomalous arrivals which synthetic seismograms show are generated by a cusp (1500-m offset) and by a shallow *P*-to-*S* conversion (2500-m offset). The arrow (2500-m offset) marks an arrival which synthetic seismograms (Figure 7) show is also cuspidal.

displays of vector data sets where analysis of smaller time separations is required.

The data sets from the two walkaways show many similarities with the largest differences being between the relative amplitudes of the three-component signals. All eight walkaways show very similar features and most of the following comments and modelling results, including observations of cuspidal arrivals, apply equally to all walkaways. There are many anomalous features in Figure 3, particularly the multiple shear-wave arrivals with different velocities (leading to different arrival times) and different polarizations. These multiples have similar arrival times at the corresponding offsets and geophone levels along the different walkaways, but the relative three-component amplitudes vary substantially between offsets and geophone levels and between walkaways (compare the two walkaways in Figure 3).

The arrivals we attempt to model directly are the anomalous fast arrivals at the 1500-m and 2500-m offsets, marked by open triangles. These appear on record sections of both walkaways in Figure 3, and on all other walkaways to all geophone levels, as does the cross-coupling between arrivals on the sagittal plane and the transverse horizontal direction that would not be expected in a flat-layered isotropic or azimuthally isotropic structure. We match the field seismograms with synthetic seismograms by proceeding successively from isotropic models to transversely isotropic to azimuthally anisotropic models. The synthetic seismograms are computed by a reflectivity technique (Taylor, 1990).

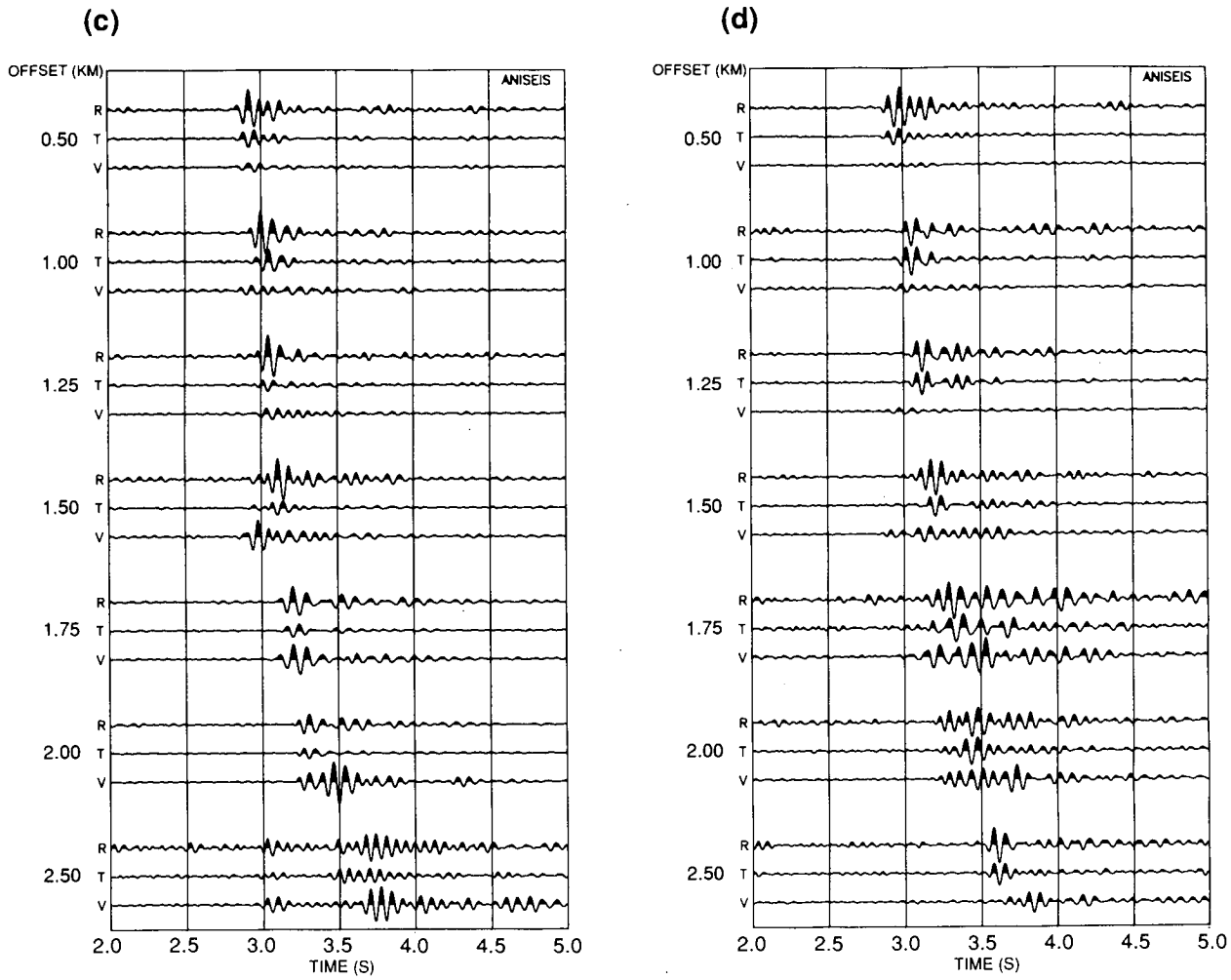

Fig. 3 (Cont'd).

Modelling raypaths in an isotropic structure

Figure 2a shows the isotropic velocity structure obtained from a near-offset VSP survey and Figure 2b shows shear-wave ray tracing from the walkaway offsets through this structure [density was derived from the algorithm of Gardener et al. (1974)]. Figure 4 shows the corresponding synthetic seismograms for in-line and cross-line source orientations to the 1950 m-level geophone. Substantial differences in arrival times between the field data in Figure 3 and the synthetic seismograms in Figure 4 show that, although the model gives appropriate arrival times for near-vertical propagation at the 500 m offset as would be expected, the differences in traveltime increase with offset to about 700 ms for the 2500 m offset. This indicates that horizontal velocities are substantially greater than vertical velocities which is characteristic of transversely isotropic structures.

Modelling raypaths in a transversely isotropic structure

The shear-wave ray tracing in Figure 2b shows that, except for the 2500 m offset, the raypaths are quite close to straight lines, particularly through the clay from 870 m to 1900 m. Although the incidence angles at the geophone are different from the isotropic raypaths in Figure 2b, the deviations of the raypaths are comparatively small and source-to-geophone straight lines are a good first-order approximation to the true raypaths. Arrival times were picked, as indicated by small solid triangles in Figures 3a and 3b. Figure 5a shows the estimated (group) velocity variations derived from these picks plotted against incidence angle assuming straight-line raypaths for walkaway WA1 in Figure 3. The estimated velocities for WA2 are almost identical. Extrapolation to the axes in Figure 5a suggests substantial transverse isotropy of about 34% *qSH*-wave and 24% *qSV*-wave anisotropies and 19% *P*-wave velocity anisotropy.

For transverse isotropy, the square of the *P*-wave phase velocity is expected to have an approximately sin 2θ variation with angle from the symmetry axis (with a, usually small, sin 4θ contribution), and the squares of the *SH*- and *SV*-wave phase-velocity variations are similarly expected to have approximately sin 2θ and sin 4θ variations, respectively, where the coefficients of the sin 4θ variations of the squares of *P*- and *SV*-wave phase velocities are equal and opposite in sign (Crampin, 1981). Seismic rays propagating at the group velocity, derived by differentiating the phase velocity, have more complicated surfaces, which may in some circumstances contain cusps. However, these simple geometric relationships are strictly valid at the axes (0° and 90°) where phase and group velocities are equal and provide simple inversion techniques for elastic constants.

Projecting the variations in Figure 5a to the axes at 0° and 90° provides four of the five elastic constants specifying a transversely isotropic solid. The fifth constant can be adjusted to match the details of the separation (in percent) between the two shear-wave group velocities. The elastic constants of this transversely isotropic model are listed in Table 2 and the velocity variations are shown in Figure 5b. The solid lines in the figure are the phase velocities showing the sin 2θ and sin 4θ variations. The dashed lines are the group velocities (joined to the appropriate phase velocity) where the *SV* curve displays the expected cusps. Estimated field group velocities are superimposed from Figure 5a and show a good match with the modelled group velocities. This model is used to provide a base from which to prepare further anisotropic models for the individual layers.

Since most of the transverse isotropy is expected to be in the clay interval (Brodov et al., 1984) from 870 m to 2050 m, a fifteen-layer model was made up containing 15% *SV*- and 18% *SH*-wave anisotropy in the layers above 870 m and 27%

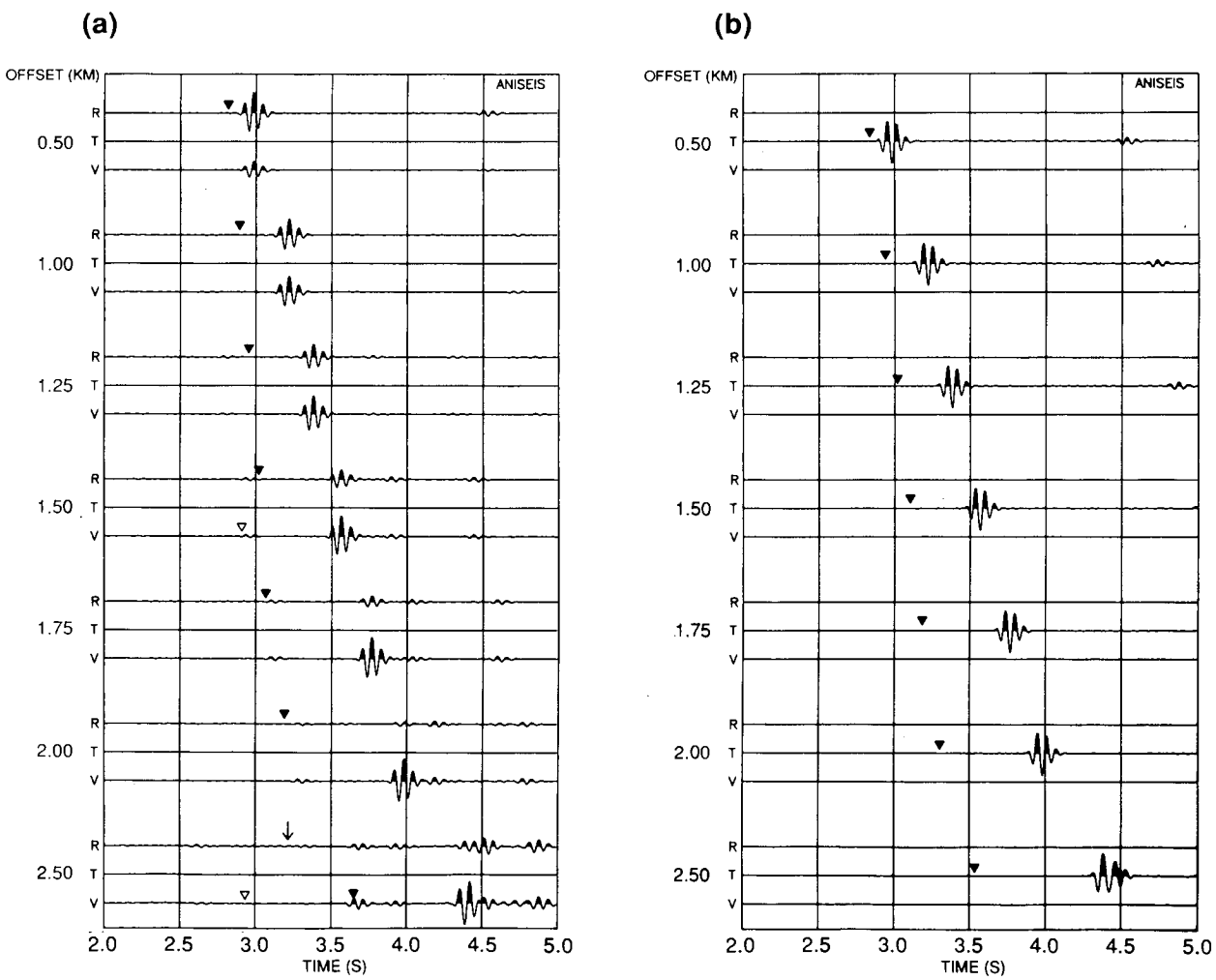

Fig. 4. Three-component synthetic seismograms for a walkaway survey to a geophone at 1950-m level through the multilayered isotropic structure in Figure 2a for **(a)** in-line, and **(b)** cross-line source orientations. Notation as in Figure 3.

SV- and 41% *SH*-wave anisotropy in the clay layers below level 870 m . A program was written to insert given percentages of *P*- and shear-wave anisotropy in each layer, given the velocities along the vertical symmetry axis in Figure 2a. The fifth constant was adjusted to match the *SV*-wave (and *P*-wave) sin 4θ variations. Figure 5c shows the velocity variations through layer No. 9 with 41% *SH*- and 27% *SV*-wave anisotropy in the anisotropic clay interval. There is a pronounced cusp. Figures 6a and 6b show synthetic seismograms calculated for in-line and cross-line source orientations for walkaways through this fifteen-layer transversely-isotropic model. Despite the relative simplicity of the modelling, most essential features of the field data in Figure 3 are reproduced, except for the variable sagittal to transverse coupling. The arrival times and amplitudes of all of the main phases are similar and, in particular, the arrival times and amplitudes of the anomalous phases at offsets of 1500 m and 2500 m marked by open triangles are similar. The anomalous phase at 1500 m offset is wholly determined by the cusp and is generated near the centre of the cusps in Figures 5b and 5c.

The first anomalous arrival at the 2500 m offset, marked by an open triangle in Figure 3a and matched by the synthetic seismograms, is the shear wave from a *P*-to-*S* conversion at the larger impedance contrasts above the top of the clay (above 870 m). There is a possible second anomalous arrival on the radial-component seismograms at 2500 m offset marked by an arrow. To demonstrate these arrivals in more detail, Figure 7 shows synthetic seismograms calculated for 100 m-interval offsets between 1000 and 2500 m in the transversely isotropic structure. The arrival just later than the arrow at the 2500 m offset can be traced directly to the cusp at 1500 m offset, showing that the arrival in Figure 3a is cuspidal. The cuspidal arrivals at the intervening 1750 m and 2000 m offsets are not sufficiently separated in time from the

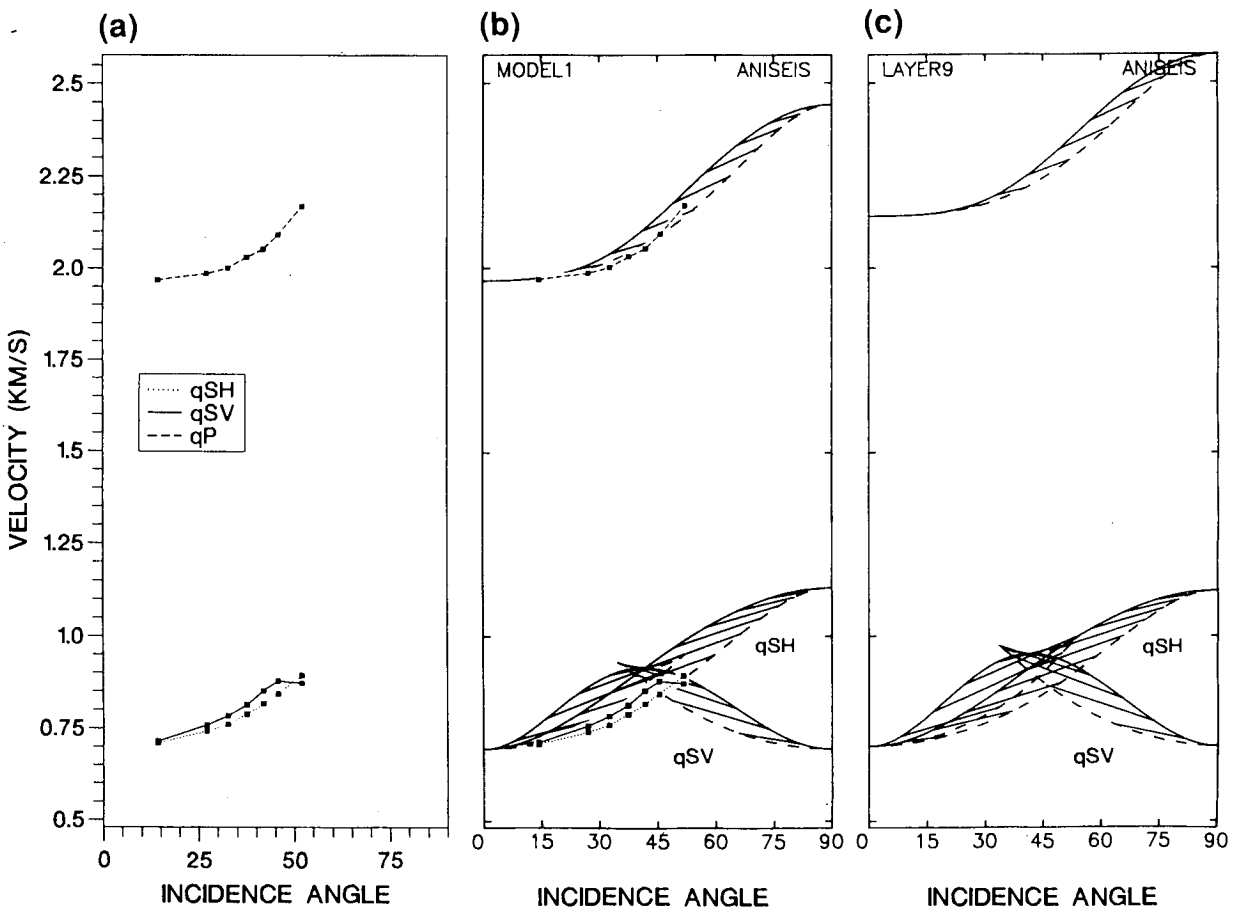

Fig. 5. **(a)** Velocities estimated from seismograms in Figures 3a and 3b assuming straight raypaths: dashed line is *P*-wave velocity variations; solid line is *SV*-wave variations; and dotted line is *SH*-wave variations. **(b)** Velocities in the transversely isotropic model matching the estimated velocities in (a). Solid lines are phase velocities and dashed lines are group velocities joined to equivalent phase velocity by lines at every 10° of phase-velocity direction. The group velocities from the observations in (a) are superimposed in (b). **(c)** Velocities in transversely isotropic layer 9 with same notation as (b).

main shear-wave arrivals to be clearly identified in Figure 3, but the general form of the arrivals from the *SV*-source orientation are well reproduced by the synthetic seismograms in Figures 6a and 6b.

We suggest that these models confirm that anomalously fast arrivals at offsets of 1500 m and 2500 m are generated by cusps. However, a characteristic feature of the field records that is not modelled by the transversely isotropic model in Figures 6a and 6b is the coupling between motion in the sagittal (V-R) plane and the transverse (T) direction which is a dominant feature of the field seismograms in all eight walkaways. Such coupling between sagittal and transverse-horizontal directions is characteristic of the azimuthal anisotropy of aligned vertical cracks (Crampin and Lovell, 1991).

Table 2. Elastic constants in 10^9 Pa for straight raypaths in Figure 5b and Layer 9 in Figure 5c. Density is $\rho = 2.11$ g/cm^3.

ELASTIC CONSTANTS FOR FIGURE 5.					
	$c_{1111} = c_{2222}$	c_{3333}	c_{1122}	$c_{3311} = c_{2233}$	$c_{2323} = c_{3131}$
Figure 5b	12.585	8.155	7.178	6.550	1.019
Figure 5c	14.027	9.663	8.052	7.796	1.040

Modelling raypaths in an azimuthally anisotropic structure

The presence of azimuthal anisotropy must be invoked to model the sagittal to transverse coupling in the field data; however, a full discussion of the azimuthal anisotropy is beyond the scope of this paper. In summary, the near-offset VSPs at Wells Nos. 85 and 87, not shown here, both display evidence of strong but very different near-surface azimuthal anisotropy in a homogeneous flat "layer-cake" stratigraphy. Well No. 87 shows a 20-ms delay between split shear waves established by a depth of 300 m, whereas No. 85 shows insignificant splitting at 300 m. The field data in Figure 3

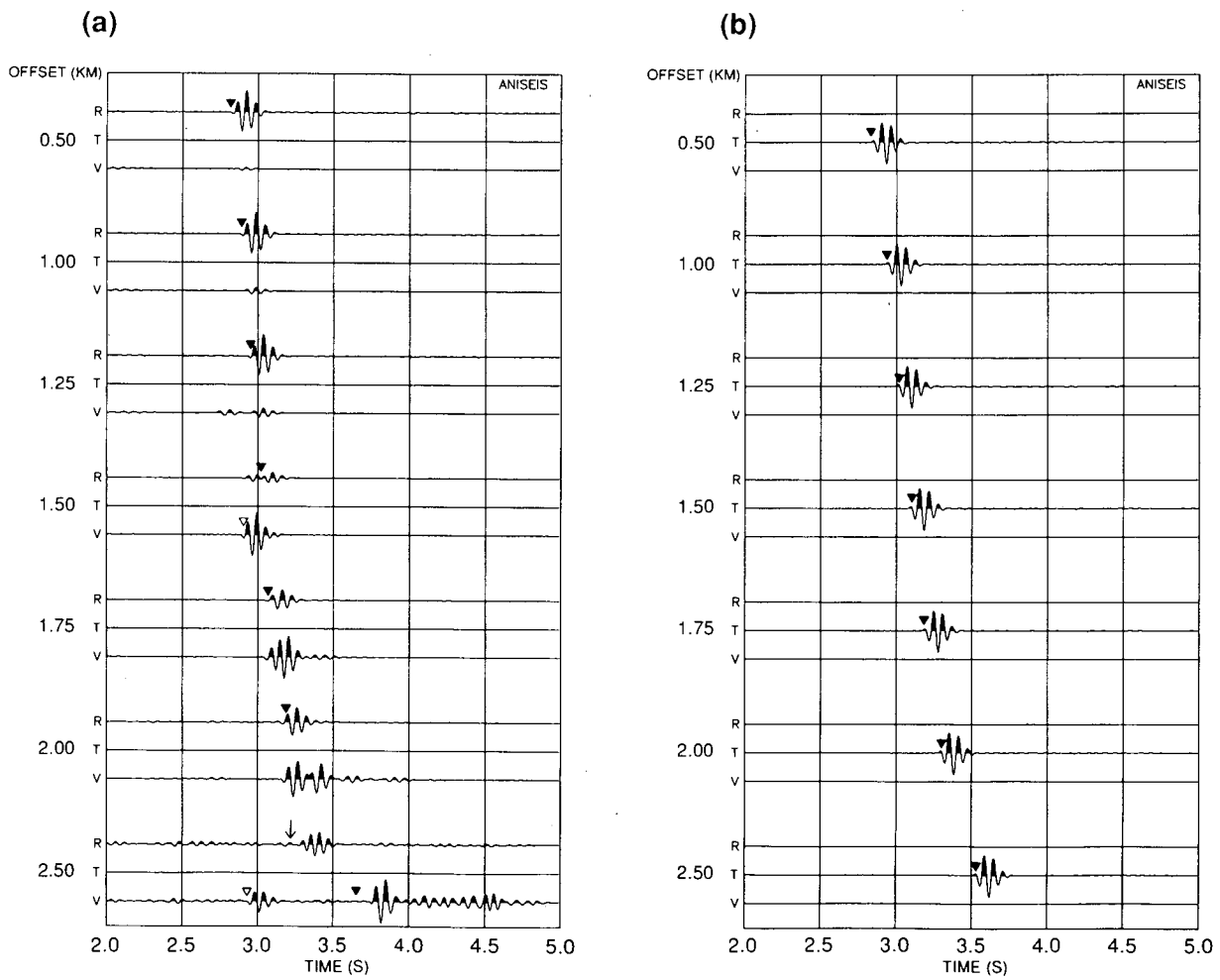

Fig. 6. Synthetic seismograms for a walkaway at azimuth N355°E modelling WA1 recorded with the geophone at the 1950 m level through the fifteen-layered transversely isotropic model for **(a)** in-line, and **(b)** cross-line source orientations.

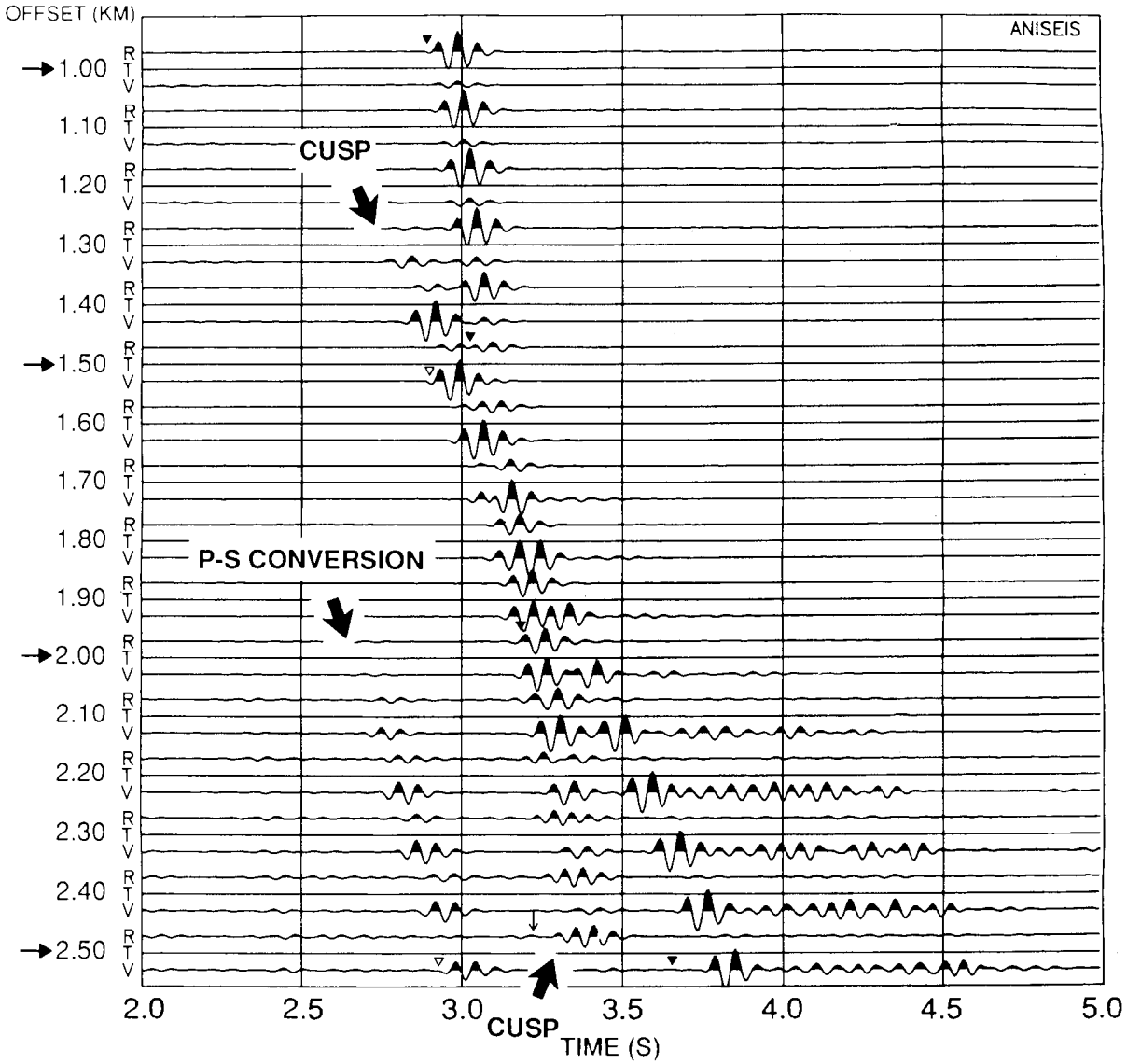

Fig. 7. Synthetic seismograms modelling WA1 (Figures 3a and 3b) from 1000-m offset to 2500-m offset at 100-m intervals, through the same transversely isotropic structure as Figure 6. Arrows in the left margin indicate offsets for which there are observations.

show strong coupling for near-vertical incidence at the 500 m offset. This can be modelled by introducing vertical cracks (Crampin and Lovell, 1991; Crampin, 1993) into the top 870 m with crack density $\varepsilon = 0.014$ and strike N203°E.

Figures 8a and 8b show synthetic seismograms through this orthorhombic structure for in-line and cross-line source orientations along an azimuth of N355°E modelling walkaway WA1. Comparison with the field data in Figure 3 shows that all the previous similarities in the sagittal plane and the transverse motion are preserved and that many features of the coupling between the sagittal and transverse motion are also reproduced. In particular, some features of the multiple shear-wave arrivals with different arrival times and polarizations as well as reverberatory *P*- and shear-wave coda (which could easily be mistaken for instrumental noise) also appear in the synthetic seismograms in Figures 8a and 8b. However, many details are not explained, particularly the relative amplitudes of the three-component signals which sometimes vary substantially between offsets in Figure 3a and 3c. These anomalies appear to be near-surface effects at the various source offsets caused by a phenomenon known as natural directivity, which we describe below.

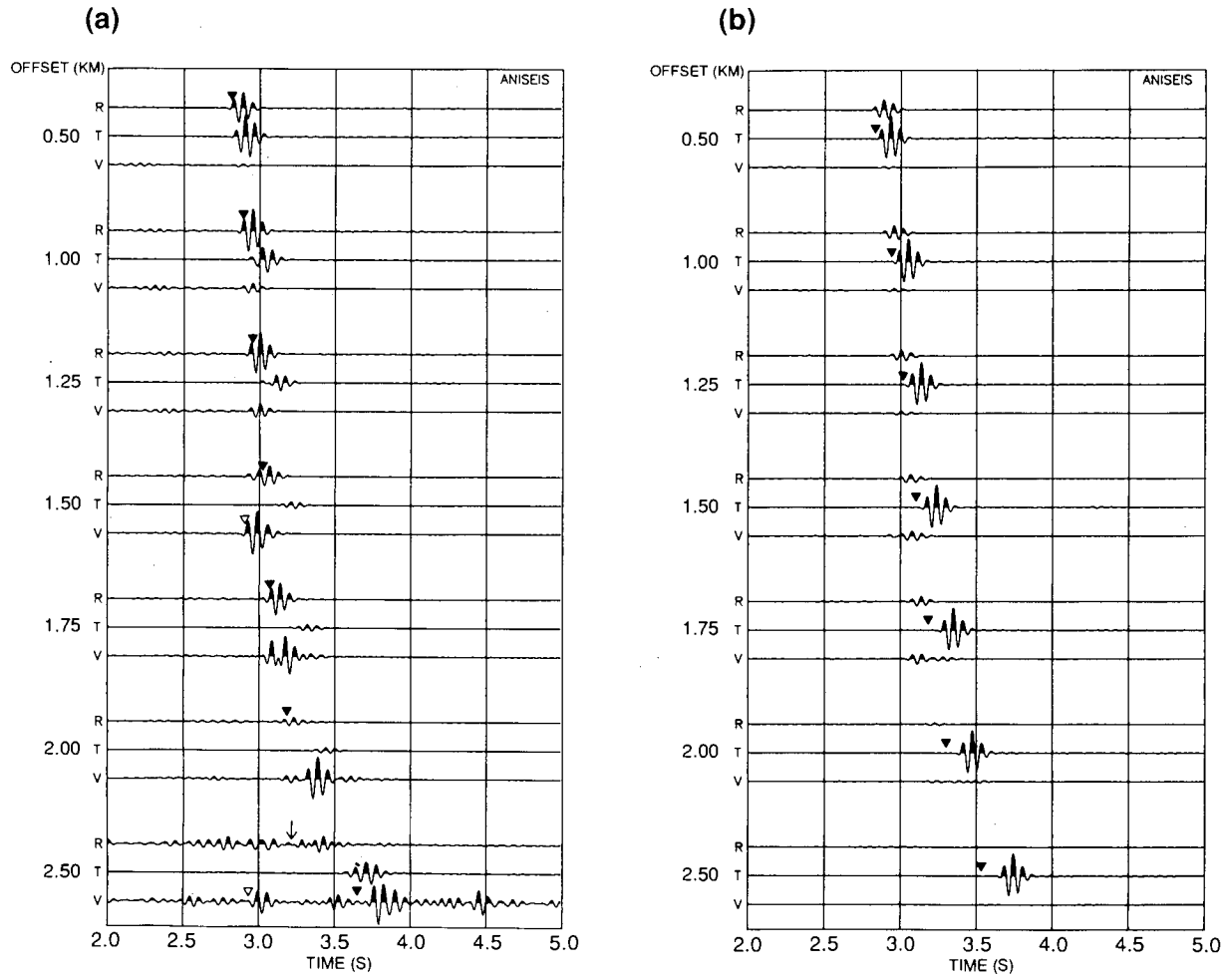

Fig. 8. Synthetic seismograms modelling WA1 (Figures 3a and 3b) through the same fifteen-layered model as in Figure 6, but now containing parallel vertical cracks in the layers above 870 m leading to azimuthal anisotropy for **(a)** in-line, and **(b)** cross-line source orientations.

Natural Directivity

The presence of strong near-surface anomalies in shear-wave behaviour, particularly the nonorthogonality of radiation patterns from orthogonal shear-wave sources, has been recognized in Russia (Puzirev et al., 1985) where it is known as natural directivity (ND). It may result in unpredictable shear waves from explosions and anomalies in polarization and radiation from surface shear-wave sources. The causes of ND are not fully understood. Variations in ND can sometimes be correlated with varying consolidation in poorly consolidated sediments and may vary substantially over distances of metres (Puzirev et al., 1985). ND may also be caused by multiple reflections from inclined interfaces and near-surface bedding.

It is tempting to dismiss ND as shear-wave statics, in the same way as *P*-wave statics is usually dismissed as an uninteresting necessity. However, since details of waveforms are essential for interpreting shear waves correctly, identifying ND is essential for accurate evaluation of shear-wave behaviour. Pronounced delays between split shear waves (100 ms in 600 m) at a VSP experiment in the Geysers geothermal site in California were originally thought to be caused by the presence of parallel cracks (Majer et al., 1988). These large delays were actually caused by *P*-to-*S* conversions in an 11 m-thick isotropic surface layer with very low shear-wave velocity (Campden et al., 1990) and the large delays were independent of the crack geometry below the surface layer.

Since the effects of ND frequently display characteristic anisotropic features and can vary rapidly over short distances, it has implications for the detailed interpretation of any shear-wave source deployed at the surface. Unless recognized, ND can complicate the interpretation of shear-wave reflection surveys and, as here, walkaway shear-wave VSPs, where it would be impracticable to make a detailed study of

the uppermost few hundred metres at each offset. We suggest that the irregularities of the relative amplitudes of three-component field data in Figure 3 were probably caused by variations in ND near each offset source location. The amplitudes of each three-component seismogram could be matched by varying the near-source structure, particularly the orientation of cracks, at the site of each shear-wave source.

Conclusions

To model arrival times of shear waves in the walkaway VSPs transverse isotropy with a vertical axis of symmetry was included, with 41% *SH*- and 27% *SV*-wave anisotropy in 1200 m-thick Maikop clay. Subsequently, anomalously fast arrivals, particularly the 200 ms early precursor at 1500-m offset, have been identified and matched with synthetic seismograms. These arrivals are generated at cusps in the *SV*-wave group-velocity sheets. Such arrivals cannot be explained without assuming pronounced transverse isotropy and modelling with full-wave synthetic seismograms. They may be important for exploration seismology as they provide additional signals, with different characteristics that may be used to examine the internal structure of a zone of interest. Moreover, if wrongly identified, they could lead to (possibly severe) misinterpretations of subsurface structure. Azimuthal anisotropy of vertical cracks, with crack density $\varepsilon = 0.014$ and strike N203°E in the top 870 m, must also be included to reproduce the sagittal to transverse coupling of the three-component recordings.

The data show anomalies in the relative amplitudes of three-component seismograms that are probably caused by variations of natural directivity (ND) near the positions of the shear-wave source locations. The effects of ND could have serious implications for the detailed interpretation of all experiments involving near-surface shear-wave sources.

References

Brodov, L.Y., Evstifeyev, V.I., Karus, E.V. and Kulichikhina, T.N., 1984, Some results of the experimental study of sedimentary rocks using different types of waves: Geophys. J. Roy. Astr. Soc. **76,** 191-200.

_____, Zatsepin, S.V. and Tertychniyi, V.V., 1992, Kinematic inversion of seismic data for determination of crack and pore structure in anisotropic reservoir rock: Presented at the 5th Internat. Workshop on Seismic Anisotropy, Banff, Abstr. 22.

Campden, D.A., Crampin, S., Majer, E.L. and McEvilly, T.V., 1990, Modelling the Geysers VSP: a progress report: The Leading Edge **9,** 8, 36-39.

Castagna, J.P., Batzle, M.L. and Eastwood, R.L., 1985, Relationships between compressional-wave and shear-wave velocities in clastic silicate rocks: Geophysics **50,** 571-581.

Crampin, S., 1981, A review of wave motion in anisotropic and cracked elastic-media: Wave Motion **3,** 343-391.

_____, 1987, Geological and industrial implications of extensive-dilatancy anisotropy: Nature **328,** 491-496.

_____, 1989, Suggestions for a consistent terminology for seismic anisotropy: Geophys. Prosp. **37,** 753-770.

_____, 1993, Arguments for EDA: Can. J. Expl. Geophys. **29,** 18-30.

_____ and Lovell, J.H., 1991, A decade of shear-wave splitting in the Earth's crust: what does it mean? what use can we make of it? and what should we do next?: Geophys. J. Internat. **107,** 387-407.

Gardener, G.H.F., Gardener, L.W. and Gregory, A.R., 1974, Formation velocity and density - the diagnostic basics for stratigraphic traps: Geophysics **39,** 770-780.

Jolly, R.N., 1956, Investigation of shear waves: Geophysics **21,** 905-938.

Kaarsberg, E.A., 1968, Elasticity studies of isotropic and anisotropic rock samples: Trans. Soc. Min. Eng. **241,** 470-475.

Levin, F.K., 1979, Seismic velocities in transversely isotropic media: Geophysics **44,** 918-936.

MacBeth, C., Wild, P., Crampin, S. and Brodov, L.Y., 1993, Optimal acquisition geometry for recording shear-wave anisotropy: Can. J. Expl. Geophys. **29,** 132-139.

Majer, E.L., McEvilly, T.V., Eastwood, F.S. and Myer, L.R., 1988, Fracture detection using *P*-wave and *S*-wave vertical seismic profiling at the Geysers: Geophysics **53,** 76-84.

Musgrave, M.J.P., 1954, On the propagation of elastic waves in aeolotropic media II. Media of hexagonal symmetry: Proc. Roy. Soc. London **A226,** 356-366.

Nalivkin, D.V., 1973, Geology of the U.S.S.R.: Oliver and Boyd, Edinburgh.

Postma, G.W., 1955, Wave propagation in a stratified medium: Geophysics **20,** 780-806.

Puzirev, N.N. and Brodov, L.Y., 1969, Efficient *SH*-wave generation: Geol. Geofiz. **5,** 81-88.

_____,Trigubov, A.V. and Brodov, L.Y., 1985, Seismic prospecting methods in shear and converted waves (in Russian): Nedra, Moscow.

Riznichenko, Y.V., 1949, On seismic quasi-anisotropy (in Russian): Izv. Akad. Nauk SSSR, Ser. Geogr. Geofiz. **13,** 518-544.

Taylor, D.B., 1990, ANISEIS manual: version 4.5: Applied Geophysical Software Inc., Houston.

Uhrig, L.F. and Van Melle, F.A., 1955, Velocity anisotropy in stratified media: Geophysics **20,** 774-779.

White, J.E., 1982, Computed waveforms in transversely isotropic media: Geophysics **47,** 771-783.